DROP DEFORMATION AND BURST IN TWO-DIMENSIONAL FLOWS

Thesis by

Barry Jerome Bentley

In Partial Fulfillment of the Requirements

for the Degree of

Doctor of Philosophy

California Institute of Technology

Pasadena, California

1985

(Submitted August 14, 1984)

ACKNOWLEDGMENT

I wish to express my appreciation to my advisor, Professor Gary Leal, for suggesting the research topic and for his patient guidance and help with the project and with the preparation of this manuscript. I have greatly benefitted from my association with him and his research group.

Caltech has provided me an excellent environment for this research, for which I am grateful, The faculty, students, and staff have been a pleasure to know and to work with. It would be impossible to mention everyone who has contributed to this thesis, but I would like to acknowledge a few who have made direct contributions. Seichi Nakatawase constructed a major portion of the experimental apparatus with great care and fine craftsmanship. Gerry Fuller made numerous valuable suggestions concerning the experimental design. Howard Stone conducted several of the experiments discussed in this thesis. Ray Eskenazi of the Jet Propulsion Laboratories designed the camera - computer interface. I would also like to thank Professor Acrivos of Stanford for several enlightening discussions during his sabattical year at Caltech and for consenting to return to Caltech for my doctoral examination .

My years at Caltech have been immensely enjoyable, largely due to the interactions with the people I have met here. To mention just a few, Bill Olbricht, Mike Duncan, Gary Whatley, Russ Bone, Dave Strand, Tony Geller, Joe Leone, Rohit Khanna, and Chris Chow have made my stay here interesting and pleasurable.

Three years of my research were funded by the National Science Foundation through their Graduate Research Fellowship program. My thanks to them and to the Chemical Engineering Department for the Research Assistantships

which funded the remainder of my research.

Finally, I would like to thank my family for their support, especially my wife Therese who has been my main source of inspiration. Without her, this thesis would never have been completed, and it is to her and to our unborn child that this work is dedicated.

ABSTRACT

The deformation and burst of small fluid droplets suspended in a second immiscible fluid undergoing a steady linear shearing motion are discussed. The effects of Capillary number, ratio of fluid viscosities, and flow type are considered both experimentally and theoretically.

The experiments are unique in that a spectrum of strong two-dimensional flows (those with the magnitude of the strain rate exceeding that of the vorticity) was considered. These flows were generated in a four roll mill specifically designed for the experiments. Previous investigations had been limited to one specific strong flow owing to the difficulty in holding drops stationary at the stagnation point in such flows. We overcame this obstacle by using a computer interfaced to a digital video camera to locate the drops in the flow field and adjust the roller speeds to effect an inferential feedback control scheme. It is believed that the control system implemented for the present experiments could be adapted to a variety of fluid flow experiments with similar control problems.

Drop deformation and burst experiments were performed for viscosity ratios ranging from 0.001 to 27., and flows with ratio of vorticity to strain rate ranging from zero to 0.667. In a typical experiment a drop went through a succession of increasingly deformed steady shapes as the Capillary number was slowly increased with the flow type constant. The appearance of the drop was recorded photographically. In most cases, a Capillary number was reached where no steady shape was possible, and this was recorded as the critical Capillary number for drop burst. In a few cases with high viscosity ratio and large vorticity to strain rate ratio, drop burst was impossible. In cases where burst occurred, the transient motion of the drops at the critical Capillary number was

observed. The drops continued to deform, but did not break into fragments until the flow was turned off. They then either fragmented or returned to the spherical shape through a complex interfacial tension driven motion.

The experimental deformation and burst observations were compared to the predictions of several available theories. Separate theories apply to cases where the deformation is small (nearly spherical drops) or large (threadlike drops). Comparisons to existing numerical results for one particular viscosity ratio are also included. Agreement between the experimental observations and the predictions of the theories was very good.

TABLE OF CONTENTS

LIST OF FIGURES

LIST OF TABLES

NOMENCLATURE

a	undeformed drop radius
a_i	coefficients in small deformation theory
A	$(1+\alpha)/2$
$\mathbf{A}$	matrix
b	four roll mill dimension; measure of eccentricity of particle
$\mathbf{b}$	vector
b_i	coefficients in small deformation theory
B	shortest semi-axis of deformed drop
c	constant
Ca	Capillary number ($= G\mu a/\sigma$)
Ca_c	critical Capillary number for drop burst
D	linear combination of components of deformation tensor
D_f	scalar deformation measure ($=(L-B)/(L+B)$)
$D_{f,c}$	deformation at critical Capillary number
$\mathbf{E}$	symmetric portion of velocity gradient tensor
f_i	four roll mill calibration functions
f	function of viscosity ratio in Taylor [1934] theory
f	internal viscosity of microstructure; shape function
F_{ij}	component of $\mathbf{F}$
$\mathbf{F}$	second order deformation tensor
$\mathbf{F}'$	disturbance to $\mathbf{F}$
g	measure of microstructure response to straining motion
G	shear rate
G_0	overall transfer function
G_c	controller transfer function
G_d	drop response transfer function

G_f	fluid response transfer function
G_m	measurement delay transfer function
G_v	disturbance transfer function
H_{ijkl}	component of **H**
H	fourth order deformation tensor
H'	disturbance to **H**
K_c	gain of proportional controller
K^2	parameter in slender drop theory
L	longest semi-axis of deformed drop
L	normalized velocity gradient tensor
m_1, m_2	major and minor axes of elliptical streamlines
M	geometric point
n	unit outward normal to surface
N	geometric point
p	pressure in suspending fluid
p'	pressure in drop fluid
P	geometric point
r	control parameter; magnitude of position vector
r_e	equivalent axis ratio of particle
r_r	roller radius
R	position of drop surface
R_1, R_2	principal radii of curvature
Re	Reynolds number ($= \rho G a^2 / \mu$)
R	vector characterizing microstructure
s	Laplace variable; integration variable
S	set of points on drop surface; linear combination of F_{ij}
t	time

t_d	measurement delay
T	contraction of **F** with itself
T	total stress tensor
u	velocity vector in exterior fluid
u'	velocity vector inside drop
u_r	component of velocity in cylindrical coordinates
u_x	component of velocity in cylindrical coordinates
u_ϑ	component of velocity in cylindrical coordinates
x	position vector
x	coordinate
x'	position in rotated coordinate system
x_0	initial position
x_s	stagnation point position
x_{ss}	stagnation point set point
y	coordinate
y'	position in rotated coordinate system
y_0	initial position
y_s	stagnation point position
y_{ss}	stagnation point set point
z	coordinate
z_s	displacement of stagnation point along eigenvector
z_{ss}	displacement of stagnation set point along eigenvector
$\tilde{z}$	Laplace transform of drop position
$\tilde{z}_s$	Laplace transform of stagnation point position
$\tilde{z}_{ss}$	Laplace transform of stagnation set point
α	flow type

β	parameter in tensor microstructure theory
ε	small parameter
κ	density ratio ($= \rho'/\rho$)
λ	viscosity ratio ($= \mu'/\mu$)
ν	parameter related to internal pressure in slender drop theory
ν	eigenvalue in flow classification theory
ν^+	real part of eigenvalue with largest real part
μ	viscosity of suspending fluid
μ'	viscosity of drop fluid
ω_i	rotational velocity of roller i
ω_v	rotational velocity of particle due to vorticity
ω_e	rotational velocity of particle due to extension
Ω	vorticity tensor
ρ	density of suspending fluid
ρ'	density of drop fluid
σ	interfacial tension
τ	response time of suspending fluid
ϑ	angle with x axis
ϑ_c	angle at critical Capillary number
ϑ_e	angle of exit streamline
ξ	dimensionless length in slender drop theory
ξ	elastic restoring force in microstructure deformation theory
ξ	eigenvectors

1.0 INTRODUCTION

In this work, we consider the behavior of a fluid drop, freely suspended in a second, immiscible, viscous fluid which is undergoing a general linear two-dimensional flow. The flow-induced stress on the drop surface tends to deform the drop, and the interfacial tension between the phases resists this deformation. Under some conditions, the interfacial forces are insufficient to balance the viscous stresses, and the drop bursts. The problem is of both practical and academic interest, and has thus received considerable attention in the fluid mechanics literature over the past fifty years.

In most practical applications, the objective is to disperse one fluid phase in another, either to form an emulsion, or to increase the surface area between the two phases for more efficient heat and/or mass transfer. In these cases, determination of flow conditions which result in drop breakup is of paramount importance. Examples include dispersion of anti-static or anti-soiling agents, dispersion of color concentrates, and blending of immiscible polymer systems to form two phase structures of unique properties (Grace [1971]).

Even when the drop does not break, the distortion produced by a given flow is of interest in understanding the rheological behavior of flowing emulsions. Emulsions are known to exhibit such non-Newtonian characteristics as shear-dependent viscosity, viscoelasticity, and normal stress differences in rectilinear flow, even when the concentration of the dispersed phase is small (Frankel and Acrivos [1970], Barthes-Biesel and Acrivos [1973b]). From a knowledge of the deformation of the drops forming the dispersed phase and of the disturbance flow in their vicinity, a constitutive equation can be developed (at least in principle) for the emulsion. The advantage of this microstructural approach is that it exposes the functional relationship between the stress and the physical

properties of the two phases. This is in contrast to the phenomenological approach to development of rheological equations of state, which generally results in constitutive equations which contain parameters that are not directly related to physical properties and are difficult or impossible to measure experimentally. A possibility is that the study of emulsion rheology will aid in formulating constitutive equations which can be applied to a more general class of materials exhibiting similar non-Newtonian behavior (e.g., polymer solutions and melts).

The drop deformation problem also presents interesting theoretical challenges. The equations of motion must be solved for the flow within and around the drop, and boundary conditions applied on the surface of the drop, the shape of which must be determined as part of the solution. To date, no general solution has been found, but progress has been made through asymptotic analyses, considering conditions for which the drops are either nearly spherical, or highly deformed. In addition, several numerical methods have been employed, but they have been limited to either special flow fields (e.g., axisymmetric extensional flow (Rallison and Acrivos [1978])), or particular values of the viscosity ratio (Rallison [1981]).

A relatively large number of experimental studies of drop behavior in viscous shear flows have been reported. However, almost all of the available data concern drops in either two-dimensional irrotational flow or in simple shear flow, where the vorticity and strain rate are equal. In irrotational flow produced in a four roll mill (Taylor [1934], Rumscheidt and Mason [1961], Grace [1971]), the experiments are particularly difficult because drops positioned at the lone stagnation point in the flow field are highly unstable to disturbances in position, tending to be carried away from this point by the flow with a velocity that is pro-

portional to displacement. Naturally, this makes observations difficult, and consequently fewer data are available for this flow than for simple shear. In simple shear flow, the problem of controlling the drop position is considerably less severe, since there is a plane of stagnant flow, and drops not centered in the plane merely move parallel to it with constant velocity.

Several qualitative features of drop behavior differ dramatically between the two flows, owing to the presence of vorticity in simple shear and its absence in irrotational flow. For example, drops whose viscosity is greater than about 3.5 times the viscosity of the suspending fluid burst readily in irrotational flow, but refuse to burst in simple shear, instead attaining a limiting deformation as the shear rate is increased. Motivation thus exists for studies of other so-called "strong" flows (where the magnitude of the strain rate exceeds that of the vorticity) intermediate between simple shear and irrotational flow. These flows can be conveniently generated in the four roll mill (which is also used to produce the irrotational flow), but unfortunately the above-mentioned control problem exists for these flows as well, and is in some ways even more difficult.

The present paper discusses the implementation of a computer-based system to control the drop at the stagnation point of strong flows generated in a four roll mill. This technique allowed us to obtain better data for irrotational flow than was previously possible with hand controlled experiments, and also allowed studies of intermediate strong flows for which experiments would have otherwise been impossible. The observations are compared to the predictions of several of the available theories and numerical studies.

1.1 PROBLEM STATEMENT

A drop of volume $4\pi a^3/3$, viscosity μ' and density ρ', is freely suspended in an infinite bath of a second fluid of viscosity μ and density ρ. The interfacial tension between the two immiscible fluids is σ. The interface is assumed to transmit tangential stresses undiminished, thus other possible surface effects such as interfacial viscosity and interfacial tension gradients are neglected. The suspending fluid is undergoing a steady motion at infinity which is a linear shear flow in a frame of reference in which the drop center is stationary. This situation is illustrated schematically in Figure 1.1. Both fluids are Newtonian and incompressible, so that the governing equations are the Navier-Stokes equations and the continuity equation, applied inside and outside the drop, with appropriate boundary conditions on the drop surface.

The fluid velocity inside the drop, $\mathbf{u}'$, and the fluid velocity outside the drop $\mathbf{u}$ are both governed by the Navier-Stokes equations and continuity equations, i.e., inside

$$\rho'\left(\frac{\partial \mathbf{u}'}{\partial t} + \mathbf{u}'\cdot\nabla\mathbf{u}'\right) = \mu'\left(\nabla^2\mathbf{u}'\right) - \nabla p' \,, \tag{1.1}$$

$$\nabla\cdot\mathbf{u}' = 0 \,, \tag{1.2}$$

and outside

$$\rho\left(\frac{\partial \mathbf{u}}{\partial t} + \mathbf{u}\cdot\nabla\mathbf{u}\right) = \mu\left(\nabla^2\mathbf{u}\right) - \nabla p \,, \tag{1.3}$$

$$\nabla\cdot\mathbf{u} = 0 \,. \tag{1.4}$$

The appropriate boundary condition far from the drop is

$$\mathbf{u} \to \nabla\mathbf{u}\cdot\mathbf{x} \text{ as } \mathbf{x}\to\infty \,. \tag{1.5}$$

At the drop surface S, the velocity is continuous,

$$\mathbf{u}' = \mathbf{u}\,, \tag{1.6}$$

but the stress suffers a jump in the normal direction owing to the interfacial tension:

$$p' - p + \mu \mathbf{n}\cdot\mathbf{E} - \mu' \mathbf{n}\cdot\mathbf{E}' = \sigma\left[\frac{1}{R_1} + \frac{1}{R_2}\right]. \tag{1.7}$$

R_1 and R_2 are the principal radii of curvature of the surface S, $\mathbf{n}$ is the unit outward normal, and $\mathbf{E}'$ and $\mathbf{E}$ are the symmetric portions of the velocity gradient tensors $\nabla\mathbf{u}'$ and $\nabla\mathbf{u}$, respectively. Finally, the equation for the evolution of the drop shape is written symbolically as:

$$\frac{dS}{dt} = \mathbf{u}\cdot\mathbf{n}\,. \tag{1.8}$$

When these equations are put in dimensionless form, with the undeformed radius of the drop, a, as the characteristic length scale, the inverse of the magnitude of the velocity gradient tensor, G^{-1}, as the characteristic time scale, and Ga as the velocity scale, the following dimensionless parameters appear:

$$\lambda = \frac{\mu'}{\mu} \qquad \text{(viscosity ratio)}\,, \tag{1.9}$$

$$Ca = \frac{G\mu a}{\sigma} \qquad \text{(Capillary number)}\,, \tag{1.10}$$

$$Re = \frac{\rho G^2 a}{\mu} \qquad \text{(Reynolds number)}\,, \tag{1.11}$$

$$\kappa = \frac{\rho'}{\rho} \qquad \text{(density ratio)}\,. \tag{1.12}$$

We will restrict our attention to cases where the viscous effects dominate, so that the Reynolds number based on the drop size is negligible. We also consider only neutrally buoyant drops, so that $\kappa = 1$. In this case, the evolution of the drop shape will depend only on the viscosity ratio, the Capillary number, and

the nature of the applied flow. Our experiments were limited to two-dimensional flows of the type which can be generated in the four roll mill. The form of the velocity gradient tensor is characterized by a single parameter α, defined by (2.1), which specifies the relative strength of the strain rate and vorticity in the flow. In particular, $\alpha = -1$ for pure rotational flow, $\alpha = 0$ for simple shear flow, and $\alpha = +1$ for irrotational flow.

In drop deformation experiments, photographs of the drop are taken with the camera mounted perpendicular to the plane of the flow, yielding a projection of the drop in the $z = 0$ plane. For convenient comparisons to theoretical predictions, two distinct scalar measures of drop deformation are customarily defined. These are illustrated in Figure 1.2. The first, which is appropriate for nearly spherical drops, defines the deformation in terms of the longest and shortest semi-axes of the elliptical drop cross section (L and B respectively). The definition is given by (Taylor [1934]):

$$D_f = \frac{L - B}{L + B}. \tag{1.13}$$

This quantity is zero for spherical drops and asymptotically approaches one for infinitely extended drops. When L/B is large (the drops are highly deformed), D_f changes very little with increasing L/B, so in this case a different measure of the deformation is more appropriate. We choose the ratio of the half-length of the deformed drop to the undeformed radius, L/a. In both cases, the orientation angle of the drop (the angle between the longest axis of the drop and one principal axis of the rate of strain tensor) is also measured.

In our experiments we have focussed attention on two aspects of drop behavior. First, we have investigated the equilibrium deformation of drops (where $dS/dt = 0$ for all points of S) in steady flows as a function of Ca, for various values of

viscosity ratio and flow type:

$$D_f = D_f\,(\,Ca\,;\lambda,\alpha) \quad \text{or} \quad L/a = L/a\,(\,Ca\,;\lambda,\alpha)\,. \tag{1.14}$$

For some combinations of viscosity ratio and flow type, no stable steady shape is possible for Capillary numbers greater than some critical value, Ca_c. The conditions which lead to this drop burst are of considerable practical interest, so we have also investigated the critical Capillary number as a function of viscosity ratio in a variety of different flow types:

$$Ca_c = Ca_c\,(\lambda;\alpha)\,. \tag{1.15}$$

The maximum stable deformation (the deformation at Ca just below Ca_c) and corresponding orientation angle have also been measured:

$$D_{f_c} = D_{f_c}\,(\lambda;\alpha)\,, \tag{1.16}$$

$$\vartheta_c = \vartheta_c\,(\lambda;\alpha)\,. \tag{1.17}$$

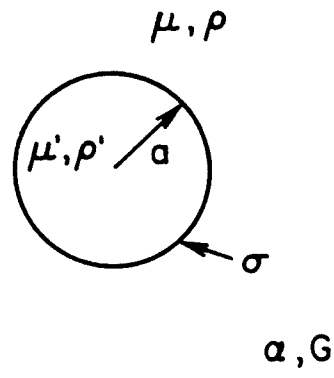

Figure 1.1
Schematic of problem

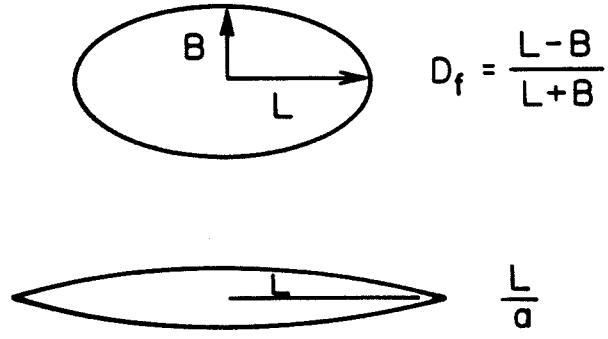

Figure 1.2
Scalar measurements of deformation

1.2 PREVIOUS WORK

Studies of drop deformation and burst date back at least fifty years, to the pioneering work of G.I. Taylor [1932, 1934]. He investigated drop behavior experimentally in simple shear flow, using a parallel band apparatus to generate the flow, and apparently invented the four roll mill in order to study the same problem for an irrotational flow field. Although few in number, Taylor's experiments uncovered most of the qualitative aspects of the drop deformation and burst process, including the following observations:

1. At low flow strengths, drops of all viscosity ratios deform into prolate spheroids. The longest axis of the drop is initially aligned with the principal axis of strain for both irrotational and simple shear flows.
2. When the drop viscosity is low compared to that of the suspending fluid, the critical Capillary number for burst becomes quite large, and the drops prior to burst attain highly deformed shapes with pointed ends. Under some conditions, small drops are ejected from these pointed ends, a phenomenon which has come to be called "tip streaming."
3. When the ratio of drop to suspending fluid viscosity is large, drop behavior is qualitatively different in simple shear and irrotational flow fields. In irrotational flows, burst occurs at low Ca. In simple shear, on the other hand, the drops assume slightly deformed shapes which are unaffected by further increases in the shear, and drop burst becomes impossible.

To explain some of his observations, Taylor [1932, 1934] developed two theories valid for small departures from sphericity, the first for $Ca \ll 1$ and $\lambda = O(1)$, and the second for $\lambda \gg 1$ and $Ca = O(1)$ for a simple shear flow. In both cases, Taylor used the general solution of the creeping flow equations due to Lamb to calculate the velocity fields in and around a spherical drop, which

satisfied all of the boundary conditions on the spherical surface except for the normal stress condition. This latter condition was then used to calculate the first correction to the spherical shape. In the first case, $Ca \ll 1$ and $\lambda = O(1)$, Taylor's analysis showed that the the deformation parameter, D_f, is related to the Capillary number by

$$D_f = Ca\, f(\lambda)\,, \tag{1.18}$$

with $f(\lambda)$ given by

$$f(\lambda) = \frac{19\lambda + 16}{16\lambda + 16}. \tag{1.19}$$

This relation proved valid at low deformations for all cases considered by Taylor, and was at least qualitatively accurate for surprisingly large values of D_f in some cases.

Taylor's [1934] high viscosity ratio theory for simple shear flow led to the result

$$D_f \to \frac{5}{4\lambda} \text{ as } \lambda \to \infty\,. \tag{1.19}$$

Subsequent researchers refined the small deformation theory. Cox [1969] analyzed the situation for which the deformation was slight, using an expansion in a small parameter representing the deviation from sphericity, so that the same result could be applied when either the flow was weak or the viscosity ratio large. He also examined drop response to time dependent flow fields, including a detailed study of the approach to equilibrium of a viscous drop in a rotational flow field suddenly started from rest. Barthes-Biesel and Acrivos [1973a] carried the small deformation analysis to higher order in the deformation, using a computer to perform the extensive algebra required. Their approach, discussed more fully in Section 3.1, also provides predictions for drop burst. The predic-

tions of this theory are compared to the observations in Sections 4.1 and 4.2.

Taylor [1964] was also apparently the first to apply the techniques of slender body theory for low viscosity ratio drops, which are observed to take on highly deformed steady shapes. His analysis was somewhat sketchy, but clarifications have been published by Buckmaster [1972, 1973] and Acrivos and Lo [1978]. These papers considered bubbles or drops in axisymmetric extensional flows. Extensions of the theory to the experimentally realizable cases of two-dimensional irrotational flow and simple shear flow have been published by Hinch and Acrivos [1979, 1980]. The predictions of these large deformation theories are discussed in Section 3.2, with comparisons to the experiment found in Sections 4.1 and 4.2.

To bridge the gap between the small deformation and large deformation theories, several numerical studies have been undertaken. The problem is not easily amenable to standard finite-difference methods, since the boundaries are neither geometrically simple, nor of known conformation. Instead, use is made of the boundary integral method first applied by Youngren and Acrivos [1976]. In this technique, the Stokes equations are put into an integral form whose solution only requires evaluation of unknown velocity and stress components on the drop surface. This technique was first applied for a bubble ($\lambda = 0$) in axisymmetric flow (Youngren and Acrivos [1976]). Subsequently, solutions for a drop of arbitrary viscosity ratio in an axisymmetric flow (Rallison and Acrivos [1978], and for a drop with a viscosity ratio of one in a variety of flow fields, including simple shear and two-dimensional irrotational flows (Rallison [1981]), were published. The results of this latter study are discussed in Section 3.3, and compared to the experimental results in Sections 4.1 and 4.2.

On the experimental side, a number of additional studies of drop deformation and burst have followed Taylor's early work. Rumscheidt and Mason [1961] considered both irrotational and simple shear flows, but with the experiments in the former case being limited in scope owing to the difficulty in controlling the drop position. They classified the limiting behavior (with increasing shear rate) of drops in simple shear flow, reporting three main types of behavior; breakup by the tip streaming process originally described by Taylor [1934] (Class A), breakup by "necking" at the center of the drop (Class B), and attainment of a limiting deformation without burst (Class C). The second mode was further broken down into cases where the drop broke with only moderate extension (Class B-1), and cases where the drop extended into a long thread before breakup (Class B-2). The tip streaming mode dominated the shear flow observation for low viscosity ratios, and limiting deformations were found for a viscosity ratio above about 3.5. For the irrotational flow, Class B-2 breakup was noted for λ = 1.0 and 6.0, and Class A observed for λ = 0.0002. The later investigation of Torza, Cox, and Mason [1972] clarified the mode of burst for intermediate viscosity ratio drops in shear flows. When the shear rate was increased slowly, so that the drops went through a series of equilibrium shapes, Class B-1 burst dominated. When the drops were subjected to higher dG/dt, Class B-2 breakup was observed. They also observed that tip streaming for low λ systems seemed to be promoted by rapid changes in shear rate. When the shear rate was increased slowly, low viscosity ratio drops still formed pointed ends, but small fragments were not ejected. Torza, Cox, and Mason [1972] also considered the approach to an equilibrium deformation of a drop subjected to a simple shear started impulsively from rest, comparing their results to the theory of Cox [1969].

Grace [1971] performed the most comprehensive set of drop breakup experiments in simple shear and irrotational flow, covering viscosity ratios from

10^{-5} to about 900. He focussed attention on matters of practical importance in the formation of emulsions and design of dispersion equipment, presenting data on the critical Capillary number required for drop burst, drop draw ratio necessary for break at the critical Capillary number, the time necessary to achieve that break, and the resulting drop fragment size distribution. Also considered was the effect of exceeding the critical Capillary number on the energy required for breakup and the resulting number and size of drop fragments. A summary of Grace's data (which is typical of the data from all sources) for the critical Capillary number as a function of viscosity ratio, for the two flows he considered, is shown in Figure 1.3. Note that the burst data for low viscosity ratios includes only large-scale burst of the drop, and does not include breakup by tip streaming. In light of the significant differences between the two curves, a systematic investigation of the effects of vorticity on drop deformation and burst seemed in order.

The only experiments in flows other than simple shear and two-dimensional irrotational flows appear to be those reported by Hakimi and Schowalter [1981] in the flow produced in an orthogonal rheometer. In this device, flows of varying vorticity-to-strain-rate ratio can be generated, but the flows are always "weak", meaning that the magnitude of the vorticity is always larger than that of the strain rate. The experiments were limited to small deformations ($D_f \leq 0.2$), and only one viscosity ratio ($\lambda = 0.09$). Agreement with a truncated version of the Barthes-Biesel and Acrivos [1973a] analysis was reported.

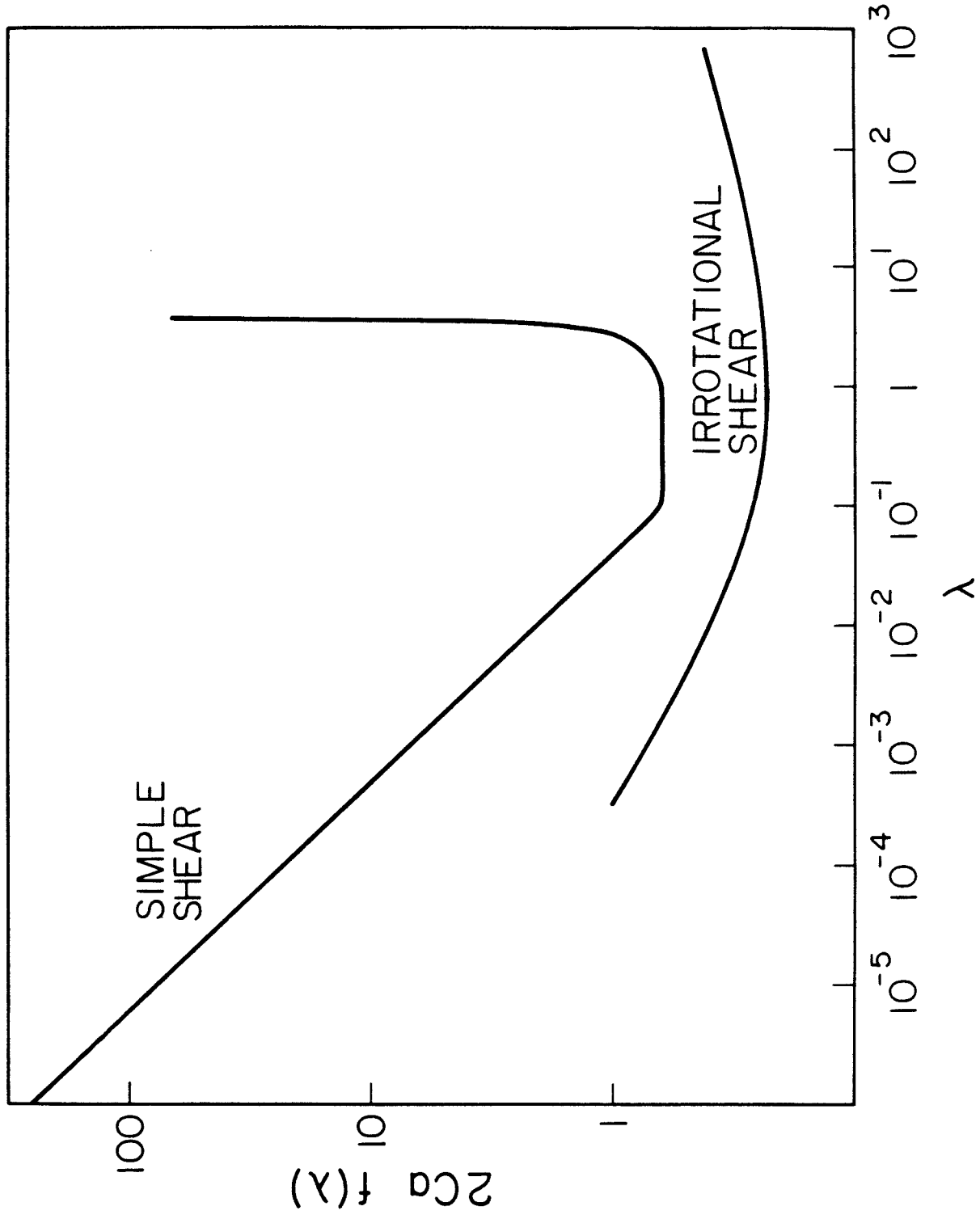

Figure 1.3
Drop burst in simple shear and irrotational shear (Grace [1971])

1.3 PRESENT WORK

As noted above, prior to this work, no experiments had been attempted in strong flows other than irrotational flow. Since these flows can more readily cause large deformations and drop burst than the weak flows considered by Hakimi and Schowalter [1981], they are actually of greater practical importance. While a complete spectrum of two-dimensional strong flows can be conveniently generated in the four roll mill, control of the drop position is too complicated to be accomplished manually except in an approximate sense for the purely irrotational case that was studied by Taylor [1934], Rumscheidt and Mason [1961] and Grace [1971]. Reasons for the difficulty of control in other strong flows are discussed in Chapter 2. A major contribution of the present work is the application of recent advances in the technology of laboratory computers and image processing to essentially solve the drop control problem for the four roll mill, allowing more accurate experiments in irrotational flow, and making experiments in intermediate strong flows possible.

The feedback control system we developed to control the drop uses a closed circuit video camera to sense the drop position. The camera is focussed on the central portion of the flow field, and the drop backlighted to obtain maximum contrast between it and the suspending fluid. In operation, the camera provides an eight-bit digital signal which sequentially reports the intensity of light falling on each picture element in a 248 by 244 grid. The data are fed into a video preprocessor which "thresholds" it by comparison to a preset value, thus reducing the data rate by a factor of eight. The thresholded data are passed to a laboratory computer. The center of mass of the drop is determined from this data stream, and appropriate flow field adjustments made through changes in the speeds of the DC stepping motors which turn the four rollers. Using a simple

model for the response of the flow field to changes in the roller speeds, and for the motion of the drop in response to the flow field, we were able to implement an inferential control scheme capable of maintaining a drop at the center of the flow field for much higher velocity gradients than could be controlled by hand. Also, the computer was able to sense much smaller disturbances to the drop position than could be detected by eye, and was thus able to respond with smaller control actions, and thus less disruption to the desired flow, than would be possible with manual control.

Using this technique, we have systematically investigated the effect of flow type on the deformation and burst of drops in Newtonian fluids, covering a wide range of viscosity ratio and strain-rate-to-vorticity ratio. Computer control of the experiment has resulted in data of improved quality for irrotational flow, as well as data for flows which had not previously been investigated. Comparisons to several of the available drop deformation and burst theories have been made to test the theories and clarify conditions for which they may be expected to apply.

Planned extensions to the work described here include investigations of the effects of viscoelasticity (of the drop and/or the continuous phase) on drop deformation and burst. In this case, the qualitative differences caused by increasing vorticity may be even more striking than for Newtonian systems, since viscoelastic fluids typically exhibit a shear viscosity which decreases with increasing shear rate, but an extensional viscosity which usually increases with increasing velocity gradient. Another area for which the computer controlled capability is particularly well-suited is in investigations of the response of fluid drops to transient flow fields. Since neither the shear rate nor the nature of the flow field seen by a drop is constant in most practical dispersion equipment, an

understanding of the effects of time-varying flows would be invaluable in the design or optimization of such equipment.

It is also hoped that this demonstration of the feasibility of real-time control based on video data will encourage other applications of this technique. Presently, technology is available to handle simple manipulations of video data in real-time (such as the thresholding used in our experiments), but development of pipelined processors which incorporate digital filtering techniques to perform higher level functions (such as edge detection) in real-time is underway, driven by applications in robotics and machine intelligence (Wong [1979]). In addition, the processing power and speed of laboratory computers is continuously improving, while prices are continuously dropping. Thus more complicated manipulations of the video data may become possible, allowing a broader range of applications.

2.0 THE EXPERIMENT

The principal objective in the design and construction of the experimental apparatus was to produce a device flexible enough to investigate a variety of phenomena associated with drop deformation and burst. The flow device chosen for the study was the four roll mill, which was evidently invented for the investigation of drop phenomena in two–dimensional straining motion by G.I. Taylor [1934] some fifty years ago. A schematic of this device is shown in Figure 2.1.

A valuable capability of the four roll mill, which has gone previously unexploited in studies of droplet behavior (for reasons discussed below), is its ability to produce two–dimensional flows of arbitrary strain-rate-to-vorticity ratio, through appropriate selection of roller speeds. This was first recognized by Giesekus [1962] who reported that the velocity gradient tensor in the central region, of dimensions comparable to the gap between the rollers, could be closely approximated by:

$$\nabla \mathbf{u} = \frac{1}{2} G \begin{bmatrix} 1+\alpha & 1-\alpha & 0 \\ -1+\alpha & -1-\alpha & 0 \\ 0 & 0 & 0 \end{bmatrix} \tag{2.1}$$

in the cartesian coordinates of Figure 2.1. The flow parameter, α, is a measure of the relative strength of the straining motion and vorticity in the flow field. It ranges from -1, corresponding to purely rotational flow, to +1, corresponding to pure straining motion. The intermediate value, $\alpha = 0$, represents the familiar simple shear. The ratio of the magnitude of the rate of strain tensor to that of the vorticity can be expressed as:

$$\frac{\text{mag. of strain rate}}{\text{mag. of vorticity}} = \frac{1+\alpha}{1-\alpha} \tag{2.2}$$

In the coordinate system of Figure 2.1, the velocity (u,v,w) is given by

$$u = \frac{1}{2}G\left[(1+\alpha)x + (1-\alpha)y\right] \tag{2.3a}$$

$$v = \frac{1}{2}G\left[(-1+\alpha)x + (-1-\alpha)y\right] \tag{2.3b}$$

$$w = 0 \tag{2.3c}$$

with streamlines given by:

$$(x+y)^2 - \alpha\,(x-y)^2 = c^2 \tag{2.4}$$

Figures 2.2 and 2.3 show streamlines for several choices of α. For positive α, the streamlines are hyperbolas, symmetric about $\vartheta = \pm\pi/4$ with asymptotes at $\vartheta = \cos^{-1}[(1\pm\alpha^{1/2})/\sqrt{2(1+\alpha)}]$, while for negative α they are ellipses with major axes aligned along $\vartheta = \pm\pi/4$ and aspect ratios of $\sqrt{-\alpha}$. The principal axes of the rate of strain tensor, $\frac{1}{2}[\nabla\mathbf{u} + (\nabla\mathbf{u})^T]$, are at $\vartheta = 0$ and $\vartheta = \pi/2$, corresponding to the maxima in extension and compression, respectively.

Giesekus [1962] and Fuller and Leal [1981] found that the flow parameter α was approximately equal to the negative of the ratio of the angular velocities of rollers 2 and 4 to those of rollers 1 and 3. The shear rate at the center of the device, G, was found to be directly proportional to the speed of the faster pair of rollers, with the constant of proportionality dependent on the geometry of the four roll mill, but independent of the flow type. These relations for the four roll mill used in the present study are discussed in Section 2.4.

The capability of generating linear two-dimensional flows with an arbitrary ratio of vorticity to strain rate makes the four roll mill an ideal choice for the present study, but there is a major difficulty associated with experiments in flows where $\alpha > 0$. In these so-called "strong" flows, there is a stagnation point at the origin, where one would like to position the drop for ease of observation, but a particle or drop at this point is unstable to disturbances in position. This

positional instability can be seen from an examination of the trajectory of a drop (or particle) assuming that it follows the path of a fluid element. Since the velocity gradient (2.1) is independent of position, the velocity at a point $\mathbf{x}$ is given by $\mathbf{u} = \nabla\mathbf{u} \cdot \mathbf{x}$, and thus the drop trajectory can be found by solving the linear system:

$$\frac{d\mathbf{x}}{dt} = \nabla\mathbf{u} \cdot \mathbf{x} . \tag{2.5}$$

For $\alpha > 0$, this linear system has nontrivial eigenvalues and eigenvectors:

$$\lambda_{1,2} = \pm G\alpha^{1/2} , \quad \xi_{1,2} = \left[(1 \pm \alpha^{1/2}) / \sqrt{2(\alpha+1)}, \ (-1 \pm \alpha^{1/2}) / \sqrt{2(\alpha+1)} , \ 0) \right] . \tag{2.6}$$

The presence of the positive eigenvalue indicates that if a drop is initially placed at the origin in a strong flow, any disturbance in its position with a component in the direction of the corresponding eigenvector will grow. Thus, a drop or particle tends to be carried from the stagnation point in the direction of this eigenvector of the velocity gradient tensor. These eigenvectors correspond to the linear exit streamlines which can be seen in Figure 2.2. For purely extensional flow, $\alpha = 1$, the exit streamline is along the x axis, while for flows with $\alpha = 0.8$, 0.6, 0.4, and 0.2, the exit streamlines are at $\vartheta_e = -3.2°$, $-7.2°$, $-12.7°$, and $-20.9°$ from the x axis, respectively.

Since strong flows induce drop deformation and breakup most readily, these flows are of most interest and the control problem represents a major obstacle to successful experiments. Previous researchers, Taylor [1934], Rumscheidt and Mason [1961], and Grace [1971], have used the four roll mill to study drop deformation and burst in two-dimensional irrotational flow ($\alpha = 1$). They controlled the drop by hand, keeping it as close to the center as possible by adjusting the speeds of the left pair of rollers (2 and 3 in Figure 2.1) relative to those of the right pair (1 and 4). All reported difficulties in keeping the drop

at the center of the apparatus, which limited the useful shear rate range of their apparatus and appears to have resulted in data of only fair reproducibility.

While the control problem in pure straining motion is the most severe in the sense that at a given G, the speed at which the drop moves away from the stagnation point is greatest (the eigenvalue in (2.6) is largest), it is less complicated than controlling the drop in a flow with $0 < \alpha < 1$, in the sense that there is only one parameter which must be varied, i.e., the ratio between the speeds of the left and right roller pairs. In the general case, the speed of each roller must be independently varied, a task requiring calculations and coordination beyond the capabilities of an operator.

To overcome this difficulty, a computer-based feedback control system was developed for the experiment. A solid state closed-circuit television camera was interfaced to a laboratory computer to detect the position of the drop, and stepping motors were interfaced to the computer to control the roller speeds to move the drop back to the center of the device. This control scheme is described in Section 2.2.

Computer control of the four roll mill made it possible to study the effect of the flow type on the deformation and burst of Newtonian droplets in Newtonian suspending fluids, with the data obtained showing very good reproducibility over a wide range of viscosity ratios. It is believed that the measured deformation and burst curves constitute an excellent test of the available theories for drop deformation and burst in creeping flow. The apparatus constructed for this study will also be useful for future experiments, including investigations of the effects of non-Newtonian rheology of the drop and/or suspending phase. The device is also expected to be particularly useful for investigations of the effect of transient flow fields on the drop breakup behavior, since computer control of

the roller speeds will allow convenient and reproducible generation of arbitrary shear rate sequences, with simultaneous control of the drop to keep it at the center of the device.

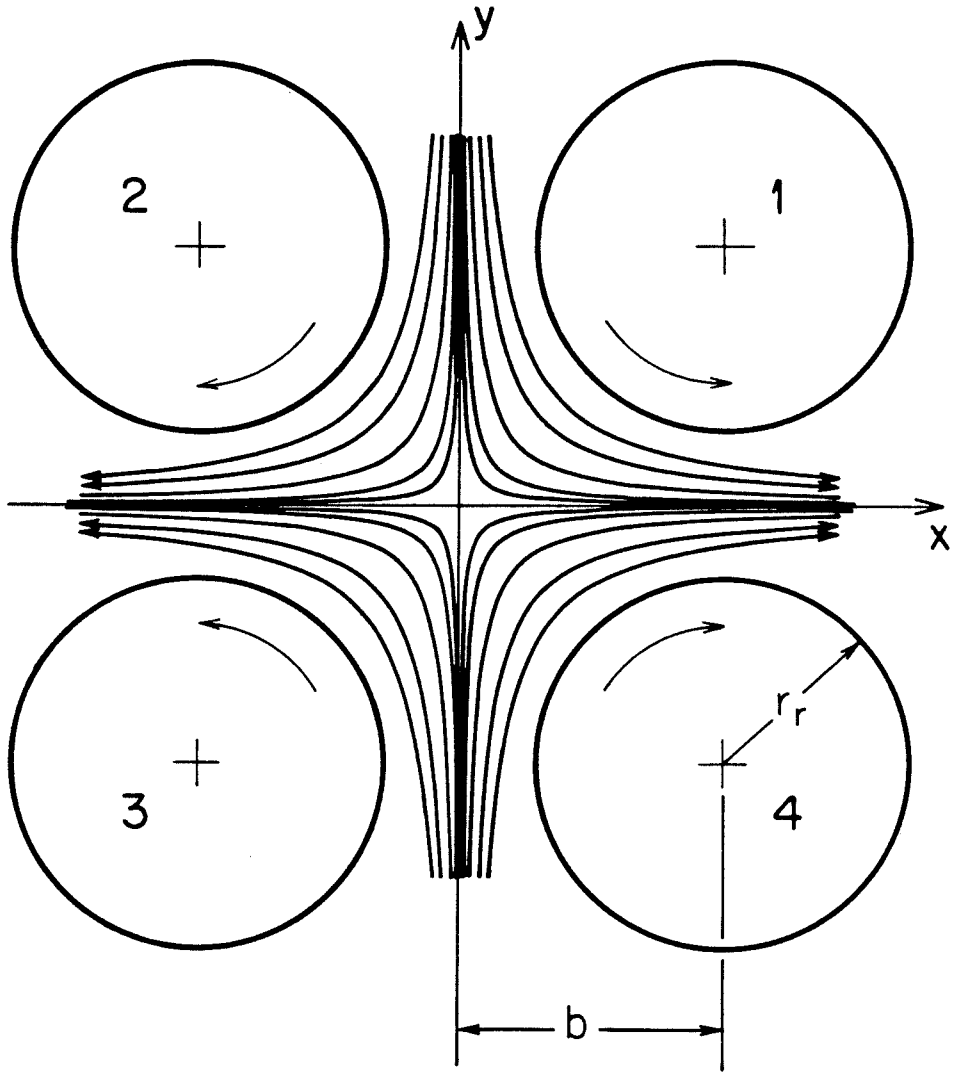

Figure 2.1
Schematic of four roll mill (top view)

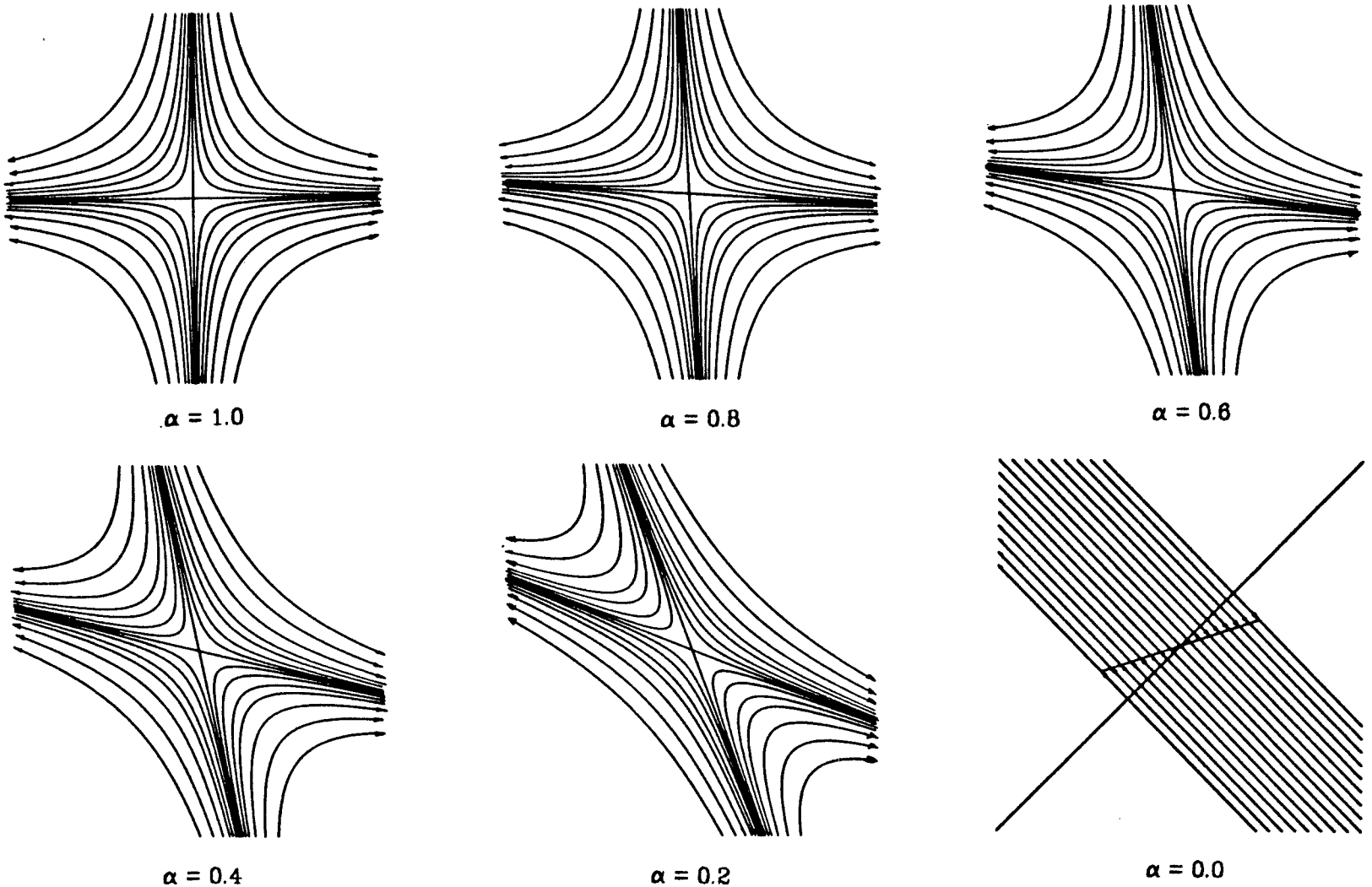

Figure 2.2
Streamlines of flow field of Equation (2.1) for $\alpha \geq 0$

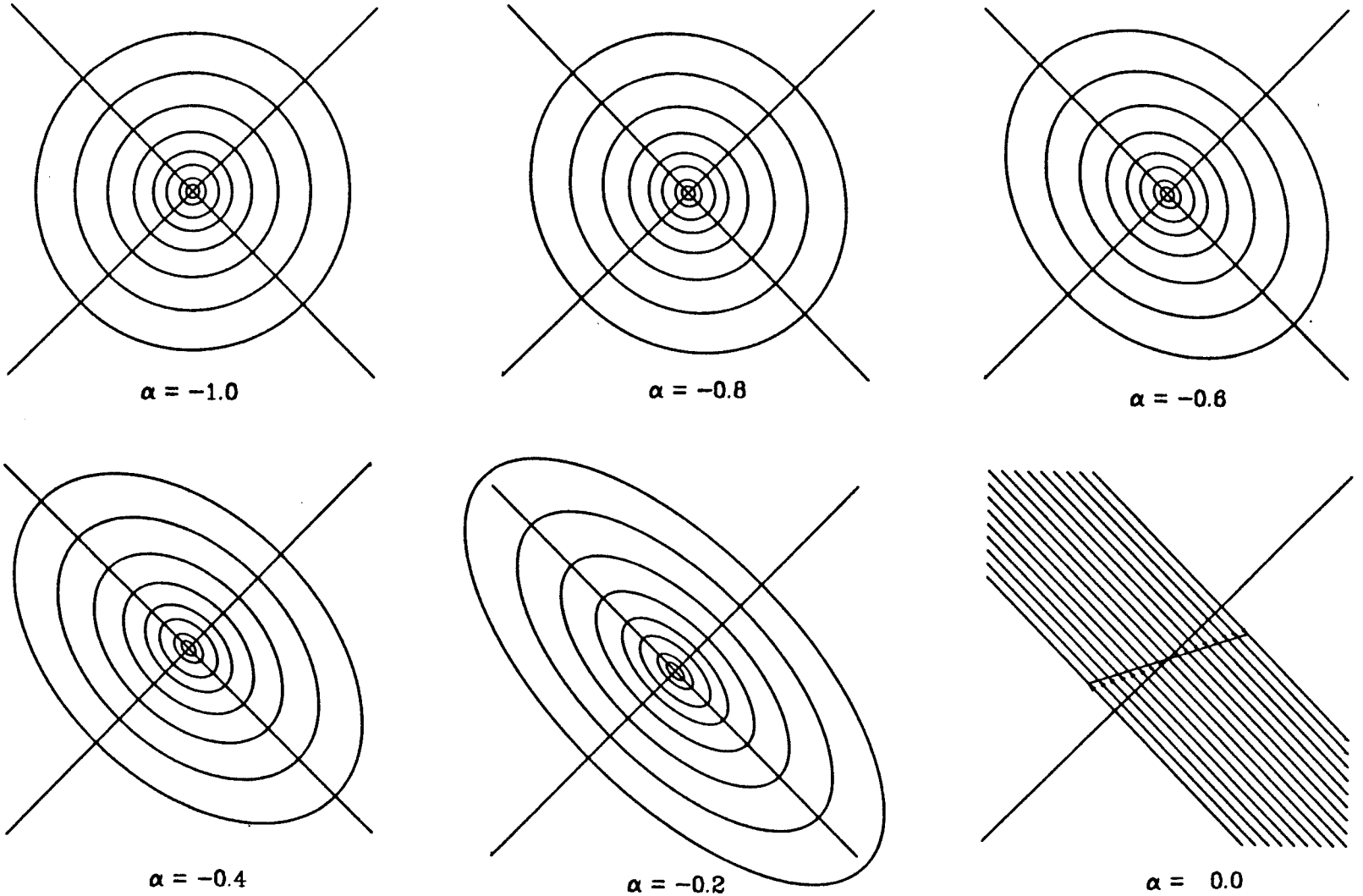

Figure 2.3
Streamlines of flow field of Equation (2.1) for $\alpha \leq 0$

2.1 DESIGN OF THE FOUR ROLL MILL APPARATUS

The design of the four roll mill and associated electronics was intended to permit investigation over as wide a range as possible of the dimensionless groups governing drop deformation and burst. By varying the suspending and/or drop fluid, drop size, or a few equipment parameters, the apparatus was capable of investigating almost any practical case.

2.1.1 Sizing and Geometry

In the four roll mill, the flow is well-represented by (2.1) in a square of dimensions comparable to the width of the gap between adjacent rollers. To accommodate drops which are highly deformed prior to burst (low viscosity ratio drops), it was desirable to make the apparatus fairly large. However, construction and filling costs increase with size, and the device Reynold's number is proportional to the square of the roller diameter, so that the onset of flow instability occurs at lower shear rate as the size increases. We chose 2.54 cm for the gap width, which is sufficient to allow a draw ratio (length divided by undeformed drop diameter) of 25 for the smallest drop thought practical. This is the extension achieved at the point of burst for a drop of viscosity ratio 10^{-5}, according to the theory for slender drops (Acrivos and Lo [1978]). The length of the rollers was chosen somewhat arbitrarily as 15.5 cm, which proved sufficient to minimize end effects for most of the depth while keeping filling costs reasonable. The dimensions of the tank containing the suspending fluid was fixed at 49.5 cm square by 17.5 cm deep. The depth of the tank was adequate to completely immerse the rollers.

The geometry of the device was made adjustable by mounting the rollers on arms which were attached to the base at 45° to the tank (see Figure 2.4). To

arrive at the range of reasonable values for the roller spacing to roller radius ratio, b/r_r (see Figure 2.1), the desired hyperbolic streamline for α=1 was forced to match the roller surface in one of a number of ways. Four methods of matching the two curves were investigated:

1. The hyperbolic streamline was forced to go through points M, N, and P in Figure 2.5, giving b/r_r = 1.207.
2. The streamline and the roller surface were forced to intersect at point N, with zero area between the curves. This yields b/r_r = 1.294.
3. The streamline and the roller surface were forced to intersect at points M and P, with zero area between the curves, resulting in b/r_r = 1.172.
4. The radii of curvature of the hyperbolic streamline and the roller were forced to match at point N. This gives b/r_r = 1.414.

This suggests that any geometry with $1.172 \leq b/r_r \leq 1.414$ is reasonable, so the four roll mill was designed so that this quantity could range from 1.1 to 1.6 without changing the rollers, which were 10.16 cm diameter. The ratio chosen for the experiments was b/r_r = 1.25.

2.1.2 Construction

The apparatus was constructed on a Unistrut frame, using a 40 x 48 x 3/4 inch plate as the base on which the motor arms were mounted. A 50.8 cm square hole was cut in the plate for the tank, which was supported by an aluminum frame suspended below the base. The tank was made of 1/2 inch thick glass for the bottom and 1/4 inch thick glass for the sides, and was cemented together with epoxy. A protective bead of silicone rubber adhesive sealant was spread on the inside of the joints to protect the epoxy from the contents of the

tank.

The rollers were driven by DC stepping motors (Superior Electric M093-FD 301 motors driven by Superior Electric TM600 translator modules). They were selected for their torque output (50 Ncm at full speed) and the ease of controlling them accurately from a computer. They could be driven from 250 steps/second to 10,000 steps/second, with each step corresponding to 1/200 of a shaft revolution in full step mode or 1/400 revolution in half step mode. Typically, they were used in half step mode and geared down by a factor of 60:1. This yielded a usable shear rate range of 0.05 sec^{-1} to 2.0 sec^{-1}, which proved adequate for our experiments. Other gears allowing reductions of 20:1 were purchased, giving a maximum shear rate of 12 sec^{-1} if needed. The gears were double threaded worm gears of 64 pitch for the 60:1 reduction and 24 pitch for the 20:1 gearing. The motors were mounted on rubber and coupled to the shafts using rubber couplings to minimize vibrations. Since the stepping rate of the motors was in the audio frequency range, they were housed in plexiglas boxes lined with styrofoam to reduce the noise. This had the undesirable side effect of insulating them from cooling air as well, but it was found that they could be run for at least half an hour without overheating.

Our original intention was to float the suspending fluid on a thin layer of a transparent, more dense, less viscous fluid to minimize the effect of the solid boundary on the bottom. Preliminary experiments with water-sugar solution as the inviscid layer, and various viscous oils as the upper phase, revealed that the pressure field generated by the flow caused unacceptably large deformations to the interface between the two phases, since the density difference between them was too small. When the lower inviscid phase was eliminated entirely, non-negligible three-dimensional secondary flow was induced. In order to retain the

lower layer without large interface deformations, mercury was used for the lower phase. The large density difference eliminated the interface deformation, and the low viscosity of the mercury reduced the secondary flow to an acceptable level. However, this choice caused another problem since the lower phase was no longer transparent. Since the control scheme depended on backlighting the drop, a small (4 cm square by 0.64 cm thick) plexiglass window was glued to the bottom of the tank, protruding above the mercury layer about 2 mm. The edges of the window were concave to conform to the hyperbolic flow field, and it was aligned with its corners pointing along the x and y axes. A similarly shaped but somewhat larger piece of plexiglass was suspended several millimeters into the fluid from the top surface, which was otherwise open. This was necessary to allow lighting from the top without the distortion which would have resulted from the deformation of a free surface. A slight secondary flow remained despite the mercury layer, with flow upward near the top surface and downward near the bottom. Also, the drop and suspending fluid densities could not be exactly matched, so there was also some vertical motion of the drop due to sedimentation. Neither of these problems proved serious, and it was found that for the shear rates needed for the experiments, the drop could be kept in the central 8 cm in the vertical direction for up to 15 minutes, which proved to be adequate for the experiment.

2.1.3 Lighting and Photography

The illumination of the flow field was very important to the success of the experiment, since high contrast was required for the thresholding process to successfully differentiate between the drop and the background. The central portion of the flow field was illuminated by a well-collimated beam of light from a point source (Oriel Model 6340). The beam of light, collimated with a 75 mm

lens, was passed through the flow field and converged onto the light sensitive array of the video camera using a 105mm lens and an 80 mm microscope objective. This technique yielded a shadowgraph, quite sensitive to refractive index differences in the field. The drops showed up as dark in the bright background, the only problem arising from occasional refractive index gradients in the suspending fluid caused by small temperature gradients or impurities. These appeared as dark streaklines. Generally, the intensity difference between these lines and the drop was great enough that a suitable choice of threshold could be made so that only the drop was below the threshold, but occasionally these lines were dark enough to be below the intensity threshold, and they would then interfere with the determination of the center of mass of the drop, and cause problems for the control scheme. The solution was to remove the drop and run the rollers for a few minutes to mix the continuous fluid.

In order to take pictures of the drop simultaneously with video and still cameras, a cubic beam splitter, 3.8 cm on a side, was inserted above the focussing lens of the video camera, and the still camera mounted at 90° from the vertical axis. Both cameras were initially focussed on the same point in the flow field, and subsequent focussing during the course of the experiment was accomplished by moving the entire arrangement vertically using a motorized measuring microscope mount specifically adapted for this purpose. The still camera was a Canon A-1 with Macro Lens FD200mm f/4.0 and 50mm extension tube, yielding a magnification of 1.34 life size with a working distance of about 40 cm. Kodak Tri-X Pan 400 ASA film was used with an f-stop of 4.0 and an exposure time of 1/15 or 1/30 second.

2.1.4 Camera - Computer Interface

The video camera (General Electric TN2500) was a solid state charge injection device (CID) closed circuit television camera. The sensor in the camera was an array of 248 x 244 picture elements, or pixels. These were sequentially scanned by the circuitry in the camera, which produced two outputs, an analog signal in standard broadcast format and an eight-bit digital representation of the intensity of light at each pixel as it was scanned. The analog signal was routed to a black and white TV monitor, and the digital output routed to a specially designed interface. Each pixel was read twice during the 1/30 second scan which comprises the broadcast standard, resulting in a data rate of 3.63 million bytes per second (MHz). This is far too fast for current generation laboratory computers such as the Digital Equipment Corporation PDP 11/23 used for this experiment. Thus, an interface was designed by Ray Eskenazi of the Jet Propulsion Laboratory Robotics Division to go between the camera and computer. This interface compared the incoming intensity data to a programmable threshold, yielding a "one" where the intensity was below the threshold and a "zero" where the intensity was above this threshold. The incoming data were thus reduced to one output bit for each eight-bit input. These were assembled into 16-bit words and sent in parallel through a direct memory access interface to the computer. This reduced the net data rate to 0.453 MHz, which is just within the limits of the PDP 11/23. The thresholded picture was also available from the interface in broadcast format, so that it could be displayed on a second TV monitor. This was invaluable in setting the threshold value.

Standard broadcast format is "interlaced," meaning that all the odd-numbered lines of information are transmitted sequentially, followed by the even-numbered lines. This is done to prevent a noticeable flicker when viewing a

television. Display time for each "field" is 1/60 second. In controlling the drop, accurate determination of the position in the x direction was more important than that in the y direction, since the exit streamline was aligned much closer to the x axis than to the y axis. Thus, only one field of information was used to determine the drop center of mass, giving a resolution of 248 in the x direction and 122 in the y direction. The field selected (odd or even) depended on which started soonest after the computer's command to "grab" a frame of picture information. The time necessary to get the frame was generally less than 1/60 second, since the size of the "window" for which thresholded information was to be sent could be adjusted by the operator. Generally, only a fairly small fraction of the screen was covered by the drop, and the window was set accordingly.

Once a frame of information was passed into the computer's memory, the next step was to determine the center of mass of all the dark (one) bits. This was done using a straightforward routine written in PDP/11 assembly language for speed. This step took between 1/20 second and 1/6 second depending on the window size and the picture composition. The elapsed time for the center of mass calculation was accurately measured using a timer interface in the PDP 11/23.

The sequence of getting a frame of information and finding the drop center of mass comprised the measurement portion of the feedback control process.

2.1.5 Computer - Stepping Motor Interface

In order to effect control of the flow field, the computer had to regulate the motor speeds. Stepping motors are ideal for precise digital control since they take one step for each voltage pulse received by a "translator," which generates the high power signals which energize the windings in the proper sequence to

step the motor. Thus, one need only generate square wave voltage signals of frequency appropriate for the desired motor speed. An Apple II+ microcomputer was programmed to generate these signals and interfaced to the stepping motor translators. The Apple was interfaced to the DEC computer using a standard RS232-C serial line, the communication protocol used between a computer and a terminal. The DEC computer calculated the desired motor speeds and transmitted this information to the Apple for implementation. To keep the time for the transmission step as short as possible, the serial interface was run at the highest possible speed, 19,200 baud (bits per second). When the motors speeds were changed, the Apple generated frequency signals ramped from the old speed to the new, as attempts to change speeds too abruptly caused the stepping motors to stall. The Apple was capable of generating frequencies from 20 to 10000 Hz (±0.1%)on each of four independent channels. These signals were sent to the inputs of the four stepping motor translators and this setup functioned as the actuator in the control process. Unlike variable speed motors controlled by analog signals (e.g., DC shunt wound motors), the speed of stepping motors is not affected by temperature or load. Thus motor speeds could be specified exactly, eliminating the need for measuring and recording motor speeds during operation of the experiment.

Figure 2.6 shows a side view schematic of the four roll mill used in the experiment.

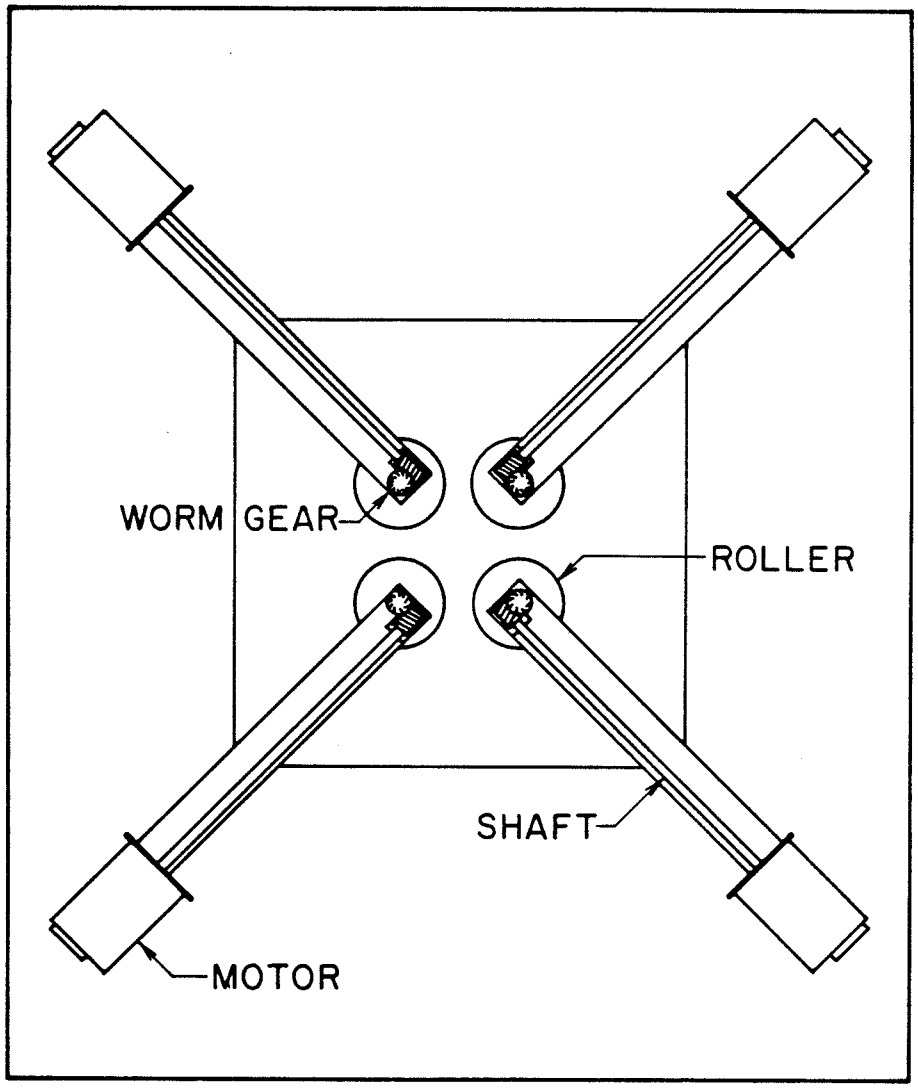

Figure 2.4
Top view of four roll mill, showing the roller mounting arrangment.

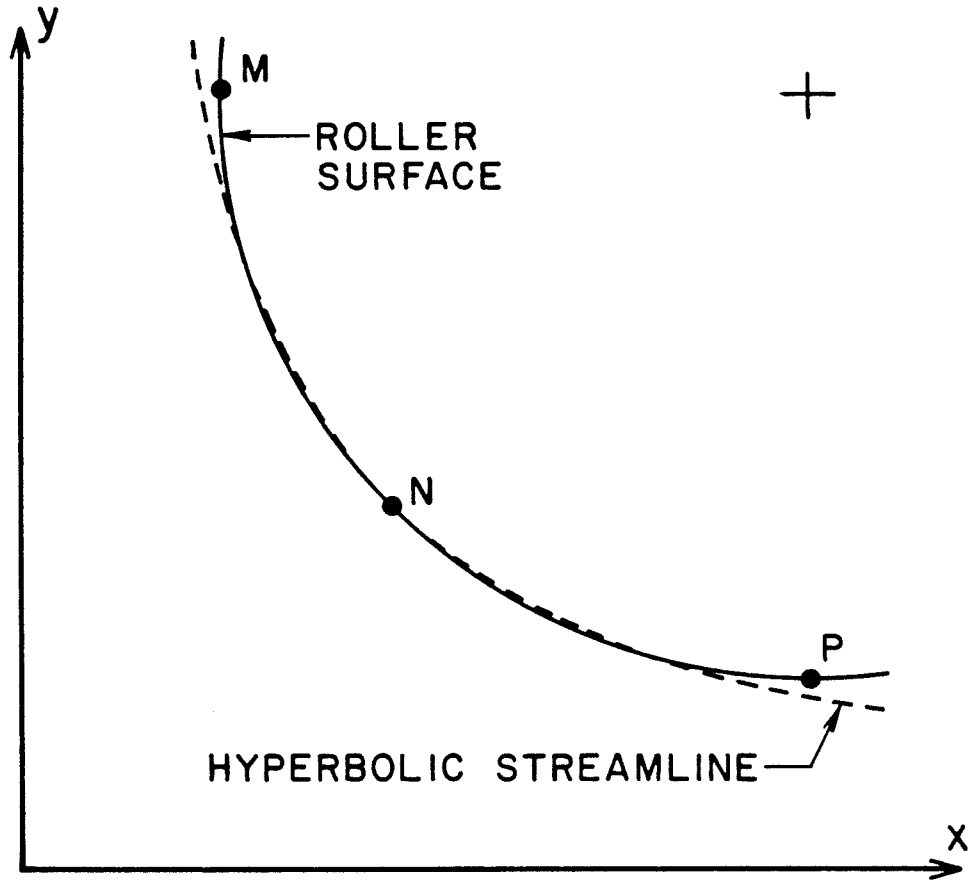

Figure 2.5
Selection of geometry of the four roll mill

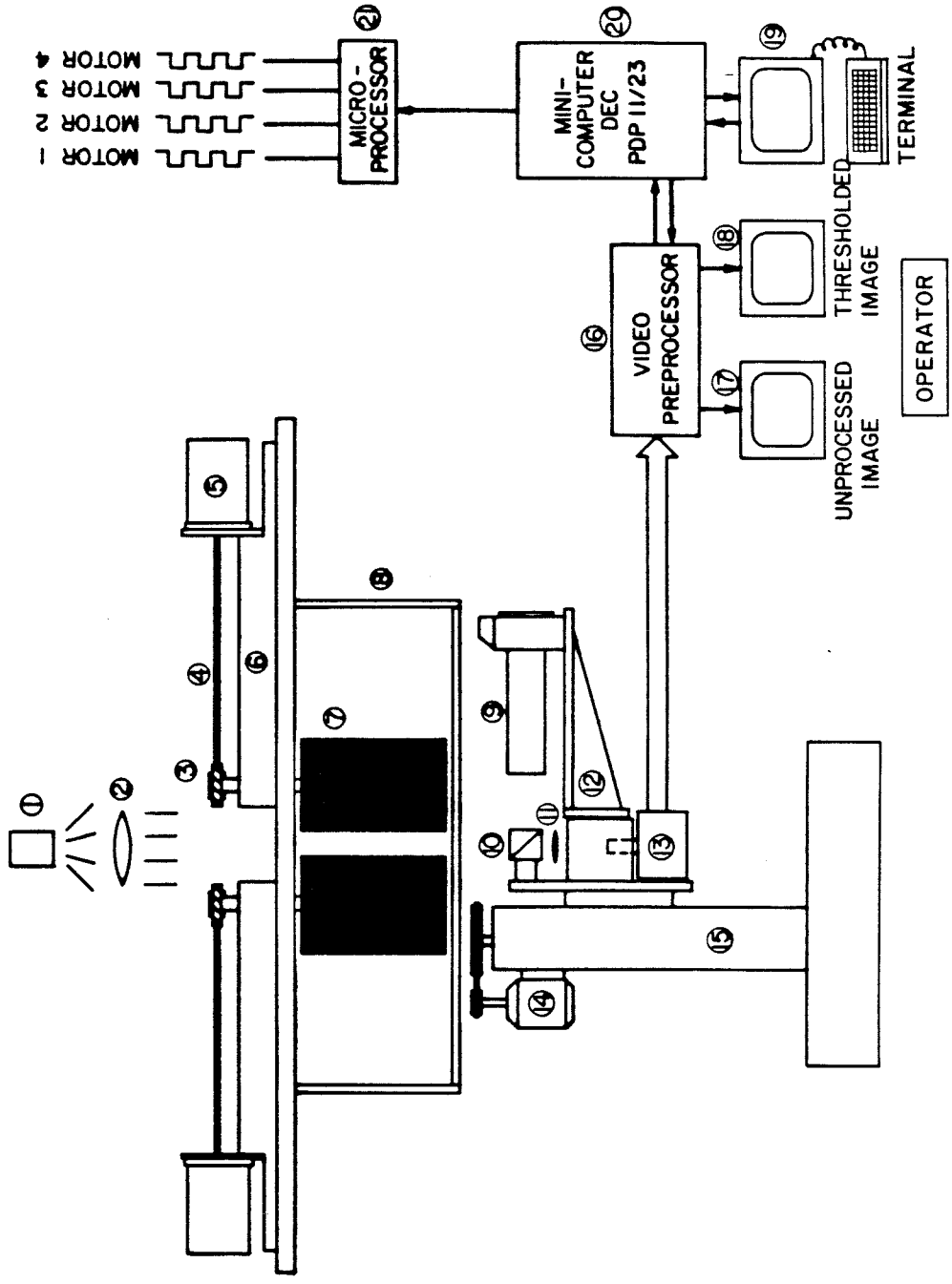

Figure 2.6
Side view schematic of four roll mill.
1) point light source, 2) collimating lens, 3) worm gears, 4) drive shafts, 5) DC stepping motors, 6) roller mounting arms, 7) rollers, 8) glass tank, 9) still camera, 10) cubic beam splitter, 11) converging lens, 12) still camera mount, 13) digital video camera, 14) motor for moving camera assembly vertically, 15) modified measuring microscope mount, 16) video preprocessor, 17) monitor for viewing unprocessed video, 18) monitor for viewing thresholded video, 19) video terminal, 20) DEC minicomputer, 21) Apple microcomputer.

2.2 CONTROL OF THE FOUR ROLL MILL

For successful drop deformation and burst experiments in strong flows ($\alpha > 0$), the drop must be kept as close as possible to the center stagnation point. The only means of controlling the drop position is by changing the flow field through variations in the roller speeds. These changes must be as small as possible to avoid significant disruptions to the characteristics of the flow field under study, i.e., the shear rate and flow type.

When the drop wanders from the origin, the flow must be altered so that it tends to return the drop to the center. For the case where $\alpha = 1.0$, the required response is obvious. If, for example, the drop drifts to the right, the left pair of rollers is speeded up and the right pair slowed down in proportion. This has the effect of superimposing a translational motion (right to left) on the hyperbolic flow field, moving the point of zero flow (stagnation point) to the right. It is clear that for the drop to tend to return to the center, it must be in a point in the flow where the net velocity is towards the origin, which requires that the stagnation point must be further from the origin than the center of mass of the drop. The same reasoning applies for any strong flow, with the only complication being that for $0 < \alpha < 1$ the drop moves along the exit streamline which is at an angle to the roller geometry, requiring a response with changes to all four roller speeds. In the discussion which follows, we consider the stagnation point position to be the control variable which is regulated by adjustments to the roller speeds, but we could alternatively consider the control variable to be the translational velocity superimposed on the flow field by roller speed changes. The two points of view are equivalent, but the former proves more convenient since the stagnation point position is more easily measured when calibrating the four roll mill, so a required control action (stagnation point movement) is more easily translated

into the corresponding roller speed changes.

The sequence of events in the control scheme is as follows:

1. The computer requests a frame of thresholded information concerning the light intensity at the pixels within the "window". This information is stored in the computer's memory via direct memory access from the custom built camera-computer interface. When the window is complete, the processor is signalled that the information is ready for processing. Elapsed time for this step is 0.01 to 0.05 seconds.

2. The computer calculates the center of mass of the drop. Elapsed time is 0.05 to 0.15 seconds.

3. The center of mass is used to calculate the required control action and corresponding rollers speeds from the control model, taking about 0.10 seconds.

4. The DEC computer transmits the new speeds to the Apple microcomputer which ramps the motors from their previous speeds to the new ones. This step takes about 0.05 seconds.

5. The computer checks to see if there is any operator input to change threshold value, window size, or shear rate, and makes requested adjustments.

6. Process starts over again at 1.

Calculation of appropriate roller speeds from the drop position data required a control model describing the flow field's response to roller speed changes, and the drop's response to flow field changes. A rigorous description

would require a solution of the equations of motion throughout the experimental device, including the region inside the deformed drop. Since this was clearly not possible in a real-time control scheme, a simple, approximate model was developed. In formulating this model we assume that the drop velocity is equivalent to that of a fluid element placed at its center of mass in the undisturbed flow. Since the drop experiences no external forces except gravity, and we are considering the case where the drops are neutrally buoyant, this approximation becomes exact as the drop size approaches zero. We also assume that the stagnation point can be moved to any position near the origin (through suitable roller speed selection) without affecting the flow type or shear rate. This assumption is plausible since we are concerned only with small departures from the uncontrolled flow. The actual selection of the roller speeds and the verification of this assumption is discussed in Sections 2.3 and 2.4. Finally, we assume that the speed of movement of the stagnation point is proportional to its distance from the "set" point. The set point is where the stagnation point would end up if the roller speeds were held at the new speeds indefinitely. Since we are considering only small displacements of the stagnation point, this last assumption can be considered a linearization of the actual stagnation point motion. These assumptions result in the following simple model:

$$2\frac{dx}{dt} = (1+\alpha)\,(x-x_s) + (1-\alpha)\,(y-y_s)\,, \tag{2.7a}$$

$$2\frac{dy}{dt} = (-1+\alpha)\,(x-x_s) + (-1-\alpha)\,(y-y_s)\,, \tag{2.7b}$$

$$\frac{dx_s}{dt} = \frac{1}{\tau}(x_{ss}-x_s)\,, \tag{2.8a}$$

$$\frac{dy_s}{dt} = \frac{1}{\tau}(y_{ss}-y_s)\,, \tag{2.8b}$$

where (x,y) is the drop position, (x_s,y_s) is the stagnation point position and

(x_{ss}, y_{ss}) is the stagnation point set point, which is the control variable. All times are rendered dimensionless with respect to G^{-1} and all distances with respect to b, the distance from the center of the device to the line joining the centers of adjacent rollers (see Figure 2.1). According to the model above, the system is noninteracting (the drop position has no effect on the stagnation point), so the latter pair of equations can be solved immediately for (x_s, y_s). We are thus led to consider the system:

$$\frac{d\mathbf{x}}{dt} = \mathbf{A}\cdot\mathbf{x} - \mathbf{A}\cdot\mathbf{b}\,, \tag{2.9}$$

where

$$\mathbf{x} = \begin{bmatrix} x \\ y \end{bmatrix}, \quad \mathbf{A} = \frac{1}{2}\begin{bmatrix} 1+\alpha & 1-\alpha \\ -1+\alpha & -1-\alpha \end{bmatrix}, \quad \mathbf{b} = \begin{bmatrix} x_s \\ y_s \end{bmatrix}. \tag{2.10}$$

Since our model assumes that the entire flow field can be moved about within the four roll mill, and that the drop follows the fluid trajectories in this translated flow, it is obvious that the homogeneous portion of this linear system is exactly the same as that for the uncontrolled flow given by (2.5). Thus the eigenvalues and eigenvectors are identical (apart from the non-dimensionalization by the shear rate):

$$\lambda_{1,2} = \pm\alpha^{1/2}, \quad \xi_{1,2} = \left[(1\pm\alpha^{1/2})/\sqrt{2(\alpha+1)}\,,\ (-1\pm\alpha^{1/2})/\sqrt{2(\alpha+1)}\,,\ 0)\right]. \tag{2.11}$$

We note that the component of a disturbance along the eigenvector with the negative eigenvalue will decay, so we are concerned only with movement along the eigenvector corresponding to the positive eigenvalue. Thus, if we define z to be the distance from the origin along this eigenvector:

$$x = z\,(\alpha^{1/2}+1)/\sqrt{2(\alpha+1)}\,, \tag{2.12a}$$

$$y = z\,(\alpha^{1/2}-1)/\sqrt{2(\alpha+1)}\,, \tag{2.12b}$$

then substituting into the homogenous portion of (2.9) gives:

$$\frac{dz}{dt} = \alpha^{1/2} z \ , \tag{2.13}$$

reducing the problem to one dimension. We further note that if we maintain the roller speeds such that (x_{ss}, y_{ss}) is always along the eigenvector with displacement z_{ss}, then (x_s, y_s) will also be on the eigenvector with displacement z_s, and (2.8) gives:

$$\frac{dz_s}{dt} = \frac{1}{\tau}(z_{ss} - z_s) \ . \tag{2.14}$$

Thus the system of (2.7) and (2.8) can be written

$$\frac{dz}{dt} = \alpha^{1/2}(z - z_s) \ , \tag{2.15}$$

$$\frac{dz_s}{dt} = \frac{1}{\tau}(z_{ss} - z_s) \ . \tag{2.16}$$

We investigate control of this simple system.

The computer based control sequence is best described as a discrete sampled system with a time lag corresponding to the sum of the frame time and the calculation time (steps 1, 2, and 3). Nevertheless, it is instructive to consider the system as a continuous controller with a measurement delay. Figure 2.7 shows a block diagram of the system in the Laplace domain. Here G_c is the controller transfer function, G_f the fluid transfer function representing the stagnation point movement described by (2.16), and G_d the drop transfer function representing the response of the drop to the flow field given by (2.15). G_v is the transfer function of the response to an unspecified disturbance $\tilde{v}$. $\tilde{z}_0$ is the desired drop position (here equal to 0, since we want the drop to be at the origin), $\tilde{z}_{ss}$ the stagnation set point, and $\tilde{z}_s$ the stagnation point. G_m is the transfer function representing the measurement delay. In the present case,

$$G_f(s) = \frac{1}{1+\tau s} \ , \tag{2.17}$$

$$G_d(s) = \frac{1}{1-\alpha^{-\frac{1}{2}s}}, \tag{2.18}$$

and for simple proportional control,

$$G_c(s) = K_c \ . \tag{2.19}$$

The measurement delay $G_m(s)$ is exactly represented in the Laplace domain by

$$G_m(s) = e^{-t_d s} \ . \tag{2.20}$$

However, to simplify the analysis, the well-known Pade approximation was used for the delay transfer function.

$$G_m(s) \approx \frac{1-t_d/2}{1+t_d/2}. \tag{2.21}$$

From the block diagram,

$$\tilde{z}(s) = \frac{G_o}{1+G_o G_m}\tilde{z}_0(s) + \frac{G_v}{1+G_o G_m}\tilde{v}(s) \ , \tag{2.22}$$

with

$$G_o(s) = -K_c G_f G_d \ . \tag{2.23}$$

The behavior of the controller is determined by the roots of $1+G_o G_m$, which must all have negative real parts for the system to be stable. A Routh array was used to determine conditions where the real part of roots were negative, yielding the following stability criteria:

$$K_c > 1 \ , \tag{2.24}$$

$$\tau < \alpha^{-\frac{1}{2}} \ , \tag{2.25}$$

$$t_d < \frac{\alpha^{-\frac{1}{2}}-\tau - \frac{2\tau\alpha^{-\frac{1}{2}}K_c}{\alpha^{-\frac{1}{2}}-\tau} + \left[(\alpha^{-\frac{1}{2}}-\tau)^2 + \left[\frac{2\tau\alpha^{-\frac{1}{2}}K_c}{\alpha^{-\frac{1}{2}}-\tau}\right]^2 + 4\tau\alpha^{-\frac{1}{2}}\right]^{\frac{1}{2}}}{1+K_c} \ . \tag{2.26}$$

The requirement of (2.24) that the controller gain be greater than unity simply means that the stagnation point must be moved further from the origin than the drop in order to move the drop in the correct direction. The second criterion specifies that the response of the fluid to changes in the roller speed must be fast compared to the shear rate (recall that τ is relative to G^{-1}). This limits the shear rate for which the drop is controllable with this simple control scheme. Since the response time of a fluid is inversely proportional to its kinematic viscosity, we would expect a proportional control scheme to be more successful with a more viscous suspending fluid. These two criteria are independent of the presence of the measurement delay, t_d.

The third stability requirement illustrates the destabilizing effect of the measurement delay. This places a greater restriction on the controllable shear rate range of the device, with the destabilizing effect magnified as the gain increases. Figure 2.8 shows the stable region of (2.24 - 26) in the τ, t_d plane, with K_c as a parameter for hyperbolic flow ($\alpha = 1$).

From the analysis above, it is clear that control schemes based on conventional continuous controllers are not ideal for control of drops in four roll mill flows owing to the finite response time of the fluid and the measurement delay in locating the drop. This was verified by computer simulations of proportional control. These simulations were performed by starting the drop at a fixed displacement from the origin, and calculating the drop and stagnation point positions based on the model above, with the stagnation point set point computed from the simple proportional scheme. The measurement time, nondimensionalized by the shear rate, was chosen in the range from 0.2 to 1.0, corresponding to shear rates from about 0.7 to 3.5 given the "worst case" measurement delay encountered in getting the thresholded image from the camera

and computing the center of mass. Various values for τ, the response time of the fluid, were tried. The proportional control scheme was successful only for low values of the measurement delay. When the t_d was larger than about 0.5, the controller failed no matter what value of the gain, K_c, was chosen. With a small gain (e.g., 1.2), the controller tended to "chase" the drop as it went further and further from the origin, since the drop was moving exponentially from the stagnation point during the time delay, and the controller was thus consistently underestimating the required control action. If the gain was increased (e.g., 2.5), the controller overshot the required response and caused the drop (and stagnation point) to oscillate around the origin in an unacceptable manner. As expected, both types of behavior were exacerbated by slow fluid response (large τ). Similar simulations using proportional-derivative control were performed, but proved no more successful. In practice, the derivative mode would have required differentiation of the drop position data as well, which would have been an inherently inaccurate calculation.

These simulations demonstrate that a simple continous control scheme would be very difficult or impossible to successfully implement. Moreover, since the apparatus incorporates a computer as part of the position sensor, the calculations necessary to implement a more sophisticated control scheme do not present an obstacle. We are thus led to consider an inferential control scheme which uses the model above to extrapolate the drop movement from the position data, known stagnation point history, and measurement delay. A stagnation point set point can then be calculated to achieve some particular control objective.

One possible objective would be to set the stagnation point to move the drop some fraction of its displacement towards the origin in some period of time, with

the most natural period being that of the control cycle. In this case, the measurement delay is the slow step, so the timer for a complete control cycle can be approximated by t_d. If $z_i, z_{s,i}, z_{ss,i}$ are the values of z, z_s, z_{ss}, at the end of control cycle i, then solution of the (2.15) and (2.16) yields:

$$z_{i+1} = e^{\sqrt{\alpha} t_d} z_i + z_{ss,i}(1-e^{\sqrt{\alpha} t_d}) + \frac{\sqrt{\alpha}\tau}{1+\sqrt{\alpha}\tau}(z_{s,i}-z_{ss,i})(e^{-t_d/\tau} - e^{\sqrt{\alpha} t_d}) , \quad (2.27)$$

$$z_{s,i+1} = z_{ss,i}+(z_{s,i}-z_{ss,i})e^{-t_d/\tau} , \quad (2.28)$$

and the control strategy requires

$$z_{i+1} = (1-r)\, z_i , \quad (2.29)$$

which, upon substitution of (2.28) and (2.29) into (2.27) gives the new stagnation set point as:

$$z_{ss,i} = \frac{(1-r-e^{\sqrt{\alpha} t_d})\, z_i - \frac{\sqrt{\alpha}\tau}{1+\sqrt{\alpha}\tau}(e^{-t_d/\tau}-e^{\sqrt{\alpha} t_d})\, z_{s,i}}{1 - \frac{1}{1+\sqrt{\alpha}\tau}e^{\sqrt{\alpha} t_d} - \frac{\sqrt{\alpha}\tau}{1+\sqrt{\alpha}\tau}e^{-t_d/\tau}} . \quad (2.30)$$

Note that for a given control cycle i, we measure z_{i-1} and compute z_i from (2.27) written for $i-1$ and the known stagnation point history. We then calculate $z_{ss,i}$ from (2.30).

Simulations of this control scheme, similar to those described above for simple proportional control, showed that it too was unsatisfactory. The drop moved closer to the origin at the end of each control cycle (as we require), but movement during each control cycle was oscillatory as was the movement of the stagnation set point. These oscillations were damped with the damping depending on the ratio τ / t_d. For τ / t_d greater than one, the oscillations grew with time, so this control scheme was also rejected.

A second approach was to bring the drop to the device center in a more

orderly fashion by requiring that the velocity of the drop be proportional to its displacement from the origin at the end of each control cycle. This is equivalent to specifying the relative positions of the drop and the stagnation point:

$$z_{s,i+1} - z_{i+1} = r\ z_{i+1} \tag{2.31}$$

Substituting (2.31) and (2.28) into (2.27) yielded for the stagnation point set point:

$$z_{ss,i} = \frac{(r+1)e^{\sqrt{\alpha}t_d} z_i + \left[(r+1)\frac{\sqrt{\alpha}\tau}{1+\sqrt{\alpha}\tau}(e^{-t_d/\tau} - e^{\sqrt{\alpha}t_d}) - e^{-t_d/\tau}\right] z_{s,i}}{1 - e^{-t_d/\tau} - (r+1)\left[1 - \frac{1}{1+\sqrt{\alpha}\tau}e^{\sqrt{\alpha}t_d} - \frac{\sqrt{\alpha}\tau}{1+\sqrt{\alpha}\tau}e^{-t_d/\tau}\right]} . \tag{2.32}$$

Simulations of this control scheme showed it to be much better behaved. The drop and the stagnation point moved monotonically to the center of the device without oscillations for any ratio τ / t_d.

This latter control scheme was implemented for the experiment. Tests of the control were made using a neutrally bouyant solid particle. The results were quite satisfying. Once the control scheme parameters were properly selected (in particular, the scheme was sensitive to the value of τ, the response time of the fluid), a particle could be maintained within a millimeter of the device center for shear rates up to 5 sec^{-1} in flows with $0.2 \leq \alpha \leq 1.0$, provided that the origin of the flow field (where the stagnation point would be in the absence of any control action) was aligned with the origin of the camera (where the computer would compute a center of mass of (0,0)). Otherwise, the misalignment would cause a systematic error in the center of mass determination, resulting in a slow drift of the particle away from the origin, as its displacement and the required control action would be consistently underestimated. To overcome this difficulty, an integral control mode was added which became active only when the particle was more than a specified distance from the camera center. This

insured that the particle did not stray far from the center of the flow field and gave the operator plenty of time to correct the misalignment by moving the entire camera assembly in the x direction. Any misalignment in the y direction was far less critical (since the maximum angle of the exit streamline was inclined only 21 degrees from the x axis for $\alpha = 0.2$). Provisions were made for aligning the origin in the y direction in software. With a little practice, the symptoms of this misalignment were easily recognized and appropriate corrections made.

No facility was available to attempt hand control of the drop, but indications from previous researchers (Taylor [1934], Rumscheidt and Mason [1961], and Grace [1971]) were that manual control was possible for shear rates of no higher than 0.7 sec^{-1}, and then, of course, was limited to irrotational flow. Undoubtedly, the computer-based scheme was also superior in that it was able to detect and correct movements away from the center before they were large enough to be recognized by eye.

In the drop deformation experiments, the drop size, interfacial tension, suspending fluid viscosity, and viscosity ratio were such that drop burst usually occurred for shear rates less than 0.7 sec^{-1}, leaving a substantial overcapacity in the controller. Under these conditions, the drop and the stagnation point were maintained within 0.05 cm of the device center at all times, and the control scheme was considered an unqualified success.

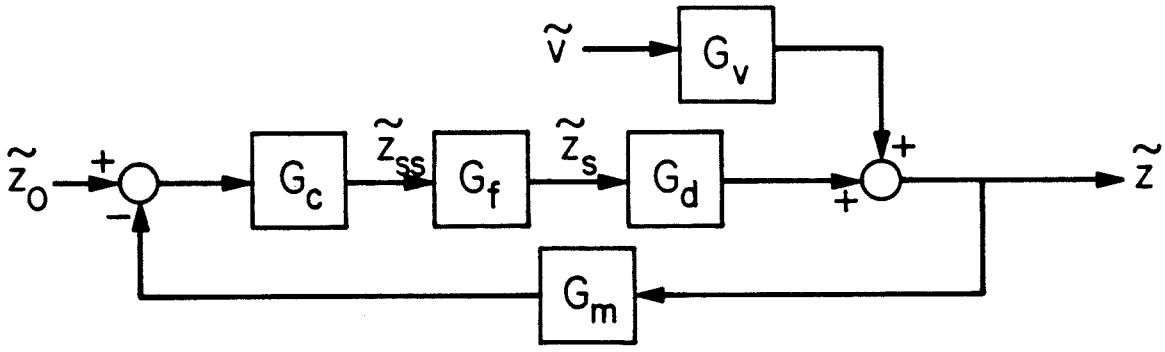

Figure 2.7
Block diagram for proportional control of drop position

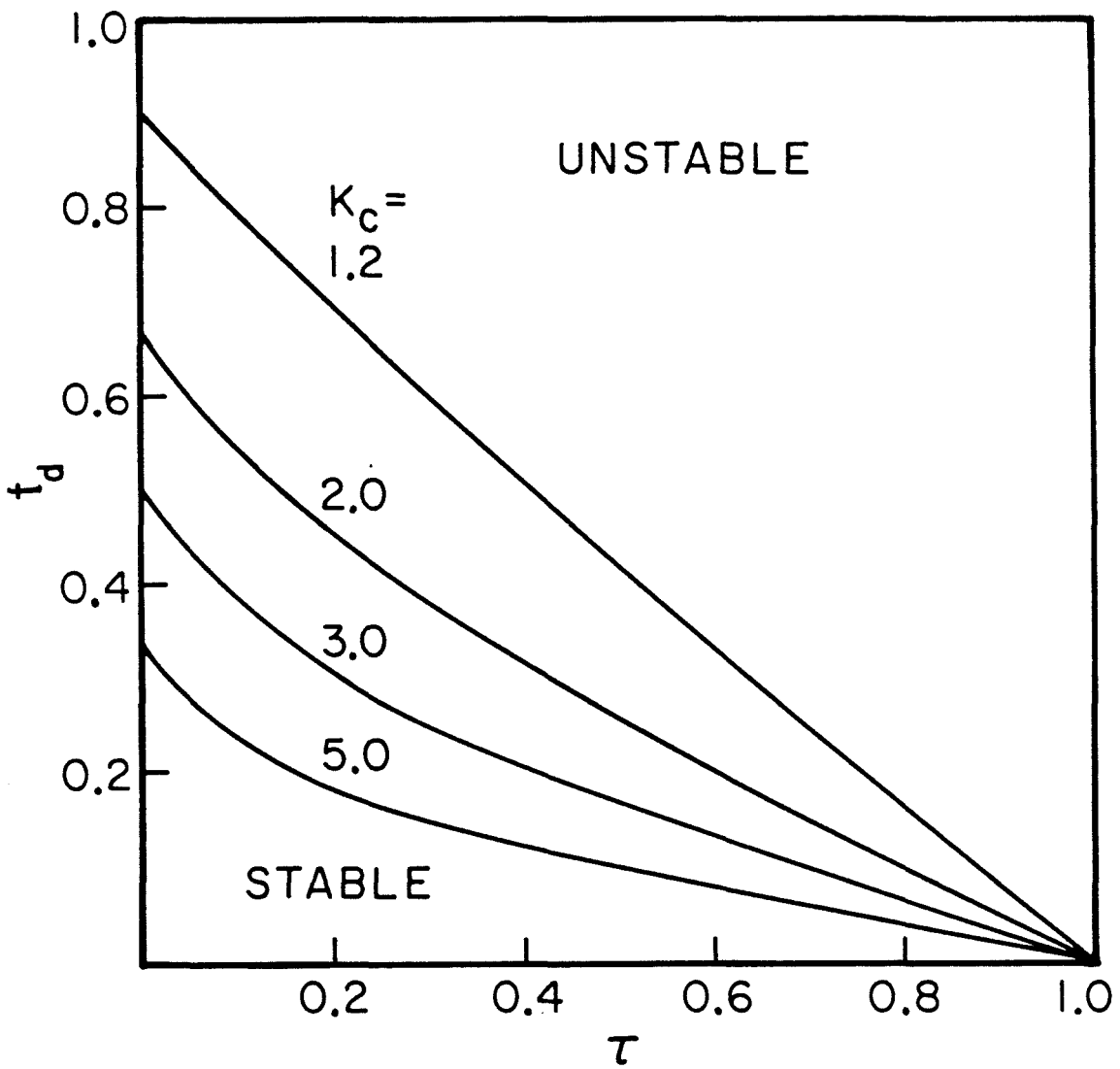

Figure 2.8
Stablity diagram for simple proportional control

2.3 STAGNATION POINT POSITION

Controlling the drop position in the four roll mill required that the stagnation point be moved within the device without upsetting the shear rate or the flow type significantly. In this section we propose a simple model which will allow calculation of the four roller speeds given the stagnation point position, shear rate, and flow type. This model has been tested and found adequate for small displacement of the stagnation point from the origin. In the experiment, we specify the flow type and shear rate, and use the model to calculate the roller speeds necessary to achieve the stagnation point movement required for drop position control.

In the uncontrolled four roll mill flow, the flow type is determined by the ratio of the speeds of the two diagonal pairs of rollers, and the shear rate is governed by the speed of the faster pair. Since the stagnation point is at the center, the speeds of diagonally opposed rollers are always equal. When the stagnation point is to be moved, this is no longer true so these relations require some generalization.

We start by assuming that in the case where the speeds of the faster pair of rollers, ω_1 and ω_3, are unequal, the shear rate can be kept constant by fixing the sum of their speeds, with the required sum depending on the desired shear rate:

$$\omega_1 + \omega_3 = f_1(G) \,. \tag{2.33}$$

Similarly, we assume that a given flow type can be generated by fixing the ratio of the sum of the speeds of diagonally opposed rollers. The required ratio depends on the flow type to be generated:

$$-\frac{\omega_2 + \omega_4}{\omega_1 + \omega_3} = f_2(\alpha) \,. \tag{2.34}$$

The minus sign appears because rollers 2 and 4 are turned in the opposite direction from rollers 1 and 3.

We further propose that the position of the stagnation point along the line joining rollers one and three depends only on the ratio of the speeds of these two rollers and similarly for rollers two and four:

$$\frac{\omega_3}{\omega_1} = f_3(x_s') \,. \tag{2.35}$$

$$\frac{\omega_4}{\omega_2} = f_4(y_s') \,. \tag{2.36}$$

Here (x_s', y_s') is the position of the stagnation point in the (x', y') coordinate system of Figure 2.9.

For a given desired flow type, shear rate, and stagnation point, f_1, f_2, f_3, and f_4 are determined from the calibration data, and the roller speeds ω_1, ω_2, ω_3, and ω_4 calculated by solving the four equations above. These form the linear system:

$$\begin{bmatrix} 1 & 0 & 1 & 0 \\ f_2 & 1 & f_2 & 1 \\ -f_3 & 0 & 1 & 0 \\ 0 & -f_4 & 0 & 1 \end{bmatrix} \begin{bmatrix} \omega_1 \\ \omega_2 \\ \omega_3 \\ \omega_4 \end{bmatrix} = \begin{bmatrix} f_1 \\ 0 \\ 0 \\ 0 \end{bmatrix} , \tag{2.37}$$

which has the solution:

$$\omega_1 = \frac{f_1}{(f_3 + 1)} , \tag{2.38}$$

$$\omega_2 = -\frac{f_1 f_2}{(f_4 + 1)} , \tag{2.39}$$

$$\omega_3 = \frac{f_1 f_3}{(f_3 + 1)} , \tag{2.40}$$

$$\omega_4 = -\frac{f_1 f_2 f_4}{(f_4 + 1)} \,. \tag{2.41}$$

Calibration experiments were performed to test the assumptions which lead to (2.38) through (2.41). These experiments demonstrated that the approximations were adequate for small displacements of the stagnation point from the device center. The functions f_1 through f_4 were also determined from these calibration experiments.

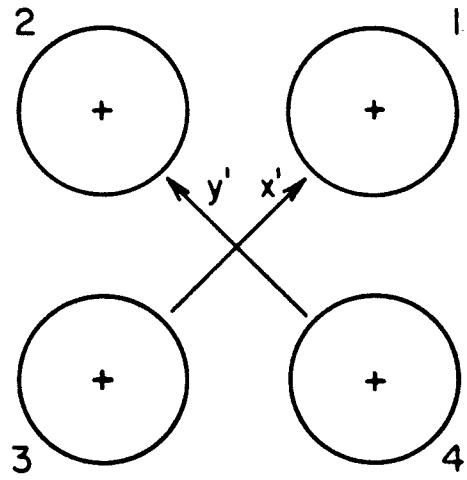

Figure 2.9
Schematic of four roll mill with rotated coordinate system

2.4 FLOW FIELD CALIBRATION

In order to relate the the flow field characteristics to the roller speeds, the flow in the four roll mill was investigated photographically. This was necessary to determine the following:

1. The precise flow type, α, for a given ratio of the speeds of rollers 2 and 4 to those of rollers 1 and 3 (i.e., the function f_2 of (2.34) with the stagnation point in the center.)
2. The relationship between the rollers speeds and the shear rate (i.e., the function f_1 of (2.33)).
3. The position of the stagnation point in the device as a function of the roller speeds (i.e., the functions f_3 and f_4 of (2.35) and (2.36)).

To visualize the streamlines in the flow, the four roll mill was filled with Chevron Polybutene 16 laced with a low concentration of Emerson and Cummings Ecosphere Microballoons. These were hollow glass spheres of 30 to 50 micron diameter, which were highly reflective and served as tracer particles. The flow field was illuminated from two sides with thin (~ 1/2 cm) horizontal planes of light produced with projector bulbs shined through a deep slit formed from two parallel aluminum plates held .3 cm apart. These were positioned midway between the top and bottom of the tank. Time exposure pictures were taken from below the tank at a lens opening of f/3.5 for periods ranging from 1/4 to 1 second.

Comparison between the streaklines from the photographs and those calculated from (2.4) showed good agreement within a 2.5 cm square region in the central portion of the four roll mill. Of course, this does not necessarily mean that the flow field is given exactly by (2.1), since the shape of the streaklines

gives sufficient information to determine the ratio of the velocities in the x and y direction on points along the streakline, but not enough information to determine the magnitude of the velocity nor the relative magnitudes of velocities on adjacent streamlines. Support for the hypothesis that the flow is well-represented by (2.1) comes from two sources. First, the shear rate as measured by the procedure outlined below was essentially constant for different streaklines selected from a particular photograph. Second, a direct measurement of the velocity gradient along the x axis in a flow with $\alpha = 1.0$ was made by Fuller et. al. [1980] using the technique of homodyne light scattering. Their results showed that the velocity gradient was nearly constant in a region of the dimensions of the gap between the adjacent rollers. We thus conclude that the representation of (2.1) is adequate for our purposes and proceed to the determination of the functions f_1 through f_4 of equations (2.33) through (2.36).

The flow type parameter, α, could be easily determined from macroscopic features of the streamlines of the flow given by (2.4). For $\alpha > 0$ the dividing streamlines, found by taking $c^2 = 0$ in (2.4), are linear, corresponding to the eigenvectors of (2.5) for the trajectories of the fluid elements. These streamlines are termed the entrance and exit streamlines, corresponding to the eigenvectors with the negative and positive eigenvalues, respectively. The angle between the entrance and exit streamlines is related to the flow type, α, by:

$$\tan(\vartheta/2) = \alpha^{1/2} . \tag{2.42}$$

This angle could be measured to within ± 1 degree, yielding an uncertainty of 3% in α. For $\alpha < 0$, the flow type could be deduced from the ratio of the length of the minor to major axis of the elliptical streamlines of (2.4):

$$\frac{m_1}{m_2} = \sqrt{-\alpha} . \tag{2.43}$$

A series of photographs was taken to determine the relationship between the roller speeds and the flow type α. In this series, rollers one and three were driven at the same rate, and the speeds of rollers two and four were also identical. The ratio of the speeds of crosswise pairs and the sum of the four rollers speeds (to verify that the flow type was independent of the shear rate for a given ratio) was varied. Figure 2.10 shows the measured value of α versus the ratio of roller speeds for $-1 < \alpha < 1$. In later experiments (discussed below) the constraint that the speeds of diagonal pairs of rollers were equal was removed, and the relationship shown on Figure 2.10 applied in that case as well. Thus Figure 2.10 supplies the function f_2 in graphical form.

Determination of the relationship between the shear rate and the roller speeds required the more difficult procedure of measuring the beginning and end of a number of streaklines for each of the time exposure photographs of the flow. The shear rate could then be calculated from the expression for the particle paths:

$$x = x_0\left[\cosh(G\alpha^{1/2}t) + \frac{1+\alpha}{2\alpha^{1/2}}\sinh(G\alpha^{1/2}t)\right] + y_0\left[\frac{1-\alpha}{2\alpha^{1/2}}\sinh(G\alpha^{1/2}t)\right], \quad (2.44)$$

$$y = y_0\left[\cosh(G\alpha^{1/2}t) - \frac{1+\alpha}{2\alpha^{1/2}}\sinh(G\alpha^{1/2}t)\right] - x_0\left[\frac{1-\alpha}{2\alpha^{1/2}}\sinh(G\alpha^{1/2}t)\right]. \quad (2.45)$$

For the shear rate calculations, accurate measures of the exposure times were required. These were determined by the following method: A black disk with a reflective radial stripe was attached to the shaft of one of the stepping motors, which was then driven at a precise speed by applying a signal of known frequency. Several photographs at each exposure time setting on the camera were taken, and the angle swept by the motor during the exposure was used to calculate the exposure time. The exposure time measurements using this method were reproducible to within about 4%.

Since only flows with positive α were used in this study, the relationship between the shear rate and roller speeds were determine for these flows only.

Figure 2.11 shows the measured shear rate as a function of the speed of rollers 1 and 3, for $0 \leq G \leq 10$ sec $^{-1}$ with α of 1.0, 0.75, 0.50, and 0.25. As for the determination of the flow type, rollers 1 and 3 were driven at the same rate in these initial studies. The relationship is evidently linear and independent of flow type. The least-squares best fit for the data is given by:

$$G = 0.0399(\omega_1 + \omega_3) \qquad (\omega_1 \text{ and } \omega_3 \text{ equal}) \tag{2.46}$$

where ω_1 and ω_3 are the speeds of rollers 1 and 3 in revolutions per minute. Later experiments verified that the sum of the speeds of rollers 1 and 3 could indeed be used when the two were unequal, provided that the difference between their speeds was less than about 10%. Thus the function $f_1(G)$ in (2.33) is given by:

$$f_1 = \frac{G}{0.0399}. \tag{2.47}$$

To determine the position of the stagnation point as a function of the roller speeds (functions f_3 and f_4 in (2.35) and (2.36)), photographs similar to those used for determination of the flow type were used, except that a laser beam was shined through the flow field in a fixed position to serve as a reference from which to measure the position of the stagnation point. Initially, attention was restricted to $\alpha = 1$, varying the ratio of the speeds of rollers 3 and 4 to those of rollers 1 and 2 so that the stagnation point moved along the x axis only. Two different shear rates were studied to verify that the relationship between the stagnation point position and the ratio of the speeds of the left and right roller pairs was independent of shear rate. The results of these measurements are shown in Figure 2.12. The stagnation point position, x_s, is reduced by the dis-

tance b from the center of the device to the line joining the centers of two adjacent rollers (in the four roll mill used in these experiments b = 6.35 cm.) The line in Figure 2.12 represents the empirically determined best fit of the data for $x_s > 0$, given by

$$\frac{x_s}{b} = 0.055\left[\frac{\omega_3-\omega_2}{\omega_1-\omega_4} - 1\right]^{0.825} . \tag{2.48}$$

Decomposing the stagnation point into its components (x_s', y_s') in the rotated coordinate system of Figure 2.9 yields

$$\frac{x_s'}{b} = 0.039\left[\frac{\omega_3}{\omega_1} - 1\right]^{0.825} , \tag{2.49}$$

$$\frac{y_s'}{b} = 0.039\left[\frac{\omega_4}{\omega_2} - 1\right]^{0.825} , \tag{2.50}$$

which allows us to determine the functions f_3 and f_4 of (2.35) and (2.36) above:

$$f_3(x_s') = 1+51.20\,(x_s'/b)^{1.2121} , \tag{2.51}$$

$$f_4(y_s') = 1+51.20\,(y_s'/b)^{1.2121} . \tag{2.52}$$

These relationships show that for a stagnation point movement of 0.02 cm from the device center (a typical control action), a roller speed change of less than 2% is required.

A final set of experiments was performed to verify that the generalizations made from the somewhat restrictive conditions used to determine the functions f_1 through f_4 were indeed valid when the restrictions were relaxed to allow the four roller speeds to vary independently. Roller speeds required to generate various shear rates and stagnation point positions along the exit streamlines for flows with α of 1.0, 0.8, 0.6, 0.4, and 0.2 were calculated by determining f_1-f_4 from the calibration results discussed above, and then computing the roller

speeds from (2.38) to (2.41). The four roll mill was run with the rollers at these speeds, and photographs similar to those used for the initial calibration were taken. Flow type, shear rate, and stagnation point position were determined from these photographs and compared to those that the combination of roller speeds was intended to produce. The agreement between the intended and actual flow parameters was generally within about 5% provided that the stagnation point displacment was less than about 0.2 cm. Since the control actions required stagnation point movements which were generally substantially less than this displacement, the simple model of Section 2.3 was judged adequate for our purposes.

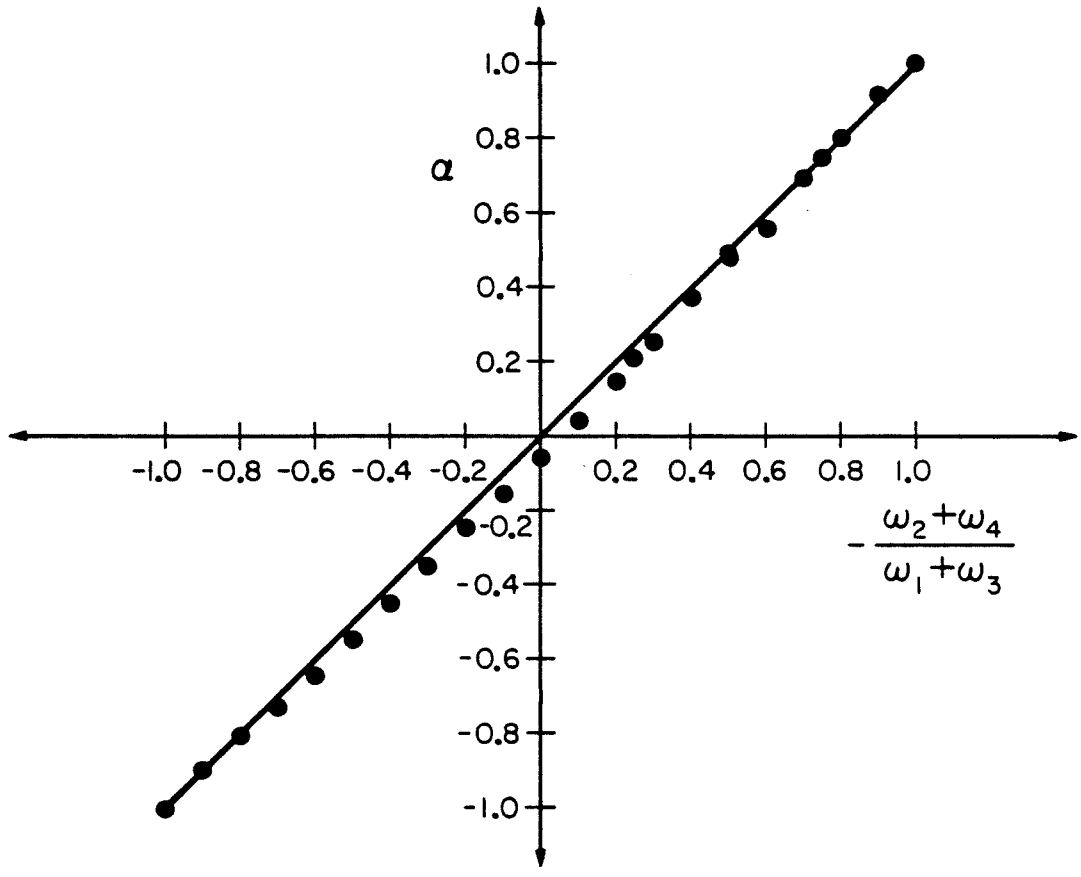

Figure 2.10
Observed flow type vs. roller speed ratio in four roll mill

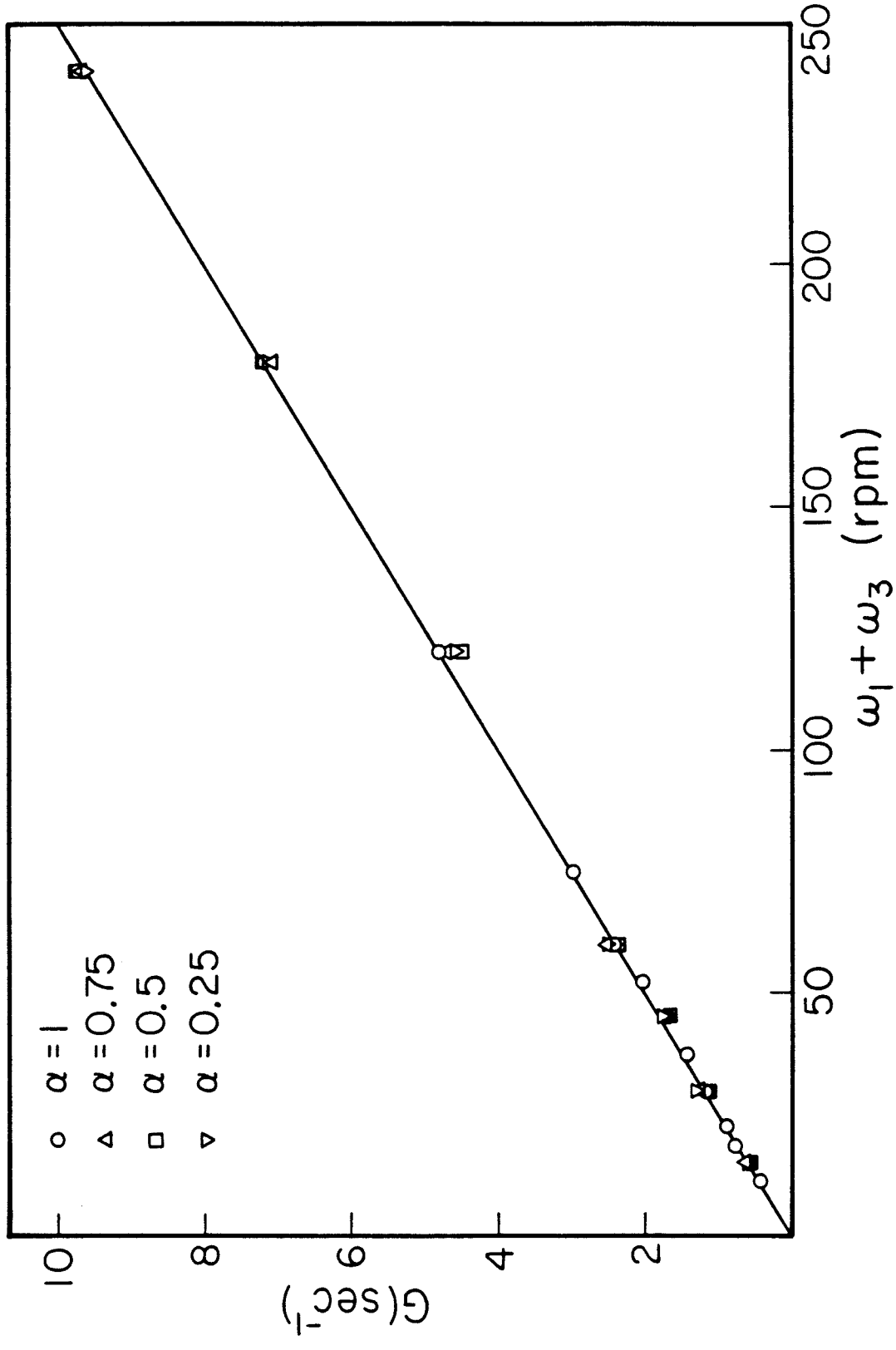

Figure 2.11
Measured shear rate vs. speed of fastest pair of rollers

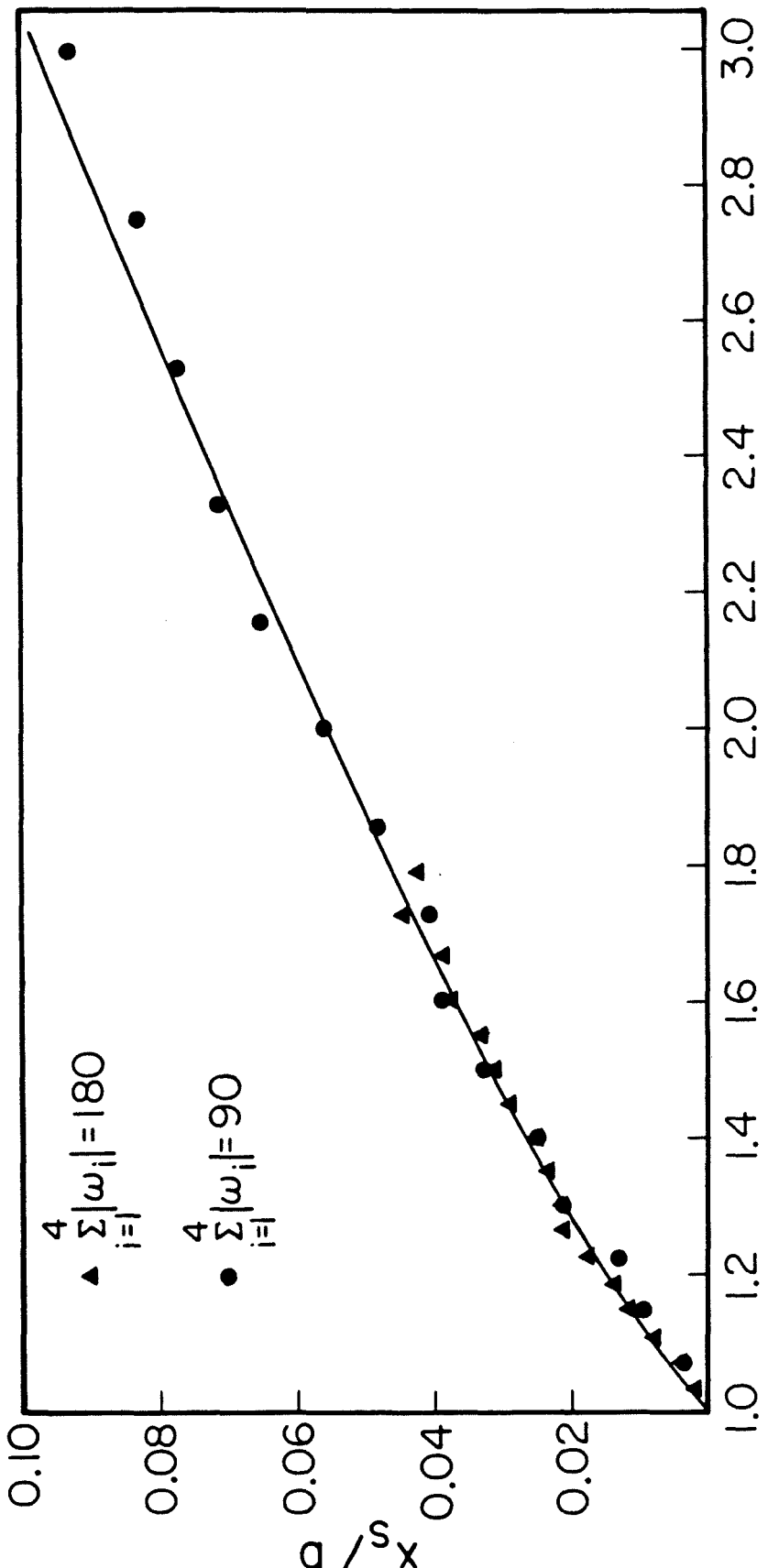

Figure 2.12
Stagnation point position vs. roller speed ratio for $\alpha = 1$

2.5 FLUID SYSTEMS AND PROPERTIES

The suspending fluid used for the experiments was Pale 4 Oil, an oxidized castor oil available from CasChem Inc. of Bayonne, N.J. The drop fluids were a series of silicone fluids (Dow Corning 200 Fluid from Dow Corning of Midland, Mi.) with nominal kinematic viscosities of 5, 50, 100, 200, 500, 1000, 30000, and 60000 centistokes, plus three blends of the 1000 and 30000 centistoke fluids with kinematic viscosities of 2500, 6700, and 12000 centistokes. These Pale 4 Oil - silicone fluid systems were chosen because the densities match closely, and the interfacial tension between the drop and suspending fluid (4-6 dynes/cm) falls in a range where deformation and burst phenomena occur over a reasonable range of shear rates (0-1 sec^{-1}) for reasonable drop sizes (about .2 cm diameter).

Stone [1984] performed some experiments in the same device using Pale 170 oil, another grade of oxidized castor oil with viscosity approximately one fourth that of Pale 4 oil, as the suspending fluid. He used 30000 centistoke silicone fluid as the drop fluid to investigate a higher viscosity ratio than was possible using Pale 4 oil as the suspending fluid.

The kinematic viscosities and densities of the fluids were measured as a function of temperature in the range from 20° C to 25° C using a series of Cannon-Fenske capillary viscometers and a pycnometer. All of the fluids have been reported to be Newtonian (Rumscheidt and Mason [1961]) in the shear rate range covered by these experiments.

The interfacial tension between each of the silicone fluids and the Pale 4 Oil was measured using a ring tensiometer (Fisher Scientific Model 20). There were several weaknesses associated with this technique. The measurements could not be made as a function of temperature since facilities were not available to do

this. But a more serious difficulty is that the force for interface rupture as the ring is pulled through the interface in the ring tensiometer is generated by the density difference between the two fluids. Thus the accuracy of the measurement suffers as the densities of the two fluids approach each other. For the fluid system considered by Stone [1984], the density difference was so small that no reliable results could be obtained from the ring tensiometer measurement.

On the other hand, the results of the drop deformation experiments, in the limit of small drop deformations, furnish a measure of the interfacial tension which is independent of the density difference (so long as the density difference is small). The interfacial tension can be inferred from comparison of the observed slightly deformed drop shapes to the shapes predicted by the linear theory of Taylor [1934]. This theory predicts that the scalar measure of deformation D_f of (1.13), is directly proportional to the dimensionless shear rate Ca of (1.10), with the slope a weak function of the viscosity ratio. Our experiments confirmed this linear relation for nearly spherical drops, and the initial slope of D_f vs. $G\mu a$ yielded a value for the interfacial tension. We thus determined an interfacial tension from the small deformation observations by averaging the values calculated for the five different flow types for each drop - suspending fluid system, and it was this value that was used in subsequent data reduction for the same fluids. Although this forced agreement between the experimental observations and the small deformation theory at the lowest deformations, we expect that values of the interfacial tension from this method are more reliable than those obtained using the ring tensiometer. The difference between the interfacial tension measured using the ring tensiometer and that inferred from the drop deformation data averaged 3.3%, with a maximum difference of 14.2%. Rumscheidt and Mason [1961] reported better agreement (average deviations of only 1%) between the deformation measure of interfacial tension and the

pendant drop and drop volume methods they employed. Since these two methods are more accurate than the ring tensiometer method, particularly when the density difference between the two fluids is small, this further suggests that discrepancies between the deformation and ring tensiometer measures used in our experiments are probably due to inaccuracies in the latter.

It is interesting to note that the small deformation measure of the interfacial tension yielded a consistently higher result than the ring tensiometer measure, possibly reflecting an aging of the interface in the ring tensiometer measurement which does not occur for the small deformation measurement since internal circulation in the drop is continually moving fresh fluid to the interface. An effect similar to this was reported by Grace [1971].

All of the plots in this manuscript use the interfacial tension calculated from the small drop deformation. Using the ring tensiometer value instead would have the effect of rotating the experimental points toward the x axis for the deformation curves and displacing the experimental points upward for the burst curves. Table 2.1 shows the measured values of viscosity and density as a function of temperature for each fluid used, and Table 2.2 shows the drop and suspending fluid viscosities, and the interfacial tension from the ring tensiometer and small deformation measurements for each fluid combination investigated. Figure 2.13 shows the comparison between the interfacial tension measurements made using the two different techniques.

Table 2.1 - Fluid Properties

Fluid #	Fluid	Viscosity (P)			Density (g/cm^3)		
		20.0°	22.5°	25.0°	20.0°	22.5°	25.0°
1	Pale 4 oil	53.32	41.97	33.55	.9961	.9953	.9931
2	Pale 170 oil	14.28	11.84	9.431	.9773	.9756	.9736
3	5 cs SF [1]	.0519	.0495	.0474	.9181	.9161	.9138
4	50 cs SF	.5273	.5008	.4774	.9623	.9602	.9578
5	100 cs SF	1.050	.9964	.9483	.9645	.9618	.9598
6	200 cs SF	2.139	2.031	1.937	.9692	.9667	.9657
7	500 cs SF	5.336	5.059	4.807	.9721	.9697	.9676
8	1000 cs SF	11.07	10.56	10.02	.9716	.9697	.9675
9	2000 cs SB [2]	27.76	25.69	24.41	.9732	.9718	.9696
10	5000 cs SB	70.21	66.88	63.46	.9737	.9721	.9699
11	10000 cs SB	126.1	119.1	113.0	.9747	.9724	.9703
12	30000 cs SF	320.6	303.2	289.0	.9754	.9729	.9707
13	60000 cs SF	673.3	638.8	607.7	.9777	.9751	.9726

[1] SF = Commercially available grade of silicone fluid

[2] SB = Blend of 1000 cs SF and 30000 cs SF to get intermediate viscosity

Table 2.2 - Properties of Fluid Systems Used

System #	Susp. Fluid [1]	Drop Fluid [1]	Temp. °C	μ_c (P)	μ_d (P)	σ_{RT} [2] (d/cm)	σ_{SD} [3] (d/cm)
1	1	3	20.8	49.5	.051	3.44	3.98
2	1	4	21.6	46.45	.511	5.34	5.32
3	1	5	21.6	46.45	1.015	4.55	5.23
4	1	6	22.3	42.80	2.038	4.52	5.27
5	1	7	22.5	42.00	5.059	5.25	5.54
6	1	8	21.8	45.25	10.70	5.14	5.51
7	1	9	22.8	40.80	25.52	5.34	5.37
8	1	10	21.9	44.60	67.68	5.41	5.41
9	1	11	22.4	42.45	119.3	5.40	5.46
10	1	12	21.2	47.8	313.0	5.52	5.98
11	1	13	21.8	45.25	648.6	5.66	5.94
12	2	12	22.0	11.93	308.0	...	5.19

[1] Fluid number refers to Table 2.1

[2] Interfacial tension (dynes/cm) measured with ring tensiometer

[3] Interfacial tension (dynes/cm) inferred from drop deformation experiments for small D_f.

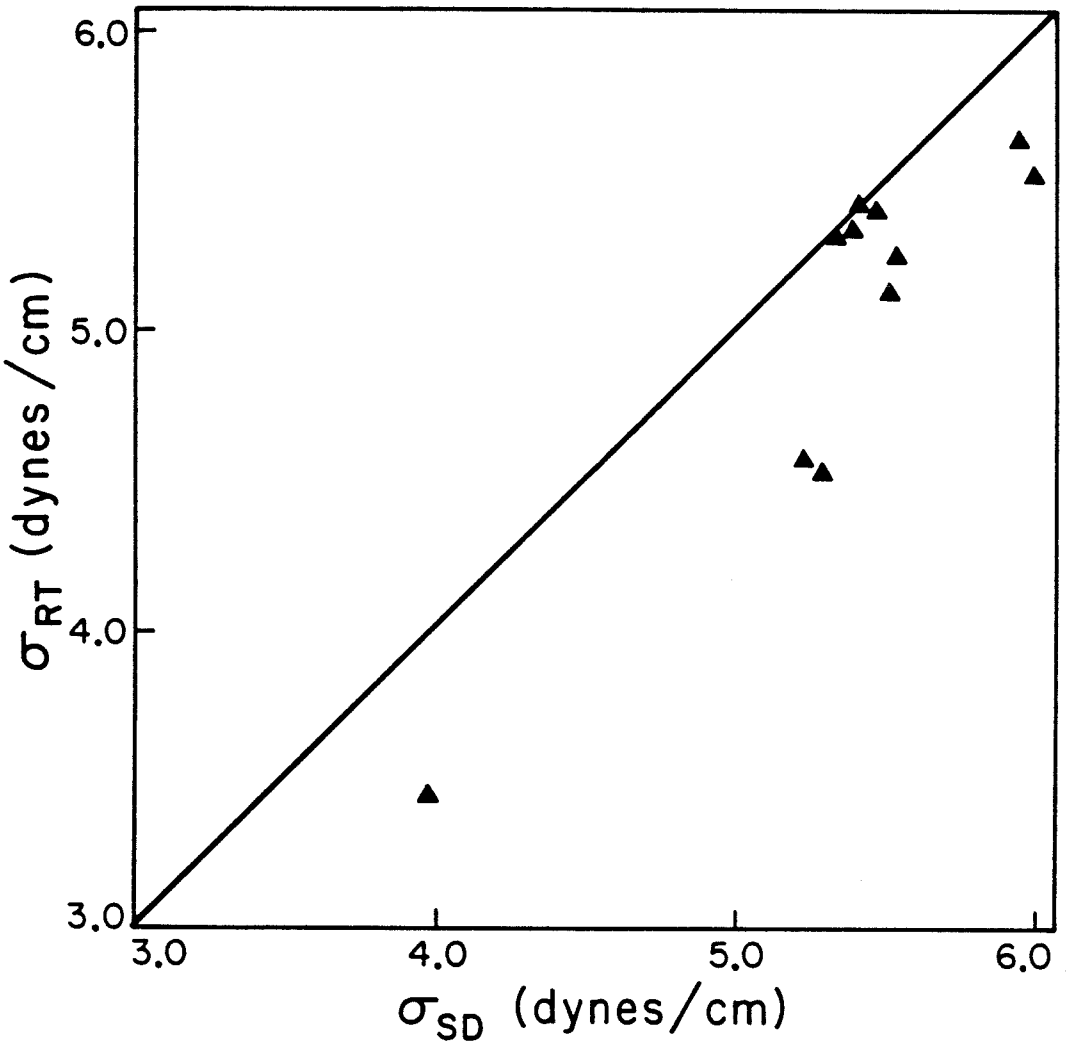

Figure 2.13
Comparison of ring tensiometer and drop deformation interfacial tension measures.

2.6 EXPERIMENTAL PROCEDURE

Drop deformation and burst experiments were performed for eleven different drop - suspending fluid systems, with viscosity ratios ranging from 0.001 to 14.5. Stone [1984] considered a fluid system where the viscosity ratio was about 27. For each fluid system, five different flow types, with α of 1.0, 0.8, 0.6, 0.4 and 0.2 were investigated, with the deformation measured as a function of the reduced shear, and the reduced shear necessary for burst established for each flow type. Generally three different drops were used for each viscosity ratio - flow type pair, with excellent reproducibility between the drops. The experiments thus covered more than four orders of magnitude in viscosity ratio for the entire range of strong flows which could be generated in the four roll mill.

The following procedure was used in performing the experiments. First, the equipment was turned on, including the DEC PDP 11/23 computer and terminal, the Apple computer, the General Electric video camera, the camera-computer interface, the two video monitors, and the light source.

The experiment was run under the supervision of a program written for the DEC computer. The second step was thus to run this program and enter some of the parameters needed by the program to keep track of the data generated and execute the control scheme. Information concerning the date, fluids used and their physical properties, the flow type, and an identifier for the roll of film taken were entered and stored in a disk file to which the experimental data were added as the experiment progressed.

The dimensions of the field of view of the control camera, the gear reduction ratio, the mode (full or half step) of the stepping motors, the inital shear rate, and the shear rate step size were also specified to allow the computer to

calculate the drop displacement from the information from the video camera, and to determine the stepping rate required for each motor to implement the calculated shear rate, flow type, and stagnation point. Finally the parameters for the control scheme (the parameter r in (2.31) and the response time of the fluid τ in (2.6)) were specified.

At this point a drop was introduced into the device by first injecting the drop with a precision syringe into a small external bath of the suspending fluid, and then using a glass tube large enough to accommodate the drop to remove the drop along with a small amount of the suspending fluid from this bath. The drop was inserted into the center area of device with this tube. This method proved much more efficient than attempting to directly inject the drop, which often resulted in drops with encapsulated bubbles.

Then, the operator adjusted the light - dark threshold to achieve maximum contrast between the drop and the background. The camera combination was focussed by moving the entire arrangement vertically until the still camera came into good focus. This insured that the video camera was also in focus since the two were set to be focussed on the same point at all times. Once these adjustments were made, the computer was directed to center the drop. The position of the drop was determined from the camera data, and the appropriate pair of rollers rotated to center the drop first in the x direction and then in the y direction. This centering step was necessary to allow the control scheme to start with the drop near the origin.

At this point, a picture of the drop was taken for later determination of its exact size. The camera focus was never changed throughout the exeriments, so that the size of the drop could be accurately determined from comparison with a picture of a ruler taken at the same camera settings. The temperature was

also measured and entered into the experimental data file, so that the viscosity of the fluids could be accurately interpolated from the measured temperature - viscosity curves. Then the experiment was started by another command to the computer. The motors were started at the speeds needed to generate the initial shear rate and flow type, and the control loop entered.

While the experiment was in progress, the operator directed the apparatus through various inputs to the terminal keyboard. Once each time through the control loop (i.e., 5 to 10 times per second) the program checked to see if one of the valid command keys had been pressed. Seventeen keys were defined to cause different actions by the program.

Eight of these keys were used to affect the size of the "window" in use, one to expand the window in each of the four directions, and a corresponding key to contract the window in each direction. These keys were located on the numeric keypad of the terminal in a cross shape to make it easy to remember the effect of each key.

The "R" key was designated to raise the light-dark threshold, and the "L" key designated to lower the threshold. The threshold was adjusted during the run to compensate for the changing light blocking characteristics of the drop as it deformed.

The "I" key was used to increase the shear rate, and the "D" key to decrease it. Changes in the shear rate were in the increments entered at the start of the program.

Two keys were used to affect the computer's perception of the center of the device in the y direction. The camera assembly could be moved in the x direc-

tion to align the center of the camera and the device along this axis, but no corresponding adjustment was possible in the y direction. Thus, the program was designed to allow for a misalignment in this direction by adding an offset to the calculated y component of the drop center of mass. The "Y" and "B" keys were used to adjust this offset up and down.

The "P" key was used to inform the program when a still picture was taken of the drop. The computer recorded the number of the picture on the roll and the current shear rate in the experiment data file and incremented the picture number. After most of the experiments had been completed, a facility was added to record the time of the picture as well, in order to allow analysis of transient deformations. The data logging feature was very helpful since it eliminated the need for the operator to write the conditions for each picture, thereby reducing the possibilities for human error associated with this task.

To terminate the experiment, the "T" key was used. This turned off all four motors, and put the program into a loop which simply waited for keyboard input. This was done to allow the operator to take more pictures after the rollers had been stopped, and record them in the data file. The "X" key was pressed to exit from this loop and return to command mode.

The sequence of events in a typical run was to start the rollers at a shear rate of about 0.05 sec^{-1}. The operator would wait for a time sufficient to allow the drop to come to a steady state shape. This time depended on the drop viscosity, varying from less than a second for the least viscous fluids up to about a minute for the most viscous drops used. A picture would then be taken with the still camera for later analysis, and conditions (i.e., picture number, shear rate, and time) recorded in the data file. The shear rate was then increased and the process repeated. A total of about 35 pictures was taken for each viscosity

ratio - flow type combination. During the course of an experiment, the operator would raise or lower the camera assembly to keep the drop in focus, adjust the threshold value and the window size to accommodate the drop, and make sure that the camera and device center were in alignment. With a little practice, the experiment could be easily operated.

As the shear rate was slowly increased, the drop proceeded through a succession of steady shapes of increasing deformation. For all but one flow type - viscosity ratio combination investigated, a shear rate was reached where the interfacial tension forces could no longer balance the viscous stresses, and no steady drop shape was possible. This was defined as the point of drop burst for these experiments. The only exception was for the highest viscosity ratio drop in the most rotational flow studied. In this case, Stone [1984] found that no burst was possible for $\lambda = 27$ in a flow field with $\alpha = 0.2$, up to the limit of shear rates realizable in the device. The vorticity in the flow field, which tends to rotate viscous drops to alignments where the effective strain rate is small, is responsible for this lack of burst. The effect of vorticity on drop deformation and burst is discussed in Chapter 3.

In cases where drop burst was realized, the flow was continued at the critical shear rate for a variable period after it was clear that no steady shapes existed. The drops became increasingly deformed, but did not break into fragments while the flow was on. At some point, the flow was turned off and the drop motion became governed by interfacial forces. Either the extended drop would fragment into a number of satellite drops through a complicated interfacial tension driven motion, or it would relax back to the original spherical shape, with the type of behavior depending on the degree of extension prior to turning the flow off and the viscosity ratio. Transient motions of the drops are discussed in

Chapter 5.

When the experiment was over, the drop fragments were carefully removed with a glass tube. This was done to prevent accumulation of debris in the suspending fluid which could interfere with locating the drop in future runs. Other than this and routine precautions to prevent dust and macroscopic dirt from entering the fluid bath, no extraordinary attempts were made to keep the suspending fluid clean. So far as can be determined from the data, no problems of contamination arose.

The pictures taken of the drops were analyzed by projecting the negatives onto the screen of a microfiche viewer. The resulting magnification (determined by projecting a picture of a ruler photographed at the same camera settings as the drops) was 41 times actual size. The undeformed radius (needed for calculation of the reduced shear) was determined by measuring the size of the drop in the picture taken at zero shear rate. The longest axis of the deformed drops was determined by eye, and the measured length recorded as L in (1.13). The angle between this axis and the exit streamline of the flow was measured so that the orientation of the drop could be calculated. The exit streamline was visible as a faint streak caused by small refractive index gradients. In a similar manner, the length of the shortest axis of the drop (90° from the longest axis) was recorded as B in (1.13).

The drop lengths and breadths, along with the shear rate for each picture and the viscosity interpolated from the measured temperature, was used to plot D_f vs. $G\mu a$. The initial slope of this curve was used to determine the apparent interfacial tension, σ. This process was repeated for each drop in all of the flow types for a particular drop - suspending fluid pair. The interfacial tension values thus obtained were very consistent from drop to drop, with variations less than

3%. The interfacial tension for the fluid system was then taken as the average of all the interfacial tensions calculated from this method.

Once the interfacial tensions were accurately determined for each fluid system, the Capillary number, Ca could be calculated, and the deformation curve, D_f versus Ca, plotted for each flow type. Of particular practical interest was the point at which drop burst was realized. Consequently, the critical Capillary number, Ca_c, was plotted as a function of viscosity ratio, with the flow type as a parameter. Similarly, the maximum stable deformation and corresponding drop orientation angle were noted for each experiment, and also plotted versus viscosity ratio, with α as a parameter. The deformation and burst curves are included in Sections 4.1 and 4.2, where they are compared to the predictions of several relevant theories and numerical calculations, as well as with the observations of previous experimenters.

3.0 DROP DEFORMATION AND BURST THEORIES

The theoretical problem of determining the deformation and burst of a drop in a viscous flow is complicated by the necessity of applying boundary conditions on the surface of the drop whose shape is, of course, *a priori* unknown. As a consequence, most theoretical investigations have concentrated on the two extreme cases, where the drop is either nearly spherical, or highly deformed and approximated as a slender body. In these two cases, progress can be made through an asymptotic approach. For intermediate deformations, numerical methods have been employed.

3.1 SMALL DEFORMATION THEORY

Solutions for slightly deformed drops date back to the pioneering work of G.I. Taylor in the 1930's. He developed a solution for small deformations by applying Lamb's general solution for the Stokes' equations to find the flow field inside and around an undeformed drop. The boundary conditions for continuity of tangential stress and continuity of velocity were satisfied at the spherical drop surface, but the normal stress discontinuity could not be balanced by interfacial tension for a spherical drop shape, and so provided a means for determining the first correction to the drop shape.

Taylor's analysis has been extended to higher order in the deviation from sphericity by a number of investigators, including Cox [1969], and Barthes–Biesel and Acrivos [1973a]. These results were unified and clarified by Rallison [1980].

Rallison [1980] presented an analysis valid for inertialess drops in a linear shear field whenever the deformation from sphericity is small. In this

formulation, the drop surface R is represented by a superposition of spherical harmonics of second and fourth order:

$$R = 1 + \varepsilon\, r^3\, \mathbf{F}\!:\!\nabla\nabla(1/r) + \varepsilon^2\,[(-6/5)\mathbf{F}\!:\!\mathbf{F} + r^5\mathbf{H}\vdots\nabla\nabla\nabla\nabla(1/r)] + O(\varepsilon^3)\,. \quad (3.1)$$

Here $r = (x\cdot x)^{1/2}$, and the dimensions are scaled by a, the undeformed radius of the drop. The tensors $\mathbf{F}$ and $\mathbf{H}$ are symmetric and traceless tensors of second and fourth rank, respectively. Rallison [1980] gives equations for the evolution of these tensors as:

$$\varepsilon\frac{D\mathbf{F}}{Dt} = a_0\mathbf{E} + \varepsilon\,\{Ca^{-1}a_1\mathbf{F} + a_2 Sd(\mathbf{E}\cdot\mathbf{F}) \;+\; \varepsilon^2\,\{Ca^{-1}a_3 Sd(\mathbf{F}\cdot\mathbf{F}) + a_4\mathbf{E}\,\mathbf{F}\!:\!\mathbf{F} + a_5\mathbf{F}\,\mathbf{E}\!:\!\mathbf{F} + a_7 Sd(\mathbf{E}\cdot\mathbf{F}\cdot\mathbf{F}) + a_8\mathbf{H}\!:\!\mathbf{E}\} \;+\; O(\varepsilon^3, Ca^{-1}\varepsilon^3) \quad (3.2)$$

$$\varepsilon\frac{D\mathbf{H}}{Dt} = b_1 Sd_4(\mathbf{EF}) \;+\; \varepsilon\,\{b_0 Ca^{-1}\mathbf{H} + b_2 Ca^{-1}Sd_4(\mathbf{FF}) + b_3 Sd_4(\mathbf{E}\cdot\mathbf{H}) + b_4 Sd_4(\mathbf{E}\cdot\mathbf{FF})\} \;+\; O(\varepsilon^2, Ca^{-1}\varepsilon^2)\,, \quad (3.3)$$

where $\mathbf{E}$ is the rate of strain tensor. The vorticity enters through the Jaumann, or corotational, derivative which is defined for a second order tensor, $\mathbf{A}$, as:

$$\frac{D\mathbf{A}}{Dt} = \frac{\partial\mathbf{A}}{\partial t} + \mathbf{v}\cdot\nabla\mathbf{A} + (\Omega\cdot\mathbf{A} - \mathbf{A}\cdot\Omega) \quad (3.4)$$

where Ω is the vorticity tensor. In (3.2) and (3.3), $a_0 - a_8$ and $b_0 - b_4$ are rational functions of the viscosity ratio, and all except b_3 and b_4, which have not been derived to date, are given by Barthes–Biesel and Acrivos [1973a]. The definitions of the symmetric deviators of second and fourth rank tensors, Sd and Sd_4, are also supplied.

These equations apply whenever the deviation from a spherical shape is small. Steady small deformations occur when either the flow strength is weak (Ca small), or the viscosity ratio is large in a flow with vorticity. Barthes–Biesel and Acrivos [1973a] applied (3.1) - (3.3) for the weak flow case, setting $\varepsilon = Ca$ in 3.2, and including the terms of order $\varepsilon^3 Ca^{-1}$ (the a_8 and a_9

terms in (3.5)). This yields the equations:

$$\varepsilon \frac{D\mathbf{F}}{Dt} = a_0\mathbf{E} + a_1\mathbf{F} + \varepsilon\{a_2 Sd(\mathbf{E}\cdot\mathbf{F}) + a_3 Sd(\mathbf{F}\cdot\mathbf{F})\} + \varepsilon^2\{a_4\mathbf{E}\,\mathbf{F}:\mathbf{F} + a_5\mathbf{F}\,\mathbf{E}:\mathbf{F} + a_6\mathbf{F}\,\mathbf{F}:\mathbf{F} + a_7 Sd(\mathbf{E}\cdot\mathbf{F}\cdot\mathbf{F}) + a_8\mathbf{H}:\mathbf{E} + a_9\mathbf{H}:\mathbf{F}\} + O(\varepsilon^3), \tag{3.5}$$

$$\varepsilon \frac{\partial\mathbf{H}}{\partial t} = b_0\mathbf{H} + b_1 Sd_4(\mathbf{EF}) + b_2 Sd_4(\mathbf{FF}) + O(\varepsilon). \tag{3.6}$$

Note that the Jaumann derivative was replaced by the Eulerian time derivative in going from (3.3) to (3.6), as is consistent since the right hand side is known only to $O(1)$. As noted by Rallison [1980], Hakimi and Schowalter [1980] demonstrated that calculation of steady states ignoring all $O(\varepsilon)$ terms in (3.5), with the exception of the rotational terms of the Jaumann derivative, resulted in a considerable improvement over predictions of the $O(1)$ theory, which results from considering only the first two terms on the right hand side. By analogy, it is possible that retention of the rotational terms of the Jaumann derivative in (3.6) would result in improved predictions for steady drop shapes, even though the other $O(\varepsilon)$ terms are not known. However, considerable computational complexity would be added, since the decoupling of (3.5) and (3.6) which occurs when steady shapes are considered would be destroyed. Therefore, no attempt was made in this work to retain the rotational terms of (3.6), but future improvements may require such an effort.

There are several important points concerning the expansion leading to (3.5) and (3.6). First, as noted by Barthes–Biesel and Acrivos [1973a], there are some inconsistencies in the order of expansion. From (3.5), $\mathbf{F}$ is known to $O(\varepsilon^2)$, so to be consistent $\mathbf{H}$ should be known to $O(\varepsilon)$. However, the coefficients b_3 and b_4 are unknown, so (3.3) is necessarily truncated after the $O(1)$ terms. In addition, terms of $O(\varepsilon^3)$, including a sixth rank deformation tensor, should be included in (3.1). Since none of these terms can be derived owing to their

complexity, Barthes–Biesel and Acrivos [1973a] suggest using (3.1), (3.5), and (3.6) as an approximate solution to the full problem, and that is the approach followed here, with the exception discussed below for high viscosity ratio cases.

When the small deformation is due to a high viscosity ratio in a rotational flow, a different expansion, using $1/\lambda$ as the small parameter, is more appropriate. In this case, the behavior of the coefficients a_i and b_i as $\lambda \to \infty$ cause some of the terms in (3.2) and (3.3) to "jump order". In the high λ limit, (3.2) and (3.3) yield (Rallison [1980], Equations 8 and 9):

$$\frac{D\mathbf{F}}{Dt} = \frac{5}{6}\mathbf{E} + \lambda^{-1}\left\{-\frac{20}{19}Ca^{-1}\mathbf{F} + \frac{10}{7}Sd(\mathbf{E}\cdot\mathbf{F}) - \frac{5}{4}\mathbf{E} - 3\mathbf{E}\mathbf{F}:\mathbf{F} + \right.$$
$$\left. + 18Sd(\mathbf{E}\cdot\mathbf{F}\cdot\mathbf{F}) - 6\mathbf{F}\mathbf{E}:\mathbf{F}\right\} + O(\lambda^{-2}, Ca^{-1}\lambda^{-2}), \qquad (3.7)$$

$$\frac{D\mathbf{H}}{Dt} = \frac{1}{14}Sd_4(\mathbf{E}\mathbf{F}) + b_3' Sd_4(\mathbf{E}\cdot\mathbf{H}) + b_4' Sd_4(\mathbf{E}\cdot\mathbf{F}\mathbf{F}) + O(\lambda^{-1}, Ca^{-1}\lambda^{-1}) . \qquad (3.8)$$

When terms of $O(\varepsilon^2)$ are retained in (3.5), and the limiting values of a_i as $\lambda \to \infty$ substituted, all terms of (3.7) are preserved (as well as a few which are higher order in λ^{-1} and have been truncated from (3.7)). Therefore, computations using (3.5) will remain accurate to $O(\lambda^{-1})$ for large viscosity ratio. In contrast, (3.6) does not allow calculation of $\mathbf{H}$ even to $O(1)$ in the high viscosity ratio limit. This is because the $O(\varepsilon)$ terms of (3.3) have been truncated in going to (3.6), since the functions b_3 and b_4 are unknown. These neglected terms may "jump order" (depending on the behavior of b_3 and b_4 as $\lambda \to \infty$) and thus appear as $O(1)$ in (3.8). In fact, for high viscosity ratio systems, calculations retaining the fourth order tensor terms as calculated from (3.6) give drops with unrealistic lobed shapes, apparently arising from overestimation of these terms. Therefore, for viscosity ratios greater than 3.0, the fourth order tensor terms of (3.1) were dropped. This gave much more realistic drop shapes in the high λ limit, and deformations which compared well with the experimental observations.

For the steady deformation case, certain simplifications to (3.5) and (3.6) are possible. Equation (3.6) can be solved for **H** directly in terms of **E** and **F**, and the result substituted into (3.5). Use of an identity for the fourth order symmetric deviator then yields (Barthes–Biesel and Acrivos [1973a]):

$$\begin{aligned} 0 = {} & a_0\mathbf{E} + a_1\mathbf{F} + \varepsilon\{a_2 Sd(\mathbf{E}\cdot\mathbf{F}) + a_3 Sd(\mathbf{F}\cdot\mathbf{F}) - \Omega\cdot\mathbf{F} + \mathbf{F}\cdot\Omega\} + \\ & + \varepsilon^2\{c_1\mathbf{EF}:\mathbf{F} + c_2\mathbf{EE}:\mathbf{F} + c_3\mathbf{FF}:\mathbf{F} + c_4\mathbf{FE}:\mathbf{F} + c_5\mathbf{FE}:\mathbf{E} + \\ & + c_6 Sd(\mathbf{E}\cdot\mathbf{F}\cdot\mathbf{F}) + c_7 Sd(\mathbf{E}\cdot\mathbf{E}\cdot\mathbf{F}), \end{aligned} \tag{3.9}$$

where $c_1 - c_7$ are algebraic combinations of a_i and b_i, and are given by Barthes–Biesel and Acrivos [1973a].

To apply (3.1), (3.6) and (3.9) to the four roll mill flow of (2.1), **E** and Ω are substituted into (3.9), and the component equations written. The requirements of symmetry and tracelessness yield three independent components of **F**; F_{11}, F_{12}, and F_{22}. For convenience, the first two are written in the linear combinations $S = F_{11} + F_{22}$ and $D = F_{11} - F_{22}$. **H** has five independent nonzero components; H_{1111}, H_{1112}, H_{1122}, H_{1222}, and H_{2222}. In terms of S, D, and F_{12}, (3.9) reduces to the system of nonlinear algebraic equations:

$$\begin{aligned} 0 = {} & 2a_0A + a_1D + \varepsilon\{a_2AS + a_3SD + 2(1-\alpha)\} + \varepsilon^2\{2c_1AT + 2c_2A^2D + \\ & + c_3TD + c_4AD^2 + 2c_5A^2D + c_6A\left(\frac{S^2}{2} + 2F_{12}^2 + \frac{D^2}{2}\right) + c_7A^2D\}, \end{aligned} \tag{3.10}$$

$$\begin{aligned} 0 = {} & a_1F_{12} + \varepsilon\{a_3F_{12}S - \frac{1-\alpha}{2}D\} + \varepsilon^2\{c_3TF_{12} + c_4ADF_{12} + \\ & + 2c_5A^2F_{12} + c_7A^2F_{12}\}, \end{aligned} \tag{3.11}$$

$$\begin{aligned} 0 = {} & a_1S + \varepsilon\{\frac{a_2AD}{3} - a_3(S^2 - T/3)\} + \varepsilon^2\{c_3ST + c_4ASD + \\ & + 2c_5A^2S + \frac{c_6ASD}{3} + \frac{c_7A^2S}{3}\}, \end{aligned} \tag{3.12}$$

where T is defined as $\mathbf{F}:\mathbf{F}$ and A as $(1 + \alpha)/2$. Substituting into (3.6) yields:

$$H_{1111} = -\frac{b_1A}{35b_0}(51F_{11} - 6F_{22}) - \frac{b_2}{35b_0}(57F_{11}^2 - 48F_{12}^2 + 12F_{22}^2 + 12F_{11}F_{22}) \tag{3.13}$$

$$H_{1112} = -\frac{3b_1A}{2b_0}F_{12} - \frac{b_2}{7b_0}(15F_{11}F_{12} - 6F_{12}F_{22}), \tag{3.14}$$

$$H_{1122} = \frac{b_1A}{70b_0}(51F_{11}-51F_{22}) - \frac{b_2}{35b_0}(-6F_{11}^2+54F_{12}^2-6F_{22}^2+39F_{11}F_{12}), \tag{3.15}$$

$$H_{1222} = \frac{3b_1A}{2b_0}F_{12} + \frac{b_2}{7b_0}(6F_{11}F_{12} - 15F_{12}F_{22}), \tag{3.16}$$

$$H_{2222} = -\frac{b_1A}{35b_0}(6F_{11}-51F_{22}) - \frac{b_2}{35b_0}(12F_{11}^2-48F_{12}^2+57F_{22}^2+12F_{11}F_{22}) \tag{3.17}$$

These equations reduce properly to Equations 4.1 of Barthes-Biesel and Acrivos [1973a] for two-dimensional extensional flow (α = 1) and, with appropriate rotation of the coordinate system, to Equations 5.1 for simple shear flow (α = 0), except that the coefficient of the c_7 term in Equation 5.1 of Barthes-Biesel and Acrivos [1973a] should be 1/3 rather than 1/6.

The system (3.10) - (3.12) was solved for S, D, and F_{12} using a Newton iteration scheme. Once S, D, and F_{12} are known, calculation of the components of **F** and **H** is straightforward. For purposes of computing D_f, the scalar measure of deformation defined by (1.13), (3.1) can be applied in the z =0 plane, yielding:

$$\begin{aligned} R(\vartheta) = 1 + 3\varepsilon\{&F_{11}\cos^2\vartheta + 2F_{12}\cos\vartheta\sin\vartheta + F_{22}\sin^2\vartheta\} + \\ &+ \varepsilon^2\{\frac{-6}{5}T + 105(H_{1111}\cos^4\vartheta + 4H_{1112}\cos^3\vartheta\sin\vartheta + \\ &+ 6H_{1122}\cos^2\vartheta\sin^2\vartheta + 4H_{1222}\cos\vartheta\sin^3\vartheta + H_{2222}\sin^4\vartheta)\}, \end{aligned} \tag{3.18}$$

where ϑ is the angle from the x axis in the $x-y$ plane. The maximum and minimum of $R(\vartheta)$ are then L and B, respectively. The orientation angle is defined as the angle for which $R(\vartheta)$ is maximum.

To assess the stability of the calculated shapes, a conventional linear stability analysis of (3.5) and (3.6) was performed. Small perturbations, **F'** and **H'** were superimposed on the steady state solutions and the resulting equations

linearized about the steady state, discarding terms second order in the perturbations. This process yields (Barthes–Biesel and Acrivos [1973a]):

$$\varepsilon\frac{\partial \mathbf{F}'}{\partial t} = a_1\mathbf{F}' + \varepsilon\{a_2 Sd(\mathbf{E}\cdot\mathbf{F}') + 2a_3 Sd(\mathbf{F}\cdot\mathbf{F}') - \Omega\cdot\mathbf{F}' + \mathbf{F}'\cdot\Omega\} +$$
$$+ \varepsilon^2\{2a_4\mathbf{EF}':\mathbf{F}' + 2a_6\mathbf{FF}':\mathbf{F}' + a_5\mathbf{FE}:\mathbf{F}' + a_9\mathbf{H}:\mathbf{F}' + a_5\mathbf{F}'\mathbf{F}:\mathbf{E} + a_6\mathbf{F}'\mathbf{F}:\mathbf{F} +$$
$$+ a_7 Sd(\mathbf{E}\cdot\mathbf{F}\cdot\mathbf{F}') + a_7 Sd(\mathbf{E}\cdot\mathbf{F}'\cdot\mathbf{F}) + a_8\mathbf{H}':\mathbf{E} + a_9\mathbf{H}':\mathbf{F}\}, \quad (3.19)$$

$$\varepsilon\frac{\partial \mathbf{H}'}{\partial t} = b_0\mathbf{H}' + b_1 Sd_4(\mathbf{EF}') + 2b_2 Sd_4(\mathbf{FF}'). \quad (3.20)$$

Writing the components of (3.19) and (3.20) reduces the linear stability analysis to finding the eigenvalues of two matrices, an 8 by 8 matrix of disturbances to the components of **F** and **H** which are nonzero at steady state, and a 6 by 6 matrix of disturbances to the components which are zero at steady state. The components of the two matrices are given in Appendix 1. The eigenvalues were computed using a routine supplied as part of the IMSL subroutine library. The algebra required to write the component equations of (3.19), (3.20), (3.9) and (3.6) was performed with the aid of the SMP (Symbolic Manipulation Program) package developed by the High Energy Physics department at Caltech.

The deformation and orientation curves (D_f and ϑ versus ε or Ca) were calculated for every flow type - viscosity ratio combination investigated experimentally. Following Barthes–Biesel and Acrivos [1973a], we calculated the curves to $O(\varepsilon)$ by discarding the $O(\varepsilon^2)$ terms in (3.5), and to $O(\varepsilon^2)$ by retaining these terms. In both cases, (3.1) was used in its entirety except that the fourth order tensor terms were disregarded for $\lambda > 3$ as described above. Each curve was calculated by starting at nearly zero ε (or Ca), using an undeformed sphere as the initial guess for the Newton iteration technique. The calculated deformation was used as the new initial guess, and the process repeated for higher ε.

In this manner, the deformation curve was computed until some condition indicating drop burst was reached. The calculation was then backed up a step, and the step size reduced by a factor of 20 to determine the critical Capillary number, Ca_c (or ε_c) as closely as possible. We considered burst to be indicated by the lack of a solution to (3.10) - (3.12), or an instability in the solution revealed by the linear stability analysis. In most cases, burst was manifested by inability to find a steady state solution. When unstable solutions were found, the instability was always in the 8 by 8 matrix, and continuing the calculation to higher ε revealed that the value of ε for which no solution existed was within 0.6% of the value for unstable solutions. Also, when burst was indicated by the lack of existence of a steady solution, the eigenvalues for the 8 by 8 matrix were small negative numbers, decreasing in magnitude with increasing ε. Thus, the two criteria for burst nearly coincided for the cases we investigated.

It should be noted that, *a priori*, there is no reason to be particularly optimistic about the accuracy of drop burst predictions from the small deformation theory. In general, drop burst occurs at deformations which are not especially small, outside of the range where the small deformation theory is technically valid. Even disregarding this, there is no rigorous justification for the inherent assumption that lack of a stable solution to the approximate governing equations necessarily means that a solution of the exact equations is likewise lacking. Thus the burst predictions of the small deformation theory must be tested, either through experiments or through more exact numerical calculations. As we will see in Section 4.2, it turns out that the small deformation theory not only reproduces the qualitative features of the drop burst curves quite accurately, it also provides a surprisingly good quantitative estimate for drop burst when the viscosity ratio is greater than about 0.05.

3.3 LARGE DEFORMATION THEORY

The small deformation theory does not accurately predict drop deformation or burst for λ less than about 0.05. For these cases, the drops are highly deformed, and a theory treating small perturbations from the spherical shape would not be expected to apply. Fortunately, for $\lambda \ll 1$, an analytical solution which takes advantage of the observed slenderness of the drops is available.

As for the small deformation theory, G.I. Taylor [1964] was the first to present solutions for highly elongated drops. The analysis was refined and clarified by Buckmaster [1972,1973], and Acrivos and Lo [1978]. The latter authors utilized the method of inner and outer expansions for a particularly concise and elegant solution which is summarized below.

Acrivos and Lo [1978] considered a steady slender drop in an axisymmetric extensional flow with components (in cylindrical coordinates):

$$u_x = G\,x\,,\ u_r = -\tfrac{1}{2}G\,r\,,\ u_\phi = 0\,, \tag{3.21}$$

far from the drop. This case is the simplest, since the drop cross section is circular, and the centerline position is known (aligned with the x axis). Velocities are scaled with $G\,L$ and dimensions with L. The drop surface is represented by:

$$r = \varepsilon R(x)\,, \tag{3.22}$$

where ε is proportional to the ratio of the drop diameter at $x = 0$ to its half length, and the slenderness ratio so defined is assumed small. The flow exterior to the drop is divided into an outer region, where both r and x are of $O(1)$, and an inner region, where r is $O(\varepsilon)$. Appropriate scaling of the creeping flow equations immediately reveals that, to first order in ε, the drop affects the flow only in the inner region. In this region, the tangential stress boundary condition gives $\partial u_x / \partial r = O(\varepsilon^2)$, so to a first approximation,

$$u_x = f(x), \tag{3.23}$$

and matching with the outer solution gives $f(x) = x$. The continuity equation then gives u_r:

$$u_r = -\frac{r}{2} + \varepsilon^2 \frac{A(x)}{r}. \tag{3.24}$$

The function $A(x)$ is determined from the kinematic condition at the drop surface, $\mathbf{u}\cdot\mathbf{n} = 0$, where $\mathbf{n}$ is the unit inward normal to the surface. This yields

$$u_r = -\frac{r}{2} + \frac{\varepsilon^2 R}{r}\left[\frac{R}{2} + xR'\right], \tag{3.25}$$

with $R' = dR/dx$. Substituting (3.23) and (3.25) into the equations of motion shows that, to first order, the pressure outside is not affected by the presence of the drop, and can thus be set equal to zero. The normal stress boundary condition can then be applied, giving

$$2\left[\frac{\partial u_r}{\partial r}\right]_{r=\varepsilon R} + p(x) = \left[\frac{\sigma}{G\mu L}\right]\left[\frac{1}{\varepsilon R}\right], \tag{3.26}$$

where $p(x)$ is the pressure within the drop, rendered dimensionless with respect to $G\mu$. This leads to:

$$\varepsilon = \frac{\sigma}{G\mu L}. \tag{3.27}$$

For an inviscid drop ($\lambda = 0$), $p(x)$ is an unknown constant, P, and (3.27) becomes:

$$xR' - \nu R = -\tfrac{1}{2}, \tag{3.28}$$

with $\nu \equiv \tfrac{1}{2}P - 1$. The boundary condition, $R(\pm 1) = 0$, specifies that the drop ends are closed. This equation has the solution (Acrivos and Lo [1978]):

$$R = \frac{1}{2\nu}[1 - |x|^{\nu}]. \tag{3.29}$$

The determination of ν is not easy. Prior to the work of Acrivos and Lo [1978],

Taylor [1964] selected $\nu = 2$ without providing justification. Buckmaster [1972] proposed that ν be an even integer; so that (3.29) for the shape was analytic at $x = 0$, and noted that $\nu = 2$ gives shapes with the smallest deformation and was therefore a logical choice. He also demonstrated that ν could not be determined from a detailed investigation of the solution in the exponentially small region near the end of the drops, nor from extending the analysis to higher order in ε. However, Acrivos and Lo [1978], by considering the region where both τ and x are $O(\varepsilon)$, (which they termed the "singular region") were able to show that no satisfactory solution, matching with those in the other regions, could be found unless $\nu = 2$ or some other even integer. Since all solutions for $\nu > 3$ proved to be unstable, they concluded convincingly that $\nu = 2$ is the correct branch of (3.29).

Substitution of (3.28) with $\nu = 2$ into the constant volume requirement gives the deformation relation for inviscid drops:

$$\frac{L}{a} = 20\, Ca^2 . \tag{3.30}$$

The slender drop theory thus predicts that an inviscid, inertialess drop (e.g., a bubble) will extend indefinitely, without breaking up, as the flow strength is increased.

It is interesting to note that the shape of the drop can be found to this order of approximation without consideration of the flow in the outer region (other than insuring that the inner solution matches appropriately), since the drop does not affect the outer flow at this order. A better approximation to the drop shape can be found by expanding the solution in ε in both the inner and outer regions. In the outer region, the drop's effect on the flow field is equivalent to that of a line distribution of Stokeslet and source singularities

along the portion of the x axis within the drop. The correction to the drop shape, of order $\varepsilon^2 \log(\varepsilon)$, is given by Acrivos and Lo [1978].

If the drop is assumed to be of low but finite viscosity ratio, the creeping flow equations must also be solved for the domain inside the drop. This analysis reveals that slender drops can exist only for $\lambda \leq O(\varepsilon^2)$, and in this case:

$$p(x) = p(0) + \frac{8}{K^2} \int_0^x \frac{s\,ds}{R^2(s)}, \tag{3.31}$$

with $K^2 \equiv \varepsilon^2 / \lambda$, and $p(0)$ the pressure inside the drop at $x = 0$, relative to the pressure in the undisturbed external flow. Substitution of this expression into(3.29), with $\nu \equiv \frac{1}{2} p(0) - 1$, gives, upon differentiation (Acrivos and Lo [1978]):

$$2xRR'' + 2RR' - 2xR'^2 - R' = \frac{8x}{K^2}, \tag{3.32}$$

with the additional boundary condition that $R(0) = 1/2\nu$. This equation has solutions:

$$R(x) = 1/8\left[1 + (1 - 64/K^2)^{\frac{1}{2}}\right](1 - x^2), \tag{3.33a}$$

$$R(x) = 1/8\left[1 - (1 - 64/K^2)^{\frac{1}{2}}\right](1 - x^2). \tag{3.33b}$$

Acrivos and Lo [1978] have shown that only the solutions corresponding to the positive branch are stable, and then only for $K^2 \leq 576/5$. Substitution of this solution into the volume conservation condition yields the deformation relation:

$$Ca\,\lambda^{1/6} = \left[\frac{1}{20}\right]^{\frac{1}{2}} \frac{\xi^{\frac{1}{2}}}{1 + 4/5\xi^3}. \tag{3.34}$$

This equation implicitly relates the dimensionless length, $\xi \equiv L\lambda^{1/3}/a$, to the flow strength. As can be seen in Figure 3.1, for values of $Ca\,\lambda^{1/6}$ up to about 0.12, the deformation curve of (3.34) is very similar to that for the $\lambda = 0$ case. At that point, the deformation increases sharply, reaching a maximum steady

extension of $\xi = 0.630$ at $K^2 = 576/5$. This point, defined as drop burst, occurs at a dimensionless shear rate, $Ca\,\lambda^{1/6}$ of 0.148. For this burst criterion to be applicable, the slenderness ratio, $R(0)/L$ must be small, which requires that $(5\lambda)^{1/2} \ll 1$.

Hinch and Acrivos [1979] extended the slender drop theory to the case where the applied shear was a two-dimensional straining motion ($\alpha = 1$ in (2.1)), considering this flow field to be a perturbation to axisymmetric straining flow. While the analysis was complicated by the fact that the non-axisymmetric nature of the imposed flow caused the cross section of the drop to be noncircular, the analysis of Hinch and Acrivos [1980] revealed that the deformation pattern and burst criterion for drops in the two-dimensional flow is nearly identical to that for axisymmetric extensional flow. This is because the cross-sectional area of the drops is very similar in the two flow fields even though the details of the cross-sectional shape differ, and it is apparently the area which governs the deformation and burst. Their results indicated that L/a in a two-dimensional extension differs by at most 2% from that predicted by the axisymmetric theory. The additional complexity in computing L/a using the results of Hinch and Acrivos [1979] was therefore judged unnecessary, and in comparisons between the experimental and predicted deformation curves (L/a vs. Ca), the results of the axisymmetric theory were used. The burst criterion for drops of low viscosity in two-dimensional extensional flow is nearly identical to the prediction of the axisymmetric theory:

$$Ca_c\,\lambda^{1/6} = 0.145\,. \tag{3.35}$$

This result was used in comparisons to the experimental burst data in Figure 4.26.

Extension of the slender drop theories to other two dimensional flows of interest ($0 < \alpha < 1$) has not been attempted to date. The analysis is complicated by the fact that the cross section of the drop is not only noncircular, but the position of the centerline is not known *a priori*. Fortunately, the analysis of Hinch and Acrivos [1979] for two dimensional straining flow indicates that as long as the cross-sectional area is comparable to that of a drop in axisymmetric extensional flow, the details of the cross-sectional shape are not particularly important. Also, from the experimental observations, we know that long slender drops, for which this theory is expected to apply, align with the exit streamline of the flow field for $0 < \alpha < 1$. At this orientation they experience an "effective strain rate" equal to $G\alpha^{1/2}$.

Thus, an approximate deformation curve can be calculated by assuming that the features of the deformation and burst process for α = 0.8, 0.6, 0.4, and 0.2 are similar to those for α = 1, as they appear to be from the experiments. The deformation can then be computed from (3.34), substituting the effective strain rate $G\alpha^{1/2}$ for G. The results of this calculation are compared to the experimental observations for λ = 0.001 and 0.01 in Figures 4.24 and 4.25. For comparisons of the bursting point, a similarly adapted version of (3.35) was employed:

$$Ca_c\ \lambda^{1/6} = \frac{0.145}{\alpha^{1/2}}. \tag{3.36}$$

The predictions from this equation are compared to the experimental data in Figures 4.29 through 4.37.

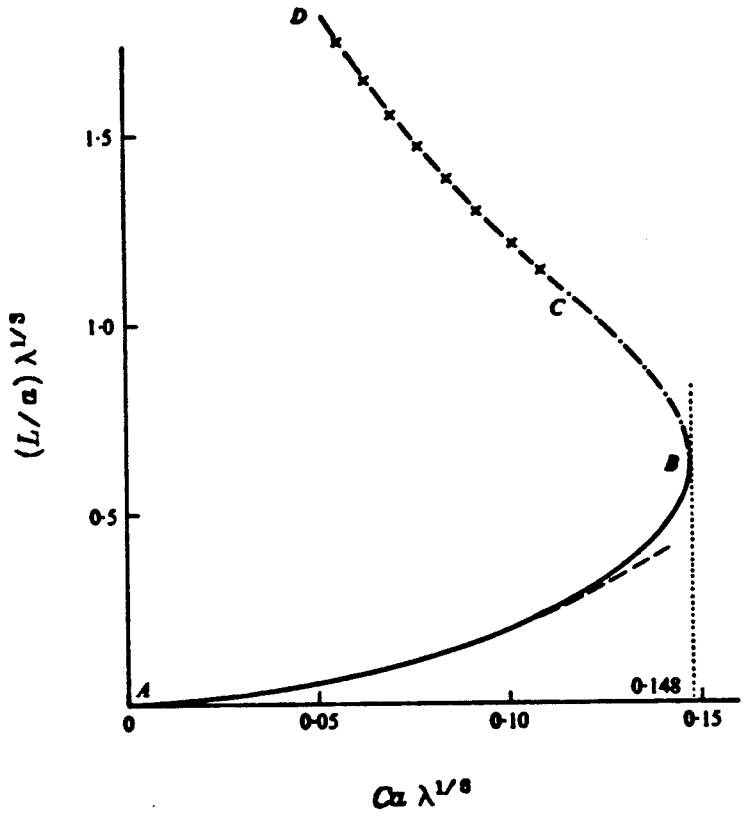

Figure 3.1
Large deformation theory predictions for drop burst. ——, stable deformation for drops with finite viscosity ratio;- - - -, $\lambda = 0$ reference. Points along BC and CD are unstable. (Acrivos and Lo [1978]).

3.3 NUMERICAL METHODS

Calculation of drop deformation is not well-suited to the finite-difference method which is frequently employed in other viscous flow problems. The boundary (i.e., drop - suspending fluid interface) is not geometrically simple nor is its conformation known in advance. In addition, information about the flow field throughout the domain is usually not required; the position and velocity of points on the interface are of primary interest. The problem is thus ideal for application of the boundary integral technique described by Youngren and Acrivos [1976]. In this formulation, advantage is taken of the linearity of the Stokes equations to express the velocity and stress at any point in the fluid as a sum of contributions from singularities distributed on the boundaries. The resulting integral equation, when applied for points on the drop surface, is then (Rallison and Acrivos, [1978]):

$$\tfrac{1}{2}(1+\lambda)u_i(\mathbf{x}) + (1-\lambda)\int_S K_{ijk}(\mathbf{x}-\mathbf{y})u_j(\mathbf{y})n_k(\mathbf{y})dS$$

$$= u_i^{\infty}(\mathbf{x}) - \frac{\gamma}{8\pi\mu}\int_S J_{ij}(\mathbf{x}-\mathbf{y})n_j(\mathbf{y})\nabla\cdot\mathbf{n}dS \ . \qquad (3.36)$$

Both $\mathbf{x}$ and $\mathbf{y}$ are points on the drop surface. The kernel functions K_{ijk} and J_{ij} are supplied by Rallison and Acrivos [1978]. The method of solution is to approximate the surface S by a number of collocation points, calculate the kernel function at each, and then solve for u_i at each collocation point by inverting the resulting matrix. The calculation is started with the drop spherical. The position of the interface is adjusted using the calculated velocity, and the process repeated until a stationary state is reached ($\mathbf{u}\cdot\mathbf{n} = 0$ for all points of S), or it is apparent that the drop will continue to deform indefinitely. The calculation is complicated by the existence of eigensolutions to (3.36) for $\lambda = \infty$ and $\lambda = 0$ which results in a singular matrix for these cases.

This numerical technique has been applied for special forms of the applied flow, and particular values of the viscosity ratio, λ. Youngren and Acrivos [1976] solved for the shape of a gas bubble in axisymmetric flow. Rallison and Acrivos [1978] extended the result to cover arbitrary viscosity ratio in the same flow. The simplifying feature for axisymmetric extensional flow is that the drop shapes are axisymmetric, so the azimuthal integrals can be performed analytically and (3.36) thereby reduces to line integrals, dramatically reducing the number of collocation points needed.

Rallison [1981] took advantage of the particularly simple form of (3.36) which results when $\lambda = 1$. In this case, no matrix inversion is required, so computation costs are low even with a large number of collocation points. This allowed Rallison [1981] to investigate flow fields for which the resulting drop shapes were three-dimensional. In particular, he applied the technique to the class of two-dimensional flows which are produced in the four roll mill for the complete range of $-1 < \alpha < 1$. The results of his calculations are compared to the experiments in Sections 4.1 and 4.2.

The numerical results have proven useful in studying cases for which the deformation cannot be adequately described by the small deformation or the large deformation theories discussed in Sections 3.1 and 3.2. It is clear, however, that numerical calculations cannot replace the asymptotic theories entirely. To date, computations have been limited to cases for which some simplification is possible (axisymmetry or equal drop and suspending fluid viscosities). Even using the efficient boundary integral technique described above, calculations for general viscosity ratios and applied flows would require inversion of large matrices, which is a time-consuming (and thus expensive) proposition. Analytic results, including asymptotic results, have the additional

advantage of clarifying the effects of physical parameters without the need for exhaustive numerical searches through multi-dimensional parameter spaces.

3.4 QUALITATIVE EFFECTS OF VORTICITY

Before discussing the quantitative comparison between the experiments and the above mentioned theories, it is perhaps useful to include some comments of a qualitative nature on the effects of vorticity on the deformation and burst of drops. The discussion is divided into two parts. We first consider the orientation of deformed drops in two-dimensional flows of the type generated in the four roll mill, and then discuss the effect of the drop orientation on the strength of the extension it experiences. Obviously, the physics of drop deformation are complicated, but the simple concepts included here are helpful in explaining a variety of the qualitative features observed.

Orientation

We first consider the orientation of a freely suspended body in a linear shear field of the type described by Equation (2.1). Analytic results are readily available for the case where the body is a solid particle, but when the body is a deformable drop the situation is considerably more complicated. Thus our approach is to consider the orientation of a solid particle, and use the insight gained from this to make qualitative predictions for a deformable drop.

Since the creeping flow equations and boundary conditions are linear for a suspended solid particle, we can separately consider the angular velocity in a purely rotational flow and a purely extensional flow, and superimpose the results to determine the angular velocity in the actual flow. In a purely rotational flow, a particle of any shape rotates with the local fluid vorticity. In the flow of Equation (2.1), the angular velocity due to the rotational component of the flow field is aligned with the z axis, and is given by:

$$\omega_v = -G(1-\alpha)\,. \tag{3.37}$$

In a two-dimensional pure-straining flow, the angular velocity depends on the orientation and shape of the particle. When the particle is isotropic, the angular velocity is zero. When the shape is anisotropic, (e.g., an ellipsoid of revolution) the angular velocity is greatest when the longest axis of the particle is aligned at $\pm 45^{\circ}$ from the principal axis of strain, since at this orientation the long axis is perpendicular to every streamline. When the long axis of the particle is aligned with the strain-rate axis, the angular velocity is zero. An expression for the angular velocity of an ellipsoid of revolution in a two-dimensional pure-straining flow ($u = gx$, $v = -gy$, $z = 0$) is given by (Chaffey, Takano, and Mason [1965]):

$$\omega_e = -g\, b\, \sin 2\vartheta\,, \tag{3.38}$$

where b is a scalar characterizing the eccentricity of the particle. It is related to the equivalent axis ratio of the ellipsoid r_e by

$$b = \frac{(r_e^2 - 1)}{(r_e^2 + 1)}. \tag{3.39}$$

This quantity ranges from zero for a sphere to +1 for an infinite rod. In (3.38) ϑ is the angle between the longest axis of the particle and the x axis. In the flow of (2.1), the strength of the extensional portion of the flow (i.e., g in (3.38)) is just $G(1+\alpha)$.

Superimposing the angular velocities in the rotational and extensional flows then gives the angular velocity in the actual flow:

$$\omega = \omega_v + \omega_e = -G(1-\alpha) - G(1+\alpha)\, b\, \sin 2\vartheta \tag{3.40}$$

To find the steady orientations, we set the angular velocity equal to zero and solve:

$$\vartheta = 1/2 \sin^{-1}\left[\frac{\alpha - 1}{b(\alpha + 1)}\right]. \tag{3.41}$$

This equation has no solutions for small b (unless $\alpha = 1$, a vorticity-free flow), which means that nearly spherical solid particles will rotate in the flow. For $b \geq (\alpha - 1)/(\alpha + 1)$, solutions exist, with particle alignment depending on b and α. The least eccentric particle which has a steady orientation, $b = (\alpha - 1)/(\alpha + 1)$, is aligned at $-45°$. As b increases (increasing eccentricity) the magnitude of the orientation angle decreases. An infinite rod ($b = 1$) aligns with the exit streamline of the flow field, $\vartheta = \frac{1}{2}\sin^{-1}[(\alpha - 1)/(\alpha + 1)]$. For a solid particle, no steady orientations with ϑ less than this value are possible.

The orientation of viscous drops is much more complicated since drops can accommodate viscous stresses through deformation. Therefore, there are two time scales which are of importance. The first is the time scale of the flow given by G^{-1}. This time scale characterizes the strength of the vorticity which is tending to rotate the drop. It appears in the solid particle case as well, but since it is the only time scale, it does not affect the equilibrium orientation in that case. The second time scale characterizes the response of the drop to viscous stresses, and is given by $\lambda\mu a/\sigma$. For a deformable drop, the ratio of the second time scale to the first, $Ca\,\lambda$, is an additional parameter affecting the equilibrium drop orientation. The other two parameters (which affect the orientation of a solid particle as well) are the flow type and the anisotropy of the drop or particle. Unfortunately, these three parameters are not independent because the deformation of the drop is related to the time scale ratio (through both Ca and λ) and to the flow type. Thus it is difficult to determine the effect of each parameter separately, and it is necessary to consider increases of the time scale ratio due to increasing viscosity ratio and increasing Capillary number separately.

When the deformation time scale is short compared to the flow time scale (low $Ca\,\lambda$), the drop can be thought of as responding instantaneously to the deforming viscous stresses. Since the extensional portion of the flow field is responsible for these deforming stresses (c.f., the $O(1)$ terms in the small deformation theory of Equation (3.2)), it follows that when $Ca\,\lambda$ is small, drops will be aligned with the principal axis of strain (the x axis in our experiments). This applies as long as the deformation is small. If λ is small and Ca moderate, the deformation will be too large for instantaneous response and the drop will be rotated away from the x axis.

Now suppose we could perform an experiment in which the time scale ratio, $Ca\,\lambda$, is increased by increasing the response time of the drop (e.g., by increasing λ with Ca constant). As the response of the drop is slowed, the vorticity in the flow rotates fluid elements away from the principal axis of strain faster than they can respond to the extension. Consequently, the magnitude of the orientation angle increases. In the limit as $\lambda \to \infty$, solid-like behavior is approached, and the drop aligns between the exit streamline and $-45°$.

When the time scale ratio $Ca\,\lambda$ is instead increased by decreasing the flow time scale (increasing G and thus Ca at fixed λ, as is the case in our experiments), the situation is more complicated because increasing Ca also causes greater deformation. From (3.41) above, it is clear that the effect of greater deformation is to align the drop more closely with the exit streamline of the flow. When the viscosity ratio is low, orientation of the drop is between the x axis and the exit streamline. Thus when Ca is increased, both the increase in $Ca\,\lambda$ and the increase in deformation serve to rotate the drop towards the exit streamline, and the result is a monotonic increase in the magnitude of the orientation angle with increasing Ca.

In contrast, when λ is large, for some values of Ca, the value of $Ca\,\lambda$ is such that the magnitude of the orientation angle exceeds that of the exit streamline. In that case, further increases to Ca have two competing effects. The effect of increasing the time constant ratio is to rotate the drop further from the extensional axis. However, the consequential increase in deformation acts to align the drop closer to the exit streamline of the flow, thus decreasing the magnitude of the orientation angle. The net result of these competing effects is the appearance of a maximum in the magnitude of the orientation angle as the shear rate is increased in some high viscosity ratio experiments.

The orientation of a drop has a strong bearing on the "effective strain rate" which it experiences. We define "effective strain rate" as the constant of proportionality between the component of fluid velocity (in the undisturbed flow field) parallel to the longest axis of the drop and the displacement along that axis. When $\boldsymbol{x}$ is a unit vector in the direction of the orientation of the drop, this is given by $\mathbf{x}\cdot\mathbf{v}$. Since the flow is a linear shear field, $\mathbf{v} = \nabla\mathbf{v}\cdot\mathbf{x}$, and substitution of (2.1) gives:

$$\text{effective strain rate} = G\left[\frac{1+\alpha}{2}\right]\cos 2\vartheta \tag{3.40}$$

Thus, the effective strain rate is a strong function of orientation, ranging from $G(1+\alpha)/2$ when the drop is aligned with the $\boldsymbol{x}$ axis, to zero when the drop is aligned at -45°. Note that when the drop is aligned with the exit streamline ($\sin 2\vartheta = (\alpha - 1)/(\alpha + 1)$), the effective strain rate is $G\alpha^{1/2}$.

This very simple analysis clearly illustrates the reason for the difficulty in breaking up viscous drops in rotational flows. The drops are rotated to orientations where the effective strain rate is very low. For example, in a simple shear flow, drops of viscosity ratio greater than about 3.5 align very close to -45°,

where the effective strain is nearly zero, so there is little tendency for the drops to extend further. Increases to G cause the drops to align still closer to the −45 line, so the orientation effects compensate for the increased flow strength, and the drops do not burst, no matter how high the shear rate. This same phenomenon occurs for other rotational flows as well, but at a higher viscosity ratio, since the ratio of vorticity to strain is lower. In our experiments, drops with viscosity ratios above 27 could not be broken up for $\alpha = 0.2$.

Another conclusion which can be drawn from the above physical description is that the effect of the flow type on the deformation characteristics is too complicated to allow definition of a dimensionless "effective strain rate" of the form $Ca\, f(\alpha)$ which would govern the deformation and burst for any α at fixed viscosity ratio. If, for example, drops were always aligned along the extensional axis, then one would expect that for a given viscosity ratio, the drop deformation and burst characteristics would depend on the quantity $Ca(1+\alpha)$ only. Similarly, if the drops were always aligned with the exit streamline of the flow field, the quantity $Ca\,\alpha^{1/2}$ would be appropriate. Since the orientation is instead a complicated function of α and $Ca\,\lambda$, the flow type must be investigated as an independent parameter in studies of drop deformation and burst.

4.0 COMPARISON BETWEEN THEORY AND EXPERIMENTS

In this chapter we compare the predictions of the small and large deformation theories, and the results of the numerical studies, to the experimental observations. The first section covers drop deformation, and the second section discusses the drop burst results.

4.1 DROP DEFORMATION

This section includes quantitative comparisons between the experimental drop deformation observations and the predictions of the small deformation and slender drop theories. A few viscosity ratio - flow type combinations have been selected to illustrate general features of the drop deformation and burst process. These are discussed in detail below. Data and comparisons with the theories for the remaining cases are presented in a more compact format.

Comparisons with the small deformation theory discussed in Section 3.1 are presented as plots of the scalar deformation parameter defined by (1.13), D_f, and orientation angle, ϑ (measured from the x axis), versus the Capillary number, Ca. The experimental observations are plotted using a different symbol for each drop for the given fluid system, and the predictions of both the $O(\varepsilon)$ and $O(\varepsilon^2)$ small deformation theories are presented as solid and dashed lines, respectively. The theoretical curves are terminated with an asterisk if the corresponding theory predicts drop burst, with the asterisk indicating the bursting point.

Similar plots are presented for comparison to the large deformation theory, which is applicable for low viscosity ratio systems. In this case, the quantity L/a is plotted versus Ca, since D_f is insensitive to shape changes at high

deformations.

For the cases chosen as examples, direct comparisons between the observed shapes (photographs) and calculated shapes are also included. These reveal that in some cases, the shapes calculated from the small deformation theory may deviate significantly from those observed, even though the value of D_f is in reasonable agreement.

4.1.1 Low Viscosity Ratio Drops

For very low values of the Capillary number, Ca, the behavior of the drops was independent of viscosity ratio and flow type. All drops were deformed into ellipsoids aligned along the extensional axis (the x axis of Figure 2.1). As the shear rate was increased, the deformation characteristics became strongly dependent upon the viscosity ratio and the rotational character of the applied flow.

Low viscosity ratio drops ($\lambda < 0.02$) required quite large values of the Capillary number for burst, and were able to attain steady shapes which were highly deformed. The lower the viscosity ratio, the greater the sustainable steady deformation and the greater the Capillary number at the point of burst. As the shear rate was increased, the radius of curvature at the ends of the drop decreased, and eventually the ends appeared to be pointed. The transition from ellipsoidal deformation to pointed ends occurred at $Ca(1+\alpha)$ approximately 0.5. The ends were more cusplike for lower viscosity drops, and for all pointed drops the ends became sharper as the shear rate increased. The drop orientation angle monotonically approached the angle of the exit streamline of the flow field ($-3.2°$, $-7.2°$, $-12.7°$, and $-20.9°$ for α = 0.8, 0.6, 0.4, and 0.2, respectively) as

the shear rate increased, and the drops became more elongated, with steady aspect ratios as high as 20 observed for the lowest viscosity ratio systems. Even in the most rotational flow considered ($\alpha = 0.2$), the centerline of the drop remained straight, without any signs of the "S" shape which is characteristic of low viscosity ratio drops in simple shear flows (Taylor [1934], Grace [1971], Torza, Cox, and Mason [1972]).

At the point of burst, the drops simply continued to extend with the ends remaining pointed, becoming drawn into a thread of essentially constant radius. The "tip streaming" phenomena reported by previous researchers (Taylor [1934], Mason et al. [1961,1972], Grace [1971]) was not observed in our experiments. It is possible that the magnification of our optical equipment was insufficient to resolve tiny drops being ejected from the drop ends. However, Torza, Cox, and Mason [1972] reported a correlation between tip streaming and the rate of change of the shear rate. They indicated that tip streaming occurred when the shear rate was changed rapidly, but apparently was suppressed for low dG/dt. Absence of tip streaming in our experiments (if it could be proven) would support this conclusion, since care was taken to increase the shear rate slowly to avoid transient phenomena.

Figure 4.1 shows a plot of the deformation parameter and orientation angle versus Capillary number for a viscosity ratio of 1.08×10^{-3} in a flow with $\alpha = 0.8$. The error bars shown in the figure are typical for the uncertainties in D_f and Ca in all of the deformation plots. The small deformation theories agree with the observed deformation within the experimental error only for small values of Capillary number, where D_f is essentially linear with Ca as predicted by the classic analysis of Taylor [1934]. The $O(\varepsilon)$ and $O(\varepsilon^2)$ corrections to the Taylor result predict a positive curvature in D_f vs. Ca, with the $O(\varepsilon)$ theory predicting

a larger deformation at a given Ca and burst at lower Ca than the $O(\varepsilon^2)$ theory. The $O(\varepsilon^2)$ theory is in better agreement with the experiment, but the predicted burst point (Ca_c = 0.280) still differs from the observed bursting point (0.51) by 45%. The experimental deformation curve exhibits positive curvature at low Ca, but has an inflection point at about Ca = 0.3, which is close to the value at which the transition to pointed ends occurs and where the $O(\varepsilon^2)$ theory fails. The rather poor agreement between the predictions of the small deformation theory and the experiment (except at low Ca) is expected, since low viscosity ratio drops require high Ca for burst, and exhibit highly deformed steady shapes, while the theory is valid only when D_f is small. We would expect a more accurate prediction for the elongated steady shapes from the slender drop theory.

Figure 4.2 shows the dimensionless length, L/a, plotted versus Ca for the same experimental conditions. The curve represents the predictions of the slender drop theory. The agreement between the theory and the experiment improves with increasing deformation, as is expected since the theory is asymptotically valid as $L/a \to \infty$. The predicted bursting point, Ca_c = 0.513, compares favorably with the observed 0.51.

Figure 4.3 shows a comparison between actual photographs of the deformed drops and the predictions of the small deformation and slender drop theories. The lines visible in the photographs are caused by small refractive index gradients in the suspending fluid which arise from minute temperature gradients. They appear along the exit streamlines of the flow, where fluids from opposite sides of the tank meet. The second and third photographs are compared to the $O(\varepsilon^2)$ small deformation theory, and the last four to the slender drop theory. The comparison with the $O(\varepsilon^2)$ theory is reasonable for the second photograph, with Ca = 0.175 and $D_f \approx 0.31$, although there are larger differences between the

experimental and calculated shapes than are suggested by the 1% difference between the experimental and predicted D_f. The ends of the calculated shape are more blunt, and the approximations inherent in representing the shape with only tensors of order two and four are apparent from the slight "bump" in the sides of the drop. As the Capillary number is increased, the shapes predicted by the small deformation theory become increasingly unrealistic, and as can be seen from the comparison with the third photograph, at $Ca = 0.265$ the shape bears only a superficial resemblance to the experimental shape (the length and breadth, and hence D_f are comparable). The $O(\varepsilon^2)$ small deformation theory predicts burst at $Ca_c = 0.28$, so for the remainder of the photographs the comparison is to the predictions of the slender drop theory. Qualitatively, the predicted and observed shapes are similar, especially for $Ca \geq 0.409$. The theory predicts values of L/a which are fairly consistently low by about 1, with the percentage error thus decreasing with increasing Ca. For the most extended drop in this sequence, the difference between the theoretical and experimental L/a was about 20%. The predictions of the slender drop theory would undoubtedly improve for lower values of λ, the viscosity ratio.

Clearly, the lowest viscosity ratio drops represent the cases for which inertia would be the most important in our experiments, both because the viscosity is the smallest, and because the length scale of the deformed drop is the largest. To verify that these effects were indeed negligible in our experiment, the inertial parameter, $\rho a \sigma / \mu^2$, defined by Acrivos and Lo [1978], was calculated. The largest value for our experiments was 0.00032, for the case where the viscosity ratio was 0.001. Thus, the quantity $(\rho a \sigma / \mu^2)^{1/5} \lambda^{-1/6}$ was 0.63. From Figure 4 of Acrivos and Lo [1978] and Figure 3 of Brady and Acrivos [1982], it is clear that inertial effects in the exterior flow and within the drop were negligible.

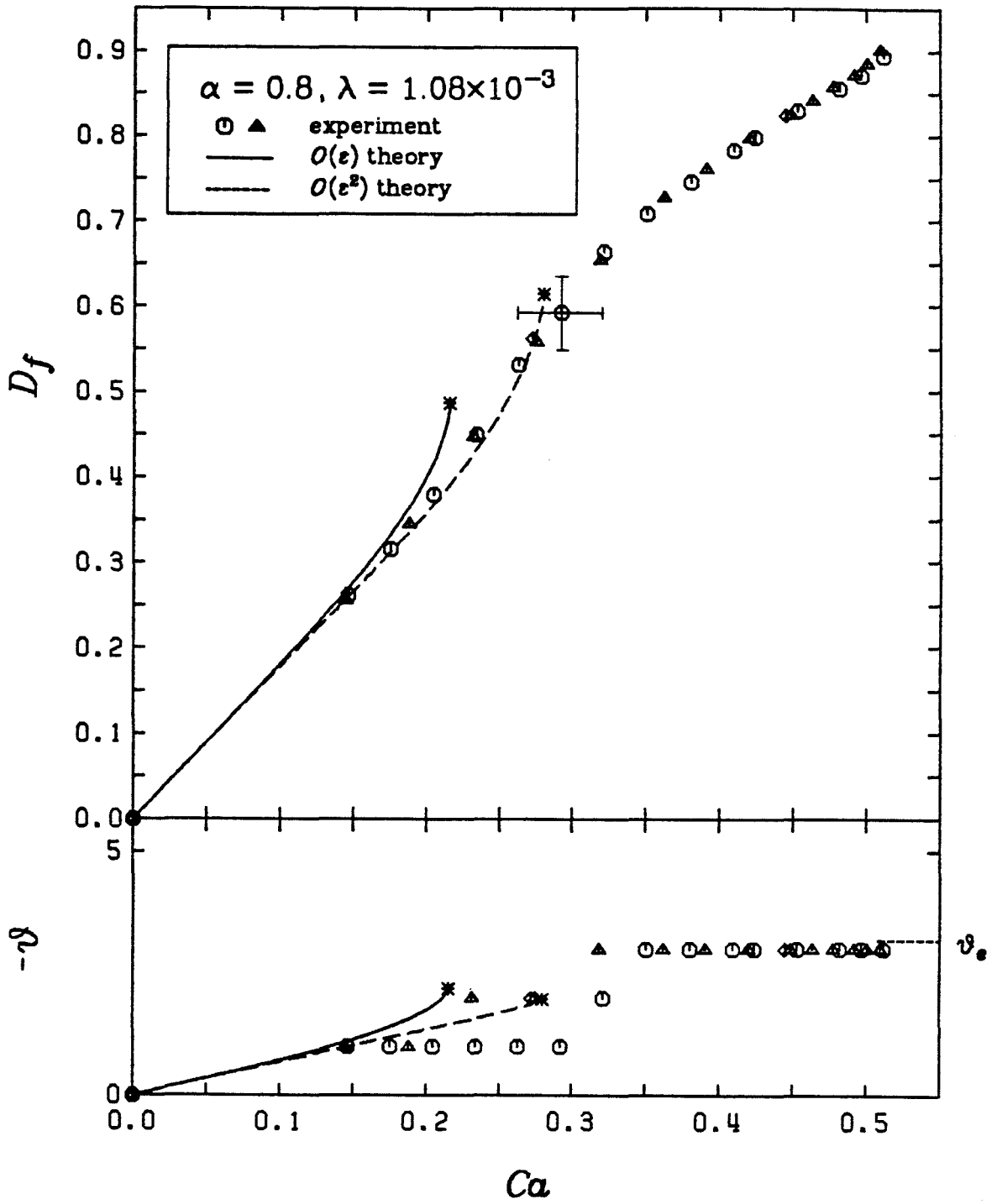

Figure 4.1
Deformation curve for $\alpha = 0.8$, $\lambda = 1.08\times10^{-3}$

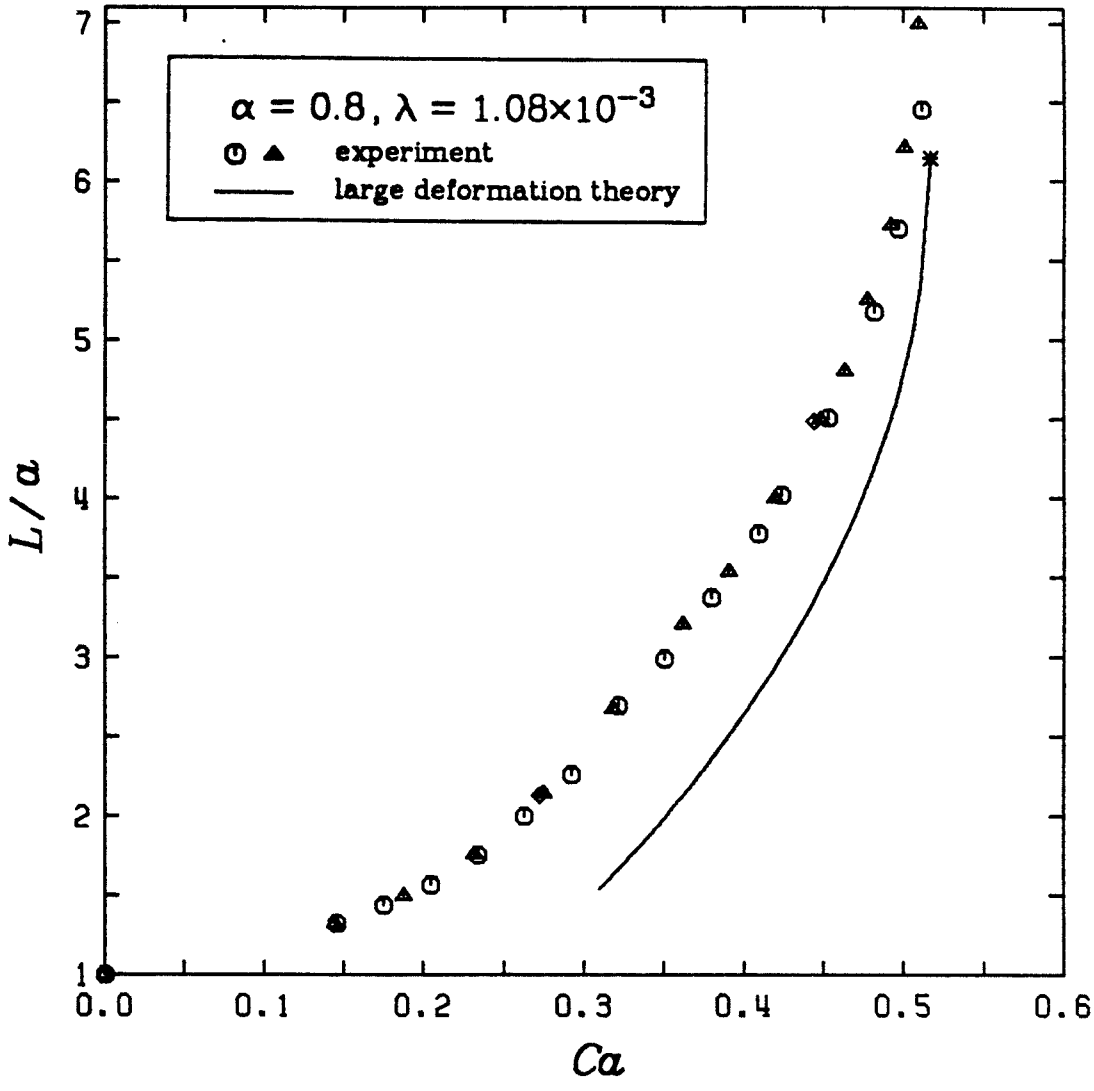

Figure 4.2
Dimensionless length vs. Ca for $\alpha = 0.8$, $\lambda = 1.08\times10^{-3}$

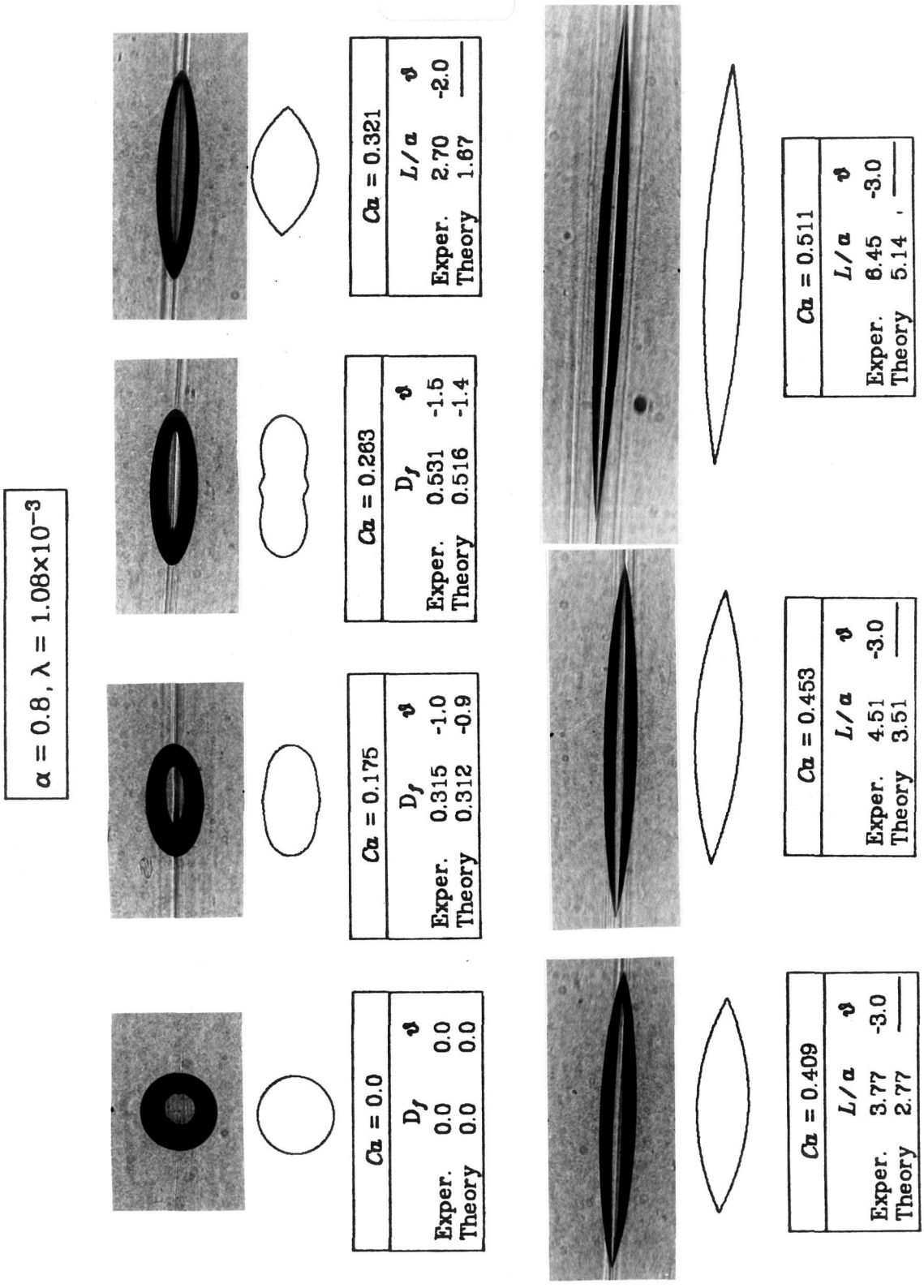

Figure 4.3
Comparison between experimental and calculated shapes for conditions of Figures 4.1 and 4.2.

4.1.2 Intermediate Viscosity Ratio Drops

All systems with the viscosity ratio between 0.02 and 2.0 behaved in a qualitatively similar manner. The ends of the drops remained rounded to the point of burst (with less viscous drops exhibiting a lower radius of curvature), and the orientation angle varied monotonically from zero (aligned with the x axis) at low Capillary number to alignment with the exit streamline of the flow as the bursting point was approached. The critical Capillary number and the maximum stable deformation both decreased as the viscosity ratio increased for all flow types investigated. As the critical shear rate was approached, drop burst was indicated by the appearance of "flat sides", where the radius of curvature in the $x-y$ cross section became infinite along the length of the drop. Once this point was reached, no steady shapes seemed possible. The drop sides became concave and the drop was pulled into a thread, with the smallest radius at the central portion. The shapes of drops undergoing this transient motion at the critical Capillary number were surprisingly similar over a wide range of viscosity ratios (all $\lambda > 0.02$). The qualitative aspects of the burst phenomena and the maximum stable deformation seemed independent of the flow type. The mode of burst observed corresponds roughly to the "B-2" mode described by Mason and coworkers [1961, 1972]. This is consistent with the descriptions of burst reported by Taylor [1934], Rumscheidt and Mason [1961], and Grace [1971] for drops in two-dimensional irrotational flow.

Figure 4.4 shows a plot of D_f and ϑ versus Ca for $\lambda = 0.118$ in a flow with $\alpha = 0.6$. In this case, the predicted values of the scalar deformation measure, D_f, are in surprisingly good agreement with the experimental observations, even up to $D_f = 0.5$. The predictions of the $O(\varepsilon)$ and $O(\varepsilon^2)$ theories are similar, with the $O(\varepsilon^2)$ theory predicting slightly higher deformation near the bursting point,

and slightly lower Ca_c at burst. The data lie above both calculated deformation curves, with burst occurring at $Ca_c = 0.21$, compared to 0.228 and 0.220 predicted by the $O(\varepsilon)$ and $O(\varepsilon^2)$ theories, respectively. The orientation angles predicted by the theory agree reasonably well with those observed, particularly in view of the difficulty in accurately measuring these angles from the photographs of the drops.

Figure 4.5 shows the comparison between the actual drop shapes and those predicted by the $O(\varepsilon^2)$ small deformation theory for the same parameters as Figure 4.4. The agreement is satisfactory for Ca up to about 0.2, at which point the drops assume shapes which could only be satisfactorily represented by including higher order deformation tensors. The "bumps" in the drop shapes are present in this case also (and, as pointed out by Barthes-Biesel and Acrivos [1973a], for all but high viscosity ratios), but are less pronounced than for lower viscosity ratios. In the final photograph in the sequence, the drop is shown bursting, while the theory predicts a steady shape for that value of Ca.

The experimental observations for $\lambda = 1.58$, $\alpha = 0.4$ are compared to the calculated deformation and orientation in Figure 4.6. At a given Ca, the $O(\varepsilon^2)$ small deformation theory predicts a deformation which is greater than that observed, while the $O(\varepsilon)$ theory predicts lower-than-observed deformations. Thus the experimental points are "bracketed" by the two theoretical curves, with neither supplying a particularly accurate prediction. The bursting point ($Ca_c = 0.178$) is underestimated by 18% by the $O(\varepsilon^2)$ theory and overestimated by 43% by the $O(\varepsilon)$ theory. This bracketing of the data, with an upper bound on the bursting point supplied by the $O(\varepsilon)$ result and a lower bound supplied by the $O(\varepsilon^2)$ result, is typical of the small deformation theory for $0.5 < \lambda < 3$.

Photographs for this case are compared to shapes calculated from the $O(\varepsilon^2)$ theory in Figure 4.7. The theory predicts drop burst at $Ca_c = 0.146$, so no calculated shapes are included for the last three photographs in the sequence. The final photograph shows the drop bursting. The calculated shapes are in qualitatively good agreement with the experiment, as are the predicted orientation angles. From comparisons between the photographs of Figures 4.3, 4.5, and 4.7, it is apparent that the ends of the deformed drops become blunter with increasing viscosity ratio, and that these shapes are more readily represented by the theory, which retains only second and fourth order deformation tensors.

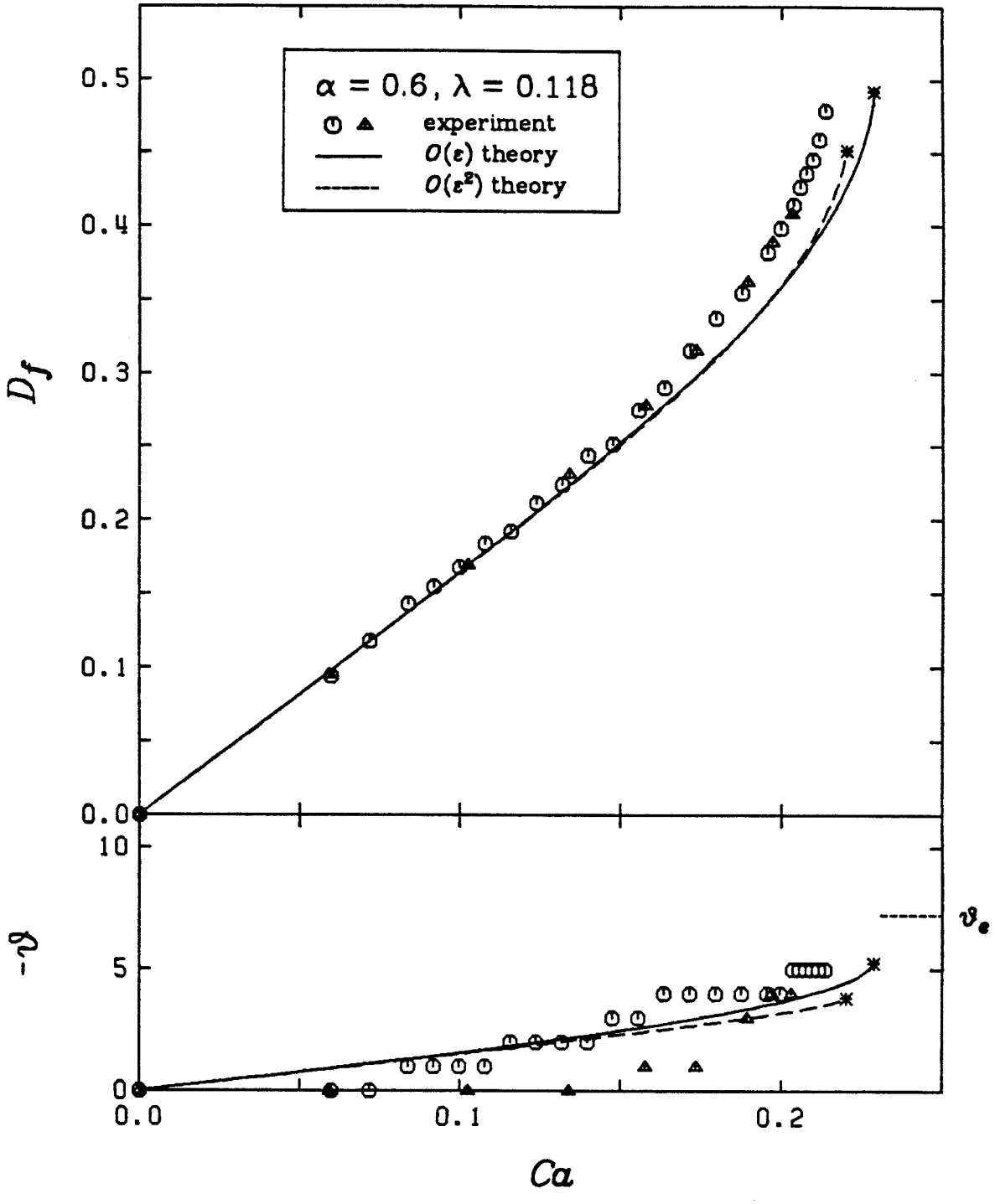

Figure 4.4
Deformation curve for $\alpha = 0.6$, $\lambda = 0.118$

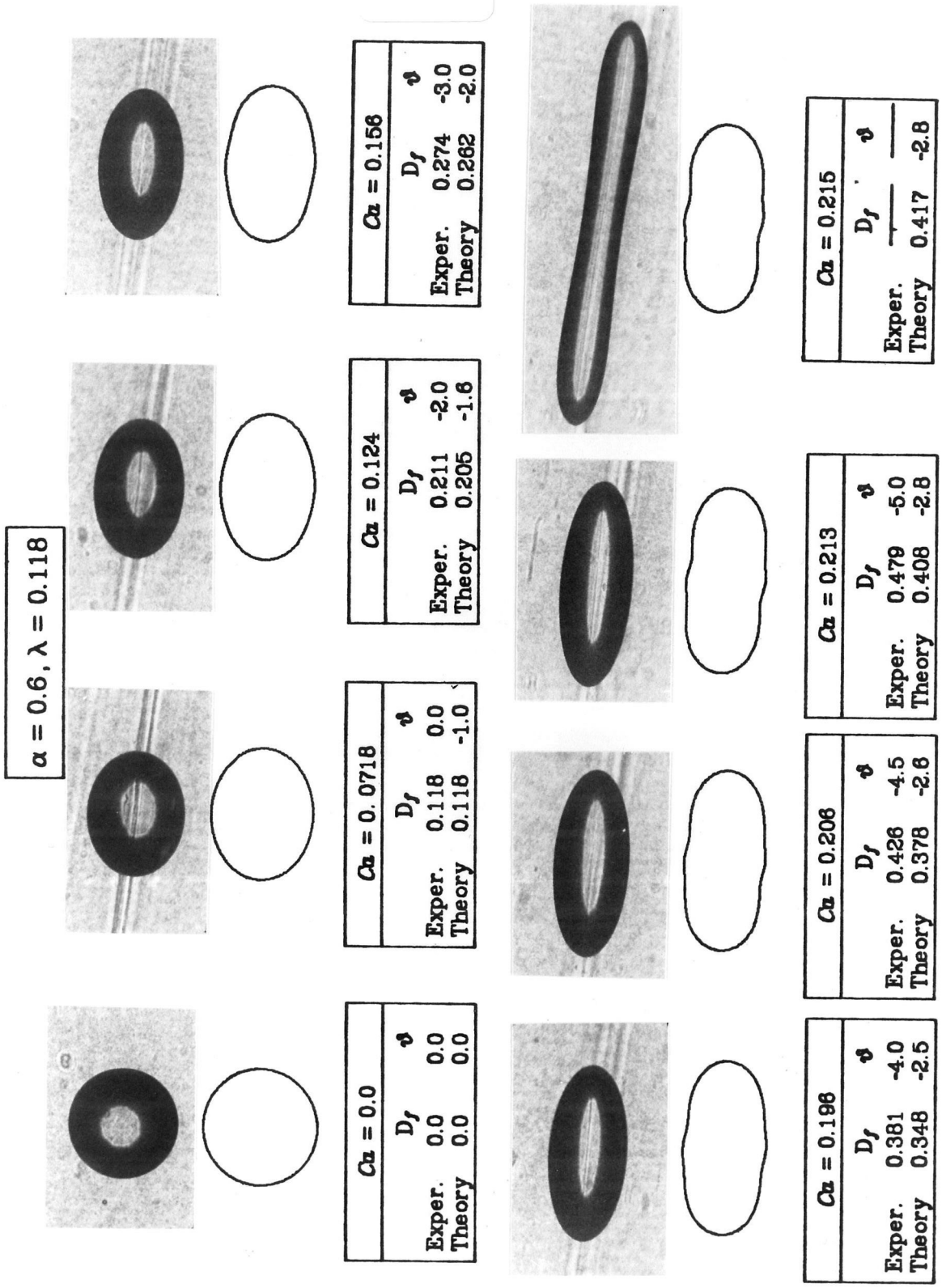

Figure 4.5
Comparison between experimental shapes and calculations using the $O(\varepsilon^2)$ theory for $\alpha = 0.6$, $\lambda = 0.118$

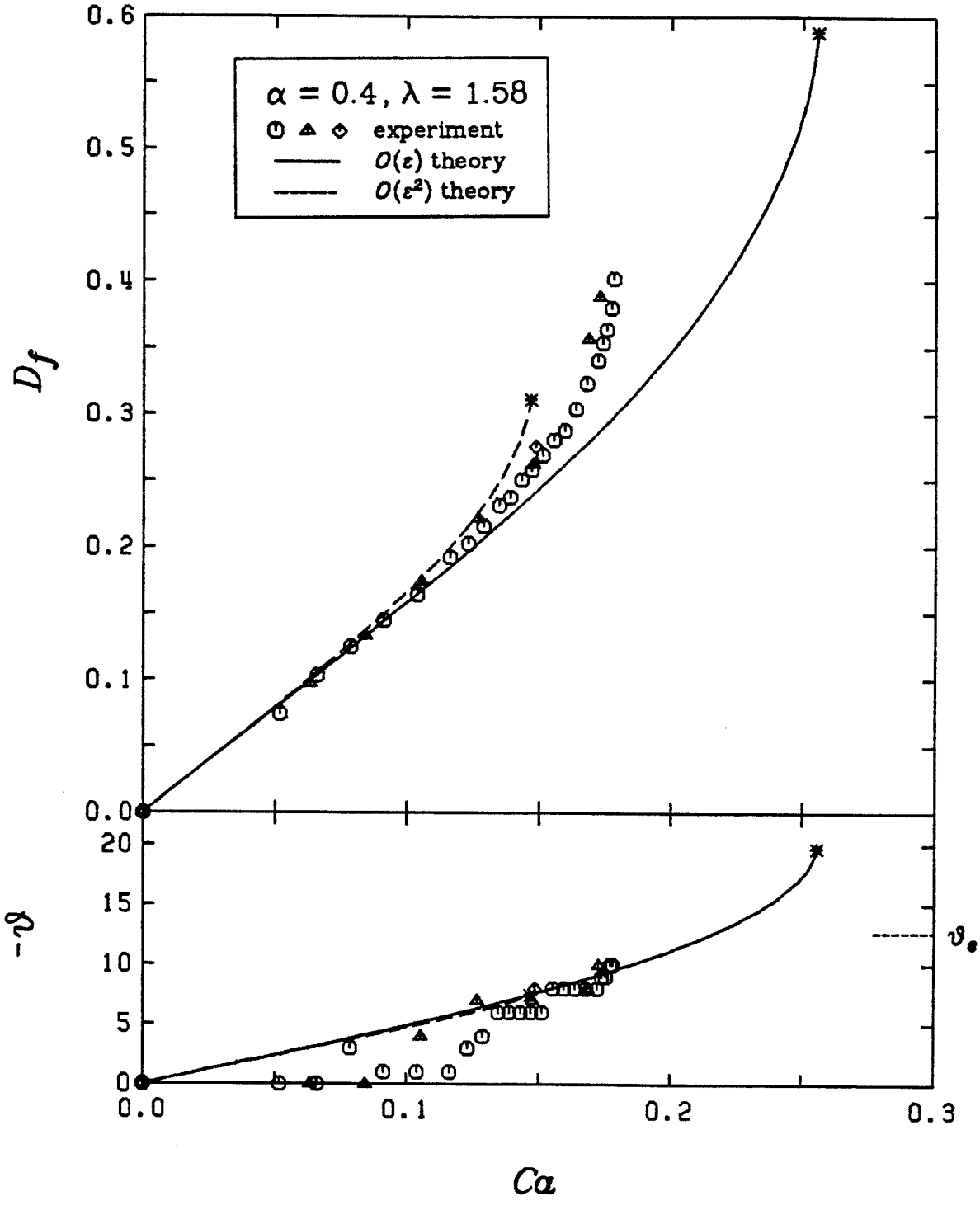

Figure 4.6
Deformation curve for $\alpha = 0.4$, $\lambda = 1.58$

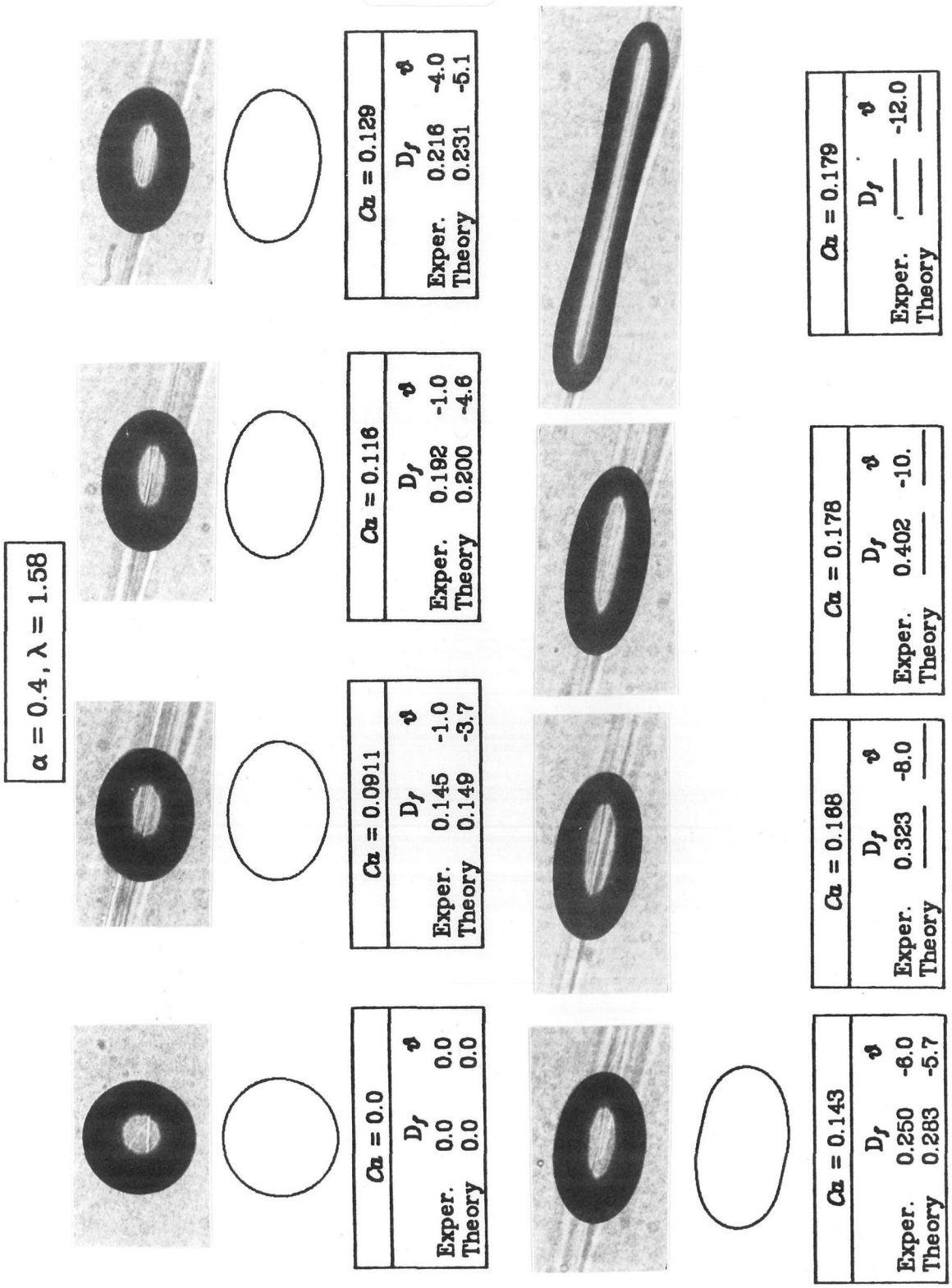

Figure 4.7
Comparison between experiment and theory for conditions of Figure 4.6

4.1.3 High Viscosity Ratio Drops

For drops of viscosity ratio greater than 3, the vorticity in the flow field had pronounced effects on the drop orientation and deformation characteristics. For flows with vorticity, ($\alpha \neq 1.0$), the drops were aligned with the x axis only for very small deformations, with the magnitude of the orientation angle increasing rapidly with increasing shear rate. At moderate deformations, the magnitude of the orientation angle even exceeded that of the exit streamline. Upon further increase of the shear rate, the magnitude of the orientation angle went through a maximum, and decreased to the angle of the exit streamline as the bursting point was approached. This behavior was most pronounced for $\alpha = 0.2$, the most rotational flow studied. In that flow, the highest viscosity ratio drops, with $\lambda = 27$, did not burst up to the highest practical shear rate ($G = 1\text{sec}^{-1}$).

Figure 4.8 shows the deformation and orientation curves for a high viscosity ratio case, $\lambda = 14.4$, in a flow with $\alpha = 0.4$. In calculating D_f, the fourth order tensor terms have been discarded as discussed in Section 3.1 above. In this case, the $O(\varepsilon)$ theory proved virtually useless, predicting that the drop attains a steady shape without bursting as the shear rate increases. In contrast, the $O(\varepsilon^2)$ theory predicts the deformation curve with surprising accuracy, and the predicted bursting point, $Ca_c = 0.165$, agrees well with the observed value of 0.176.

Both the experimental results and the predictions of the $O(\varepsilon^2)$ small deformation theory show the orientation angle ϑ going through a maximum with increasing shear rate as discussed in Section 3.4. The observed maximum magnitude of ϑ was 22°, in reasonable agreement with the theoretical prediction of 18°.

Figure 4.9 shows the comparison between the observed drop shapes and those calculated from the $O(\varepsilon^2)$ theory. The comparison is good for Ca less than about 0.10. The more eccentric shapes at higher Ca cannot be accurately represented by retaining only the second order deformation tensor, but the calculation of the fourth order tensor fails at high viscosity ratio as discussed in Section 3.2. An accurate calculation of the fourth order tensor would probably have improved the comparison for Ca = 0.13 and 0.16, particularly in the latter case where the theory with only the second order tensor predicts a steady drop shape with physically unrealistic concave sides.

Figure 4.10 shows the deformation and orientation curves for the one case considered by Stone [1984] where no drop burst was observed. In that case, the flow type was 0.2, and the viscosity ratio was 27.3. The predictions of the $O(\varepsilon^2)$ theory (without the fourth order tensor) were quite accurate, predicting a limiting deformation of about 0.083, compared to the observed 0.085±0.01. The $O(\varepsilon)$ theory predicted a value of about 0.07. The predicted limiting orientation angle for the $O(\varepsilon^2)$ theory was about $-40°$, in good agreement with the observations. At this orientation, the effective straining motion is apparently so low that the drop shape remains essentially constant.

Figure 4.11 shows the comparison between the photographs and the shapes predicted by the $O(\varepsilon^2)$ theory. In this case, the deformation is small for all Ca, and thus the theoretical and experimental shapes are very similar.

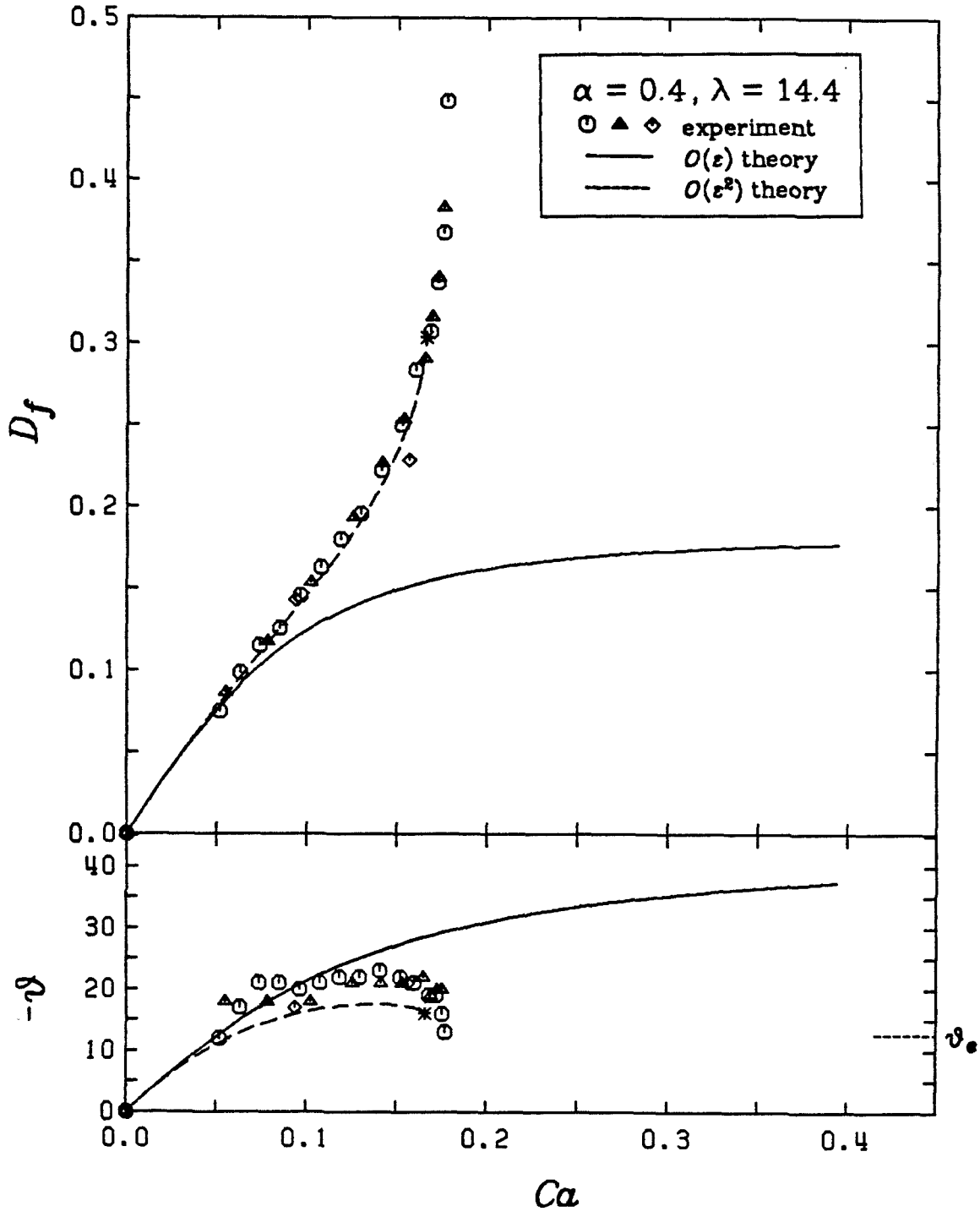

Figure 4.8
Deformation curve for $\alpha = 0.4$, $\lambda = 14.4$

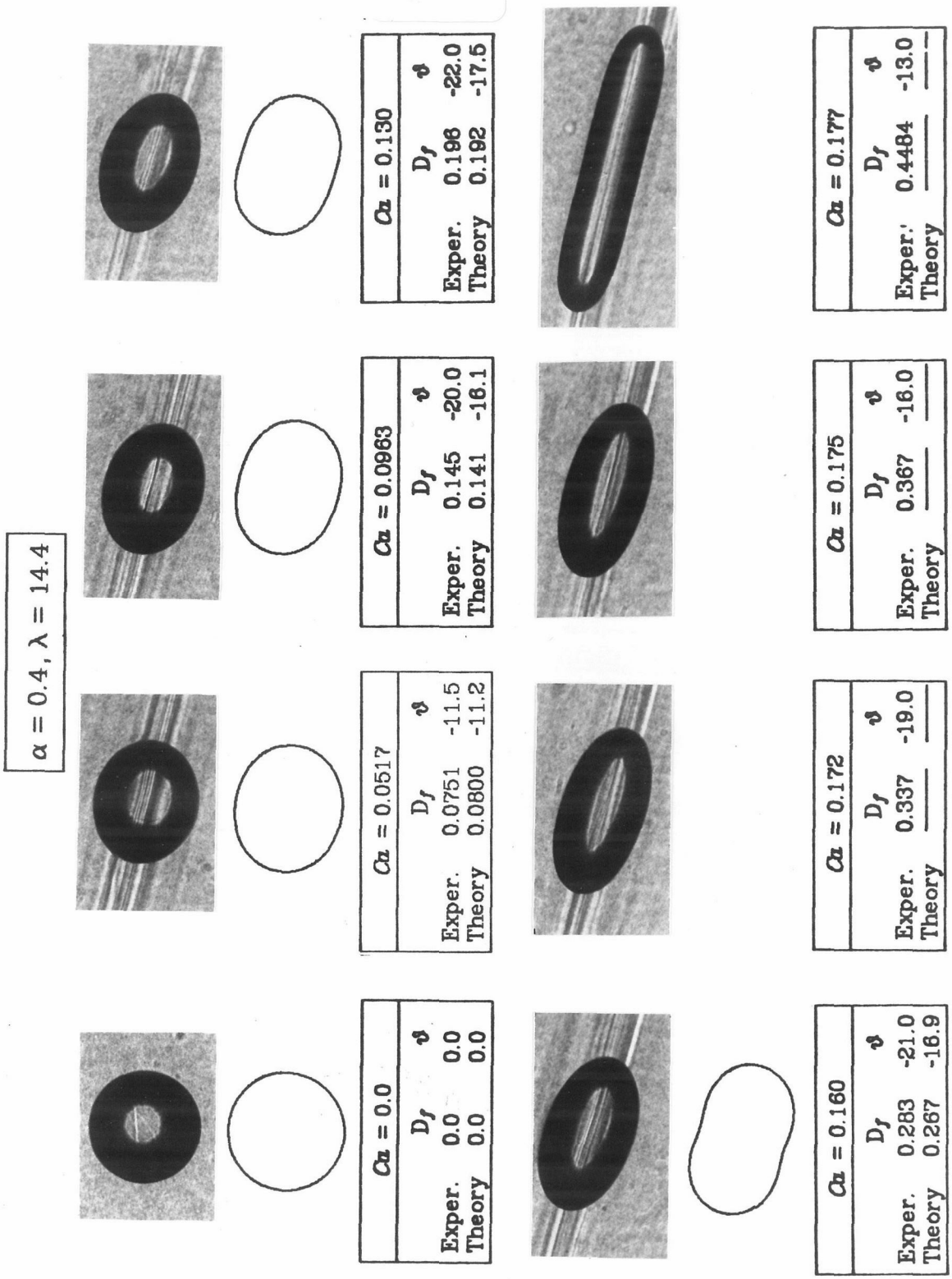

Figure 4.9
Shape comparison for $\alpha = 0.4$, $\lambda = 14.4$

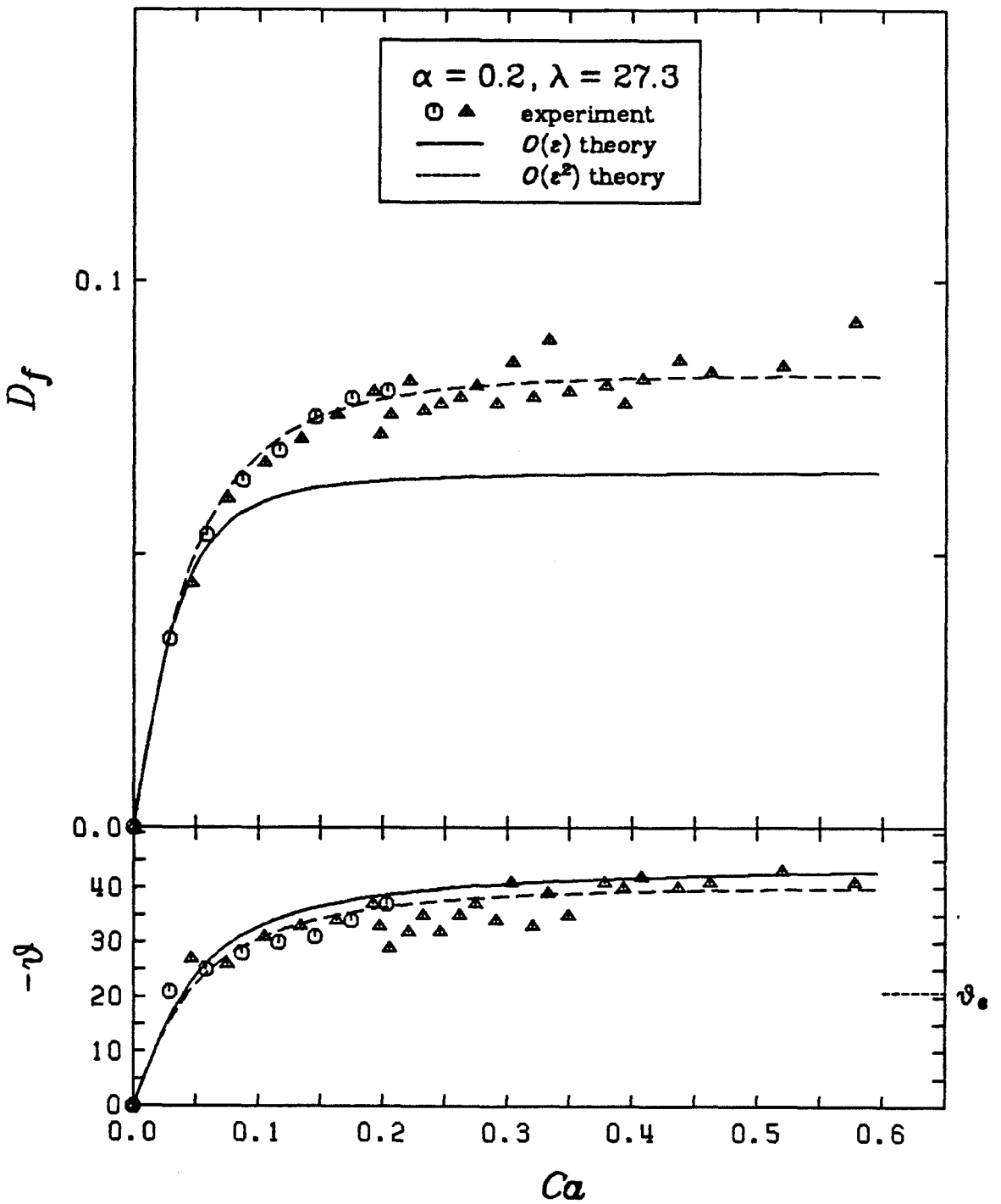

Figure 4.10
Deformation curve for $\alpha = 0.2$, $\lambda = 27.3$

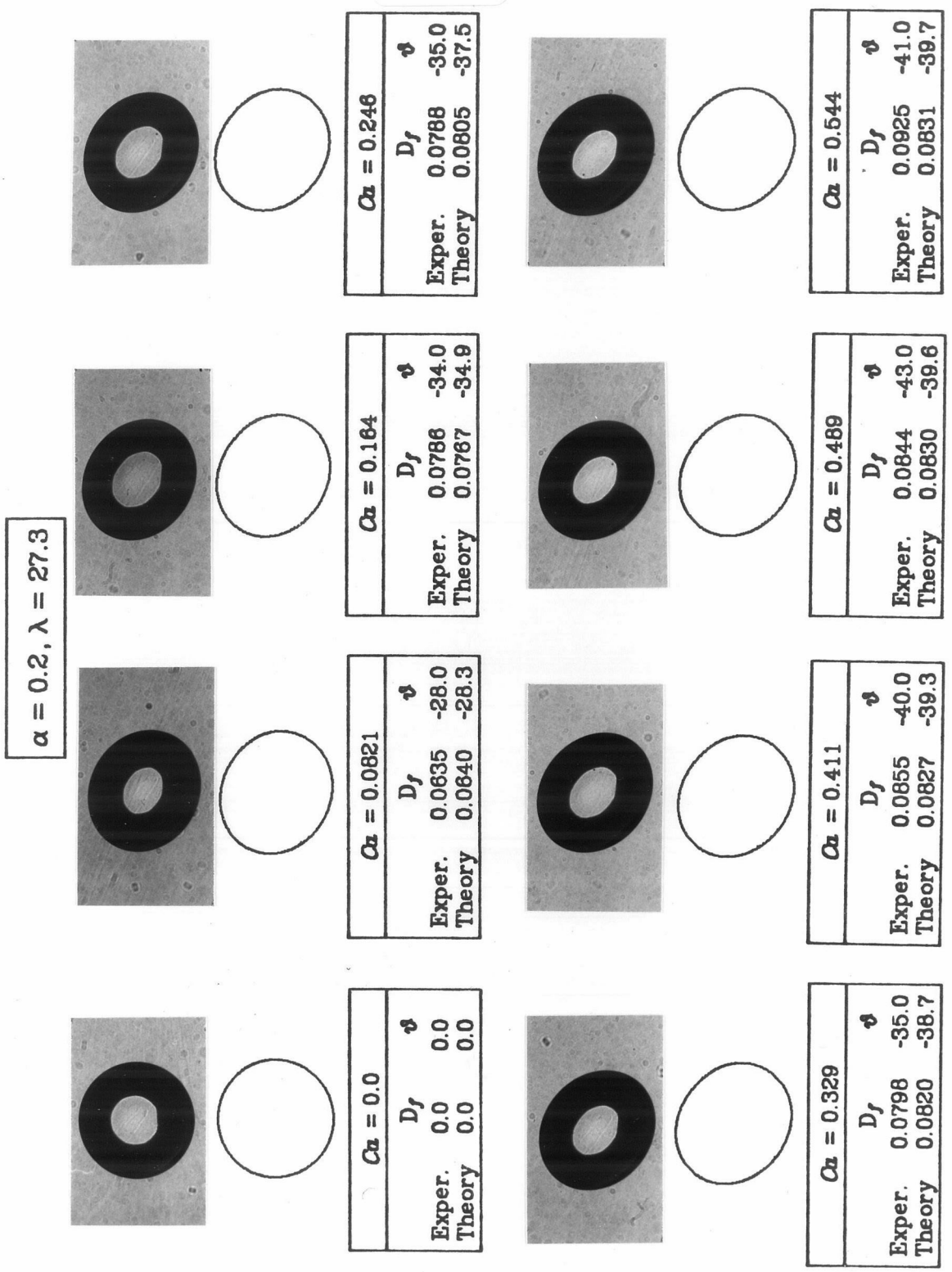

Figure 4.11
Experimental and calculated drop shapes for $\alpha = 0.2$, $\lambda = 27.3$

4.1.4 Deformation Curves

From the comparisons discussed in detail above, it is evident that the $O(\varepsilon^2)$ theory results in predictions superior to those of the $O(\varepsilon)$ theory. In every instance, the bursting point is more accurately predicted, particularly for high viscosity ratio systems. For this reason, the remaining deformation curves present comparisons between the experimental observation and the $O(\varepsilon^2)$ theory only. For compactness, the deformation and orientation curve for every flow type is included on one plot, with a separate such plot for every viscosity ratio considered. Figures 4.12 through 4.23 present these graphs for $\lambda = 1.1\times10^{-3}$, 1.1×10^{-2}, 2.2×10^{-2}, 4.8×10^{-2}, 0.12, 0.24, 0.63, 1.50, 2.80, 6.50 ,14.0, and 26. Each figure includes experimental points and predictions of the $O(\varepsilon^2)$ small deformation theory for $\alpha = 1.0$, 0.8, 0.6, 0.4, and 0.2. The experimental points for different flow types are distinguished by different symbols, and in every case the theoretical curves go in order of decreasing α from left to right. Deformation plots showing the comparison between the experiments and the predictions of both the $O(\varepsilon)$ and $O(\varepsilon^2)$ small deformation theories are included in Appendix 2.

The presentation with data for all flow types on a single plot makes it easy to see the effects of vorticity on drop deformation and burst. For low and intermediate viscosity ratios, the qualitative behavior of the drops is not highly dependent on the flow type. Deformation is smaller for lower α at fixed Ca mainly because the magnitude of the rate of strain tensor ($= G(1+\alpha)$) decreases with decreasing α. Except for the lowest viscosity ratios ($\lambda = 1.1\times10^{-3}$ and 1.1×10^{-2}, where the $O(\varepsilon^2)$ small deformation theory predicts no drop burst for $\alpha = 0.2$) the $O(\varepsilon^2)$ theory reflects the observed trends. For viscosity ratios above 2.80, the vorticity starts to have more dramatic effects, with the ratio of

Capillary number required for burst for the rotational flows to that for $\alpha = 1.0$ increasing, particularly for $\alpha = 0.4$ and 0.2. The results for drop burst as a function of viscosity ratio and flow type are discussed in detail in Section 4.2.

Figures 4.24 and 4.25 show the experimental results for the two lowest viscosity ratio systems plotted as L/a versus Ca for convenient comparison to the large deformation theory. The plots include the data for each flow type considered, as well as the predictions of the large deformation theory described in Section 3.2. This theory gives acceptable results for $\lambda = 1.1\times10^{-3}$, where L/a attains a value of about 7 at burst, but the predictions are rather poor for $\lambda = 1.1\times10^{-2}$, where L/a at burst is only about 3.5. This is in keeping with the nature of the theory, which is valid in an asymptotic sense for large L/a.

From the comparisons between the experiment and the theories presented above, we conclude the following:

1. The small deformation theory gives adequate predictions for D_f for $\lambda \geq 0.05$. The $O(\varepsilon^2)$ version of the theory generally gives better predictions for the deformation, and always gives better predictions for the critical Capillary number at which drop burst occurs.

2. The comparisons between the photographs of the drops and the shapes computed from the $O(\varepsilon^2)$ small deformation theory show that the two can differ significantly even when the scalar measure of deformation, D_f, is predicted accurately by the theory. Thus the good agreement between the experimental and theoretical deformation curves must be regarded as fortuitous in some cases. This is particularly true for low viscosity ratios, where the observed shapes cannot be adequately represented by a theory with only second and fourth order tensors.

3. The large deformation theory gives adequate predictions only for $\lambda < 0.01$. In that case, our assumption that the drops align with the exit streamline of the flow, and thus experience an effective strain rate of $G\alpha^{1/2}$, appears to be an adequate approximation at least when the drops are highly extended.

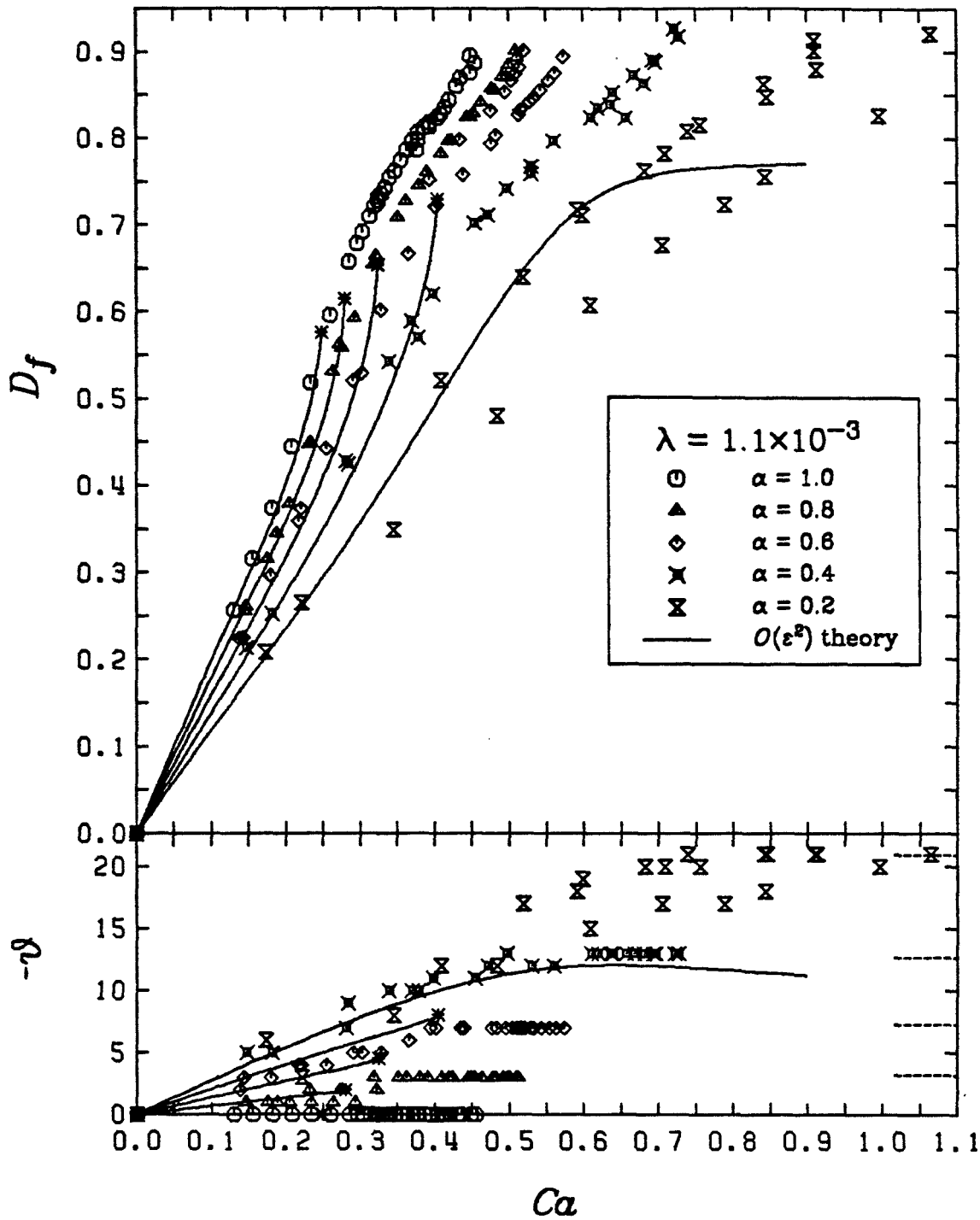

Figure 4.12
Drop deformation curves for α = 1.0, 0.8, 0.6, 0.4, and 0.2 for $\lambda = 1.1\times10^{-3}$

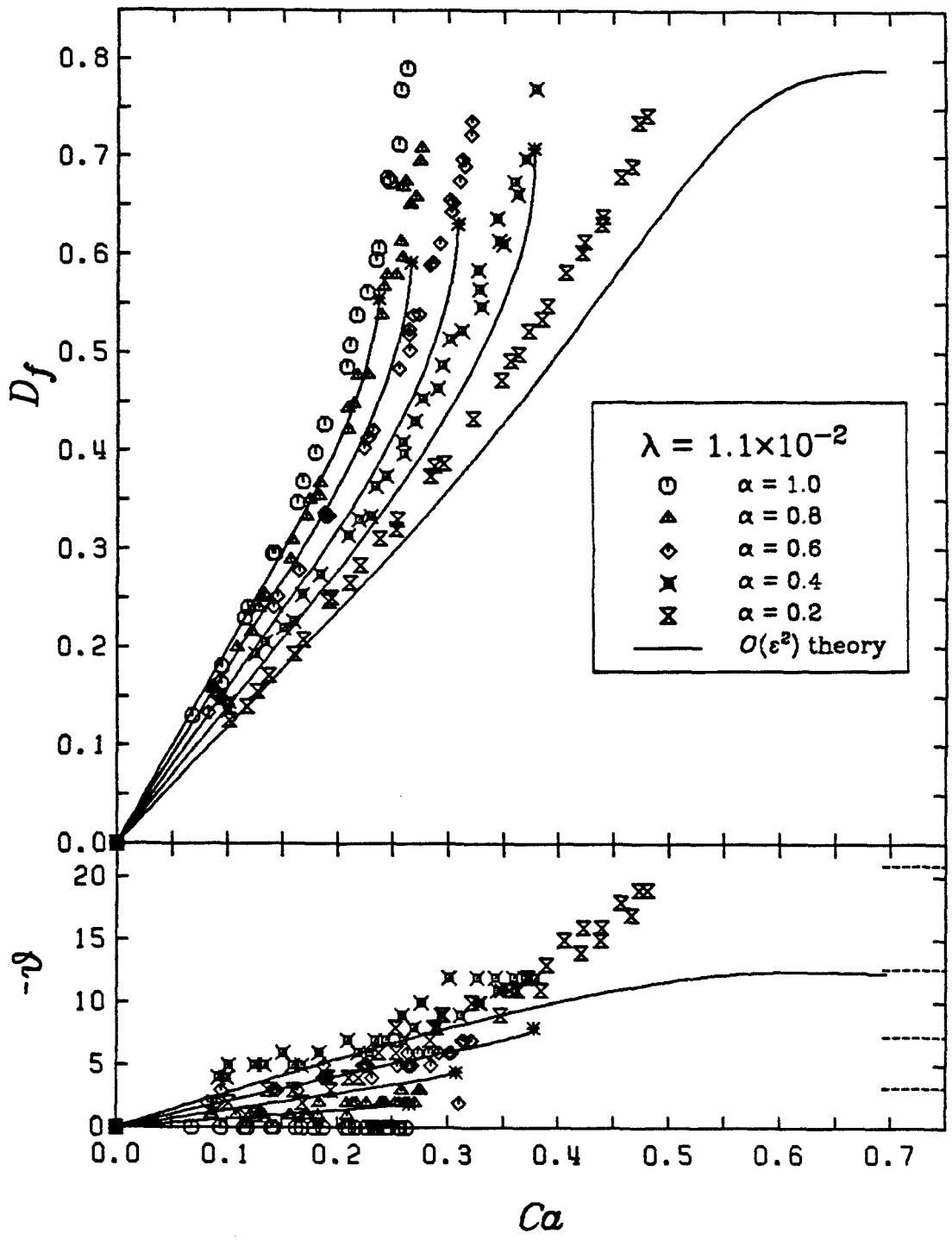

Figure 4.13
Drop deformation curves for α = 1.0, 0.8, 0.6, 0.4, and 0.2 for $\lambda = 1.1\times10^{-2}$

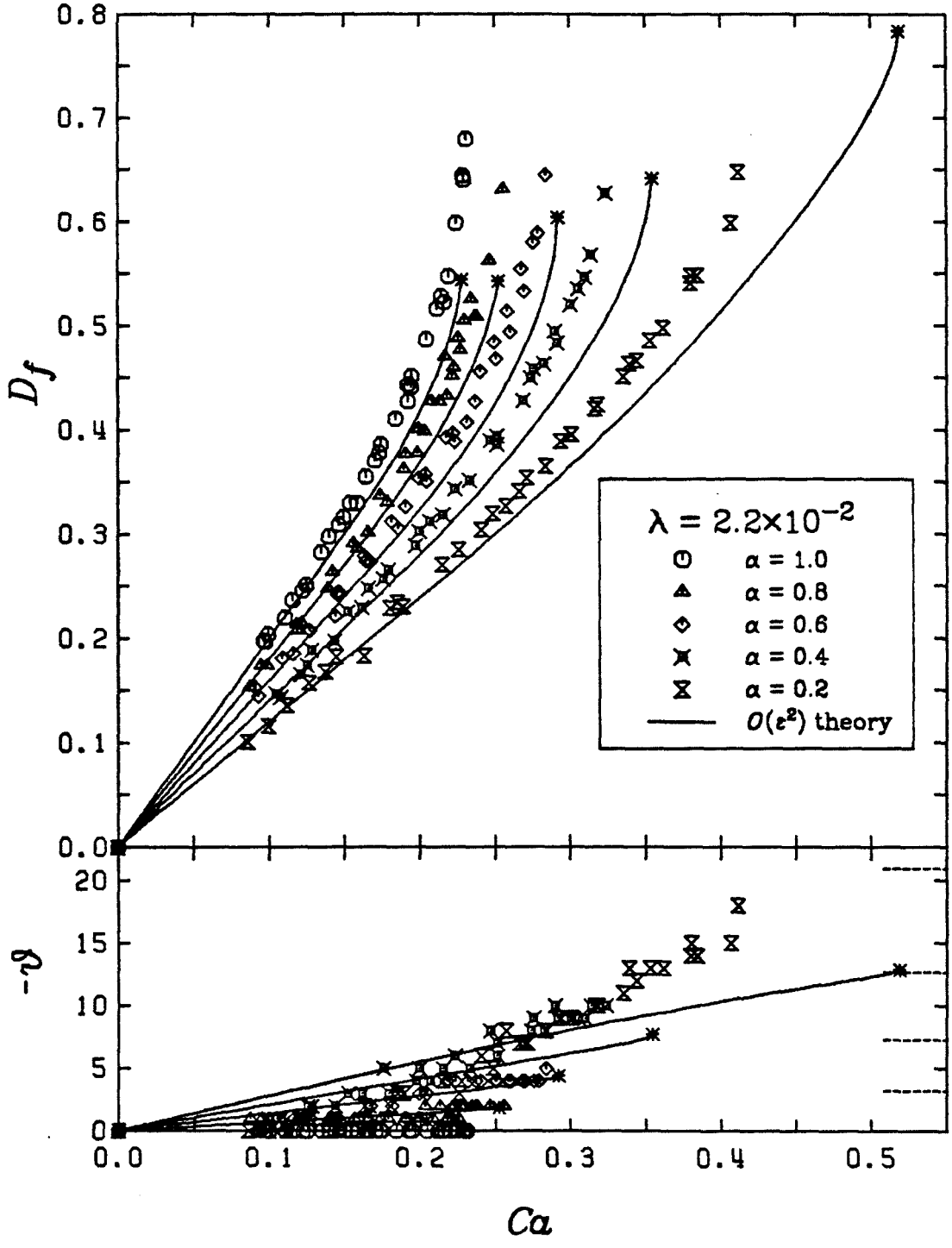

Figure 4.14
Drop deformation curves for α = 1.0, 0.8, 0.6, 0.4, and 0.2 for $\lambda = 2.2\times10^{-2}$

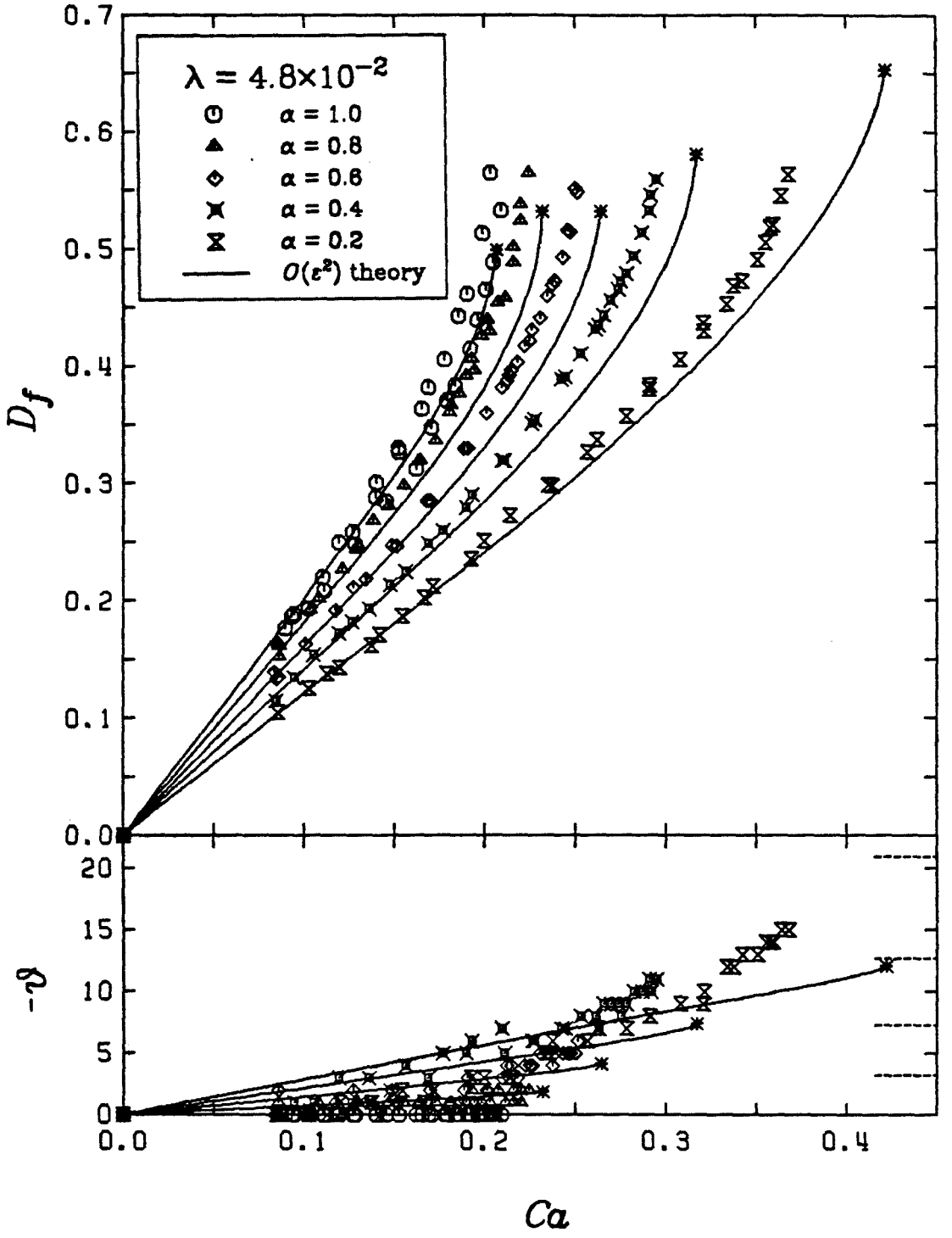

Figure 4.15
Drop deformation curves for α = 1.0, 0.8, 0.6, 0.4, and 0.2 for $\lambda = 4.8\times10^{-2}$

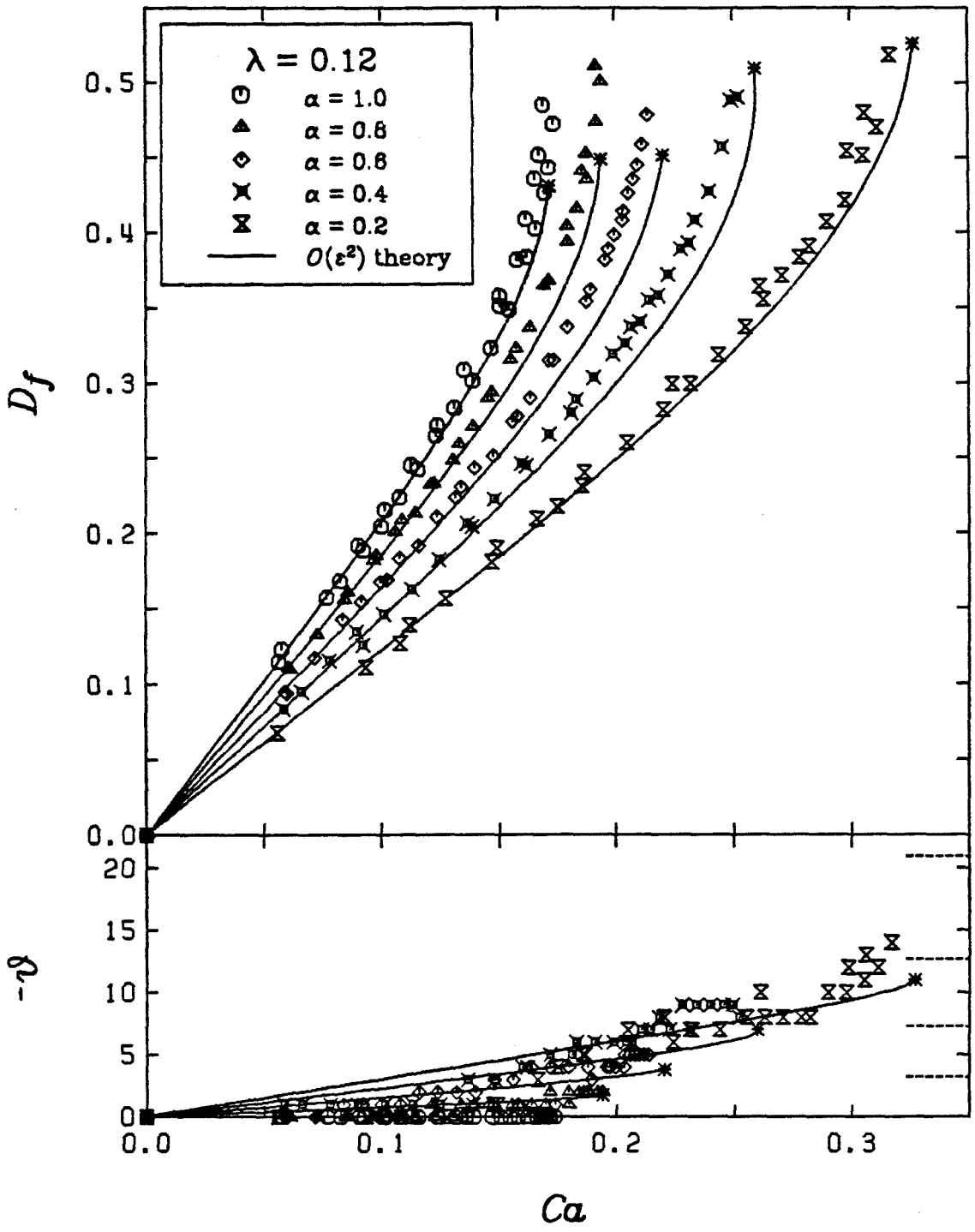

Figure 4.16
Drop deformation curves for α = 1.0, 0.8, 0.6, 0.4, and 0.2 for λ = 0.12

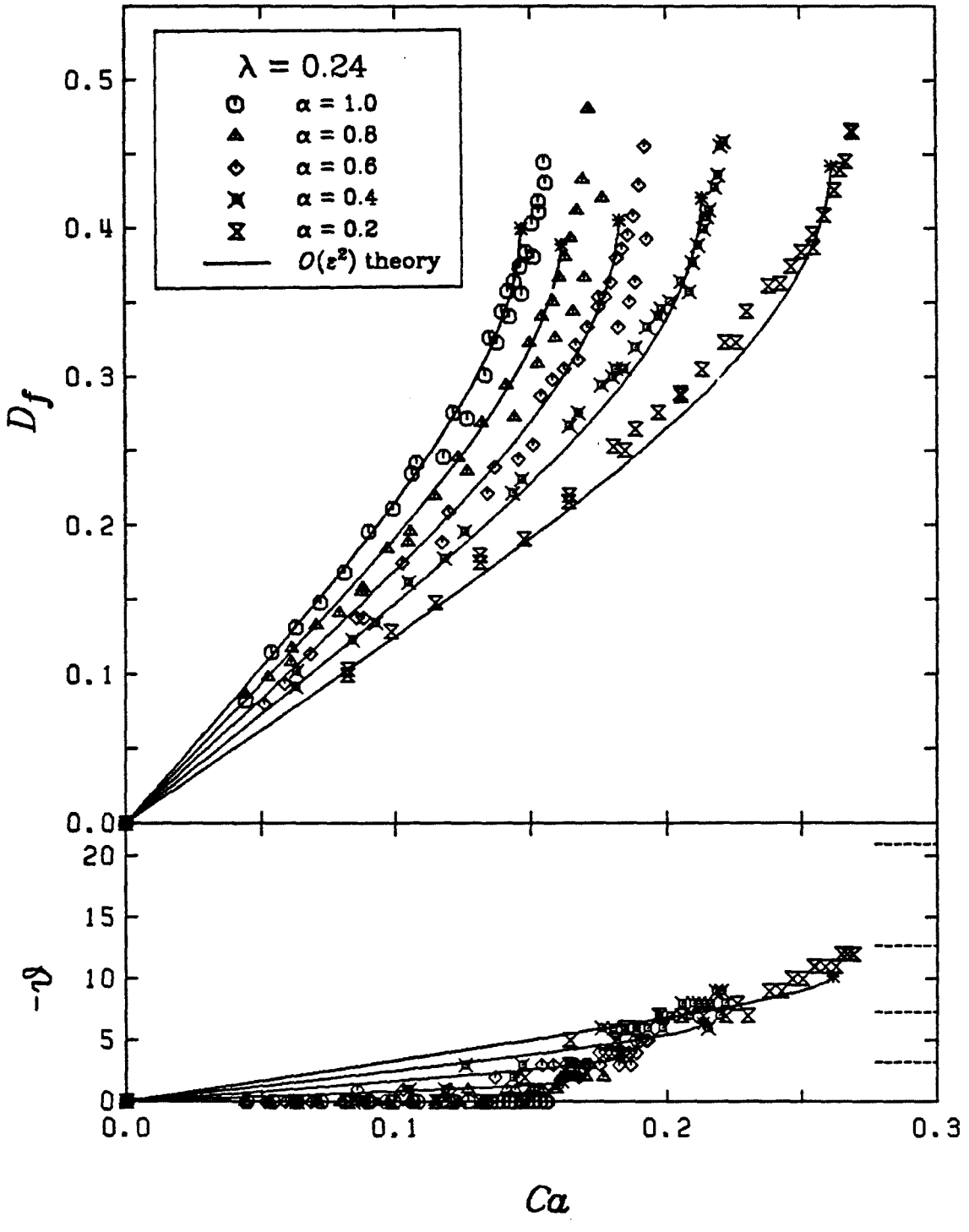

Figure 4.17
Drop deformation curves for α = 1.0, 0.8, 0.6, 0.4, and 0.2 for λ = 0.24

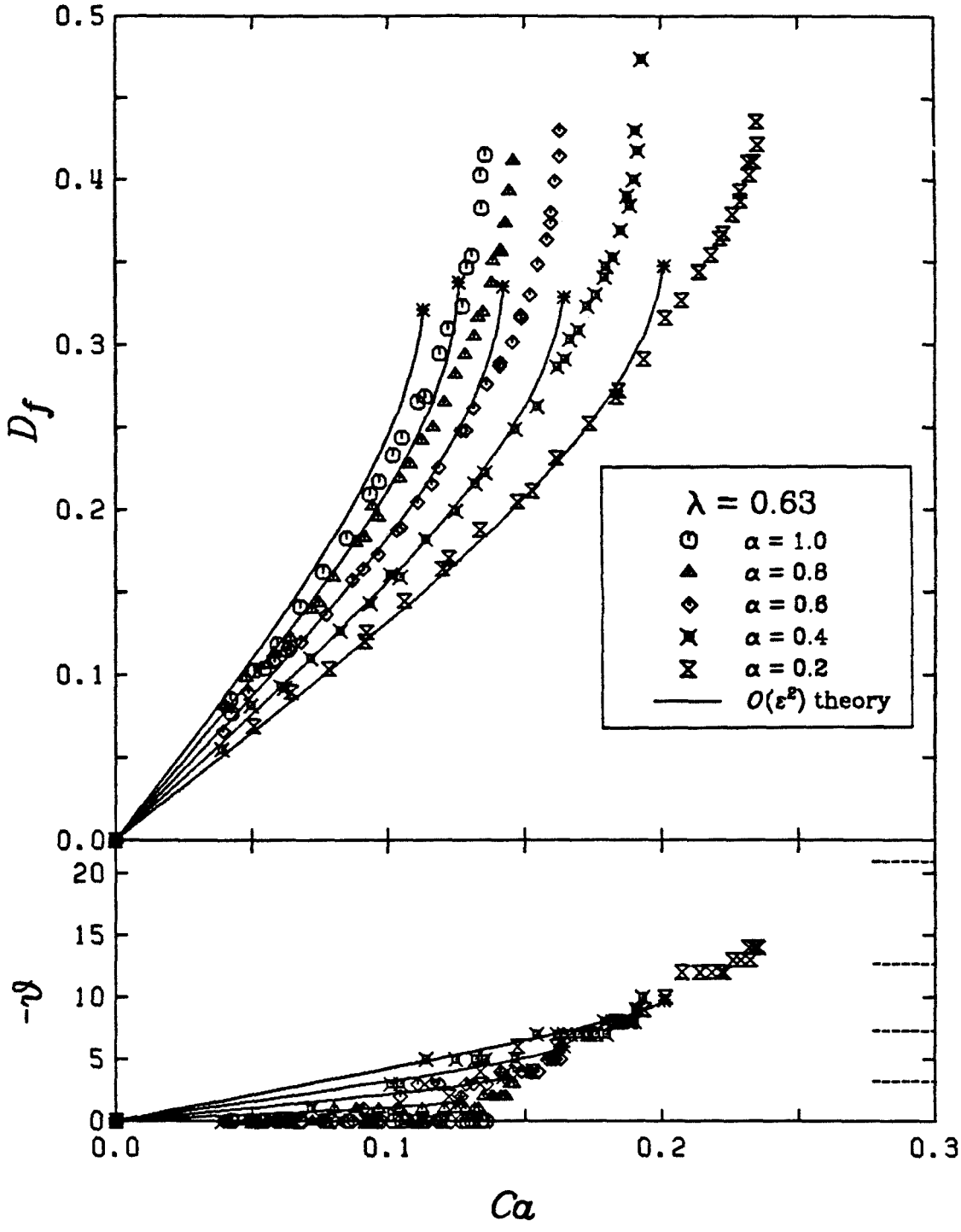

Figure 4.18
Drop deformation curves for α = 1.0, 0.8, 0.6, 0.4, and 0.2 for λ = 0.63

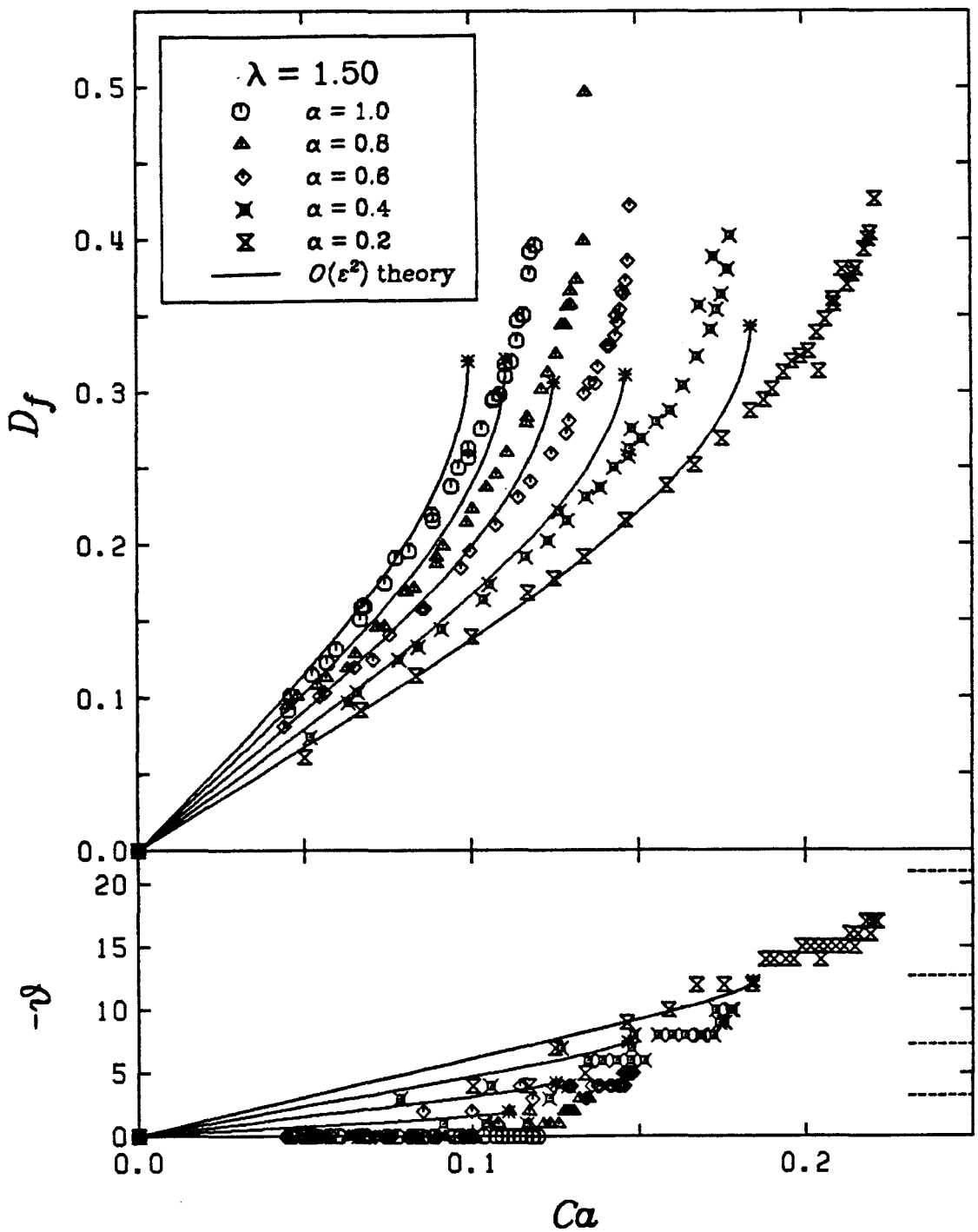

Figure 4.19
Drop deformation curves for α = 1.0, 0.8, 0.6, 0.4, and 0.2 for λ = 1.50

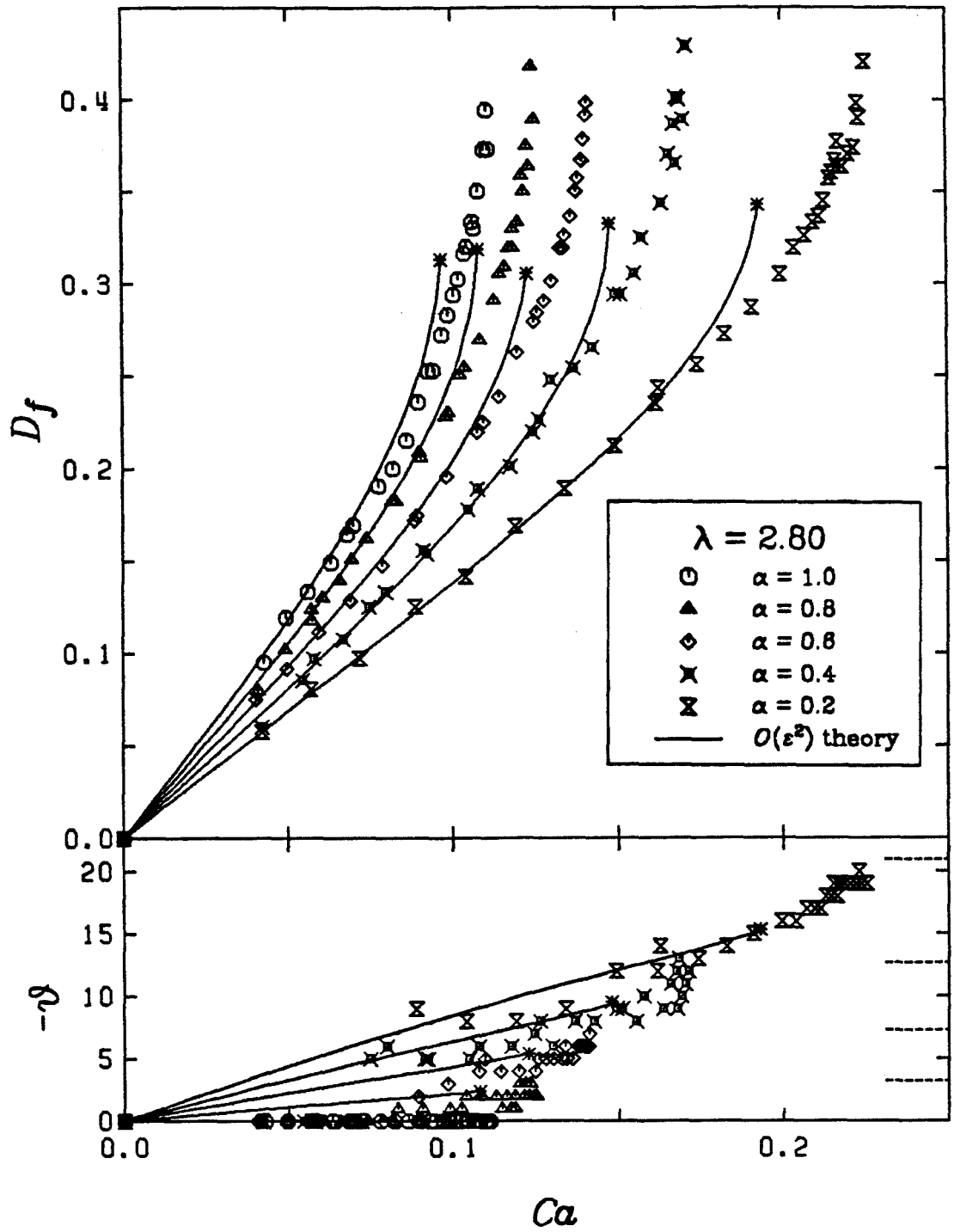

Figure 4.20
Drop deformation curves for α = 1.0, 0.8, 0.6, 0.4, and 0.2 for λ = 2.80

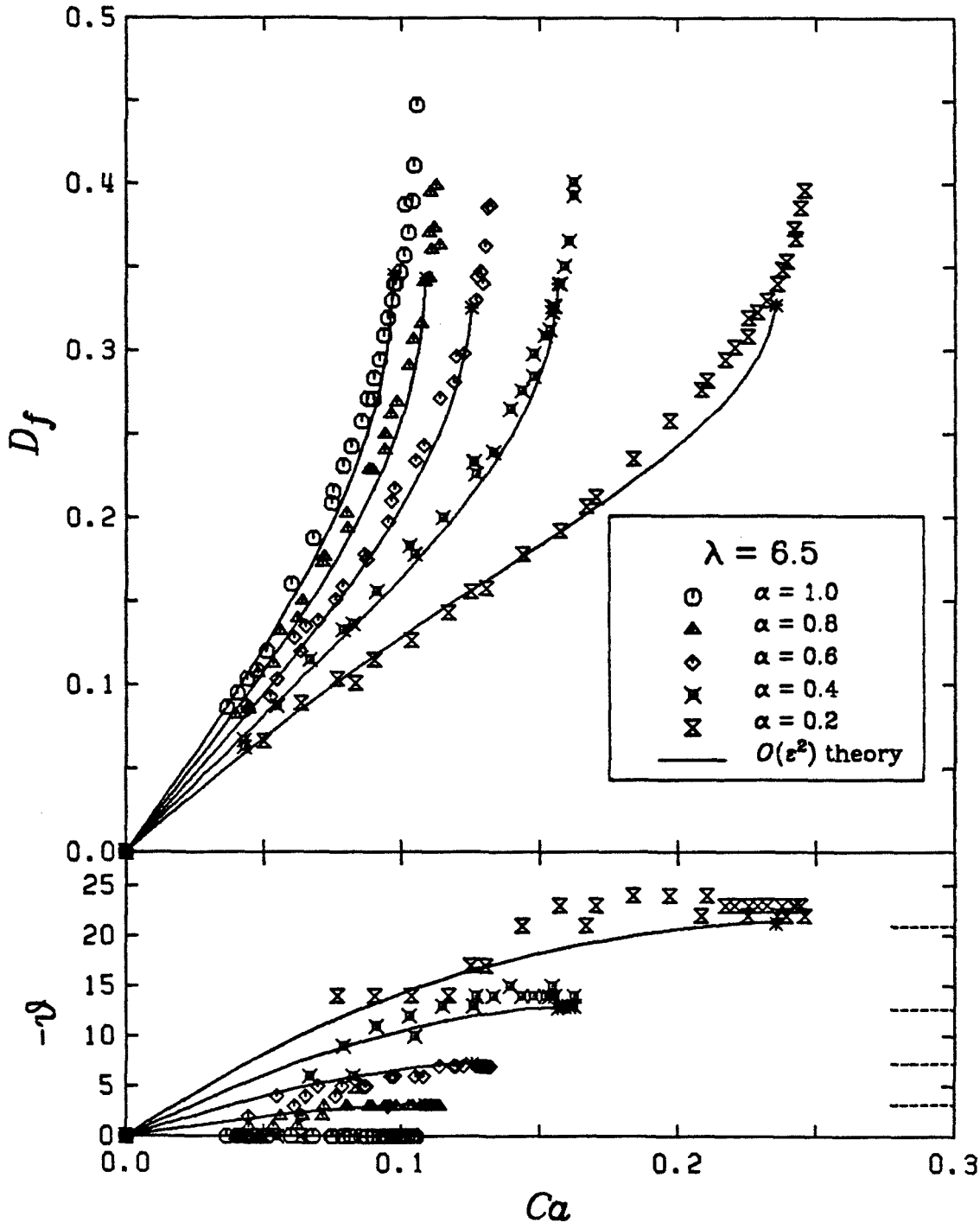

Figure 4.21
Drop deformation curves for α = 1.0, 0.8, 0.6, 0.4, and 0.2 for λ = 6.50

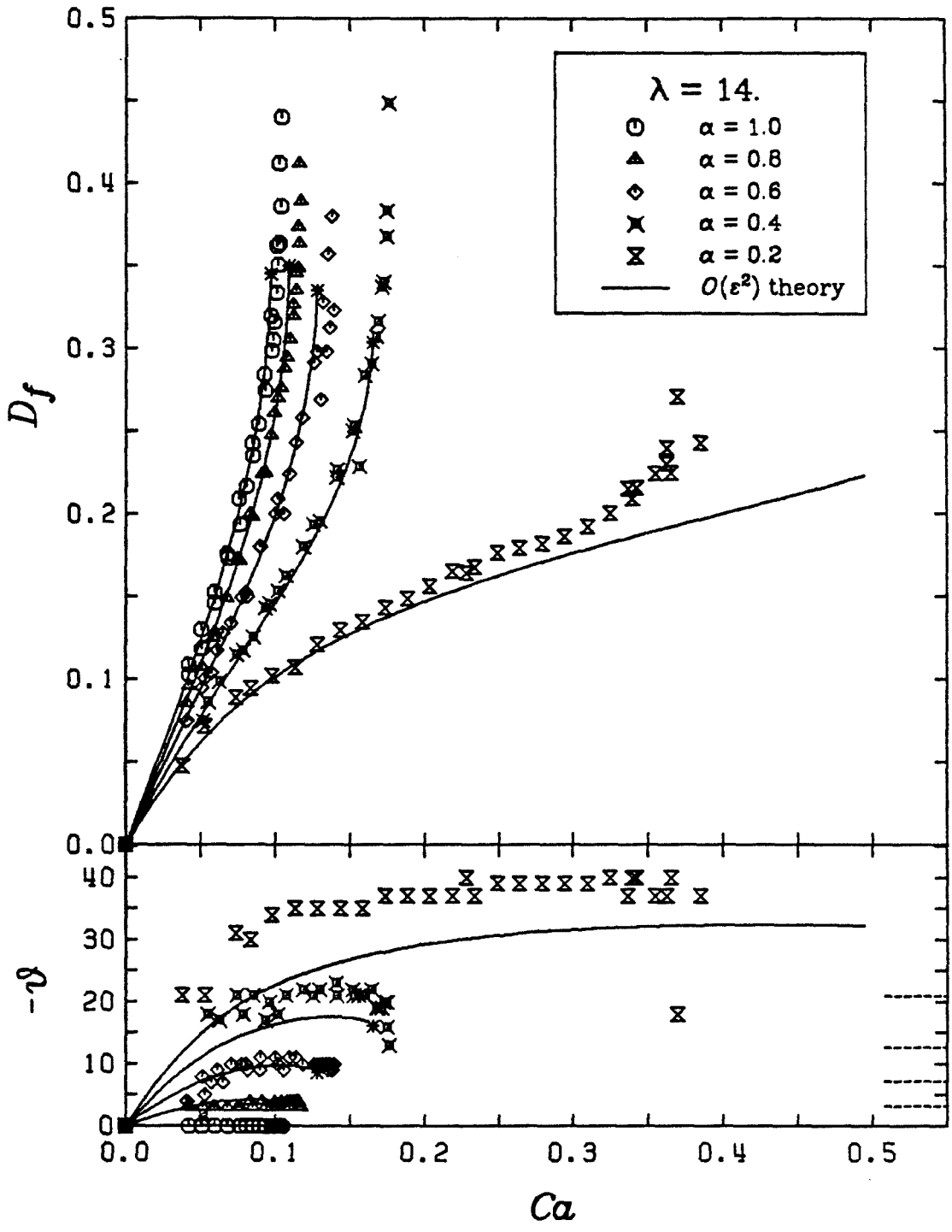

Figure 4.22
Drop deformation curves for α = 1.0, 0.8, 0.6, 0.4, and 0.2 for λ = 14.0

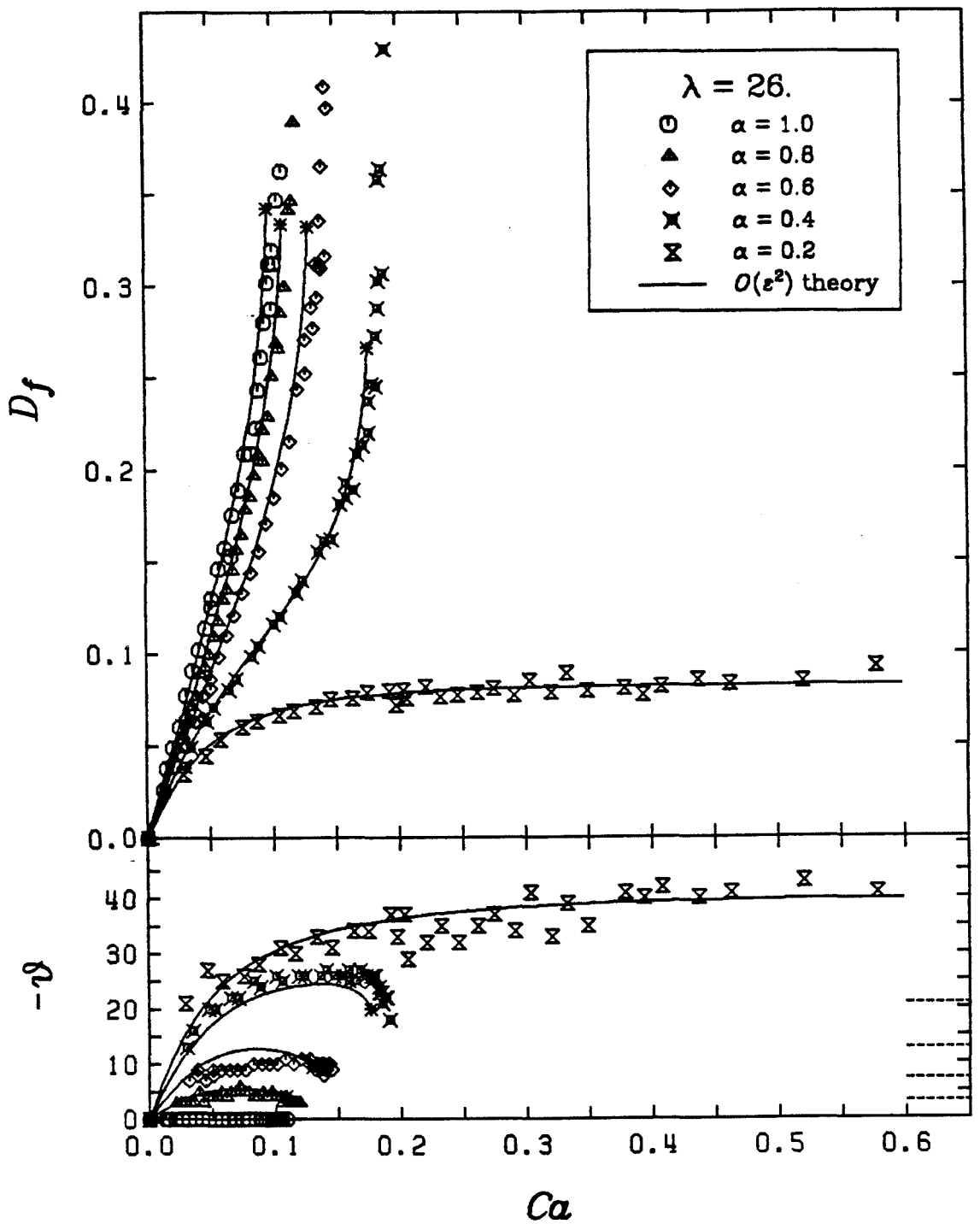

Figure 4.23
Drop deformation curves for α = 1.0, 0.8, 0.6, 0.4, and 0.2 for λ = 26.0

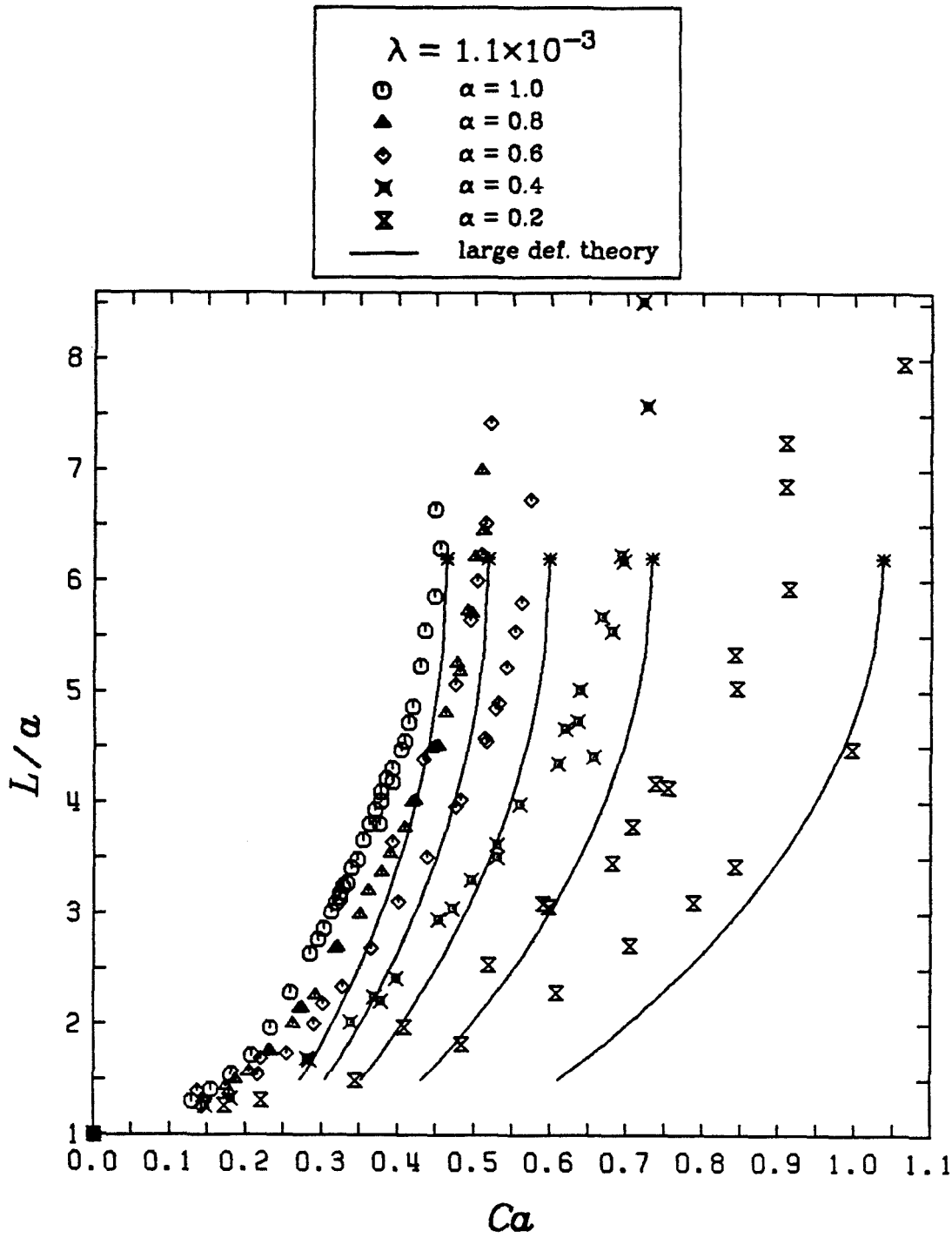

Figure 4.24
L/a vs. Ca for α = 1.0, 0.8, 0.6, 0.4, and 0.2 for $\lambda = 1.1\times10^{-3}$. Comparison with large deformation theory.

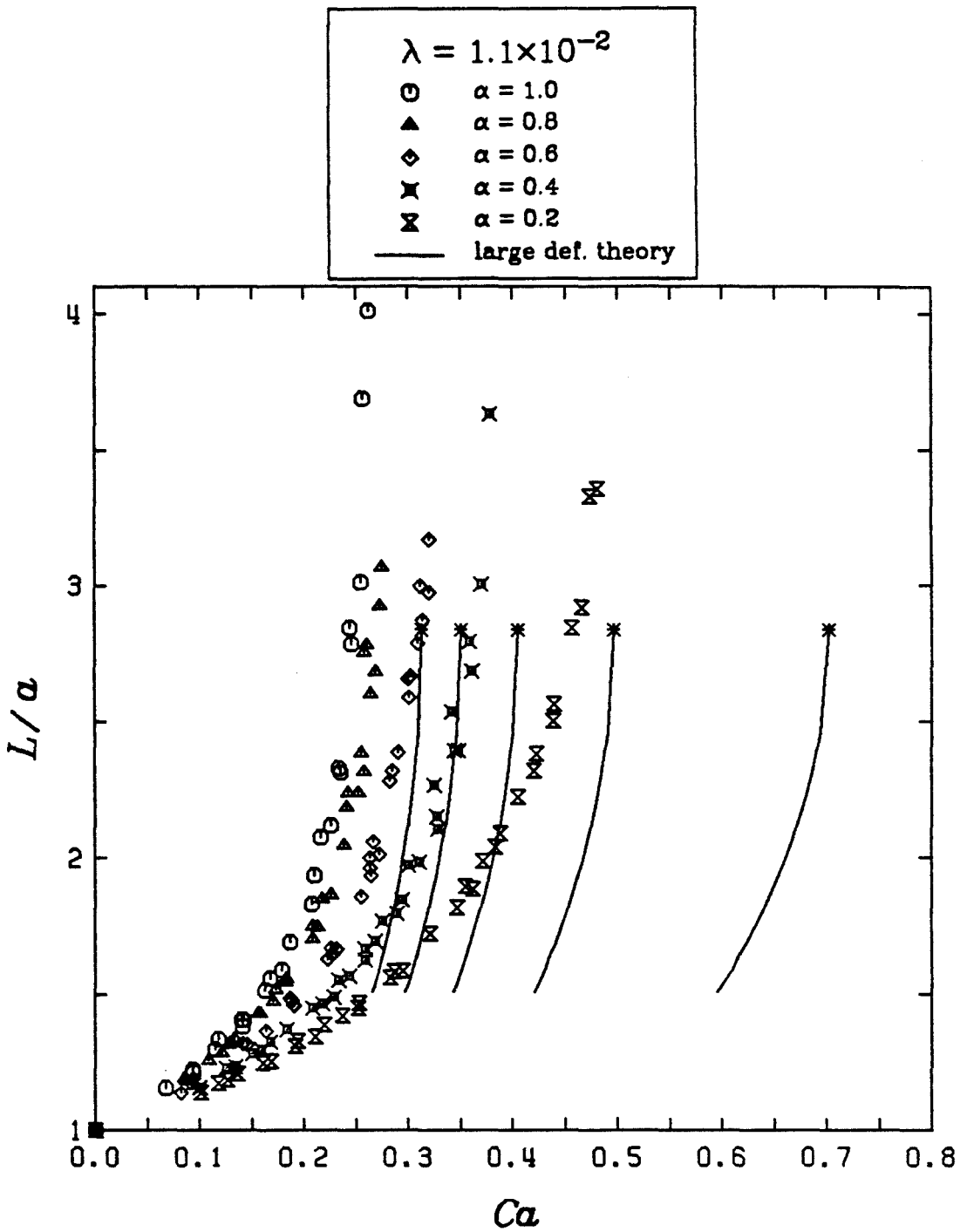

Figure 4.25
L/a vs. Ca for α = 1.0, 0.8, 0.6, 0.4, and 0.2 for $\lambda = 1.1\times10^{-2}$. Comparison with large deformation theory.

4.2 DROP BURST

In this section we consider the conditions which lead to drop burst for a given fluid system. In fact, drop burst depends not only on the instantaneous flow conditions (i.e., flow type and Capillary number), but on the entire time history of velocity gradient experienced by the drop. That is, drop burst is a functional over the history of $\nabla \mathbf{u}$. For example, Torza, Cox, and Mason [1972] reported that drops could be made to burst in simple shear by a sudden increase in shear rate to a value below that required for burst when the shear rate was slowly increased. The same behavior was observed in the theoretical study of Hinch and Acrivos [1980].

A complete investigation of the drop burst functional would be impossible, due to the many degrees of freedom available in specifying the velocity gradient history. Thus, in this work, we limit our attention to one such history. Specifically, we consider only the case where the form of the velocity gradient tensor is constant (fixed flow type) and the flow strength is increased very slowly, so that the drop goes through a progression of equilibrium states. The bursting point is defined as the shear rate for which no steady shape exists (if there is such a shear rate). This particular choice of flow history provides a sufficient condition for drop burst, in that any other approach to a constant flow field (e.g., a step increase in shear or a ramped shear rate) will result in drop burst at the same or lower final shear rate. Thus our results can be used to predict an upper bound for the size of a drop which can exist indefinitely in a given flow field.

Figure 4.26 shows the critical Capillary number for burst, Ca_c, as a function of viscosity ratio for two-dimensional irrotational flow ($\alpha = 1$). Data from this work are compared to the observations of Taylor [1934], Rumscheidt and Mason

[1961], and Grace [1971]. The unbroken curve shows the predictions of the $O(\varepsilon^2)$ small deformation theory discussed in Section 3.1, and the dashed line shows the predictions of the large deformation theory described in Section 3.2. The result of Rallison's [1981] numerical calculation (Section 3.3) is also included.

As can be seen, all of the experimental data are in reasonable agreement, with the possible exception of the data point at $\lambda = 1$ reported by Taylor [1934]. Typical error bars for our experiments are shown on the figure. Uncertainties for the earlier experiments would presumably be larger owing to the difficulties associated with hand control of the device. For $\lambda \geq 0.05$, agreement between the burst predictions of the $O(\varepsilon^2)$ small deformation theory and our observations is surprisingly good, especially considering the approximations inherent in the theory. For reasons unknown, the deviation between the theory and experiment is maximum near $\lambda = 1.0$, with the theory underestimating Ca_c by about 20%. The numerical calculation of Rallison [1981] for $\lambda = 1$ agrees very well with data. For low viscosity ratios, the large deformation theory predicts burst with acceptable accuracy.

The trend for large viscosity ratio is of some interest. In our experiments, the critical Capillary number was essentially constant for viscosity ratios above about 3.0. In contrast, Grace [1971] concluded from his data that Ca_c goes through a minimum for λ about 1, steadily increasing with viscosity ratio above that value. While our evidence to the contrary is not entirely conclusive, we believe that Grace's conclusion is in error for the following reason: As the viscosity of the drop increases, the time scale for deformation increases as well. This makes the experiments more difficult since a much longer wait between increases in the shear rate must be allowed for the drop to attain a steady

shape. In our experiment, the drop's position was controlled automatically, so great patience was possible. In a hand-controlled experiment, however, the difficulty in controlling the drop may have forced the experimenter to increase the shear rate before drop attained an equilibrium shape (or burst) at the lower shear rate. The effect of such an error would be to observe drop burst at a higher shear rate than the actual critical value. The error would be expected to be greater for larger viscosity ratio since the time constant is higher for more viscous drops.

Grace [1971] used the same fluid systems (various viscosity silicon fluids in Pale 4 Oil) as were used in most of our experiments. For the highest viscosity drops for which our experiments were successful (600 poise silicon fluid) several minutes were required for the drop to come to a stable deformation. Burst, when it was observed, proceeded extremely slowly. Experiments with more viscous grades of silicon fluid as the drop phase were unsuccessful because the drop response was so slow that the slight three-dimensionality of the flow field caused the drops to drift to the bottom of the tank (where end effects were important) before equilibrium deformation was attained. It is our opinion that the extreme difficulty of accurately performing experiments with very viscous drops casts doubt on the reliability of Grace's [1971] data for high viscosity ratio.

The predictions of the $O(\varepsilon^2)$ small deformation theory (shown in Figure 4.26) and the numerical calculations of Rallison and Acrivos [1978] for axisymmetric extensional flow both support our hypothesis that the critical Capillary number for drop burst in irrotational flows tends to some constant as viscosity ratio increases.

Figure 4.27 shows the maximum steady deformation attained by the drop (as measured by the deformation parameter D_f) at Capillary number just below the critical value. Data and theoretical predictions from the same sources as for Ca_c are presented. Accurate determination of $D_{f,c}$ is difficult, since the deformation changes rapidly with small increases in Ca near the burst point (see Figure 4.8, for example). This is reflected in the considerable scatter in the data. Agreement between our observations and the predictions of both small deformation and large deformation theories is acceptable. Most of the other available data indicates deformations at the bursting point which are considerably higher than we observed. In particular, the critical deformations reported by Grace [1971] are much higher than we observed. We attribute this discrepancy to the difficulty in distinguishing stable shapes from slowly evolving transients as discussed above.

Figure 4.28 shows photographs of the most extended stable shapes observed in irrotational flow for each viscosity ratio investigated.

Figures 4.29 and 4.30 show Ca_c and $D_{f,c}$ as a function of λ for $\alpha = 0.8$. Figure 4.30 also includes the orientation angle at the critical deformation, ϑ_c. Figures 4.31 and 4.32 are the qualitatively similar corresponding plots for $\alpha = 0.6$. In all these plots, the solid curve represents the predictions of the $O(\varepsilon^2)$ small deformation theory and the broken curve represents those of the large deformation theory. No ϑ_c is predicted by the large deformation theory since the assumption is made that the drops align with the angle of the exit streamline (designated as ϑ_e in Figures 4.30 and 4.32). There are no previous experiments to compare the results to, but the results of Rallison's [1981] calculation are included, with the exception of the orientation angle, which was not reported.

The agreement between the small deformation theory and the observations is again very good, particularly for Ca_c. More scatter in $D_{f,c}$ and ϑ_c is evident due to the difficulty in measuring these quantities. The large deformation theory and Rallison's numerical result are also in good agreement.

The data for ϑ_c provide an interesting illustration of the effects of deformation and viscosity ratio on drop orientation. At low viscosity ratio, the bursting drops are highly extended, and thus are aligned with the exit streamline of the flow. For intermediate viscosity ratios, the drops are less extended, and are still of low enough viscosity to allow the dissipation of vorticity through internal circulation, so they align closer to the extensional axis. As the viscosity ratio increases, however, the drop viscous time constant ($\lambda\mu a/\sigma$) increases, and as discussed in Section 3.4, they tend to be rotated away from the extensional axis, with the angle exceeding that of the exit streamline when λ is large. This observed behavior is qualitatively predicted by the small deformation theory.

The trends for the critical Capillary number required for burst are correlated with the orientation at burst, since the effective strain rate experienced by a drop depends on its orientation. This is particularly evident in the results at high viscosity ratio, where Ca_c goes through a weak minimum and starts to increase at about $\lambda = 5$, since higher shear rates are required for burst when the drops are rotated to orientations where the effective strain is lower.

Figure 4.33 and 4.34 and Figures 4.35 and 4.36 show the same plots for $\alpha = 0.4$ and $\alpha = 0.2$, respectively. The most interesting feature of these plots is the prediction of the $O(\varepsilon^2)$ small deformation theory of a viscosity ratio (46.6 for $\alpha = 0.4$ and 14.7 for $\alpha = 0.2$) above which no drop burst is possible. This is analogous to the behavior in simple shear flow, except that in that flow the limiting viscosity ratio is lower (3.6), since the vorticity is higher. We were unable to

verify the predicted limiting λ for $\alpha = 0.4$ directly, owing to the difficulties in investigating high viscosity ratio systems mentioned above, but for $\alpha = 0.2$, the rapid increase in Ca_c for the data points at $\lambda = 14.7$, and the lack of burst for drops with a viscosity ratio of 27 indicates agreement with the small deformation theory, at least in a qualitative sense.

Another interesting prediction of the small deformation theory for $\alpha = 0.4$ and 0.2 is a decrease in $D_{f,c}$ and increase in ϑ_c for large viscosity ratios. This is related to an interaction between the deformation and orientation which can be explained as follows: For high viscosity ratios, the drops are rotated by the vorticity such that the magnitude of the orientation angle is greater than that of the exit streamline. Near the bursting point, when the shear rate is increased slightly, the drop elongates in response, and this causes it to be rotated toward the exit streamline of the flow, where the effective strain is larger. This higher effective strain rate causes greater elongation, further decrease in the magnitude of the orientation angle, still higher effective strain rate, etc., and leads to drop burst. The maximum stable deformation, of course, is the deformation at which this process is initiated, and this apparently decreases with increasing viscosity ratio. Our data reflect this trend for $\alpha = 0.2$, but the data point for $\lambda = 27$ indicates an opposite trend for $\alpha = 0.4$, possibly due to experimental error in the (difficult) determination of $D_{f,c}$.

For $\alpha = 0.2$, the small deformation theory also predicts a lower limit in viscosity ratio for which drop burst is possible. Since the predicted deformation at the point of burst becomes very large as the viscosity ratio decreases near this limit, the small deformation theory is far outside it region of validity and predictions in this region would be of no use in any event. For both $\alpha = 0.4$ and 0.2, the large deformation theory predictions are adequate in the low viscosity

ratio region. Rallison's [1981] numerical results are also in reasonable agreement with the observations for both flow types for $\lambda = 1$.

For the sake of completeness, the results of the experiments of Torza, Cox, and Mason [1972] are compared to the predictions of the small deformation theory for simple shear ($\alpha = 0.0$) in Figures 4.37 and 4.38. The orientation angles at burst were not reported. As for $\alpha = 0.2$, both an upper an lower limit in λ for burst is predicted by the small deformation theory. The upper bound is in reasonable agreement with the experiments, but the existence of the lower bound is apparently due to a (not unexpected) failure of the theory for low viscosity ratio. The predicted deformation at burst for simple shear does not decrease with increasing viscosity ratio as it does for $\alpha = 0.4$ and 0.2. This is because the magnitude of the orientation angle is always less than that of the "exit" streamline ($\vartheta_e = 45°$) in simple shear, so the interaction between deformation and orientation described above cannot occur. Rallison's [1980] numerical result is in agreement with the data for Ca_c, but lies above the experimental curve of $D_{f,c}$, as is the case for $\alpha = 0.2$.

The effect of vorticity on drop burst is illustrated in Figure 4.39. To allow convenient comparison over the entire range of viscosity ratio, the plot shows the critical Capillary number for each flow type divided by the critical Capillary number for $\alpha = 1$. The solid curves in the figure show the predictions of the $O(\varepsilon^2)$ small deformation theory and the solid points show the results of Rallisons [1980] numerical study for $\alpha = 0.8$, 0.6, 0.4, and 0.2. Interestingly, even though the small deformation theory does a poor job of predicting the value of the critical Capillary number for low viscosity ratio, it predicts the trends for changing α at fixed low viscosity ratios reasonably well, except for $\alpha = 0.2$. At intermediate and high viscosity ratios, the small deformation theory predicts the trends quite

accurately. Even though the numerical results are in better agreement (for Ca_c) than the small deformation theory, the trend in $Ca_c(\alpha)/Ca_c(\alpha = 1)$ as predicted by the numerical results is not in particularly good agreement with the data, since the numerical results fall below the data for α = 1.0 and 0.8, and above the data for α = 0.6, 0.4, and 0.2. The reason for this discrepancy is unknown. In a recent review article, Rallison [1984] has made mention of more accurate calculations for the $\lambda = 1$ case from the as-yet-unpublished work of Duffy and Blundell. Comparisons with those results would be of obvious interest.

The burst predictions of the large deformation theory are based on the assumption that elongated drops align with the exit streamline of the flow. In this case the effective strain rate is $G\alpha^{1/2}$, and thus the ratio of Capillary numbers in Figure 4.39 should asymptote to $\alpha^{-1/2}$ for low viscosity ratios where the drops are significantly extended at the burst conditions. The expected limiting values of $Ca_c(\alpha)/Ca_c(\alpha = 1)$ for each α are shown as dotted lines at the left of Figure 4.39. While there is some scatter in the data, this appears to be an acceptable assumption in the absence of a more rigorous theory. It is probable that the agreement would be better at lower viscosity ratio.

Figure 4.40 shows $D_{f,c}$ and ϑ_c vs. λ for each flow type, allowing a convenient comparison of the effect of vorticity on the highest stable deformation and orientation angle at burst. Data from our experiments for α = 1.0, 0.8, 0.6, 0.4, and 0.2 are plotted. The simple shear data are from the experiments of Torza, Cox, and Mason [1972], and the solid points are from the numerical work of Rallison [1980]. One interesting feature of Figure 4.40 is that both the small deformation theory and the numerical results predict that the critical deformation is dependent on the flow type. In contrast, our experiments do not show any clear differences between the different flows (except as noted above for high

viscosity ratios for $\alpha = 0.2$). The reason for this discrepancy is not known, but it should be noted that the uncertainty in $D_{f,c}$ is rather large as mentioned above.

From the comparisons between the experimental and theoretical drop burst criteria presented above, we conclude the following:

1. For viscosity ratio less than unity, the Capillary number required for burst and the deformation at the point of burst both decrease with increasing viscosity ratio for all strong flows. In an irrotational flow, Ca_c approaches a constant value with further increases in the viscosity ratio. In contrast, when vorticity is present in the flow, Ca_c goes through a minimum at a viscosity ratio about 1.0, and increases steadily with viscosity ratio above that point. For flow types with the magnitude of the vorticity greater than 0.42 times that of the rate of strain (e.g., $\alpha = 0.2 \text{and} 0.4$), there is a viscosity ratio above which no burst is possible.

2. The $O(\varepsilon^2)$ small deformation theory does a remarkably good job of predicting the qualitative features of the drop burst, critical deformation, and orientation curves for viscosity ratios greater than about 0.05. This agreement is for all flow types investigated in our experiments and for simple shear. In particular, the prediction of a limiting viscosity ratio above which drop burst is impossible for has been experimentally verified for $\alpha = 0.2$ and (by Torza, Cox, and Mason [1972]) for $\alpha = 0.0$.

3. The $O(\varepsilon^2)$ small deformation theory can be used to obtain quantitative estimates of Ca_c within about 30% for the two-dimensional flows we considered for $\lambda > 0.05$.

4. The large deformation theory is in reasonable agreement with the data for $\lambda < 0.01$. The lowest viscosity ratio considered in our experiment was 0.001, and in that case the predictions for Ca_c and L/a at burst were accurate to within about 15% for all α. It is expected that the agreement would improve for lower λ, since the slenderness of the drop increases with decreasing λ.

5. The numerical calculations for $\lambda = 1$ are in good agreement with the data for Ca_c. The predicted critical deformations do not agree nearly so well with our observations, but the accurate experimental determination of $D_{f,c}$ is difficult. Numerical results for other viscosity ratios would be helpful, but to date, the three-dimensional nature of the problem has prevented investigations except for $\lambda = 1$, where the calculations are considerably simplified.

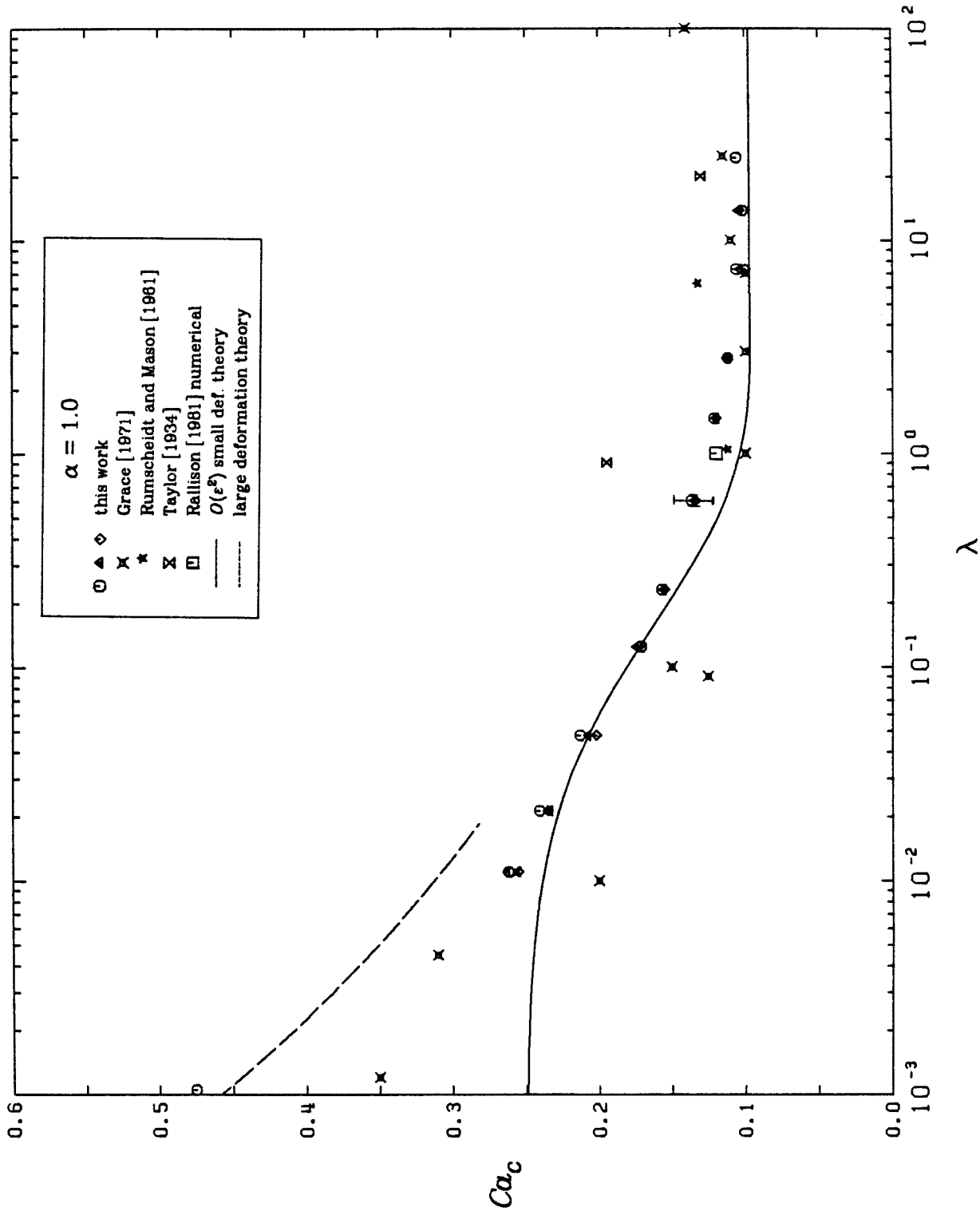

Figure 4.26
Critical capillary number for burst as a function of viscosity ratio for α = 1.0.

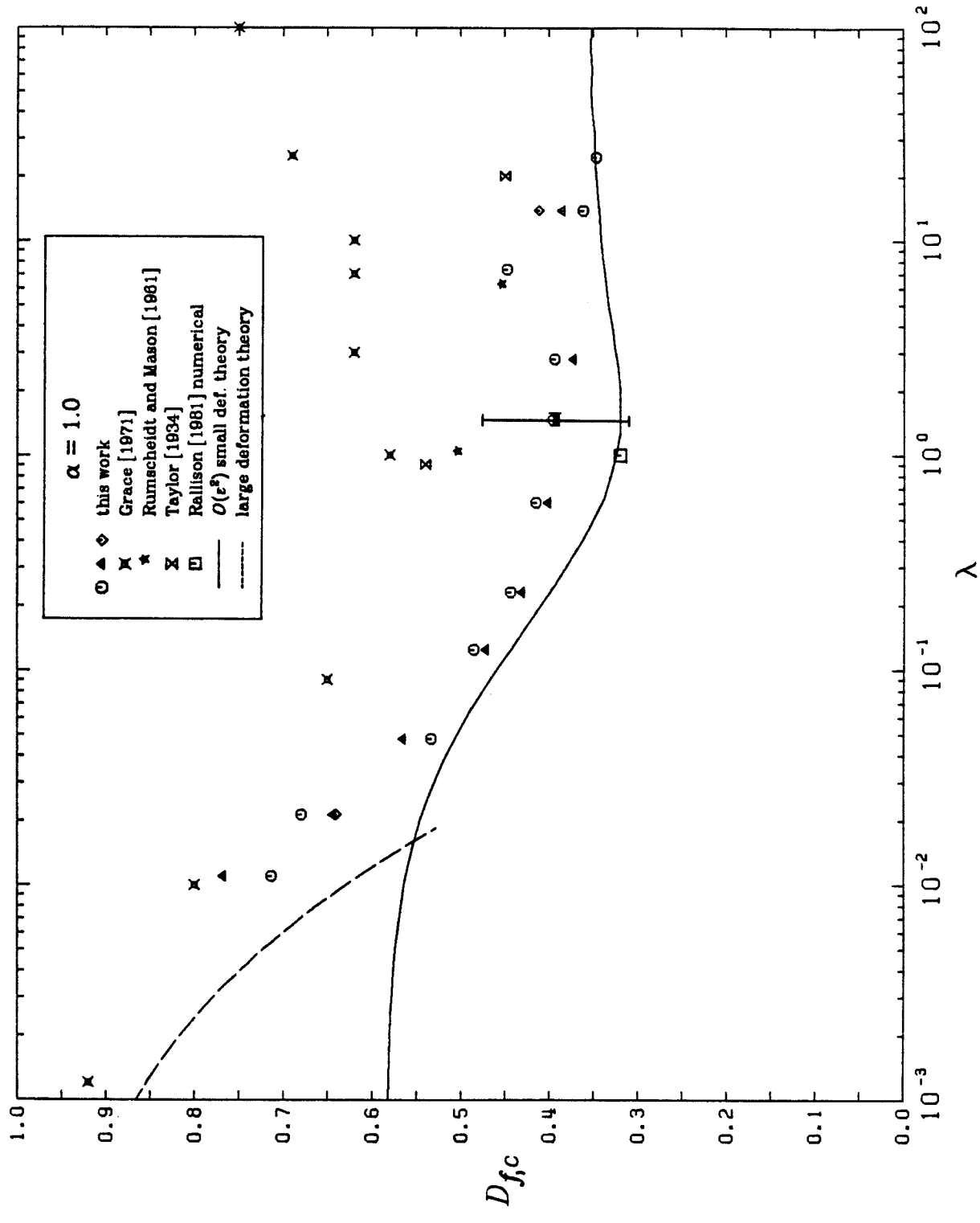

Figure 4.27
Deformation at critical capillary number as a function of viscosity ratio for α = 1.0.

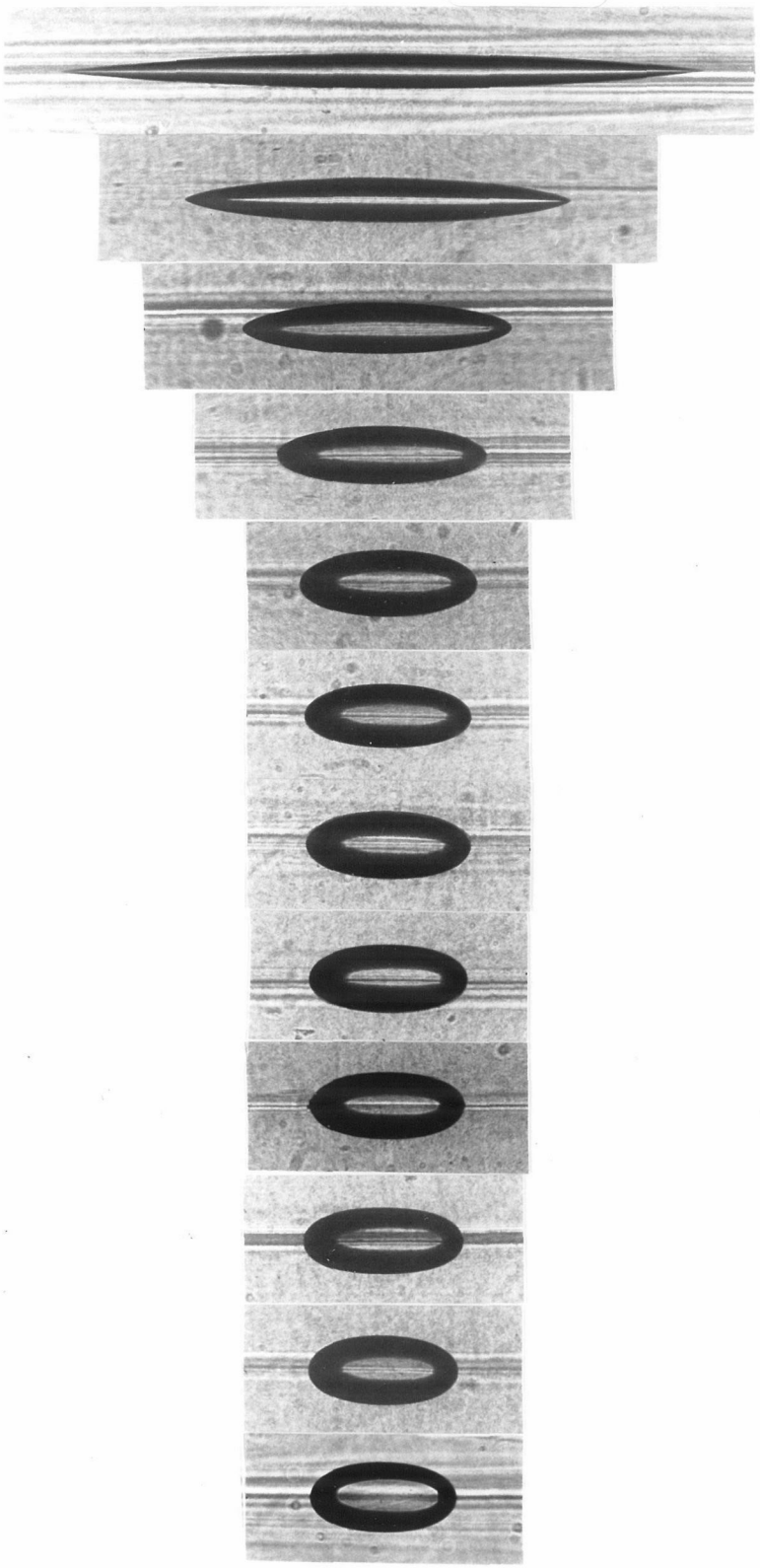

$\lambda = 1.05\times10^{-3}$
$Ca_c = 0.475$, $D_{fc} = 0.896$

$\lambda = 1.10\times10^{-2}$
$Ca_c = 0.259$, $D_{fc} = 0.791$

$\lambda = 2.13\times10^{-2}$
$Ca_c = 0.237$, $D_{fc} = 0.680$

$\lambda = 4.80\times10^{-2}$
$Ca_c = 0.208$, $D_{fc} = 0.565$

$\lambda = 0.124$
$Ca_c = 0.173$, $D_{fc} = 0.485$

$\lambda = 0.230$
$Ca_c = 0.156$, $D_{fc} = 0.444$

$\lambda = 0.60$
$Ca_c = 0.136$, $D_{fc} = 0.415$

$\lambda = 1.46$
$Ca_c = 0.120$, $D_{fc} = 0.396$

$\lambda = 2.80$
$Ca_c = 0.112$, $D_{fc} = 0.394$

$\lambda = 7.30$
$Ca_c = 0.103$, $D_{fc} = 0.411$

$\lambda = 13.8$
$Ca_c = 0.103$, $D_{fc} = 0.362$

$\lambda = 24.5$
$Ca_c = 0.106$, $D_{fc} = 0.347$

Figure 4.28
Drop shapes at critical capillary number for irrotational shear flow.

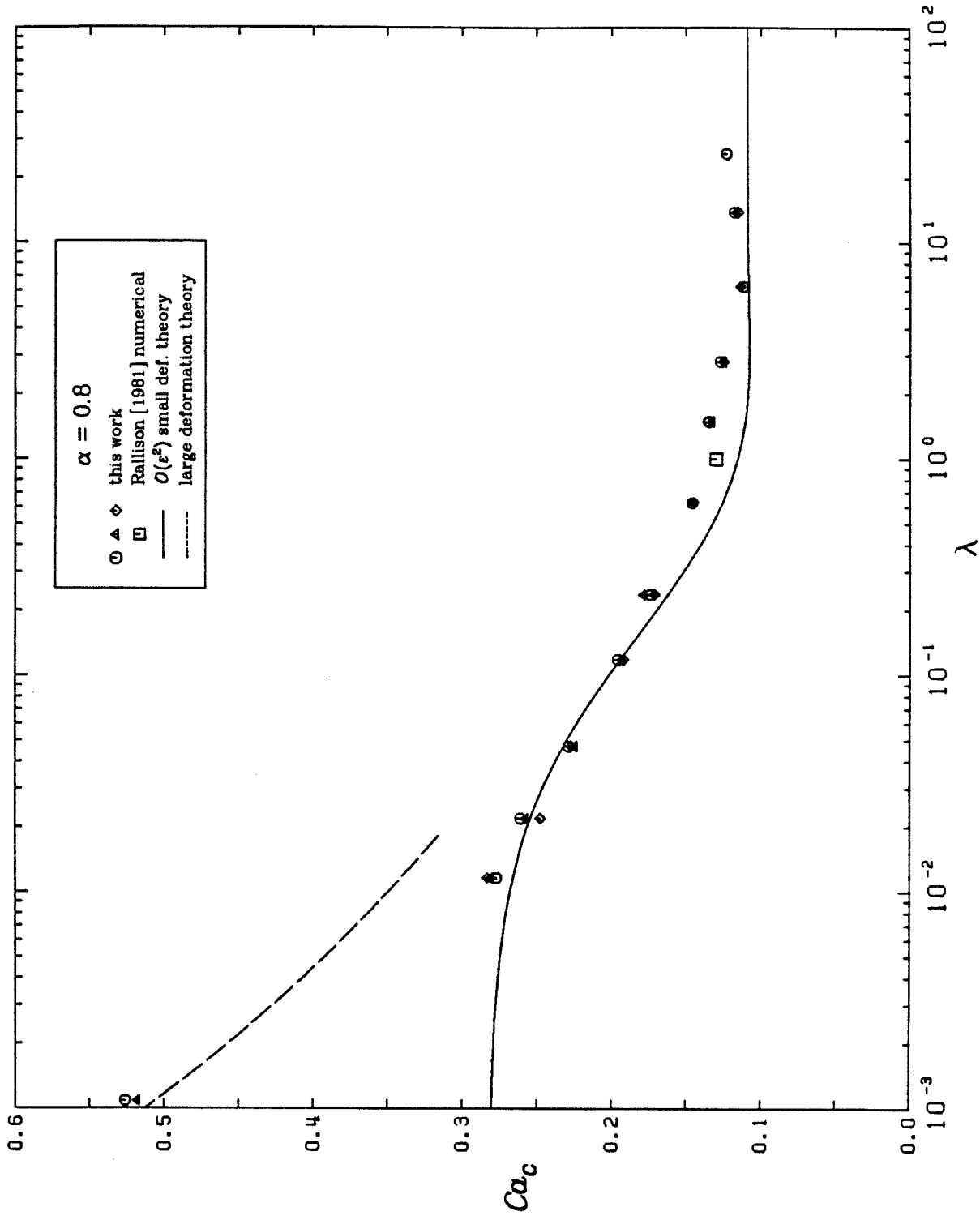

Figure 4.29
Critical capillary number for burst as a function of viscosity ratio for $\alpha = 0.8$.

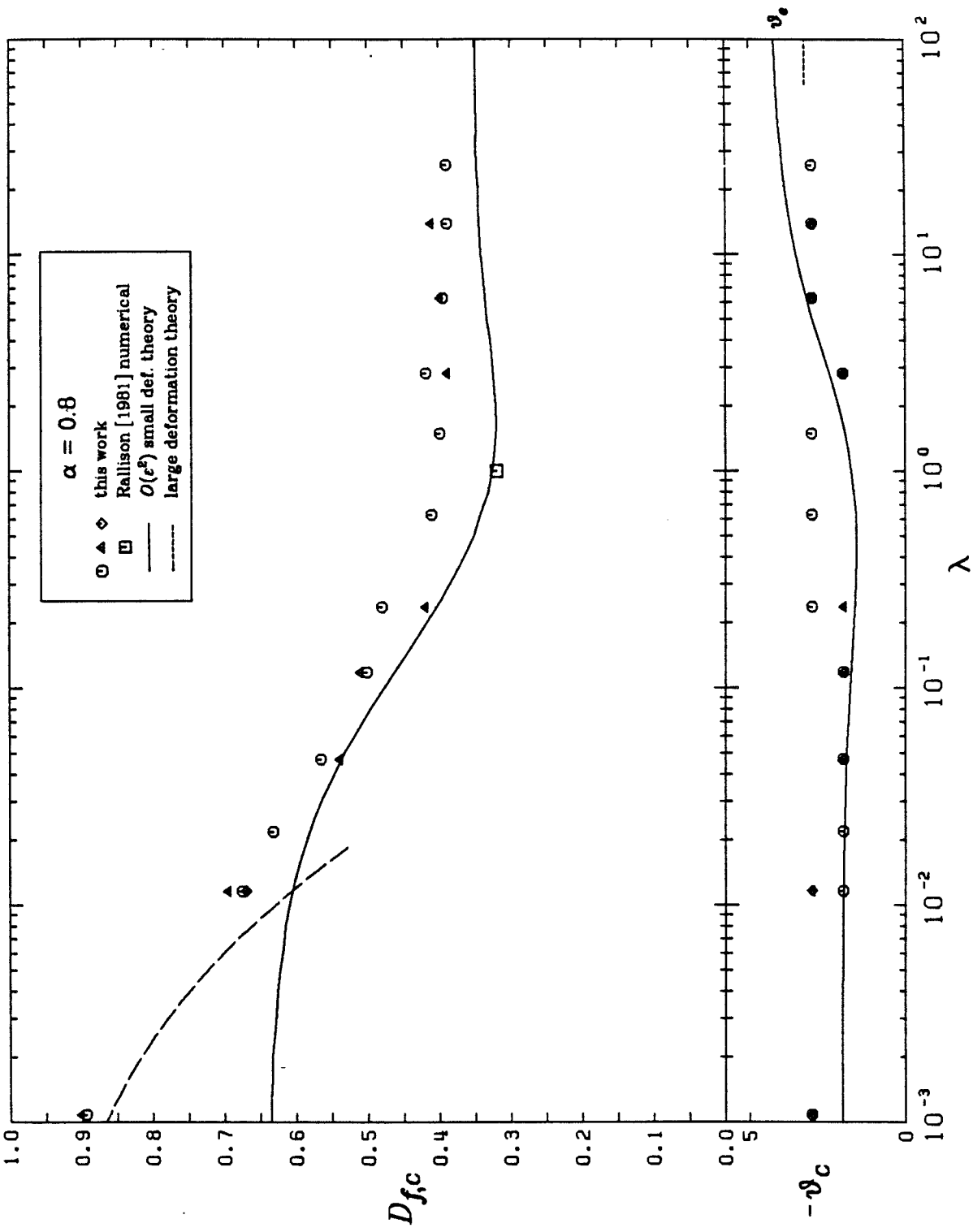

Figure 4.30
Deformation and orientation angle at critical capillary number as a function of viscosity ratio for $\alpha = 0.8$.

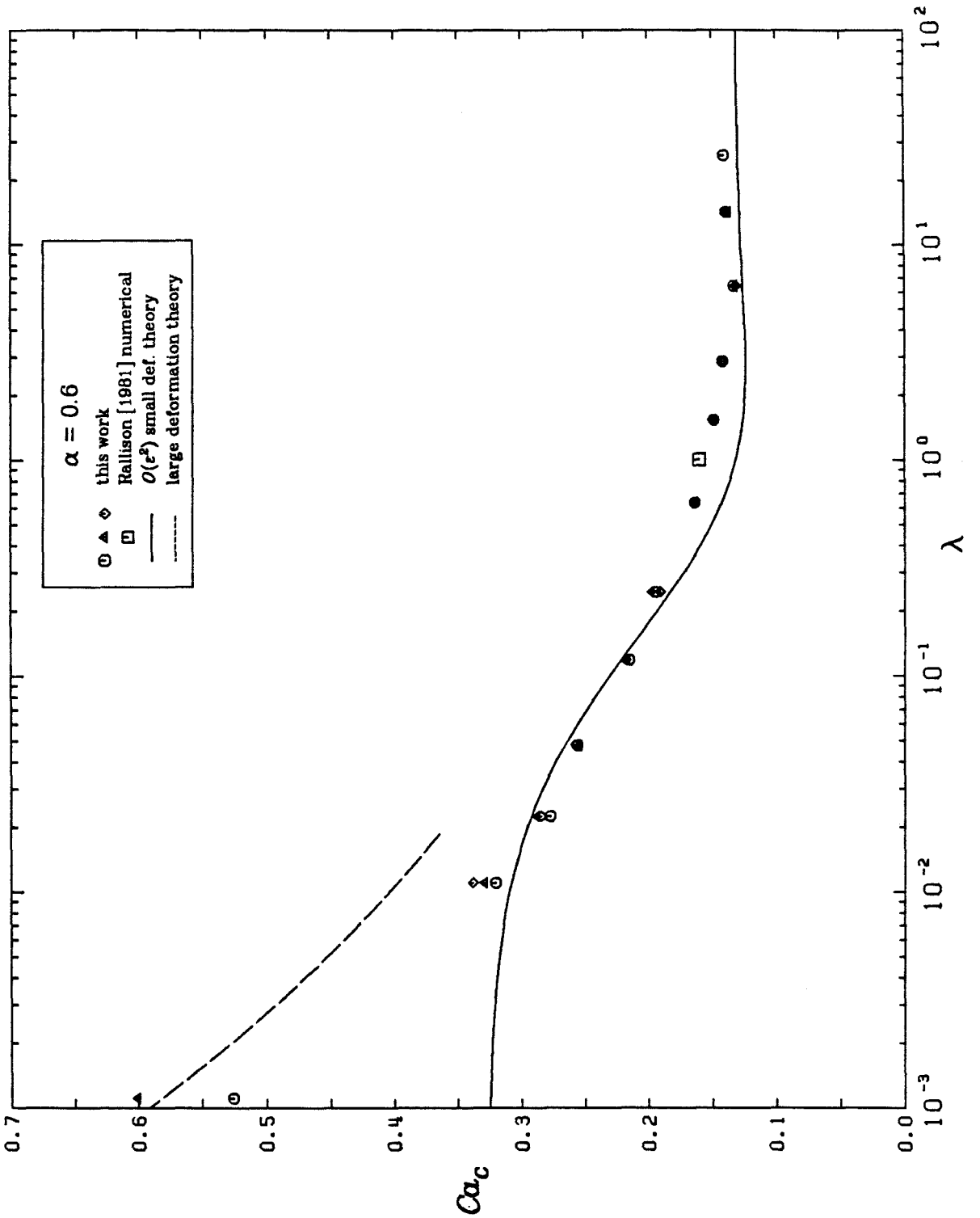

Figure 4.31
Critical capillary number for burst as a function of viscosity ratio for $\alpha = 0.6$.

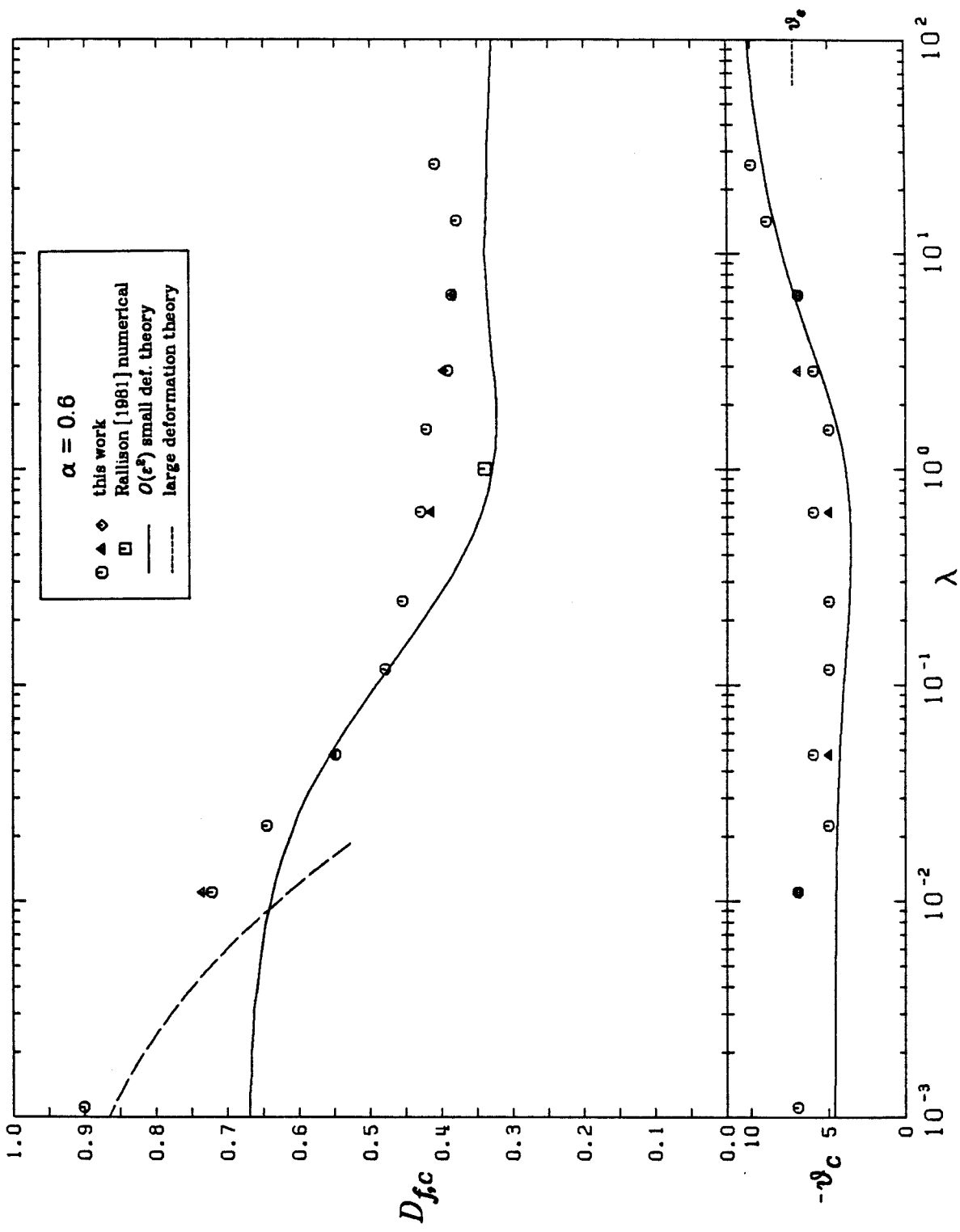

Figure 4.32
Deformation and orientation angle at critical capillary number as a function of viscosity ratio for $\alpha = 0.6$.

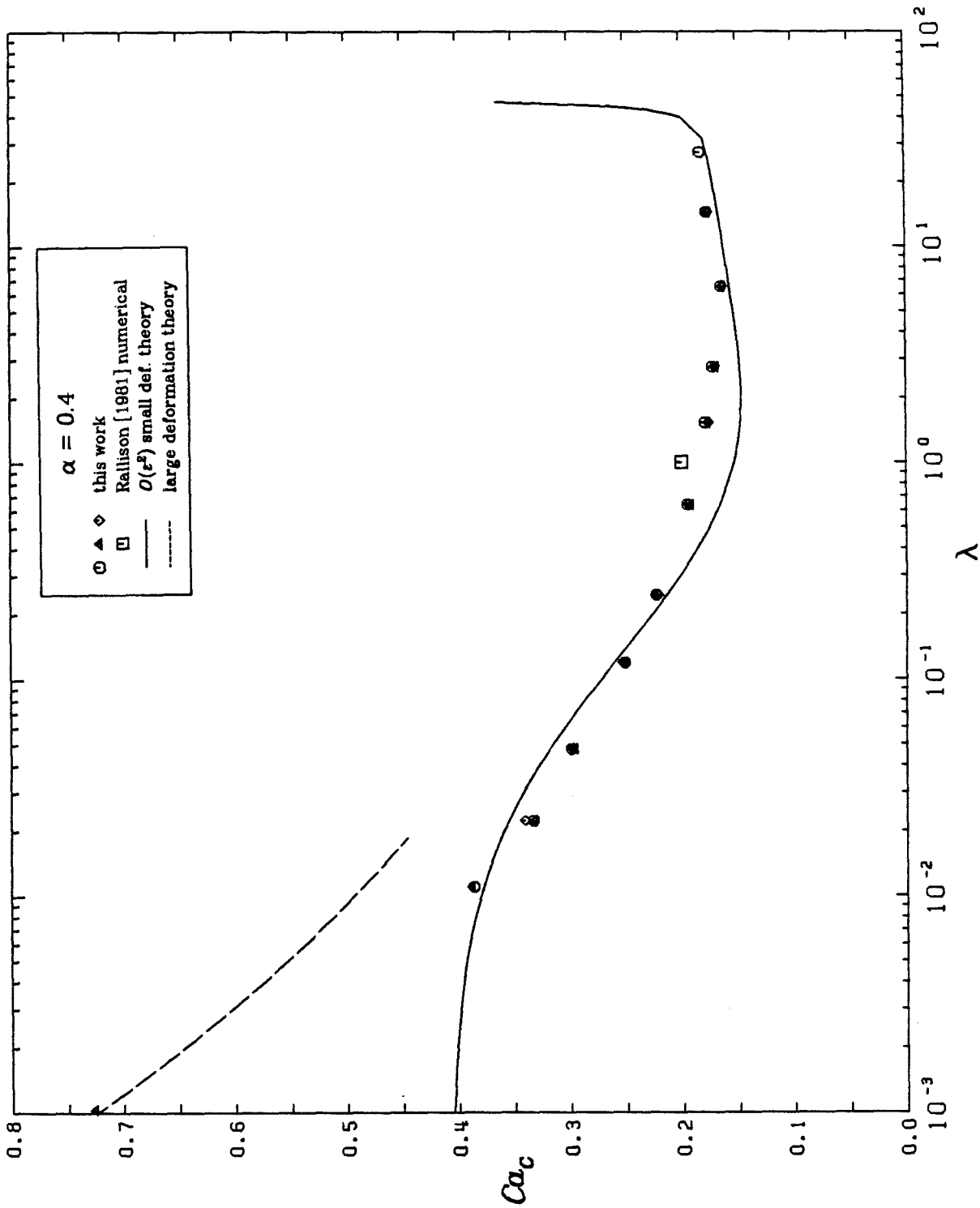

Figure 4.33
Critical capillary number for burst as a function of viscosity ratio for $\alpha = 0.4$.

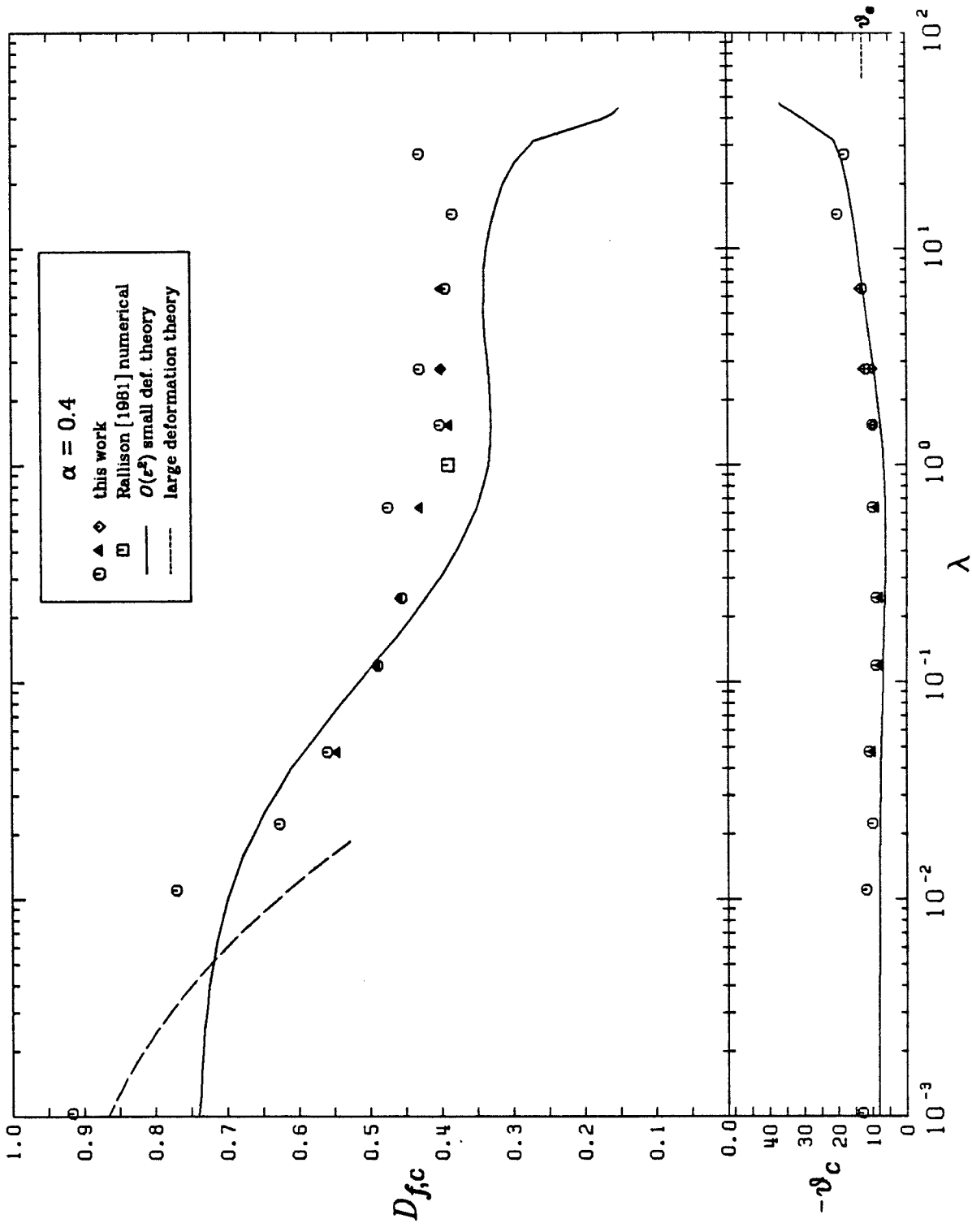

Figure 4.34
Deformation and orientation angle at critical capillary number as a function of viscosity ratio for $\alpha = 0.4$.

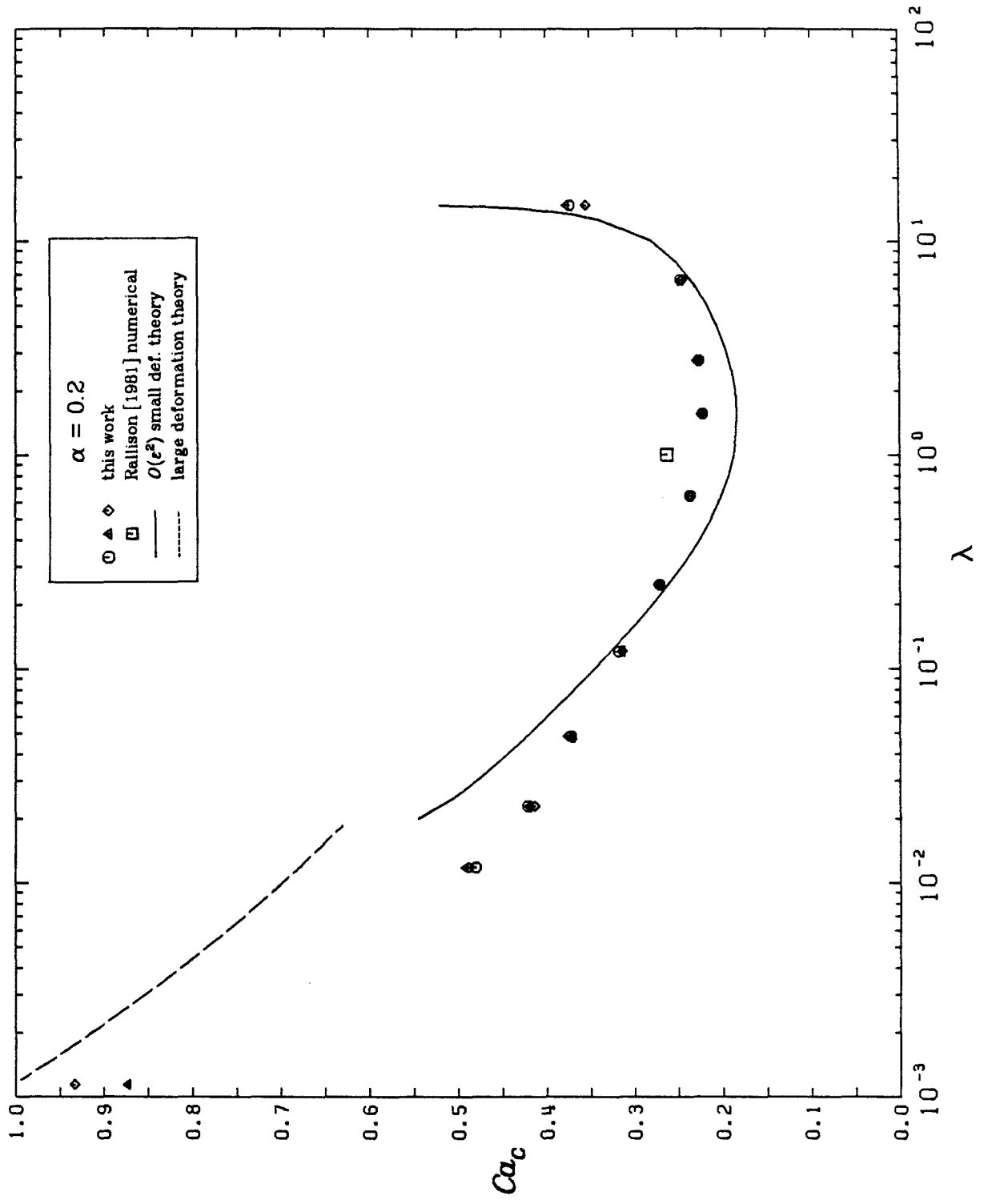

Figure 4.35
Critical capillary number for burst as a function of viscosity ratio for $\alpha = 0.2$.

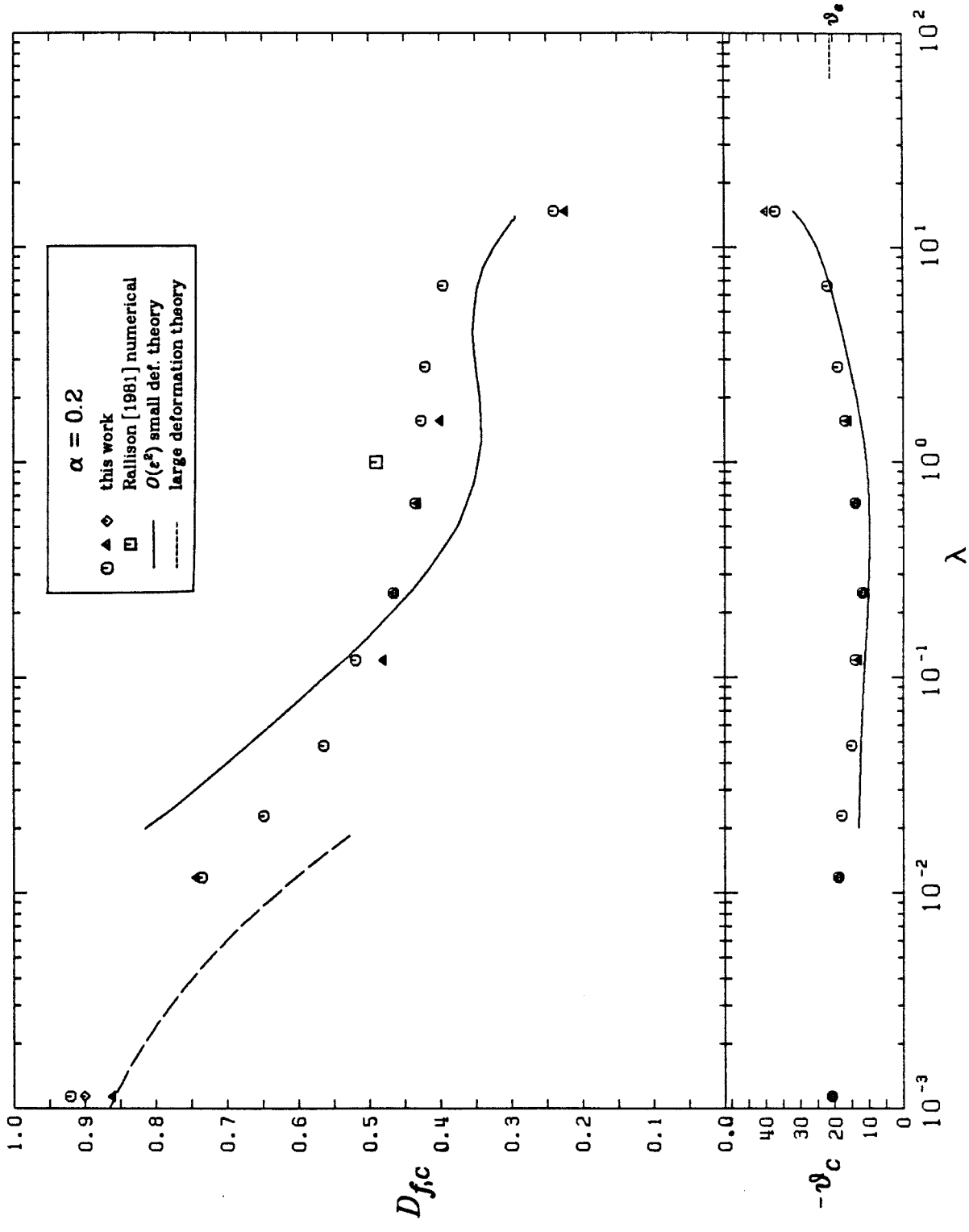

Figure 4.36
Deformation and orientation angle at critical capillary number as a function of viscosity ratio for $\alpha = 0.2$.

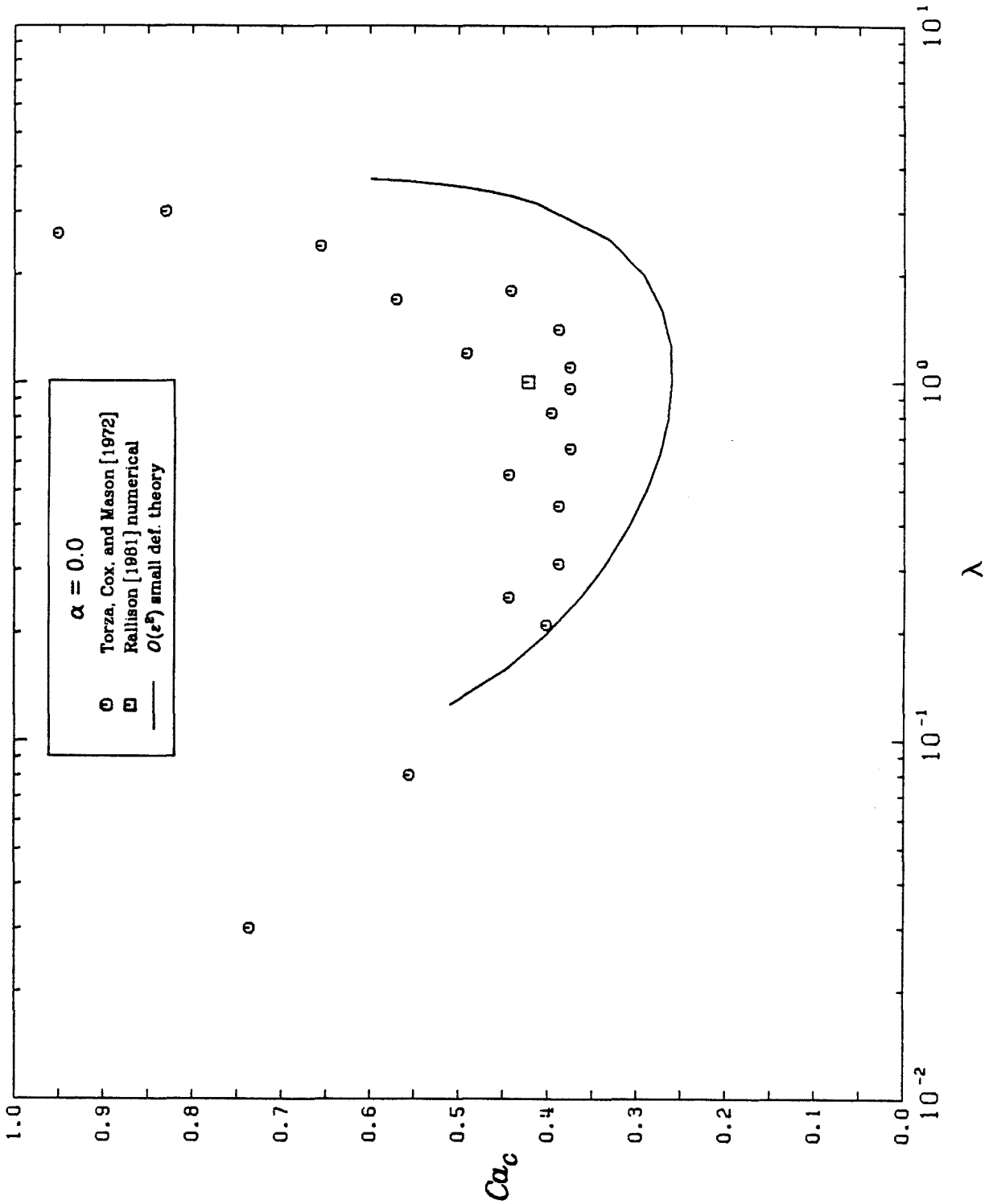

Figure 4.37
Critical capillary number for burst as a function of viscosity ratio for simple shear flow. Data from Torza, Cox, and Mason [1972].

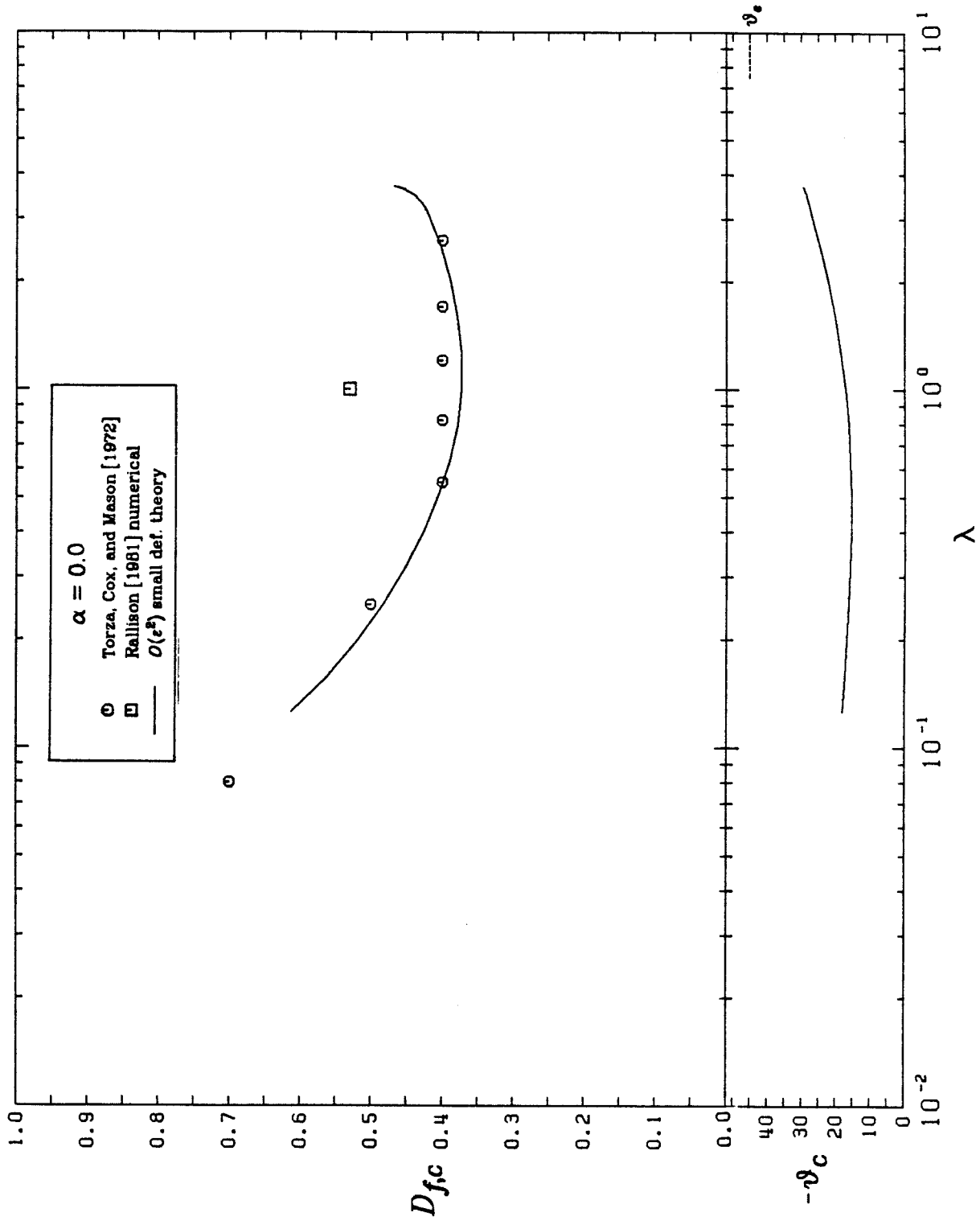

Figure 4.38
Deformation and orientation angle at critical capillary number as a function of viscosity ratio for simple shear flow. Data for orientation angle was not reported by Torza, Cox, and Mason [1972].

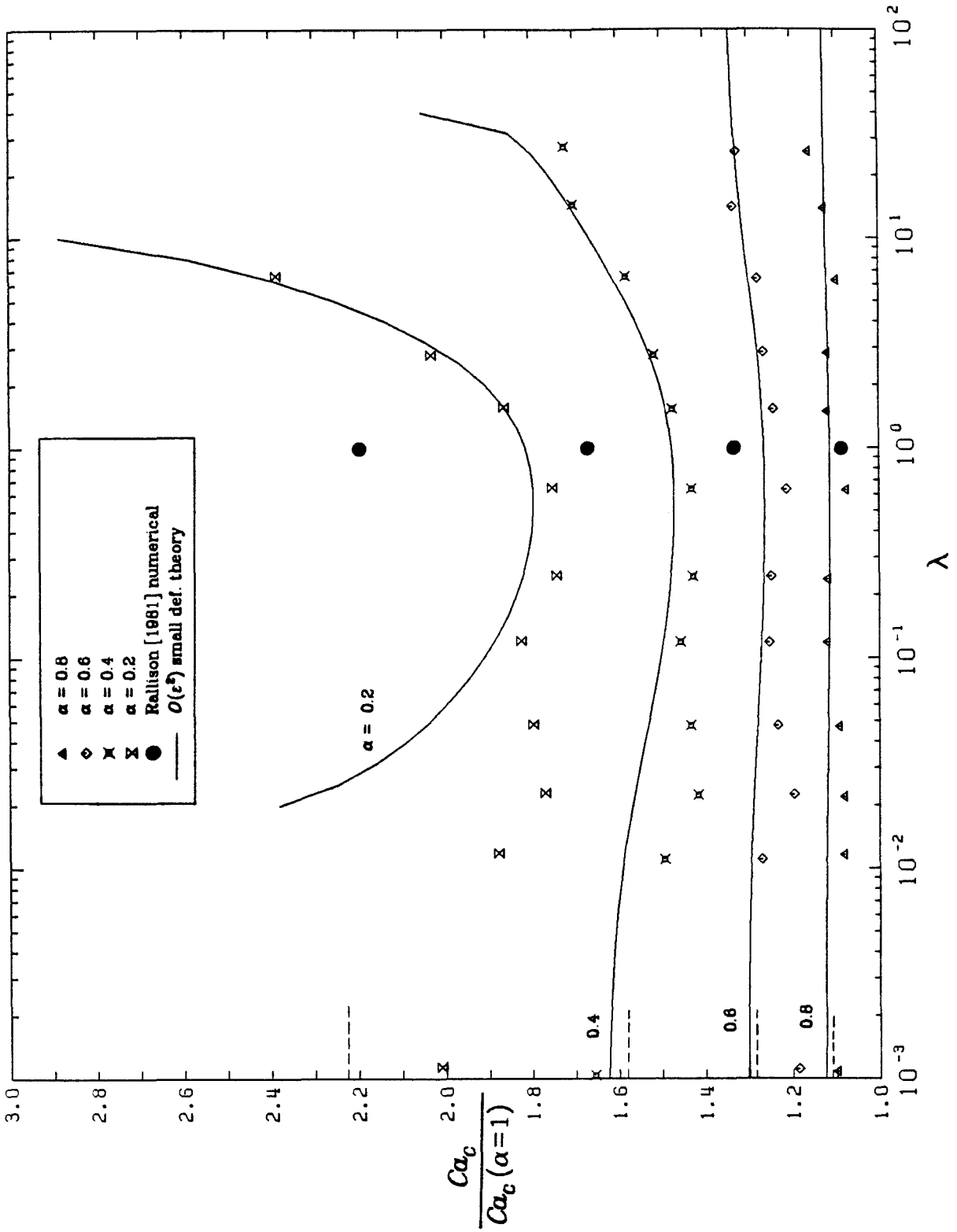

Figure 4.40
Critical capillary number for burst for each flow type, divided by Ca_c for $\alpha = 1.0$. This presentation highlights the effect of vorticity as a function of viscosity ratio.

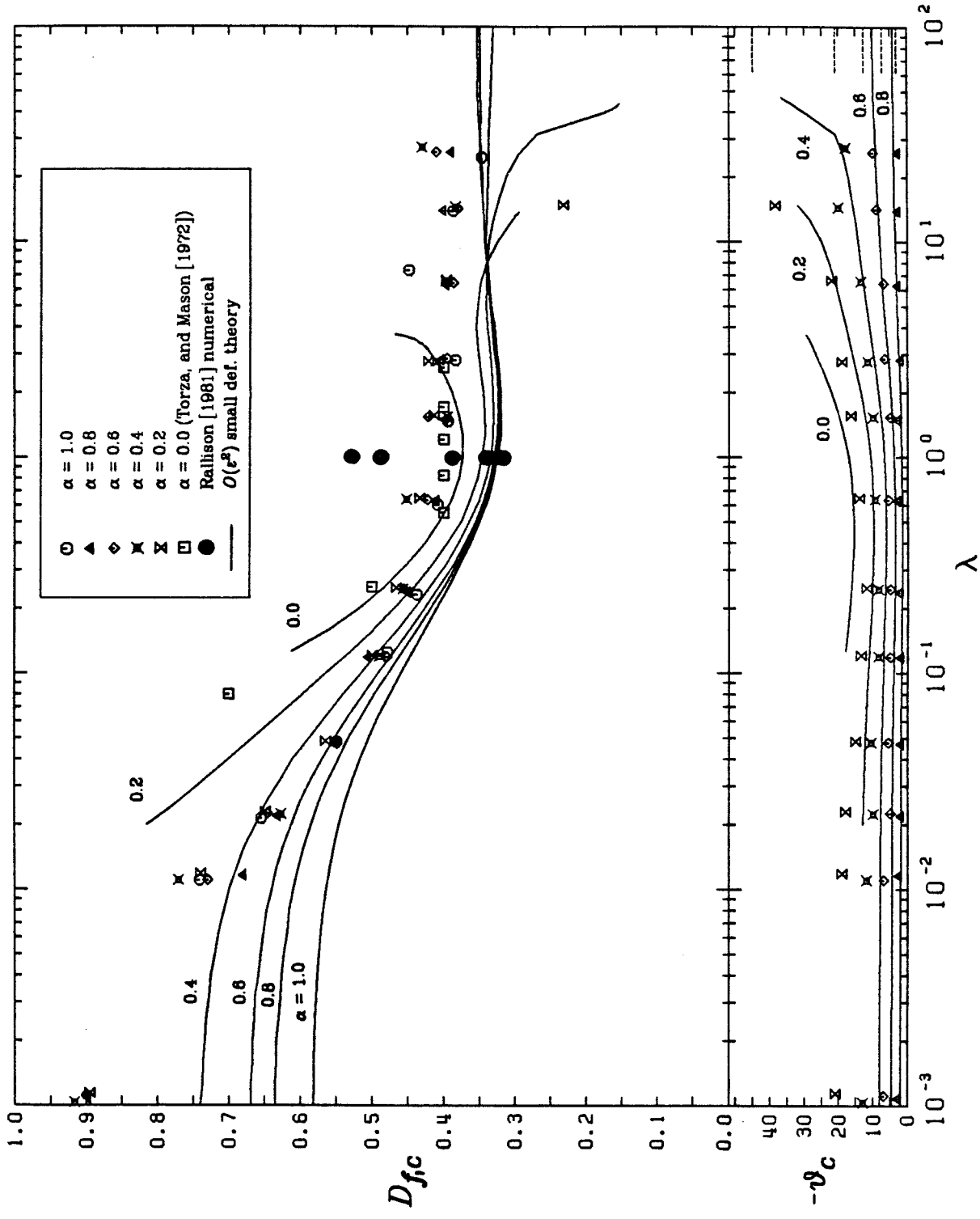

Figure 4.41
Effects of flow type on deformation and orientation angle at the critical capillary number. Numerical results of Rallison [1981] go in order of increasing α from top to bottom. Points for α = 1.0 and 0.8 coincide.

4.3 APPLICATION TO OTHER FLOW FIELDS

Prediction of drop deformation and burst in linear shear flows other than those we investigated experimentally can be accomplished in several ways. Comparisons between our data and the predictions of the $O(\varepsilon^2)$ small deformation theory of Barthes-Biesel and Acrivos [1973a] have established that their theory can be applied to finding both deformation and bursting point for viscosity ratios above about 0.05 with reasonable accuracy. The drawback of that approach is that, depending on the form of the velocity gradient tensor, a considerable amount of algebra may be required to write the tensor equations in component form. The advantage is that there are no adjustable parameters, and in principle at least, no experiments are needed to make the prediction.

If only information concerning drop burst is required, a much simpler method of extrapolating our results is possible. In this approach, described by Olbricht, Rallison and Leal [1982], the burst of a drop is considered within the framework of a flow classification scheme based on the ability of a given flow to effect finite deformations to a suspended microstructure. The microstructure (in this case the drop) is characterized by either a vector or a traceless second rank tensor, and the dynamical equations linearized about the rest configuration. The conditions leading to growth of the microstructure length scale are determined using a linear stability analysis, and in the case of a drop, conditions where such growth occurs are defined as drop burst.

The governing equation for the case where the microstructure is characterized by a vector $\mathbf{R}$, is

$$\frac{d\mathbf{R}}{dt} = \mathbf{\Omega}\cdot\mathbf{R} + g\left[\mathbf{E}\cdot\mathbf{R} - \frac{f}{f+1}(\mathbf{r}\cdot\mathbf{E}\cdot\mathbf{r})\mathbf{R}\right] - \frac{\xi}{f+1}\mathbf{R}, \tag{4.1}$$

where $\mathbf{r} = \mathbf{R}/R$, $R = |\mathbf{R}|$, g is a measure of the response of the microstructure to the straining motion, ξ denotes the elastic restoring force, and f represents the internal viscosity resisting deformation. When the microstructure is characterized by a traceless second order tensor, $\mathbf{A}$, the governing equation is:

$$\frac{d\mathbf{A}}{dt} = \mathbf{A}\cdot\boldsymbol{\Omega} - \boldsymbol{\Omega}\cdot\mathbf{A} + g(\mathbf{E}\cdot\mathbf{A} + \mathbf{A}\cdot\mathbf{E} - \frac{2}{3}(\mathbf{E}:\mathbf{A})\,\mathbf{I}) - \xi\mathbf{A} + \beta\mathbf{E}\,. \tag{4.2}$$

The analysis of the vector model of (4.1) leads to a linear system, the behavior of which depends on the eigenvalues of the normalized tensor $\mathbf{L}$, given by

$$\mathbf{L} = \frac{\boldsymbol{\Omega} + g\mathbf{E}}{(\nabla\mathbf{u}:\nabla\mathbf{u}^T)^{1/2}}. \tag{4.3}$$

The eigenvalues are the roots of the characteristic equation of $\mathbf{L}$:

$$\nu^3 - (\tfrac{1}{2}\mathrm{tr}\mathbf{L}^2)\nu - \det\mathbf{L} = 0 \tag{4.4}$$

The real part of the eigenvalue with the largest real part is termed ν^+, and growth of the microstucture is indicated when $\nu^+(\nabla\mathbf{u}:\nabla\mathbf{u}^T)^{1/2}$ exceeds ξ. Flow fields for which this is true are termed "strong", and the remaining flows, "weak".

A somewhat more complicated analysis applies when the tensor model is used, but the behavior is governed by roots of a 5 by 5 matrix, whose characteristic equation can be written in terms of $\mathbf{L}$ (Olbricht, Rallison and Leal [1982]):

$$\begin{aligned}\nu^5 + \frac{1}{6}\Big[4\mathrm{tr}(\mathbf{L}^T\cdot\mathbf{L}) - 11\mathrm{tr}\mathbf{L}^2\Big]\nu^3 + \Big[2\mathrm{tr}(\mathbf{L}^{T2}\mathbf{L}) - 5\det\mathbf{L}\Big]\nu^2 + \\ + \frac{1}{6}\Big[-2\mathrm{tr}\mathbf{L}^2\,\mathrm{tr}(\mathbf{L}^T\cdot\mathbf{L}) + (\mathrm{tr}\mathbf{L}^2)^2 - 6\mathrm{tr}(\mathbf{L}^T\cdot\mathbf{L})^2 + 6(\mathrm{tr}(\mathbf{L}^T\cdot\mathbf{L}))^2\Big]\nu - \\ - \frac{2}{3}\Big[2\det\mathbf{L}\,\mathrm{tr}(\mathbf{L}^T\cdot\mathbf{L}) - \mathrm{tr}\mathbf{L}^2\Big] = 0\end{aligned} \tag{4.5}$$

As for the vector model, the flow is defined as strong when

$$\nu^+ \equiv \max \mathrm{Re}(\nu_i) > \xi\,(\nabla\mathbf{u}:\nabla\mathbf{u}^T)^{-1/2}\,. \tag{4.6}$$

In applying their flow classification scheme to drop burst prediction, Olbricht, Rallison and Leal [1982] suggest using $\alpha_1 G/Ca$ from the small deformation theory discussed in Section 3.1 for ξ in (4.6). This gives the following expression for the drop burst criterion:

$$Ca > \frac{40(\lambda+1)}{(2\lambda+3)(19\lambda+16)} \frac{G}{\nu^+(\nabla\mathbf{u}:\nabla\mathbf{u}^T)^{\frac{1}{2}}}. \tag{4.7}$$

They suggest treat g as an adjustable parameter, using experimental results at the same viscosity ratio to estimate this quantity. In principle, the burst for drops suspended in any linear shear flow could be predicted from data for one flow type. The procedure for extrapolating our results to some other linear shear field is then clear:

1. An approximate value of g is determined from the data for the viscosity ratio of interest. Data from any flow type can be used, but it is probably best to use the flow type for which the ratio of magnitude of the vorticity to the magnitude of the strain rate is closest to that of the flow of interest.

2. This value of g is then used to compute $\mathbf{L}$ for the flow field under consideration. The eigenvectors are then computed from (4.4) or (4.5), depending on whether the vector or tensor model is to be used. The flow strength is proportional to the maximum real part of this set of eigenvectors.

3. The critical Capillary number for burst can then be determined from (4.7)

To illustrate this concept and test the vector and tensor models, we have employed this method for one case from our experiments. For a viscosity ratio of 1.53, we computed g from the burst point at $\alpha = 0.6$, and then used both models to predict the burst point for the other flow types investigated, comparing the results to the experimental observations.

For flows given by (2.1) the eigenvalues computed from the characteristic equations are given by:

$$0, \pm\left[\frac{1}{2}\frac{g^2(1+\alpha)^2-(1-\alpha)^2}{(1+\alpha)^2+(1-\alpha)^2}\right]^{1/2}, \tag{4.8}$$

for the vector model, and

$$0, \pm\left[\frac{1}{2}\frac{g^2(1+\alpha)^2-(1-\alpha)^2}{(1+\alpha)^2+(1-\alpha)^2}\right]^{1/2}, \pm\left[\frac{2/3g^2(1+\alpha)^2-2(1-\alpha)^2}{(1+\alpha)^2+(1-\alpha)^2}\right]^{1/2}, \tag{4.9}$$

for the tensor model. For the vector model, ν^+ is always the eigenvalue with the plus sign. For the tensor model, the two positive eigenvalues must be compared to determine which is larger.

Figure 4.41 shows the comparison between the experimental results and the predictions obtained from the vector and tensor models. Since the value of g was determined from the data at $\alpha = 0.6$, the agreement is exact at that point. For the other flow fields, the tensor model gives slightly better agreement than the vector model. Given the low level of effort required to "extrapolate" our drop burst data to other flow fields, this technique seems quite attactive for engineering estimates of the burst point.

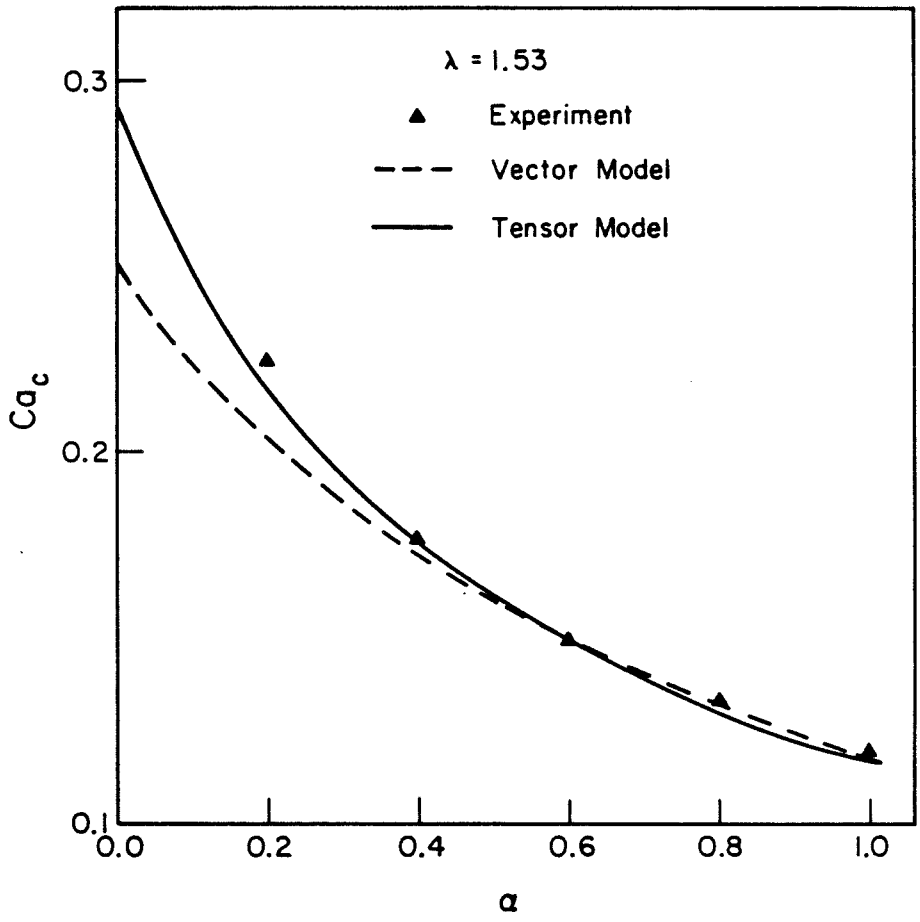

Figure 4.42
Results of "extrapolating" experimental results for $\alpha = 0.6$ to other flow types based on the flow strength classification scheme of Olbricht, Rallison, and Leal [1982]. The viscosity ratio was 1.53.

5.0 TRANSIENT DROP DEFORMATION

In this section we briefly consider the time dependent deformation of drops under conditions where no steady shapes exist. As described in Chapter 2, the drop deformation and burst experiments were performed by increasing the shear rate in very small steps and observing the resulting equilibrium deformations of the drop as a function of shear rate. In most cases, a critical shear rate, defined as the lowest shear rate for which no equilibrium shape existed, was reached. The inherently transient deformation of the drops subsequent to this point is the topic of interest in this chapter.

The transient portion of our experiments was basically a continuation of the steady state experiments. The same fluid systems and flow fields were used. When the critical shear rate (or Capillary number) was reached, the drops were allowed to extend at that shear rate for a time sufficient to stretch the drops to approximately ten times their undeformed diameter. During the period while the flow field was on, the elongating drops showed no tendency to break up into fragments. When a certain drop elongation ratio (defined as the length of the deformed drop divided by its undeformed diameter) was reached, the flow was turned off. The drop motion was then driven solely by interfacial tension. The drop proceeded to either break into satellite drops through the growth of varicosities in the extended shape, or to return to the initial spherical shape through a complex motion. The particular behavior observed depended on the viscosity ratio and degree of extension when the flow was stopped, as discussed in Section 5.2. During the transient elongation of the drop and subsequent breakup (or return to a spherical shape), still photographs were taken at recorded intervals for later analysis.

Our observations of transient drop deformation were by no means exhaustive. In particular, we limited our experiments to one particular deformation history, namely that experienced by a drop going through successive equilibrium shapes approached in a quasi-stationary manner. The transients were studied only for the lowest shear rate for which no stable steady shape existed, and no experiments were attempted where the shear rate exceeded the critical value. Extensive transient experiments have been reported by Grace [1971], whose work concentrated on the final conformation (number and size distribution of fragment drops) of drops broken up by a number of different methods. The reader interested in the effects of supercritical shear rates and/or final drop size distribution is referred to that work.

Another limitation of our experiments was that they covered only a narrow range of elongation ratios at which the flow was turned off. This elongation ratio was determined by allowing the drop to extend to about the maximum length which would remain within the field of view of the control camera. Further extension would also have put the drop ends out of the region where the flow was closely approximated by (2.1). Time did not permit a more thorough investigation of the effect of elongation ratio at cessation of shear on the resulting drop size distribution, but the preliminary experiments discussed here revealed some interesting phenomena which will hopefully motivate further research in this area.

A final weakness with our experiments was that the transient deformation was followed only with discrete still photographs taken at intervals. A careful analysis of the transient motions will probably require either motion picture photography or video tape.

Despite their limitations, the experiments did reveal some interesting features of the transient drop deformation process. Quantitative data on the elongation rate at the critical shear rate were obtained for viscosity ratios ranging from 0.01 to about 13. The effect of flow type for various strong flows was also determined. These points are discussed below.

5.1 TRANSIENT DROP THEORIES

While there is no general solution for the transient deformation and burst of a drop in a linear shear field, theoretical studies relevant to portions of the problem have been undertaken. These include studies of the transient motion of infinite fluid threads in an axisymmetric extensional flow, and studies of the stability of infinite fluid threads in a stationary suspending fluid. These theories and their applicability to the experimental situation are discussed briefly below.

5.1.1 Extending Fluid Threads

Tomotika [1935] has investigated the extension of an infinite cylinder of one fluid suspended in a second fluid undergoing axisymmetric extensional flow. The same problem was treated in more detail by Mikami, Cox, and Mason [1975]. The theory serves as an approximate model for a highly deformed drop elongating in an extensional flow.

In these studies, the growth of small sinusoidal disturbances of arbitrary wavelength on the cylindrical fluid interface was investigated. When the disturbances are small, the imposed axisymmetric extensional flow satisfies the flow and continuity equations throughout the domain, including the portion interior to the thread, and also satisfies the boundary conditions on the cylindrical

surface. Thus, the undeformed suspended fluid cylinder extends with the flow, decreasing in diameter correspondingly. As a consequence of this extension, the wavelength of a given disturbance increases exponentially with time, and the net effect is to slow the overall growth rate of the capillary waves and thus stabilize the fluid cylinder.

This theory is very helpful in explaining the observed stability of extending fluid threads. For a variety of reasons, however, its usefulness for quantitative predictions of physically important results (such as drop fragment size and breakup time) in experimentally realizable situations is limited. One difficulty arises because the nature of the experiments differs in several important respects from the situation considered theoretically. For example, in our experiments the flow fields were two-dimensional rather than axisymmetric, and thus the imposed flow could not satisfy the flow and continuity equations inside the extending drop. As a consequence, the extension rate of the drops was less than that of the imposed flow. Also, the theory applies for an infinite fluid cylinder, but the experiments investigated the motion of extending drops. Particularly in the early stages of transient deformation, the elongation-resisting effects of interfacial tension due to the drop ends cannot be neglected.

Other difficulties arise because of the inherently transient nature of the extending thread problem. In considering the stability of a problem with a steady state solution (e.g., an infinite fluid cylinder in a stationary suspending fluid, as discussed below), it is generally sufficient to find conditions under which infinitesimal disturbances will grow. In the case of an extending fluid thread, however, the wavelength of the disturbances, their growth rate, and the diameter of the thread are all time dependent. Thus, the evolution of each disturbance must be studied to determine whether the disturbance amplitude ever

becomes equal to the thread radius, a condition which would indicate thread breakup. For breakup predictions, the initial disturbance amplitude and the thread diameter at the time at which the disturbance is generated must be known. Since these can only be estimated, quantitative predictions are difficult.

The qualitative conclusion that threads are considerably stabilized by elongation in an extensional flow has been readily confirmed. Mikami, Cox, and Mason [1975] performed experiments with extending threads in a four roll mill similar to the one used in our experiments. They extended the threads to the point at which breakup occurred with the flow at a constant (supercritical) shear rate. In this two-dimensional extensional flow, threads with viscosity ratios of 0.148 and 1.46 remained intact until the thread diameter was less than 0.01 cm.

In our experiments, drops were elongated to threads with a diameter of approximately 0.03 to 0.05 cm with the flow constant at the critical shear rate, and then the flow was turned off. While the flow was on, no breakup occurred and no capillary waves were visible, but when the flow was turned off, capillary waves became visible shortly thereafter. Thus our experiments confirmed the qualitative theoretical result that some stabilization mechanism is present while the thread is elongating which is absent when the suspending fluid is stationary.

5.1.2 Stationary Fluid Threads

The breakup of an infinite cylindrical fluid thread in a stationary suspending fluid has been considered by Tomotika [1935] and in more generality by Lee and Flumerfelt [1981]. The analysis for stationary threads is similar to that for extending threads in that growth of infinitesimal sinusoidal disturbances to the

cylindrical surface is considered, but is considerably simplified since neither the radius of the cylinder nor the wavelength of the disturbance changes with time. Thus to predict the diameter of drops resulting from thread breakup, one need only determine the wavelength for which the disturbance grows fastest (this implicitly assumes that the linearization remains valid even when the waves are of finite amplitude). Lee and Flumerfelt [1975] determined this critical wavenumber and growth rate for a variety of limiting cases through asymptotic methods, and employed numerical methods for the general case (arbitrary viscosity and density ratio). Our experiments were in the inertialless regime where the time scales were determined by the fluid viscosities (the Ohnesorge number, as defined by Lee and Flumerfelt, was small). Under these conditions, the critical wavenumber depends on the viscosity ratio, with the smallest drop fragments obtained with a viscosity ratio around unity.

The theory for an infinite fluid cylinder suspended in a stationary fluid serves as an approximate model for the behavior of a fluid thread which has been generated by elongating a drop in an extensional flow which has subsequently been turned off. The theory would be expected to provide good predictions of the drop fragment size as long as the drops are highly extended and the effects of the drop ends thus negligible. Unfortunately, the theory has limited value for comparison with our observations since our experiments were restricted to elongation ratios where the effects of the drop ends remained significant. As a consequence, the breakup mechanism, particularly near the drop ends, was quite complicated. A more exact analysis, taking the ends into account, would be required for accurate drop fragment size predictions under these conditions.

5.2 TRANSIENT DEFORMATION RESULTS

5.2.1 Low Viscosity Ratio Drops

Figure 5.1 shows a sequence of photographs which illustrate the transient behavior of a drop of viscosity ratio 0.012 in a flow with $\alpha = 0.6$. The first four photographs were taken with the flow constant at the critical shear rate. In low viscosity ratio cases such as this one, the drops attained highly deformed steady shapes with pointed ends prior to burst. As can be seen, the shape of the drop did not change dramatically during transient deformation with the flow on. Instead, the drop simply continued to elongate, becoming longer and thinner with increasing time in the critical flow. Except for a small region near the drop ends, which remained pointed, the width of the elongating drop was nearly constant over its length at a given instant. While the flow was on, there was no noticeable wave formation on the drop surface, and the drop showed no tendency to fragment while extending. The appearance of the drops was the similar to that in Figure 5.1 for all flow types.

The final four photographs of Figure 5.1 show the motion of the drop after the flow was stopped. The times shown are relative to the time at which the flow was turned off. The most immediate adjustment took place near the ends of the drop, where the curvature was high due to the pointed ends. The ends immediately became rounded, forming beads which were rapidly pinched off from the main drop. Simultaneously, capillary waves became visible on the central portion. After the original ends pinched off, the ends of the remaining central portion began to likewise form spherical beads. These appeared to be pinched off by a mechanism similar to that for the original drop ends, except that growth of capillary waves played some role as well. In other experiments with the same

fluid system, we observed that the number and size of the drop fragments was determined by the degree of elongation achieved before the flow was turned off. The greater the elongation, the greater the number of drops and the more uniform the drop size distribution, since breakup via capillary wave growth played an increasingly important role.

The final photograph of Figure 5.1 shows five major drop fragments, with each pair of major fragments separated by one barely visible minor fragment. The rest diameter of the central fragment, which appeared to be formed at least partly from growth of capillary waves, was approximately one-half that of the original drop. The theory of Lee and Flumerfelt [1981] for a stationary fluid cylinder predicts that the fastest growing disturbance for this fluid system has a wavenumber of approximately 0.42. Using the diameter of the central portion of the extended drop when the flow was turned off, this yields a predicted fragment diameter of about one-fourth that of the original drop. The large discrepancy between the calculated and observed fragment size illustrates the importance of the contraction of the drop due to the presence of the ends.

Figures 5.2 and 5.3 show plots of the elongation ratio L/a vs. dimensionless time for the case discussed above and for another low viscosity ratio case with $\lambda = 0.023$. $G_c\,\alpha^{1/2}t$ is chosen for the dimensionless time because $G_c\,\alpha^{1/2}$ is the effective extension rate along the exit streamline where the elongated drops align. After the flow is turned off (indicated by the maxima in L/a) the motion is driven by interfacial tension, and the interfacial tension time scale $(L\,\mu'/\sigma)$ is obviously more appropriate under these conditions. For convenience, however, the time scale was the same throughout the plot. Measurements of L/a after the flow was stopped were continued until the first fragment separated from the main drop. In the low viscosity ratio cases shown in Figure 5.2 and 5.3, only a

slight decrease in the drop length was observed between the time the flow was stopped and the time at which the drop ends were pinched off.

Figures 5.2 and 5.3 include data for drops in several different flow types. Approximate error bars are shown on Figure 5.2. Uncertainties in the time axis arose because the operator of the experiment had to simultaneously trigger the photograph and signal the program to record the time at which the picture was taken. Since the operator was also occupied adjusting the focus of the camera and experimental parameters such as the window size and threshold value, there was some margin for error. Errors were generally more significant for low viscosity ratio drops, as the critical Capillary number was larger and the drops fragmented more quickly when the flow was stopped.

Due to a weakness (since corrected) in the computer program used to run the experiment, the time origin of all the plots of L/a vs. dimensionless time in this manuscript (the time at which the shear rate was first increased to the critical value) was not accurately determined. Consequently, the origins for the different experimental runs shown in each such figure were adjusted to cause the steeply sloping portions of the curves to coincide. This adjustment affects only the relative positions of the curves, and has no effect on the curve shape. Excellent agreement between the shapes of the curves for different flow types was obtained, indicating that our choice of $G_c \alpha^{1/2} t$ as the dimensionless time is appropriate for the period when the flow was on. This agreement also indicates that the nature of the transient deformation is roughly independent of flow type for strong flows.

As noted in Section 5.1.1, an infinite cylindrical thread in an axisymmetric extensional flow extends exactly as would a fluid element in its place. Thus if the "length" L of this infinite thread is considered to be the distance between two

particular fluid elements in the thread, log L/a (where a represents their initial separation) varies linearly with $G_c\, t$, with a slope of unity. The time dependent behavior of L/a for threads formed by deforming drops in two-dimensional flows (c.f. Figure 5.2) was considerably different for two reasons. First, at low elongation, the growth rate was much slower due to the resistance to deformation caused by the curvature of the ends of the drop. As the drops became more deformed, the influence of the ends decreased, and the extension rate increased. For elongation ratios greater than about five, the slope of log L/a versus $G_c\, \alpha^{1/2} t$ was essentially constant, indicating that deformation-resisting effects of the drop ends were negligible once that elongation ratio was attained. In Figures 5.2 and 5.3, these constant slopes were 0.47 and 0.64, respectively. These are lower than unity, the value that would be observed in axisymmetric extensional flow, because in two-dimensional flow, compression in a plane perpendicular to the extensional axis is along parallel lines, while in an axisymmetric flow, compression is directed radially inward. Consequently, the cross section of the drop was not circular in two-dimensional flow, and the constant volume constraint prevented the length of the drop from elongating at the extension rate of the imposed flow.

5.2.1 Intermediate and High Viscosity Ratio Drops

For drops with viscosity greater than about 0.02 times that of the suspending fluid, the appearance of the drops elongating in a flow held constant at the critical Capillary number was nearly independent of viscosity ratio. In these cases, burst of the drop (defined as the point at which no steady shape was possible) occurred at moderate drop deformation, and its initiation was signalled by the appearance of flat sides on the deformed shape. As the drop was elongated in the critical flow, its sides became concave, and its ends somewhat bulbous.

When the drop was extended to about five times its original diameter, the width of the central two-thirds of the drop was essentially constant at a given instant. As for the low viscosity ratio drops, no capillary waves were visible and no breakup occurred while the flow was on, up to the highest elongation ratios investigated in our experiments (approximately 12).

Figures 5.4 and 5.5 show photographic sequences of the transient behavior of drops of viscosity ratios 0.046 and 12.8, respectively. Despite the 250-fold difference in viscosity ratio, the shapes of the drops were remarkably similar while the drops were elongating in the critical flow. These shapes are shown in the first four photographs of each set. The final four photographs in the two figures show the behavior of the extended drops after the flow was turned off. As can be seen, similarities in behavior between the two viscosity ratios ended when the flow was stopped. Since the degree of elongation when the flow was stopped was comparable in the two cases, this difference was evidently due to viscosity ratio effects.

In the lower viscosity ratio case, shown in Figure 5.4, the drop ends started to approach a spherical shape when the flow was stopped, but were pinched off nearly immediately. This process repeated itself, with the new drop ends beading up and pinching off, and the drop thus appeared to be breaking up by shedding its ends. In another experiment with the same fluids, a drop was allowed to extend to approximately eleven times its undeformed diameter. In that case, capillary waves were observed to grow on the central, cylindrical portion of the drop, and breakup was through a combination of the growth of these varicosities and the end-pinching mechanism.

In the high viscosity ratio case illustrated in Figure 5.5, the motion of the drop after the flow was turned off was strikingly different. The drop ends again

formed nearly spherical beads, but rather than breaking off, these ends were pulled toward the drop center, engulfing the cylindrical portion of the drop as they moved. The diameter of the central portion of the cylinder remained essentially constant until the separation between the drop ends was approximately equal to the initial drop diameter. In the example shown in Figure 5.5, the drop returned to the spherical shape without breaking up. In another experiment with the same fluid system, the drop was allowed extend to approximately eleven times its initial diameter before the flow was stopped. In that case, the initial behavior was very similar, with the drop ends becoming spherical and starting toward the center, but the drop extension was large enough that capillary waves had sufficient time to grow to the point that they caused breakup before the drop could return to the spherical shape. The breakup was further from the drop end in that case than was observed when breakup was through the end- pinching mechanism.

In attempting to explain the difference in behavior between the intermediate viscosity ratio drops ($\lambda < 3$) and high viscosity ratio drops, several possibilities come to mind. One possibility is that some viscosity-ratio-dependent detail of the drop shapes at the point of flow stoppage causes the difference in behavior. For several reasons, this seems unlikely. First, for viscosity ratios where the end-pinching behavior occurs, it occurs for any (reasonably large) elongation ratio, and details of the shape (e.g., the ratio of the size of the bulbous ends to the diameter of the cylindrical central portion) depend more on the degree of extension than they do on viscosity ratio. Second, the end-pinching process repeats itself on the central portion when the original drop ends are pinched off. This suggests that the pinching process does not depend on a particular starting shape.

A more plausible explanation is that the viscosity-ratio-dependent behavior is caused by differences in the dynamics which arise from differences in the relative viscosities of the drop and continuous phases. To illustrate this concept, we consider the normal stress jump across an interface of the shape shown in Figure 5.6, which is typical of the drop shapes soon after the flow was turned off. The expression for the normal stress jump is given by:

$$[\mathbf{T}\cdot\mathbf{n}] = \sigma\left[\frac{1}{R_1}+\frac{1}{R_2}\right] = \frac{\sigma}{(1+f'^2)^{1/2}}\left[\frac{1}{f}-\frac{f''}{1+f'^2}\right] \tag{5.1}$$

where we have considered the surface to be axisymmetric and f' and f'' are the derivatives of the shape function f with respect to distance along the drop axis. The normal stress jump is plotted qualitatively in Figure 5.6. It is highest near the end of the drop where the radius of curvature is concave in planes both parallel and perpendicular to the drop axis, and goes through a minimum with decreasing x because the drop surface in the plane parallel to the drop axis becomes convex. In the central cylindrical portion of the drop, the normal stress jump approaches a constant. To get a qualitative idea of the flow driven by this normal stress jump, we make the approximation that the fluid is static (so the normal stress jump is just a pressure jump) and then consider the fluid motion driven by the pressure gradient caused by the interfacial tension.

The pressure gradient will induce fluid flow both from the end of the drop and from the center cylindrical region. However, the flow from the end of the drop can occur without large velocity gradients in the internal fluid, since the drop end can essentially translate without a large change in shape. Thus the motion is mostly damped by the outer fluid. Flow of the drop ends towards the pressure minimum causes the convex region (and hence the pressure minimum) to move toward the drop center as well, so the driving force for continued end movement is maintained. The dynamics of the flow from the central portion of

the drop towards the pressure minimum are different because this flow requires a velocity gradient in the inner fluid as the fluid at the drop center is stagnant. Thus this motion is inhibited by the drop fluid viscosity.

The behavior observed in our experiments can then be explained as follows. In high viscosity ratio systems, the ends are drawn toward the middle as described above, with this motion damped mostly by the outer fluid. Drainage from the center portion is comparatively slow since it is damped by the higher inner fluid viscosity. Consequently, movement of the pressure minimum accompanying the end movement is such that the flow from the central region is too slow to cause a "neck" to form in the shape, and the ends do not pinch off. In contrast, in lower viscosity ratio systems, fluid flows readily from the central portion to the pressure minimum. This causes a a local minimum in drop radius. The pressure jump at this point is thus increased, accelerating the drainage and eventually causing the ends to pinch off.

It is worth noting that the end-pinching process occurs faster than growth of capillary waves on the central cylindrical portion of the drop since a cylindrical shape is an (unstable) equilibrium conformation. Capillary waves in this region are thus the result of growing instabilities, while the the pinching flow near the drop ends arises from a nonequilibrium shape. This is why the initial breakup of intermediate viscosity ratio drops appears to be caused by shedding of the drop ends.

Figure 5.7 through 5.14 show plots of L/a versus dimensionless time for viscosity ratios of 0.046, 0.12, 0.26, 0.63, 1.38, 2.43, 6.1, and 12.8, respectively. In each case, the curves for several different elongating drops are shown. Agreement in the shape of the curves for different flow types indicates that the qualitative aspects of the elongation and breakup process are not sensitive to flow

type. This is in agreement with our observation that the shapes of the drops were essentially identical in different flows with the same viscosity ratio.

In Figures 5.7 through 5.14, the slopes of L/a versus $G_c \alpha^{1/2} t$ were nearly identical in the steeply sloping portion where L/a was greater than five. These slopes are shown in Table 5.1. As can be seen, excluding the slope for $\lambda = 0.012$, which was the least accurately measured, all of the slopes were within 10% of the mean of 0.64. Thus the theoretical result that highly extended drops extend with the suspending fluid regardless of viscosity ratio is qualitatively confirmed, taking into account the difference between the axisymmetric flow considered in the theory and the two-dimensional flow used in our experiments.

In conclusion, we point out that our transient experiments, though few in number, revealed some interesting features of the drop breakup process which may justify further research. Some possible topics include:

1. Further investigations into the effect of different flow histories on drop breakup would be useful for practical applications where the final drop size distribution resulting from breakup is of primary interest. Our experiments were limited to slow increases in the shear rate to the critical value, with the flow then held constant until it was turned off. Different approaches to a bursting condition, for example step or fast ramping increases in the shear rate, may yield different breakup behavior. Increasing the shear rate past the critical value has been shown (Grace [1971]) to dramatically effect the drop fragment size distribution. Grace also performed a few experiments in which the drop was extended for a short period at the critical shear rate, and then the shear rate was reduced in a such a way as to keep the drop length constant. This also changed the drop size distribution. One problem with experiments in this area would be

choosing a useful shear rate profile from among the many possibilities. One helpful result of our experiments was that it is probably unnecessary to consider flow type as an independent parameter, at least for strong flows.

2. More conclusive studies of the effect of the magnitude of the drop elongation when the flow is stopped would be of interest, particularly determination of the critical elongation required for drop breakup as a function of viscosity ratio. One interesting possibility is that the highly deformed steady shapes observed for low viscosity drops may actually break up when the flow is stopped. Also of interest would be a more careful observation of the interfacial-tension-driven motion of elongated drops after the flow is turned off. Use of motion picture photography with tracer particles in the drop fluid would be useful for determining whether the explanation for the viscosity-ratio dependence of the breakup behavior offered above is correct. Numerical studies of the interfacial-tension-driven flow, using the boundary integral technique, could perhaps be used to determine whether the flow is sensitive to details of the shape at the time the flow is stopped.

Table 5.1 - Elongation Rates

viscosity ratio	slope [1]
0.012	0.47
0.023	0.64
0.046	0.59
0.12	0.67
0.26	0.64
0.63	0.65
1.38	0.65
2.43	0.63
6.1	0.69
12.8	0.56

[1] Slope of L/a vs. $Gc\ \alpha^{1/2} t$

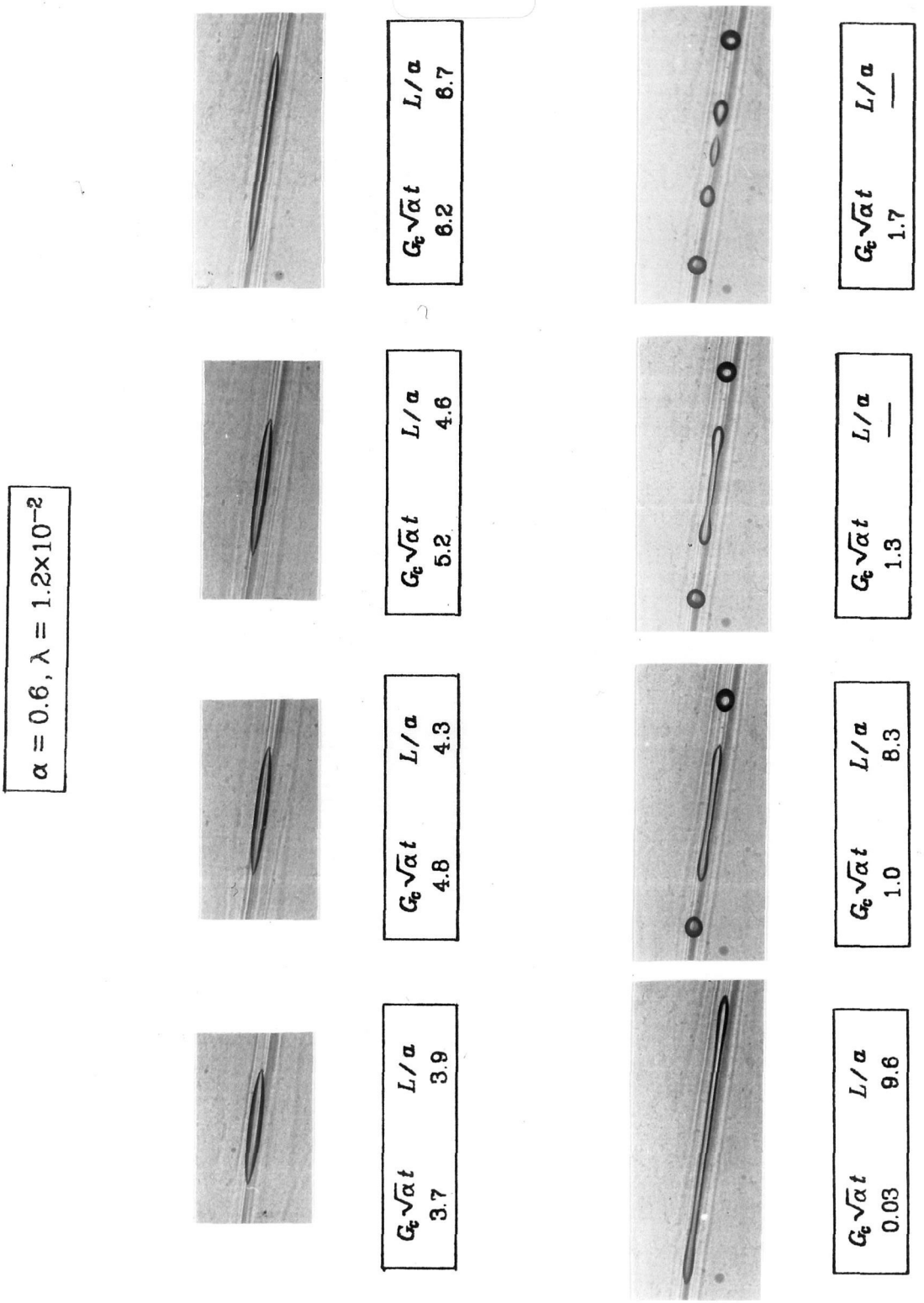

Figure 5.1
Sequence of drop deformations for $\lambda = 0.01$, $\alpha = 0.6$. First four photographs were taken with the flow at the critical Capillary number, and the final four were taken with the flow off.

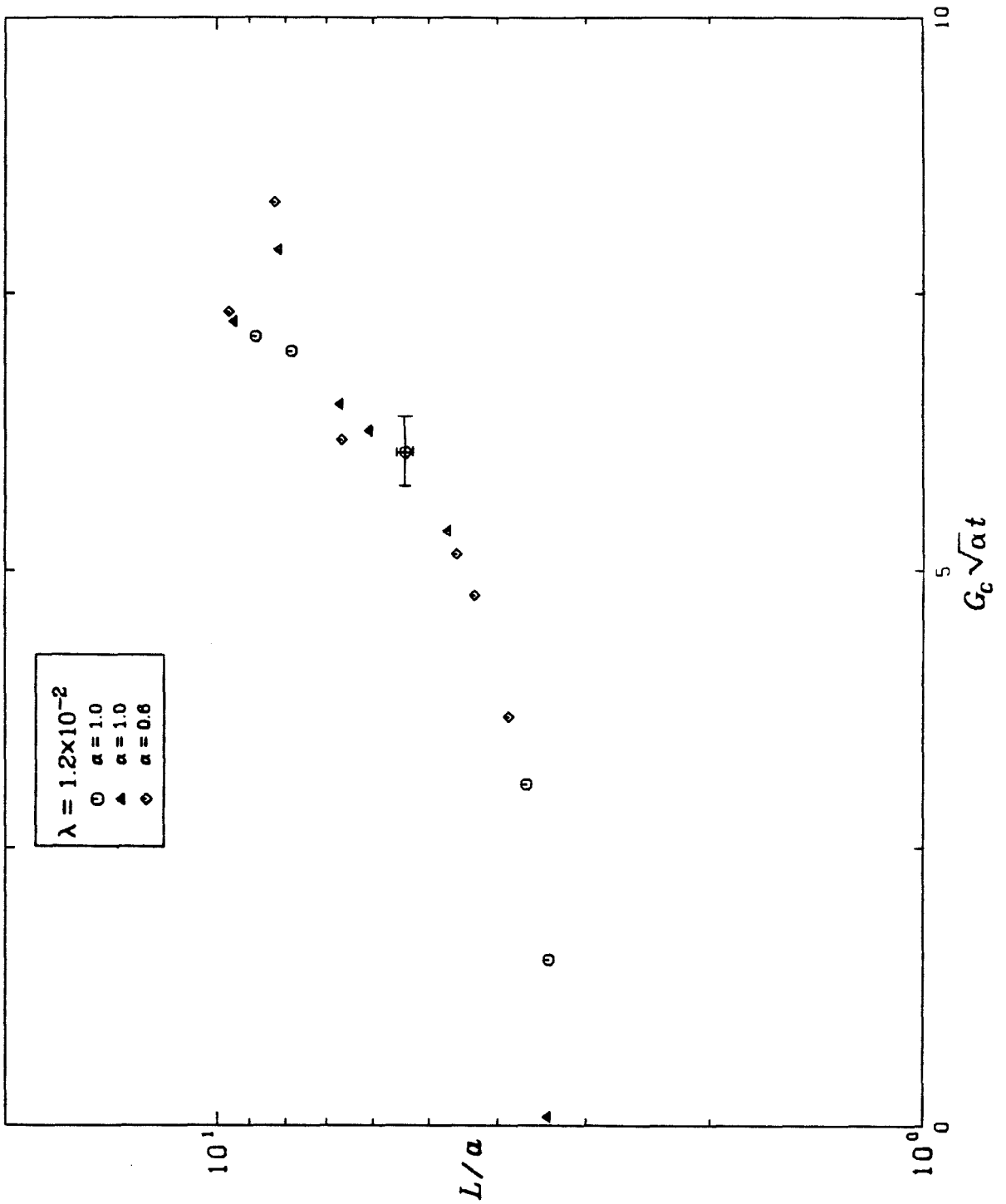

Figure 5.2
Dimensionless length versus time for $\lambda = 1.2\times10^{-2}$. The maxima in L/a occur at the point at which the flow is turned off

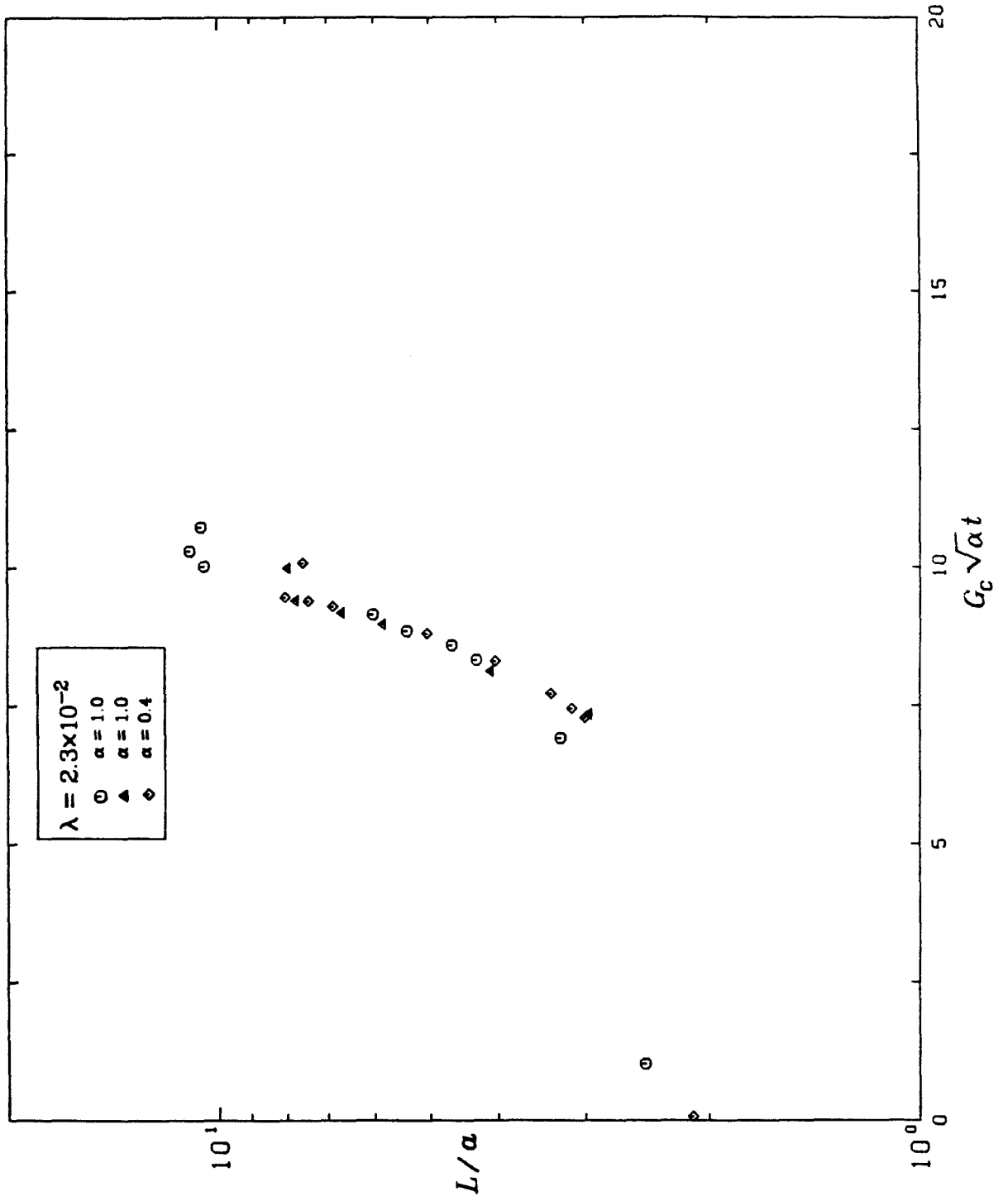

Figure 5.3
Dimensionless length vs. time for $\lambda = 2.3\times10^{-2}$.

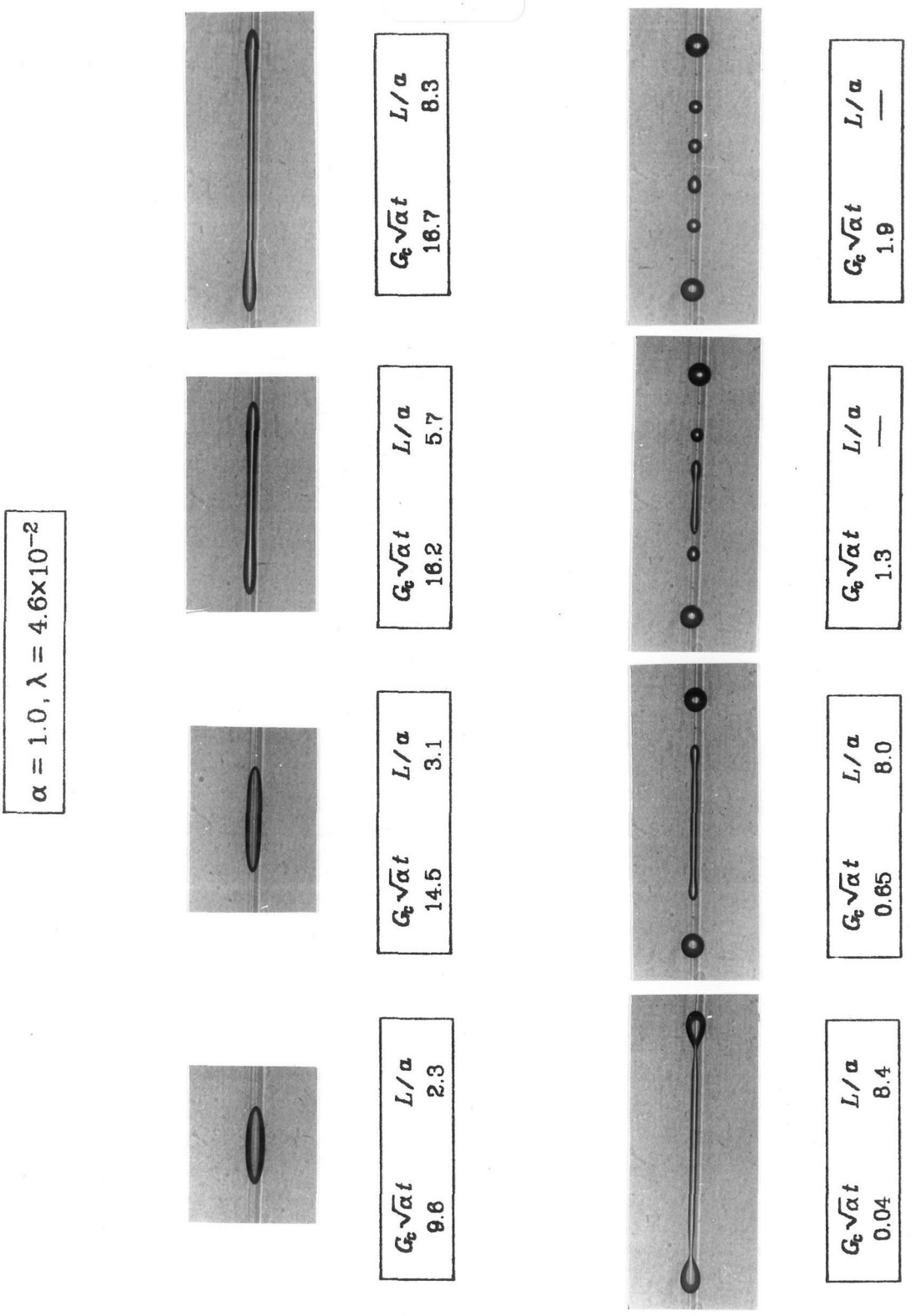

Figure 5.4
Time-dependent drop deformation for $\lambda = 0.046$, $\alpha = 1.0$. The flow was on for the first four photographs and off for the last four photographs. Times in the last four photographs are relative to the time at which the flow was stopped.

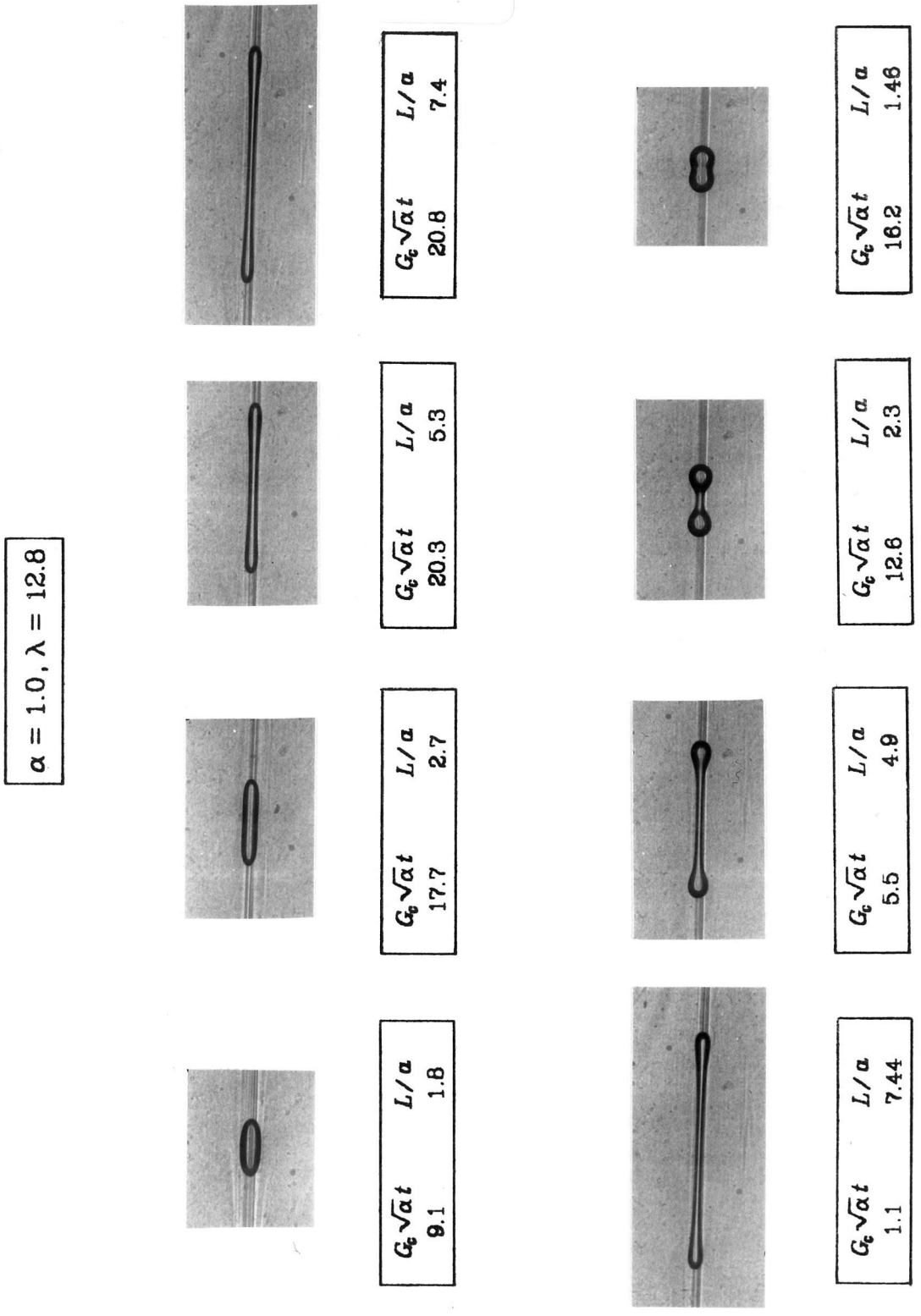

Figure 5.5
Time-dependent drop deformation for $\lambda = 12.8$, $\alpha = 1.0$. The first four photographs were taken with the flow on, and the last four were taken with the flow off.

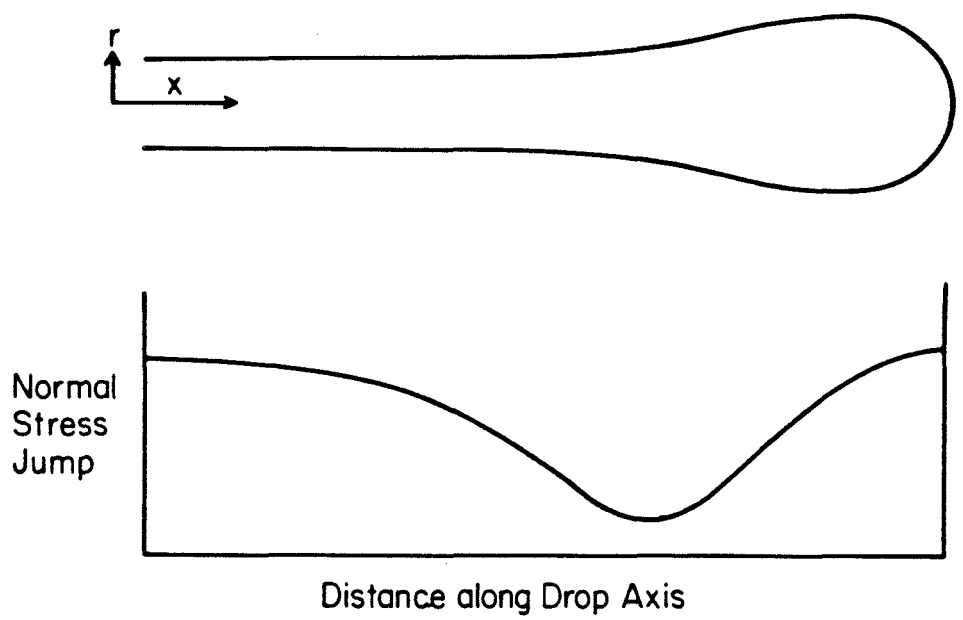

Figure 5.6
Typical drop shape shortly after flow stopped, and approximate normal stress jump across interface.

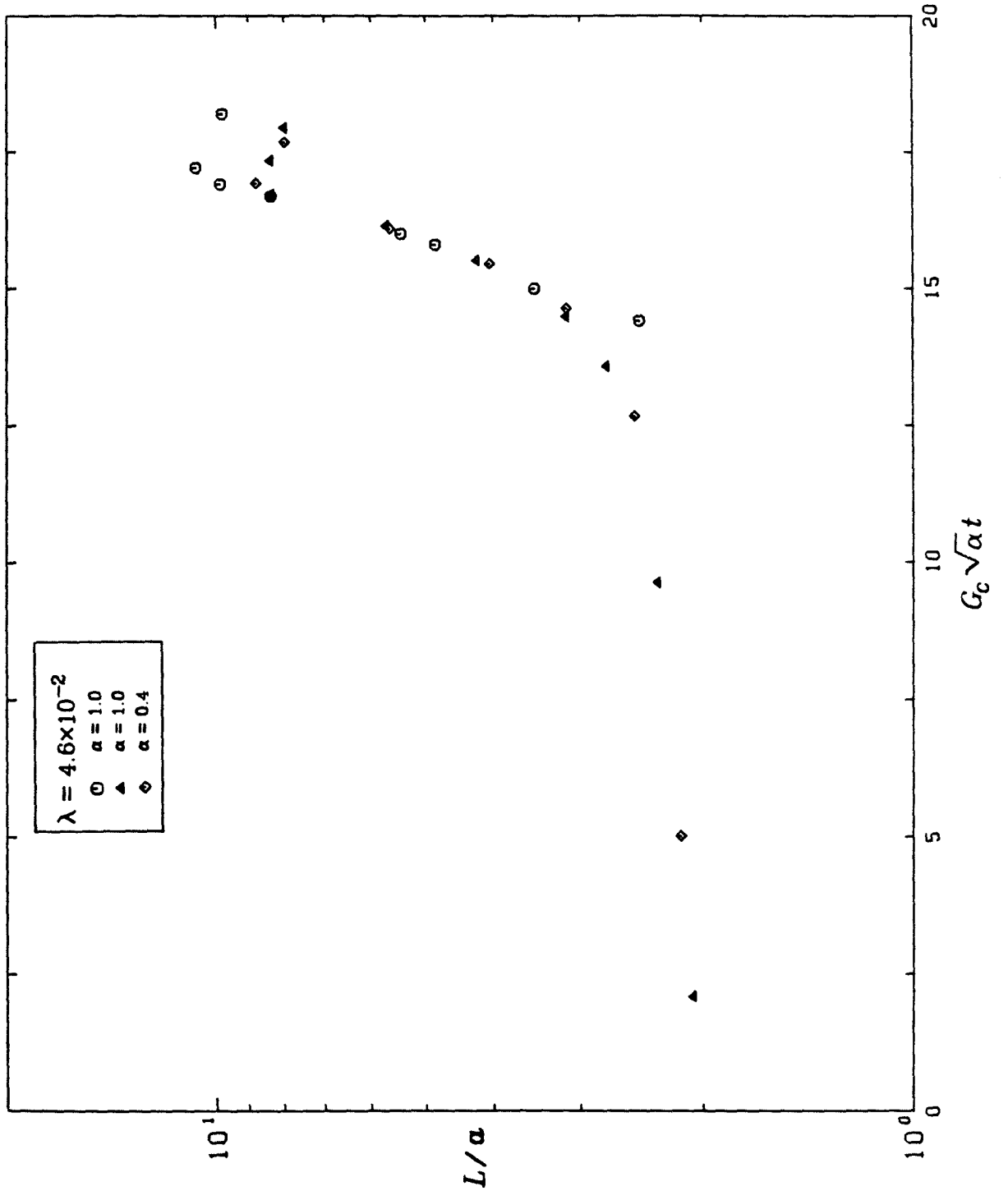

Figure 5.7
Dimensionless length vs. time for $\lambda = 4.6\times10^{-2}$.

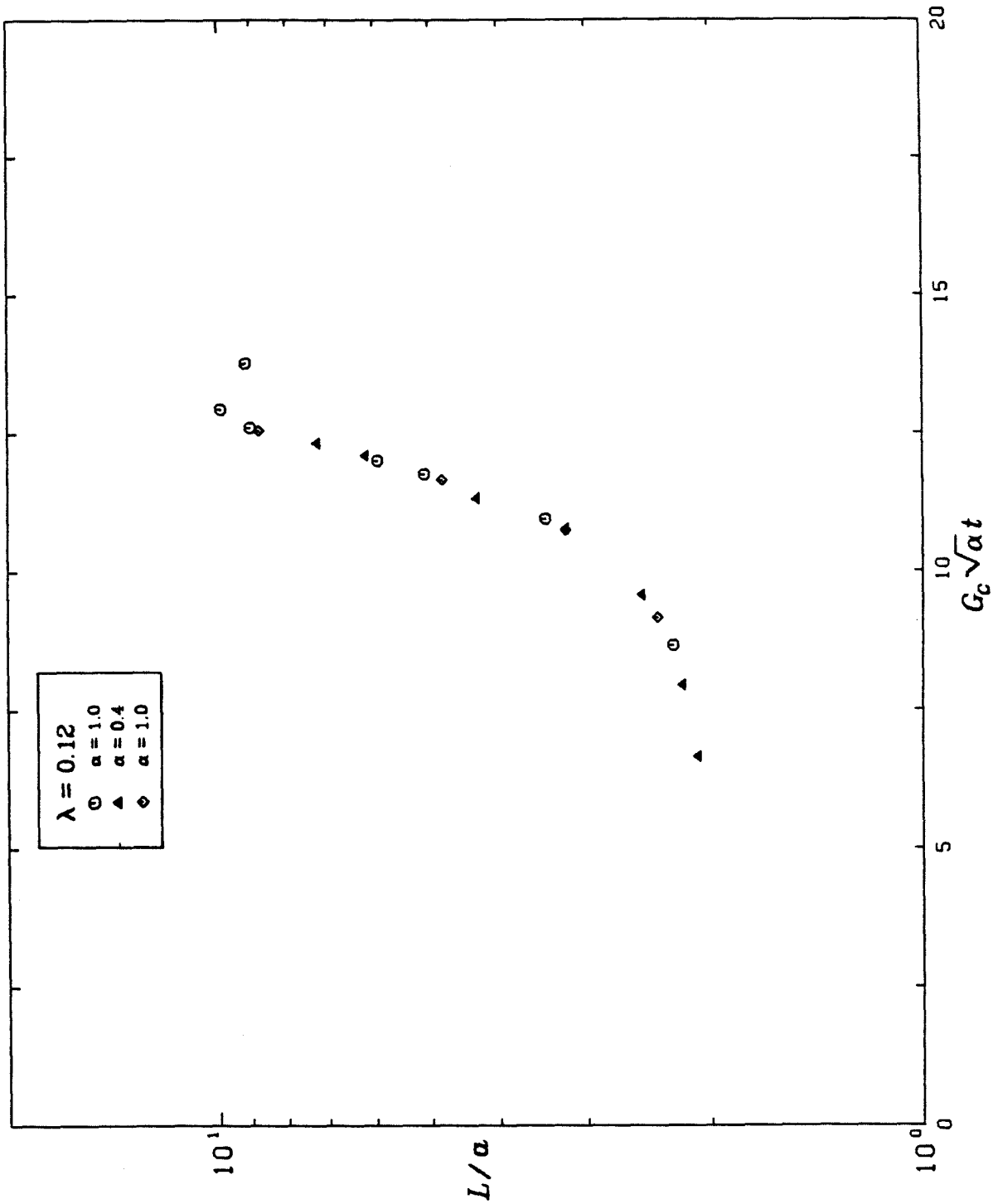

Figure 5.8
Dimensionless length vs. time for $\lambda = 0.12$.

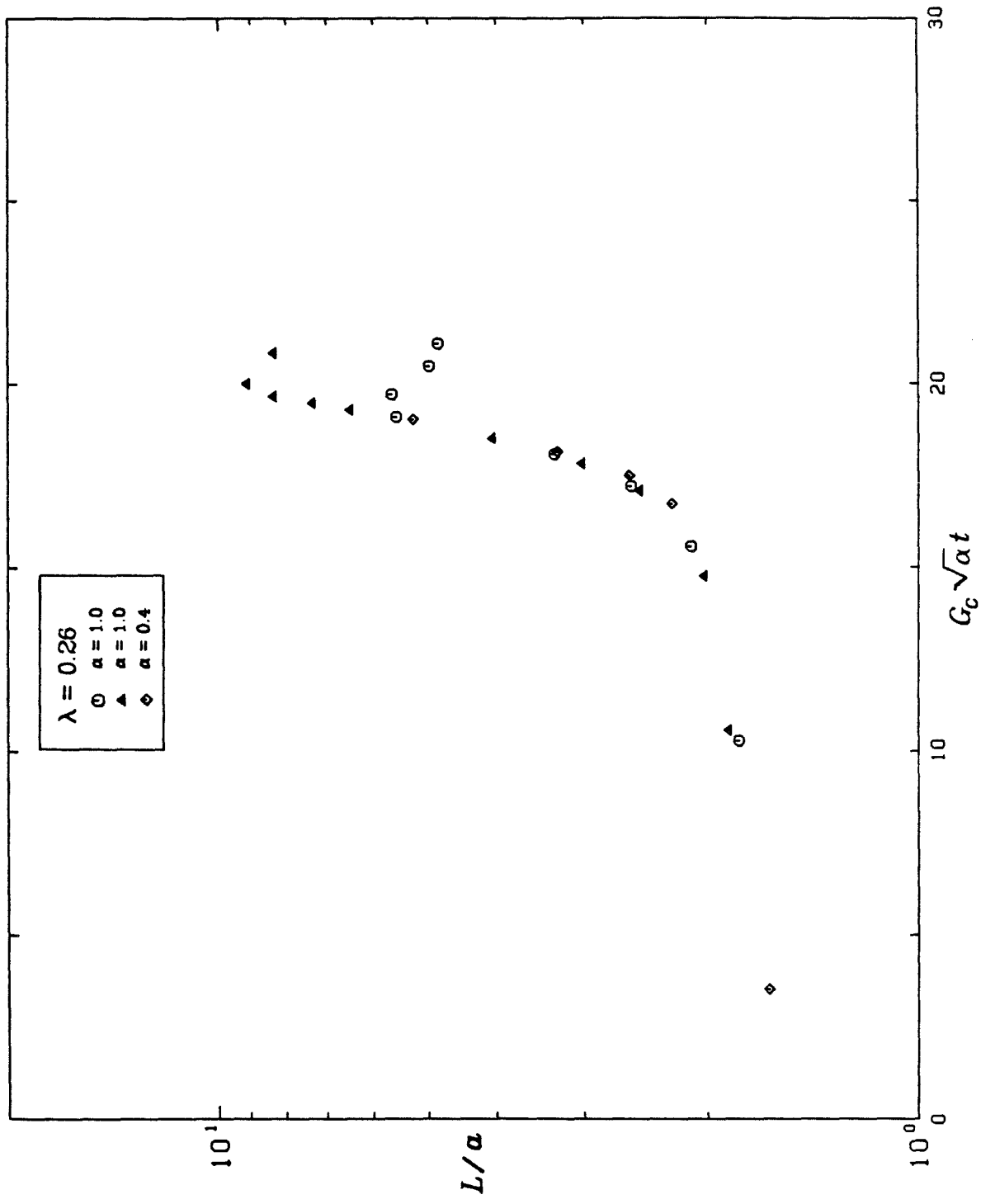

Figure 5.9
Dimensionless length vs. time for $\lambda = 0.26$.

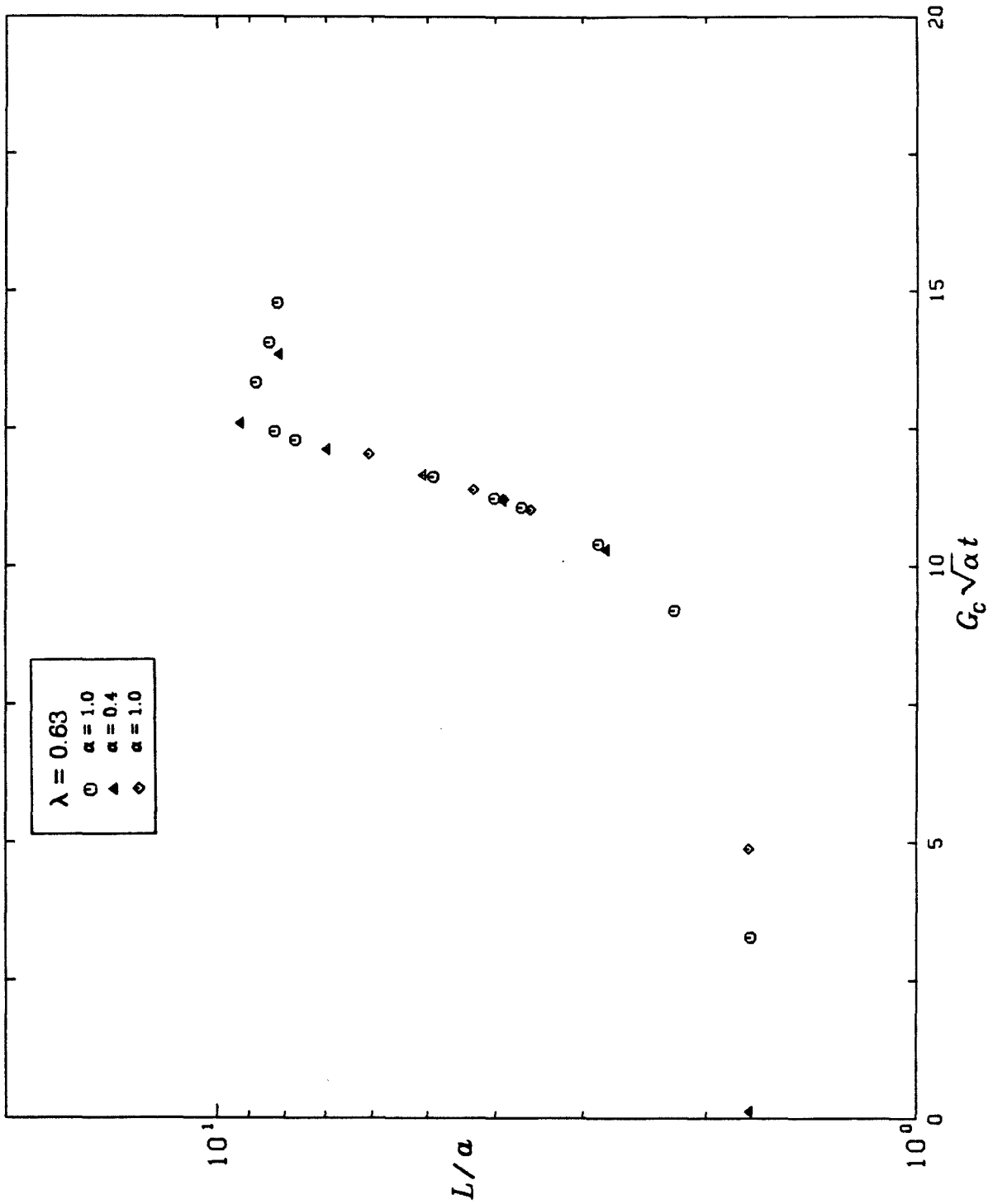

Figure 5.10
Dimensionless length vs. time for $\lambda = 0.63$.

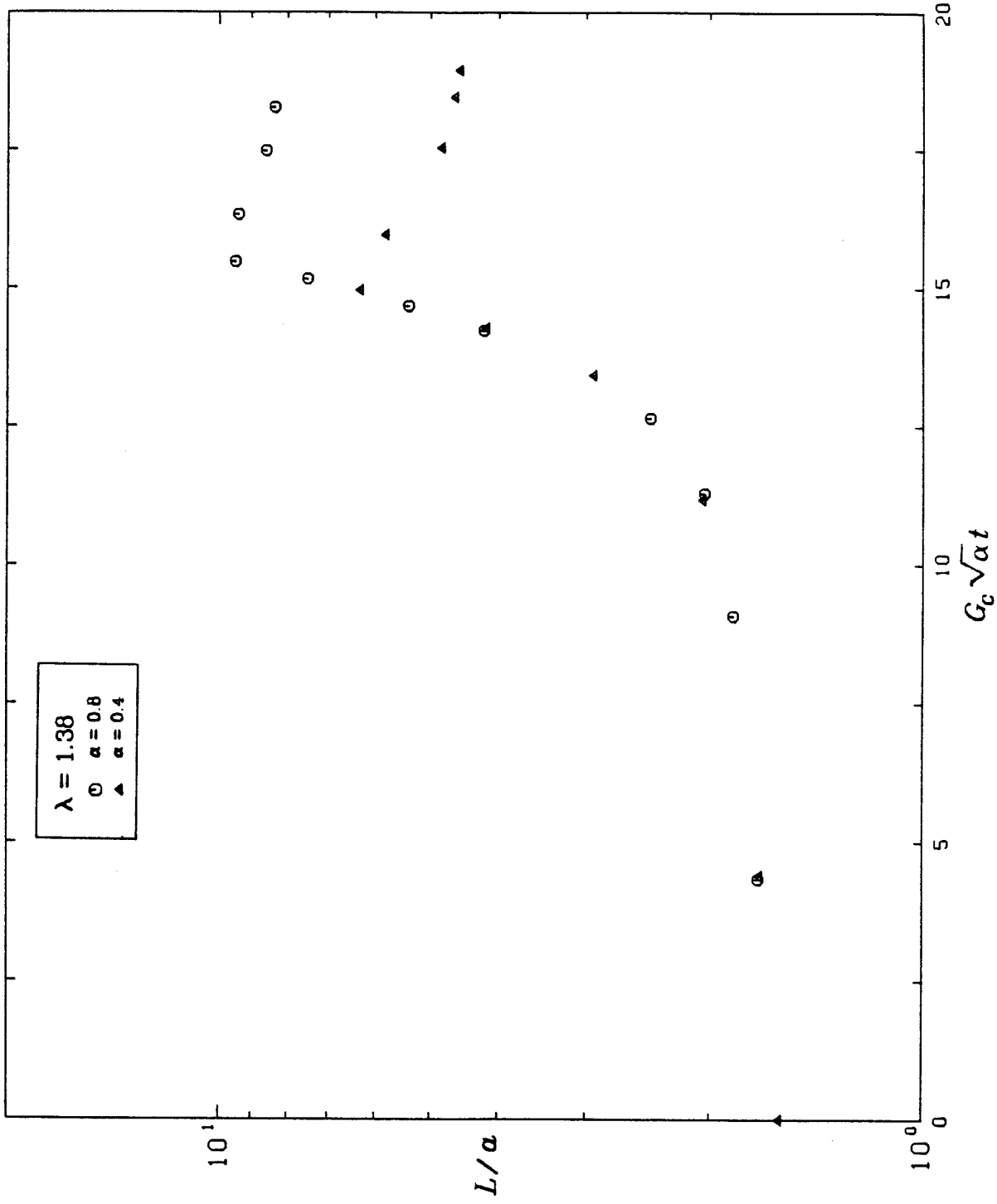

Figure 5.11
Dimensionless length vs. time for λ = 1.38.

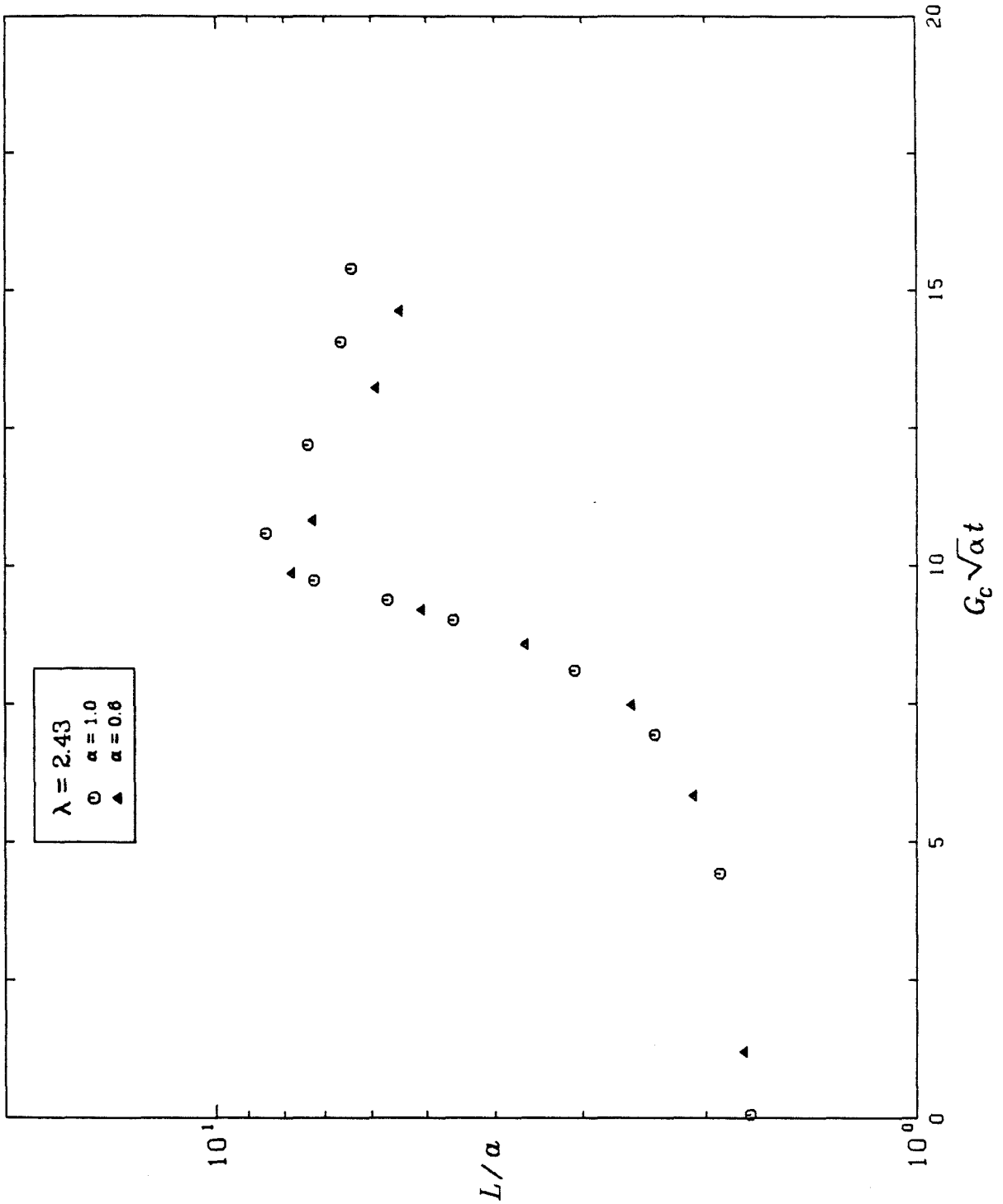

Figure 5.12
Dimensionless length vs. time for $\lambda = 2.43$.

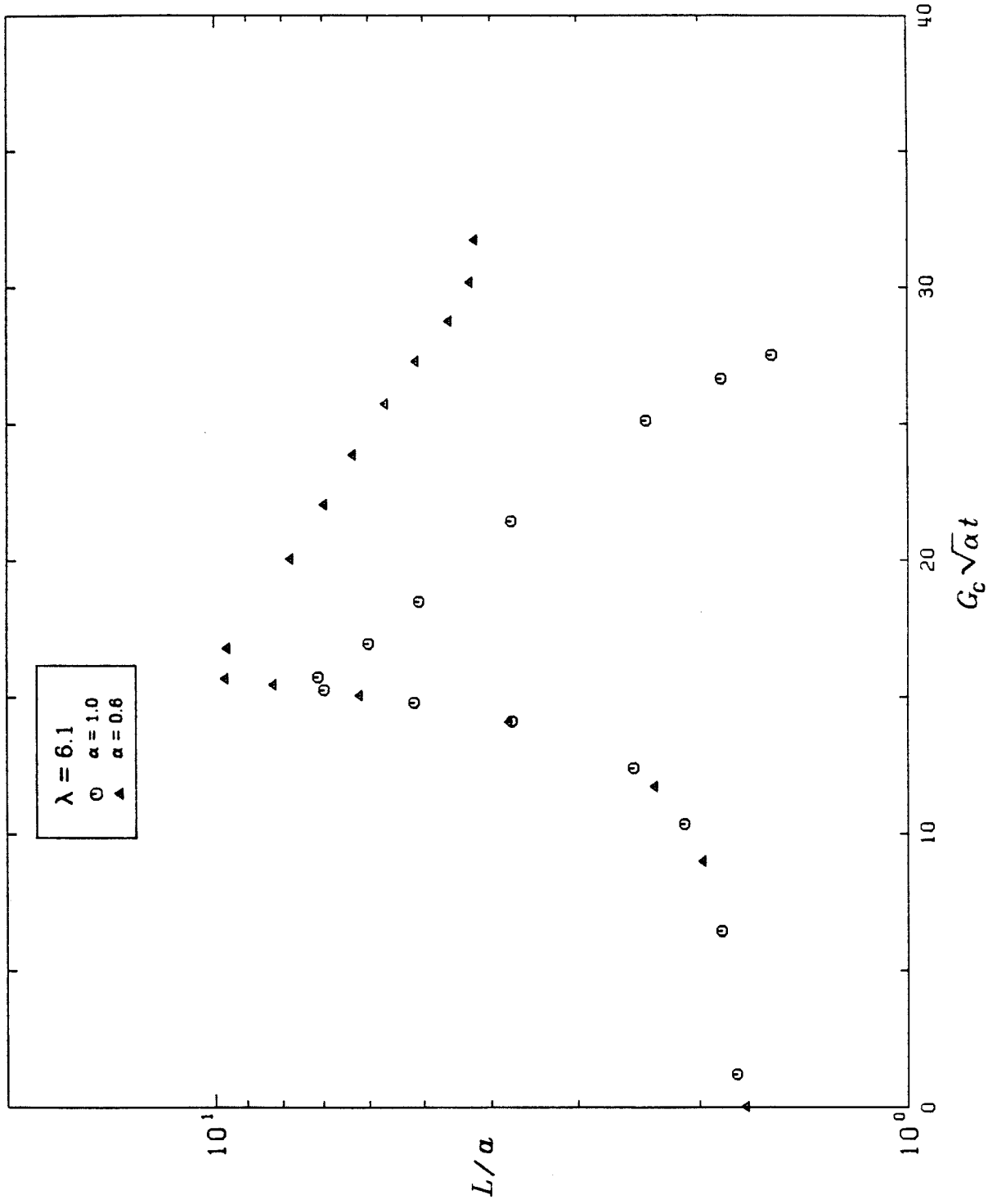

Figure 5.13
Dimensionless length vs. time for λ = 6.1.

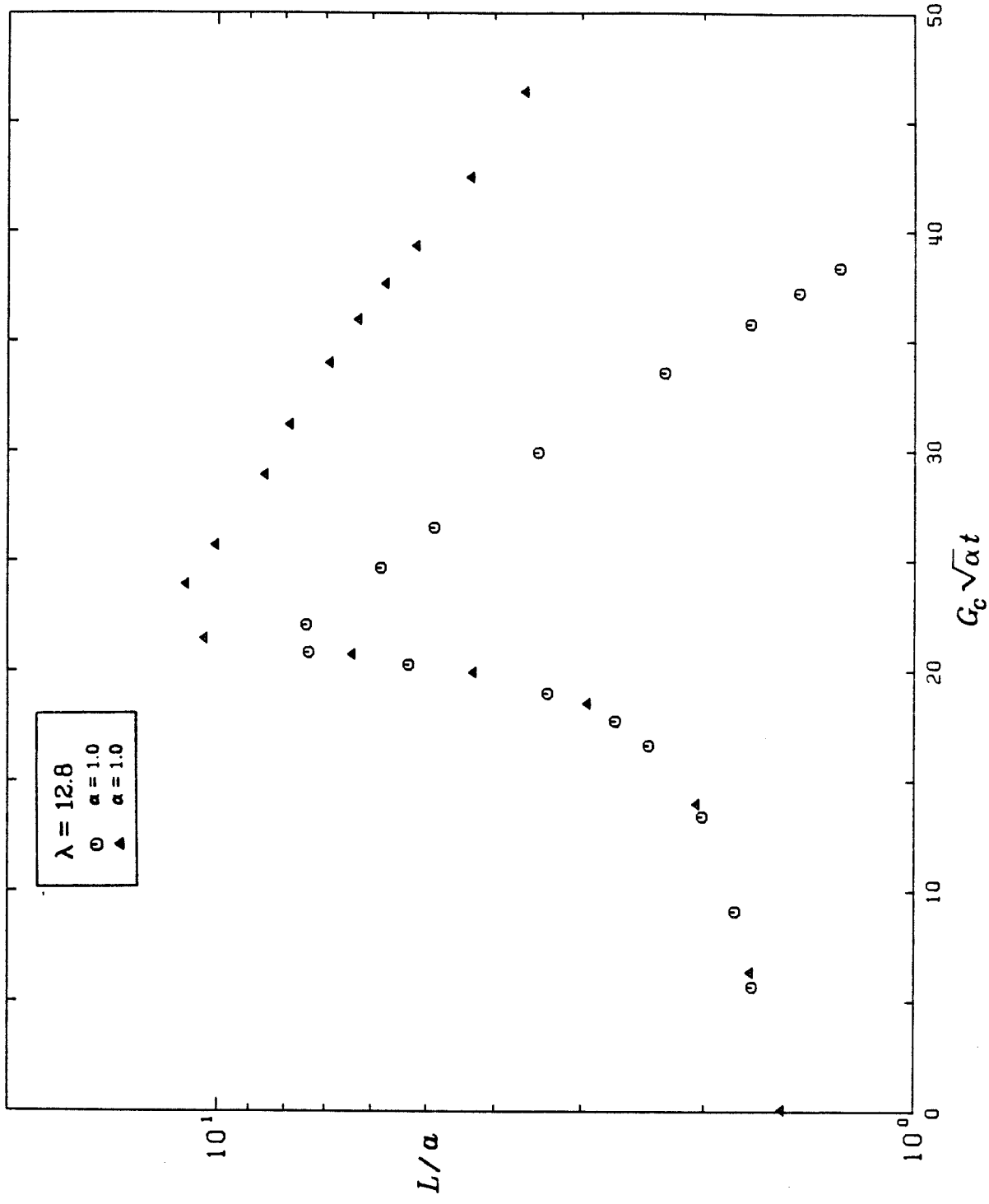

Figure 5.14
Dimensionless length vs. time for λ = 12.8

6.0 SUMMARY

The first part of this thesis described the design and construction of a flow device known as a four roll mill. The immediate objective for the apparatus was to investigate the deformation and burst of fluid drops suspended in a second fluid undergoing a steady linear shear flow. The four roll mill was chosen because it is capable of generating flows with arbitrary ratio of vorticity to strain rate. Experiments in the flows of most interest, the so-called strong flows where the magnitude of the strain rate is greater than that of the vorticity, had not been previously attempted (except for one specific such flow) due to the difficulty in controlling the drop at the lone stagnation point in such flows. To overcome this obstacle, we devised a computer-based control system to keep the drop at the device center. A digital closed-circuit television camera was interfaced to a laboratory computer to serve as the sensor in the control scheme, and the DC stepping motors which turned the rollers were interfaced to the computer to serve as the actuator. A model for the drop's response to flow field changes and the flow field's response to roller speed changes was developed and tested experimentally. An inferential feedback control system based on this model was successfully implemented. The apparatus was capable of keeping a particle or drop within 0.1 cm of the device center in flows with shear rates up to 5 sec^{-1} and flow type from 0.2 to 1.0.

We used the apparatus described above to study drop deformation and the burst in Newtonian systems. However, there are other applications for the same apparatus. Obvious extensions include investigations of drop deformation and burst in systems where the drop and/or suspending fluid are non-Newtonian. The apparatus is also ideal for studying the effects of transient flow fields on drop behavior. Other less related possibilities include investigation of the orbits

of solid particles in flows with arbitrary vorticity to strain ratio, and investigations of the coalescence of emulsions in straining flow. In the latter case, one fluid drop could be held stationary at the stagnation point while another drop approached it.

There are other experiments which could benefit from the control technology developed for the four roll mill. A very similar control scheme could be implemented to maintain a drop at the stagnation point in a device designed to produce axisymmetric extensional flows (e.g., a device with opposing tubes producing positive flow for biaxial extension or negative flow for uniaxial extension). Another class of applications would be in fluid flow experiments where it is desirable to make observations in a frame of reference which translates with a solid or deformable body. In some situations it would be possible to have a computer control the motion of the observation equipment (i.e., a camera) to keep the body in the center of the observation field.

A related application that may become feasible in the next few years is to interface a more sophisticated digital camera to a computer to record the shape of a deformable body. For this use, the resolution of the camera would have to be considerably better than that of the camera used in our experiments, and in most cases the gray-level information (which was simply compared to a threshold to yield light-dark information in our experiment) will have to be retained for more complex processing. If the camera is used for data acquisition only, and not for control purposes, longer frame times (the time necessary to get a complete picture from the camera to the computer) would be acceptable, although they would still have to be fast compared to the time scale for changes in the features being observed. Should the technology become available and affordable, a computer could be used to store and process the shape

data, considerably speeding up the task of reducing photographic data to numeric results. In the case of drop deformation experiments, this would also make it possible to do more sophisticated quantitative comparisons between the theoretical and observed drop shapes than the simple scalar comparisons used in this work.

The second portion of the thesis discussed the results of our drop deformation and burst experiments. Our goals for the experiments were to investigate the effect of flow type on drop deformation and burst, and to determine the range of applicability of several asymptotic drop deformation and burst theories. Accordingly, we performed experiments covering viscosity ratios from 0.001 to 25 for flow types with α = 1.0, 0.8, 0.6, 0.4, and 0.2. The small deformation theory of Barthes-Biesel and Acrivos [1973a] was applied to these flow fields and compared to the observations. A slightly modified version of the large deformation theory of Hinch and Acrivos [1980] was compared to the results for small viscosity ratios. In addition, the numerical results of Rallison [1981] were compared to the experiments. Our conclusions can be summarized as follows:

Effect of Flow Type on Drop Burst

For viscosity ratio less than unity, the Capillary number required for burst and the deformation at the point of burst both decreased with increasing viscosity ratio for all strong flows. In our experiments in irrotational flow, Ca_c approached a constant value with further increases in the viscosity ratio. This is in agreement with the predictions of the small deformation theory and with the numerical results of Rallison and Acrivos [1978] for axisymmetric flows, but disagrees with the observations of Grace [1971], who reported an increase in Ca_c with viscosity ratio for high viscosity drops in the same flow. We believe that the

computer control used in our experiments allowed more accurate measurements, particularly for the high viscosity ratio cases for which conflicting results exist.

When vorticity is present in the flow, Ca_c goes through a minimum at a viscosity ratio about 1.0, and increases steadily with viscosity ratio above that point. For α = 0.4,0.2, and 0.0, there is a viscosity ratio above which no burst is possible.

Small Deformation Theory

The small deformation theory gives adequate predictions for drop deformation for $\lambda \geq 0.05$. The $O(\varepsilon^2)$ version of the theory generally gives better predictions for the deformation than does the $O(\varepsilon)$ theory, and always gives better predictions for the critical Capillary number at which drop burst occurs. The $O(\varepsilon^2)$ theory predicts the qualitative features of drop burst with surprising accuracy for viscosity ratios greater than about 0.05. The agreement is for all flow types investigated in our experiments and for simple shear. In particular, the theory correctly predicts a limiting viscosity ratio above which drop burst is impossible for α = 0.2 and 0.0. It can be used for quantitative estimates of Ca_c, accurate to within about 30%, for the two-dimensional flows we considered when $\lambda > 0.05$.

Large Deformation Theory

The large deformation theory gives adequate predictions for drop shape and burst for $\lambda < 0.01$. The lowest viscosity ratio considered in our experiments was 0.001, and in that case the predictions for Ca_c and L/a at burst were accurate to within about 15% for all α. It is expected that the agreement would improve

for lower λ, since the slenderness of the drop increases with decreasing λ.

Numerical Results

The numerical calculations for $\lambda = 1$ are in good agreement with the data for Ca_c. The predicted critical deformations do not agree nearly so well with our observations, but the accurate experimental determination of $D_{f,c}$ is difficult. Numerical results for other viscosity ratios are not yet available for the flows we studied.

The final part of this thesis discussed the transient experiments we performed. These were limited in scope, but revealed some interesting phenomena. Drops extending at the critical shear rate were stabilized by the flow field. When the flow was turned off, capillary waves appeared. For low and intermediate viscosity ratios, these varicosities grew and eventually caused the drop to fragment. For high viscosity ratios, the drops sometimes returned to their initial spherical shape through a complex motion, depending on the degree of extension when the flow was turned off.

There are a wide variety of transient drop phenomena which could be investigated in the existing apparatus. Our investigations were limited to the motion of drops with the flow held constant at the critical shear rate for breakup. The drops were allowed to extend until their length was approximately ten times their initial diameter, and then the flow was turned off. More extensive experiments along the same lines could include a systematic study of the effect of the elongation ratio and/or the effect of supercritical shear rates on the final conformation (number and size of drop fragments). In such experiments, the transient motion should be followed through motion picture or video tape photogra-

phy. Lack of a suitable camera - lens combination prevented us from doing this in our experiments, so we were limited to taking still photographs at intervals.

Another largely-unexplored class of transient phenomena involves studying the drop deformation and burst pattern in an unsteady flow . In our deformation experiments, the flow type was held constant during a run, and the shear rate slowly increased so that the drops went through a series of equilibrium deformations. In most dispersion equipment, the flow type and shear rate seen by a drop vary with time. Thus experiments with time- dependent flows would be of considerable practical interest. Several well-defined transient experiments suggest themselves. The simplest would be to "step" the shear rate from some initial to some final value. There are experimental and theoretical indications (Torza, Cox, and Mason [1972], Hinch and Acrivos [1980]) that this can cause breakup in simple shear even if the final value is below the shear rate required for burst when the shear rate in increased slowly. Similar experiments in strong flows have not been attempted because of the difficulty in controlling the drop position, an obstacle which has been essentially overcome in the computer-controlled four roll mill. More complicated shear rate sequences (such as ramped or sinusoidal shear rates) could also be generated fairly easily. It would also be possible to vary the flow type. Transient experiments such as these are currently in the planning stage (Stone [1984]).

REFERENCES

Acrivos, A. and Lo, T.S. 1978. Deformation and breakup of a single slender drop in an extensional flow. *J. Fluid Mech.* **86**:641-672.

Barthes-Biesel, D. and Acrivos, A. 1973a. Deformation and burst of a liquid droplet freely suspended in a linear shear field. *J. Fluid Mech.* **61**:1-21.

Barthes-Biesel,D. and Acrivos, A. 1973b. The rheology of suspensions and its relation to phenomenological theories for non-Newtonian fluids. *Int. J. Multiphase Flow.* **1**:1-24.

Brady, J.F., and Acrivos, A. 1982. The deformation and breakup of a slender drop in an extensional flow. *J. Fluid Mech.* **114**:443-451.

Buckmaster, J.D. 1972. Pointed bubbles in slow viscous flow. *J. Fluid Mech.* **55**:385-400.

Buckmaster, J.D. 1973. The bursting of pointed drops in slow viscous flow. *J. Appl. Mech.* **40**:18-24.

Chaffey, C.E., Takano, M., and Mason, S.G. 1965. Particle motions in sheared suspensions. XVI. Orientations of rods and disks in hyperbolic and other flows. *Can. J. Phys.* **43**:1269-1287.

Cox, R.G. 1969. The deformation of a drop in a general time-dependent fluid flow. *J. Fluid Mech.* **37**:601-623.

Frankel, N.A. and Acrivos, A. 1970. The constitutive equation for a dilute emulsion. *J. Fluid Mech.* **44**:65-78.

Fuller, G.G., Rallison, J.M., Schmidt, R.L., and Leal, L.G. 1980. The measurement of velocity gradients in laminar flow by homodyne light-scattering spectroscopy. *J. Fluid Mech.* **100**:555-575.

Fuller, G.G. and Leal, L.G. 1981. Flow birefringence of concentrated

polymer solutions in two-dimensional flows. *J. Polym. Sci. Polym. Phys. Ed.* **19**:557-587.

Giesekus, H. 1962. Stromungen mit konstantem geschwindigkeitsgradienten und die bewegung von darin suspendierten teilchen. Teil II: Ebene stromungen und eine experimentelle anordnung zu ihrer realisierung. *Rheol. Acta.* **2**:113-121.

Grace, H.P. 1971. Dispersion phenomena in high viscosity immiscible fluid systems and application of static mixers as dispersion devices in such systems. *Eng. Found., Res. Conf. Mixing, 3rd, Andover, N.H.* Republished 1982 in *Chem. Eng. Commun.* **14**:225-277.

Hakimi, F.S. and Schowalter, W.R. 1980. The effects of shear and vorticity on deformation of a drop. *J. Fluid Mech.* **98**:635-645.

Hinch, E.J. and Acrivos, A. 1979. Steady long slender droplets in two-dimensional straining motion. *J. Fluid Mech.* **91**:401-414.

Hinch, E.J. and Acrivos, A. 1980. Long Slender drops in a simple shear flow. *J. Fluid Mech.* **98**:305-328.

Lee, W.K. and Flumerfelt, R.W. 1981. Instability of stationary and uniformly moving cylindrical fluid bodies - I. *Int. J. Multiphase Flow* **7**:363-383.

Mikami, T., Cox, R.G., and Mason, S.G. 1975. Breakup of extending liquid threads. *Int. J. Multiphase Flow* **2**:113-138.

Olbricht, W.L., Rallison, J.M., and Leal, L.G. 1982. Strong flow criteria based on microstructure deformation. *J. Non-Newtonian Fluid Mech.* **10**:291-318.

Rallison, J.M. 1980. A note on the time-dependent deformation of a viscous drop which is almost spherical. *J. Fluid Mech.* **98**:625-633.

Rallison, J.M. 1981. A numerical study of the deformation and burst of a viscous drop in general shear flows. *J. Fluid Mech.* **109**:465-482.

Rallison, J.M. 1984. The deformation of small viscous drops and bubbles in shear flows. *Ann. Rev. Fluid Mech.* **16**:45-66.

Rallison, J.M. and Acrivos, A. 1978. A numerical study of the deformation and burst of a viscous drop in an extensional flow. *J. Fluid Mech.* **89**:191-209.

Rumscheidt, F.D., and Mason, S.G. 1961. Particle motions in sheared suspensions. XII. Deformation and burst of fluid drops in shear and hyperbolic flows. *J. Colloid Sci.* **16**:238-261.

Stone, H.A. 1984. *An experimental and theoretical study of drop deformation and breakup: The effect of transient flow fields and non-Newtonian constitutive behavior of the separate phases.* PhD. Candidacy Report, California Institute of Technology.

Taylor, G.I. 1932. The viscosity of a fluid containing small drops of another fluid. *Proc. R. Soc.* **A 138**:41-48

Taylor, G.I. 1934. The formation of emulsions in definable fields of flow. *Proc. R. Soc.* **A 146**:501-523.

Taylor, G.I. 1964. Conical free surfaces and fluid interfaces. *Proc. Int. Congr. Appl. Mech., 11th, Munich*, pp. 790-796.

Tomotika, S. 1935. On the instability of a cylindrical thread of a viscous liquid surrounded by another viscous fluid. *Proc. R. Soc.* **A 150**:322-337.

Tomotika, S. 1936. Breaking up of a drop of viscous liquid immersed in another viscous fluid which is extending at a uniform rate. *Proc. R. Soc.* **A 153**:302-318.

Torza, S., Cox, R.G., and Mason, S.G. 1972. Particle motions in sheared suspension. XXVII. Transient and steady deformation and burst of liquid drops. *J. Colloid Interface Sci.* **38**:395-411.

Wong, V.S. 1979. *Computational structures for extracting edge features from*

digital images for real-time control applications. PhD. Dissertation. California Institute of Technology.

Youngren, G.K. and Acrivos, A. 1976. On the shape of a gas bubble in a viscous extensional flow. *J. Fluid Mech.* **76**:433-442.

APPENDIX ONE - STABILITY MATRICES

As mentioned in Chapter 3, the linear stability of the solution to the non-linear algebraic equations of the small deformation theory is determined by the eigenvalues of two linear systems:

$$\varepsilon \frac{d\mathbf{f}}{dt} = \mathbf{A} \cdot \mathbf{f} \qquad \text{A1.1}$$

and

$$\varepsilon \frac{d\mathbf{g}}{dt} = \mathbf{B} \cdot \mathbf{g} \qquad \text{A1.2}$$

The vector **f** contains the eight independent components of **F** and **H** which are nonzero at steady state, and **g** contains the six independent components which are zero at steady state. The two vectors are defined as:

$$\mathbf{f} = \begin{bmatrix} F'_{11} \\ F'_{12} \\ F'_{22} \\ H'_{1111} \\ H'_{1112} \\ H'_{1122} \\ H'_{1222} \\ H'_{2222} \end{bmatrix} \qquad \mathbf{g} = \begin{bmatrix} F'_{13} \\ F'_{23} \\ H'_{1113} \\ H'_{1123} \\ H'_{1223} \\ H'_{2223} \end{bmatrix} \qquad \text{A1.3,4}$$

The components of **A** and **B** are given below. A and T are defined in Chapter 3.

$$A_{11} = \alpha_1 + \varepsilon\left[\frac{2}{3}\alpha_2 A + \frac{2}{3}\alpha_3(F_{11} - F_{22})\right] + \varepsilon^2\left[\alpha_4 A(4F_{11} + 2F_{22}) + \right.$$
$$+ \alpha_5 A(2F_{11} - F_{22}) + \alpha_6(T + 2F_{11}F_{22} + 4F_{11}^2) + \frac{4}{3}\alpha_7 A F_{11} +$$
$$\left. + \alpha_9(2H_{1111} + H_{1122})\right] \qquad \text{A1.5}$$

$$A_{12} = \varepsilon\left[\frac{2}{3}F_{12} + 1 - \alpha\right] + \varepsilon^2\left[4\alpha_4 A F_{12} + \right.$$
$$\left. + 2\alpha_7 A F_{12} + 4\alpha_8 F_{11}F_{12} + 2\alpha_9 H_{1112}\right] \qquad \text{A1.6}$$

$$A_{13} = \varepsilon\left[\frac{1}{3}a_2 A - \frac{2}{3}a_3(F_{11}+2F_{22})\right] + \varepsilon^2\left[a_4 A(2F_{11}+4f22) - a_5 A F_{11} + \right.$$
$$\left. + a_6(4F_{11}F_{22}+2F_{11}^2) + \frac{2}{3}a_7 F_{22} + a_9(H_{1111}+2H_{1122})\right] \qquad \text{A1.7}$$

$$A_{14} = \varepsilon^2[a_8 A + a_9(2F_{11}+F_{22})] \qquad \text{A1.8}$$

$$A_{15} = \varepsilon^2[2a_9 A F_{12}] \qquad \text{A1.9}$$

$$A_{16} = \varepsilon^2[-a_8 A + a_9(F_{11}+2F_{22})] \qquad \text{A1.10}$$

$$A_{17} = 0 \qquad \text{A1.11}$$

$$A_{18} = 0 \qquad \text{A1.12}$$

$$A_{21} = \varepsilon\left[a_3 F_{12} - \tfrac{1}{2}(1-\alpha)\right] + \varepsilon^2\left[a_5 A F_{12} + a_6(4F_{11}F_{12} + \right.$$
$$\left. + 2F_{12}F_{22}) + a_9(2H_{1112}+H_{1222})\right] \qquad \text{A1.13}$$

$$A_{22} = a_1 + \varepsilon\left[a_3(F_{11}+F_{22})\right] + \varepsilon^2\left[a_5 A(F_{11}-F_{22}) + a_6(T+4F_{12}^2) + \right.$$
$$\left. + 2a_9 H_{1122}\right] \qquad \text{A1.14}$$

$$A_{23} = \varepsilon\left[a_3 F_{12} + \tfrac{1}{2}(1-\alpha)\right] + \varepsilon^2\left[-a_5 A F_{12} + a_6(2F_{11}F_{12} + \right.$$
$$\left. + 4F_{12}F_{22}) + a_9(H_{1112}+2H_{1222})\right] \qquad \text{A1-15}$$

$$A_{24} = 0 \qquad \text{A1.16}$$

$$A_{25} = \varepsilon^2\left[a_8 A + a_9(2F_{11}+F_{22})\right] \qquad \text{A1.17}$$

$$A_{26} = \varepsilon^2[2a_9 F_{12}] \qquad \text{A2.18}$$

$$A_{27} = \varepsilon^2[-a_8 A + a_9(F_{11}+2F_{22})] \qquad \text{A1.19}$$

$$A_{28} = 0 \qquad \text{A1.20}$$

$$A_{31} = \varepsilon\left[-\frac{1}{3}a_2 A - \frac{2}{3}a_3(2F_{11}+F_{22})\right] + \varepsilon^2\left[-a_4 A(4F_{11}+2F_{22}) + \right.$$
$$\left. + a_5 A F_{22} + a_6(4F_{11}F_{22}+2F_{22}^2) - \frac{2}{3}a_7 A F_{11}\right.$$

$$+ a_9(2H_{1122} + H_{2222})] \qquad \text{A1.21}$$

$$A_{32} = \varepsilon[\frac{2}{3}a_3 F_{12} - 1 + \alpha)] + \varepsilon^2[-4a_4 A F_{12} + \\ + 4a_6 F_{12} F_{22} - 2a_7 A F_{12} + 2a_9 H_{1222}] \qquad \text{A1.22}$$

$$A_{33} = a_1 + \varepsilon[-\frac{2}{3}a_2 A + \frac{2}{3}a_3(F_{22} - F_{11})] + \\ + \varepsilon^2[-a_4 A(2F_{11} + 4F_{22}) + a_5 A(F_{11} - 2F_{22}) + \\ + a_6(T + 2F_{11}F_{22} + 4F_{22}^2) - \frac{4}{3}a_7 A F_{22} + a_9(H_{1122} + 2H_{2222})] \qquad \text{A1.23}$$

$$A_{34} = 0 \qquad \text{A1.24}$$

$$A_{35} = 0 \qquad \text{A1.25}$$

$$A_{36} = \varepsilon^2[a_8 A + a_9(2F_{11} + F_{22})] \qquad \text{A1.26}$$

$$A_{37} = \varepsilon^2[2a_9 F_{12}] \qquad \text{A1.27}$$

$$A_{38} = \varepsilon^2[-a_8 A + a_9(F_{11} + 2F_{22})] \qquad \text{A1.28}$$

$$A_{41} = \frac{1}{35}[51b_1 A + b_2(114F_{11} + 12F_{22})] \qquad \text{A1.29}$$

$$A_{42} = -\frac{96}{35}b_2 F_{12} \qquad \text{A1.30}$$

$$A_{43} = \frac{1}{35}[-6b_1 A + b_2(12F_{11} + 24F_{22})] \qquad \text{A1.31}$$

$$A_{44} = b_0 \qquad \text{A1.32}$$

$$A_{45} = 0 \qquad \text{A1.33}$$

$$A_{46} = 0 \qquad \text{A1.34}$$

$$A_{47} = 0 \qquad \text{A1.35}$$

$$A_{48} = 0 \qquad \text{A1.36}$$

$$A_{51} = \frac{15}{7} F_{12} b_2 \qquad \text{A1.37}$$

$$A_{52} = \frac{3}{2} b_1 A + b_2 \left(\frac{15}{7} F_{11} - \frac{6}{7} F_{22} \right) \qquad \text{A1.38}$$

$$A_{53} = -\frac{6}{7} F_{12} b_2 \qquad \text{A1.39}$$

$$A_{54} = 0 \qquad \text{A1.40}$$

$$A_{55} = b_0 \qquad \text{A1.41}$$

$$A_{56} = 0 \qquad \text{A1.42}$$

$$A_{57} = 0 \qquad \text{A1.43}$$

$$A_{58} = 0 \qquad \text{A1.44}$$

$$A_{61} = \frac{1}{70} [-51 b_1 A + b_2 (-24 F_{11} + 78 F_{22})] \qquad \text{A1.45}$$

$$A_{62} = \frac{108}{35} b_2 F_{12} \qquad \text{A1.46}$$

$$A_{63} = \frac{1}{70} [51 b_1 A + b_2 (78 F_{11} - 24 F_{22})] \qquad \text{A1.47}$$

$$A_{64} = 0 \qquad \text{A1.48}$$

$$A_{65} = 0 \qquad \text{A1.49}$$

$$A_{66} = b_0 \qquad \text{A1.50}$$

$$A_{67} = 0 \qquad \text{A1.51}$$

$$A_{66} = 0 \qquad \text{A1.52}$$

$$A_{71} = -\frac{6}{7} b_2 F_{12} \qquad \text{A1.53}$$

$$A_{72} = -\frac{3}{2} b_1 A + b_2\left(-\frac{6}{7} F_{11} + \frac{15}{7} F_{22}\right) \qquad \text{A1.54}$$

$$A_{73} = \frac{15}{7} b_2 F_{12} \qquad \text{A1.55}$$

$$A_{74} = 0 \qquad \text{A1.56}$$

$$A_{75} = 0 \qquad \text{A1.57}$$

$$A_{76} = 0 \qquad \text{A1.58}$$

$$A_{77} = b_0 \qquad \text{A1.59}$$

$$A_{78} = 0 \qquad \text{A1.60}$$

$$A_{81} = \frac{1}{35}\left[6 b_1 A + b_2(24 F_{11} + 12 F_{22})\right] \qquad \text{A1.61}$$

$$A_{82} = -\frac{96}{35} b_2 F_{12} \qquad \text{A1.62}$$

$$A_{83} = \frac{1}{35}\left[-51 b_1 A + b_2(12 F_{11} + 114 F_{22})\right] \qquad \text{A1.63}$$

$$A_{84} = 0 \qquad \text{A1.64}$$

$$A_{85} = 0 \qquad \text{A1.65}$$

$$A_{86} = 0 \qquad \text{A1.66}$$

$$A_{87} = 0 \qquad \text{A1.67}$$

$$A_{88} = b_0 \qquad \text{A1.68}$$

$$B_{11} = a_1 + \varepsilon[\tfrac{1}{2}a_2 A - a_3 F_{22}] + \varepsilon^2[a_5 A(F_{11} - F_{22}) + a_6 T - \\ -\tfrac{1}{2}a_7 A F_{22} + a_9(-2H_{1111} - 2H_{1122})] \qquad \text{A1.69}$$

$$B_{12} = \varepsilon[a_3 F_{12} + \tfrac{1}{2}(1-\alpha)] + \varepsilon^2[\tfrac{1}{2}a_7 A F_{12} - 2a_9(H_{1112} + H_{1222})] \qquad \text{A1.70}$$

$$B_{13} = \varepsilon^2[a_8 A + a_9(2F_{11} + F_{22})] \qquad \text{A1.71}$$

$$B_{14} = \varepsilon^2[2a_9 F_{12}] \qquad \text{A1.72}$$

$$B_{15} = \varepsilon^2[-a_8 A + a_9(F_{11} + 2F_{22})] \qquad \text{A1.73}$$

$$B_{16} = 0 \qquad \text{A1.74}$$

$$B_{21} = \varepsilon[a_3 F_{12} - \tfrac{1}{2}(1-\alpha)] + \varepsilon^2[-\tfrac{1}{2}a_7 A F_{12} - a_9(2H_{1112} + 2H_{1222})] \qquad \text{A1.75}$$

$$B_{22} = a_1 + \varepsilon[-\tfrac{1}{2}a_2 A - a_3 F_{11}] + \varepsilon^2[a_5 A(F_{11} - F_{22}) + a_6 T + \\ +\tfrac{1}{2}a_7 A F_{11} - a_9(2H_{1122} + 2H_{2222})] \qquad \text{A1.76}$$

$$B_{23} = 0 \qquad \text{A1.77}$$

$$B_{24} = \varepsilon^2[a_8 A + a_9(2F_{11} + F_{22})] \qquad \text{A1.78}$$

$$B_{25} = \varepsilon^2[2a_9 F_{12}] \qquad \text{A1.79}$$

$$B_{26} = \varepsilon^2[-a_8 A + a_9(F_{11} + 2F_{22})] \qquad \text{A1.80}$$

$$B_{31} = \frac{15}{14}b_1 A + b_2(3F_{11} + \frac{6}{7}F_{22}) \qquad \text{A1.81}$$

$$B_{32} = -\frac{6}{7}b_2 F_{12} \qquad \text{A1.82}$$

$$B_{33} = b_0 \qquad \text{A1.83}$$

$$B_{34} = 0 \qquad \text{A1.84}$$

$$B_{35} = 0 \qquad \text{A1.85}$$

$$B_{36} = 0 \qquad \text{A1.86}$$

$$B_{41} = \frac{12}{7} b_2 F_{12} \qquad \text{A1.87}$$

$$B_{42} = \frac{9}{14} b_1 A + \frac{9}{7} b_2 F_{11} \qquad \text{A1.88}$$

$$B_{43} = 0 \qquad \text{A1.89}$$

$$B_{44} = 0 \qquad \text{A1.90}$$

$$B_{45} = b_0 \qquad \text{A1.91}$$

$$B_{46} = 0 \qquad \text{A1.92}$$

$$B_{51} = -\frac{9}{14} b_1 A + \frac{9}{7} b_2 F_{22} \qquad \text{A1.93}$$

$$B_{52} = \frac{12}{7} b_2 F_{12} \qquad \text{A1.94}$$

$$B_{53} = 0 \qquad \text{A1.95}$$

$$B_{54} = 0 \qquad \text{A1.96}$$

$$B_{55} = b_0 \qquad \text{A1.97}$$

$$B_{56} = 0 \qquad \text{A1.98}$$

$$B_{61} = -\frac{6}{7} b_2 F_{12} \qquad \text{A1.99}$$

$$B_{62} = -\frac{15}{14}b_1 A + b_2\left(\frac{6}{7}F_{11} + 3F_{22}\right) \qquad \text{A1.100}$$

$$B_{63} = 0 \qquad \text{A1.101}$$

$$B_{64} = 0 \qquad \text{A1.102}$$

$$B_{65} = 0 \qquad \text{A1.103}$$

$$B_{66} = b_0 \qquad \text{A1.104}$$

APPENDIX TWO - DEFORMATION PLOTS

This Appendix contains comparisons of the experimentally observed drop deformations and the predictions of the $O(\varepsilon)$ and $O(\varepsilon^2)$ small deformation theory. Similar information is included in Chapter 4, but in a more compact format and without the $O(\varepsilon)$ predictions. For the two lowest viscosity ratio cases, the observations are also compared to the predictions of the large deformation theory.

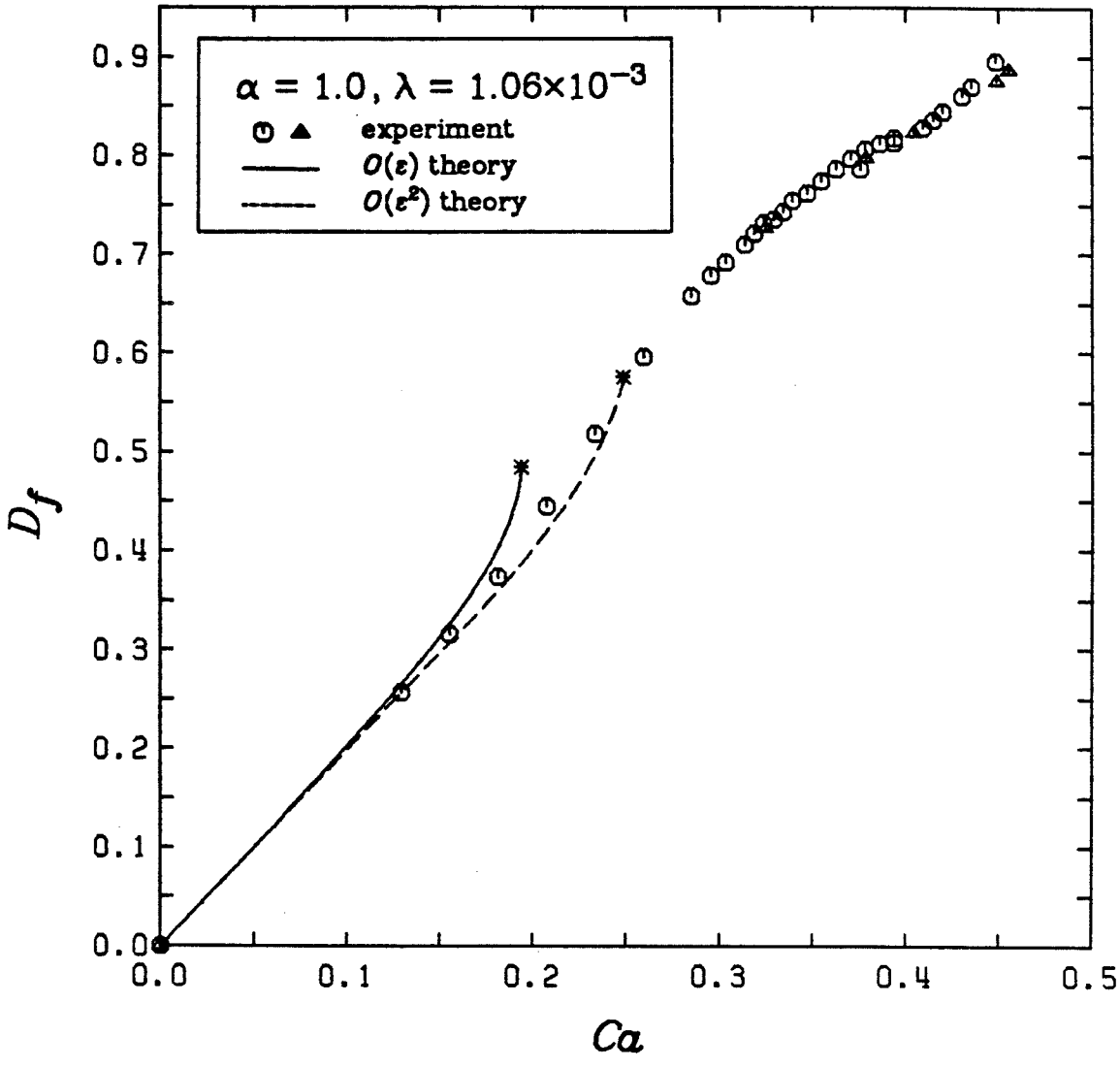

Figure A3.1
Deformation Curve for $\alpha = 1.0$, $\lambda = 1.06\times10^{-3}$

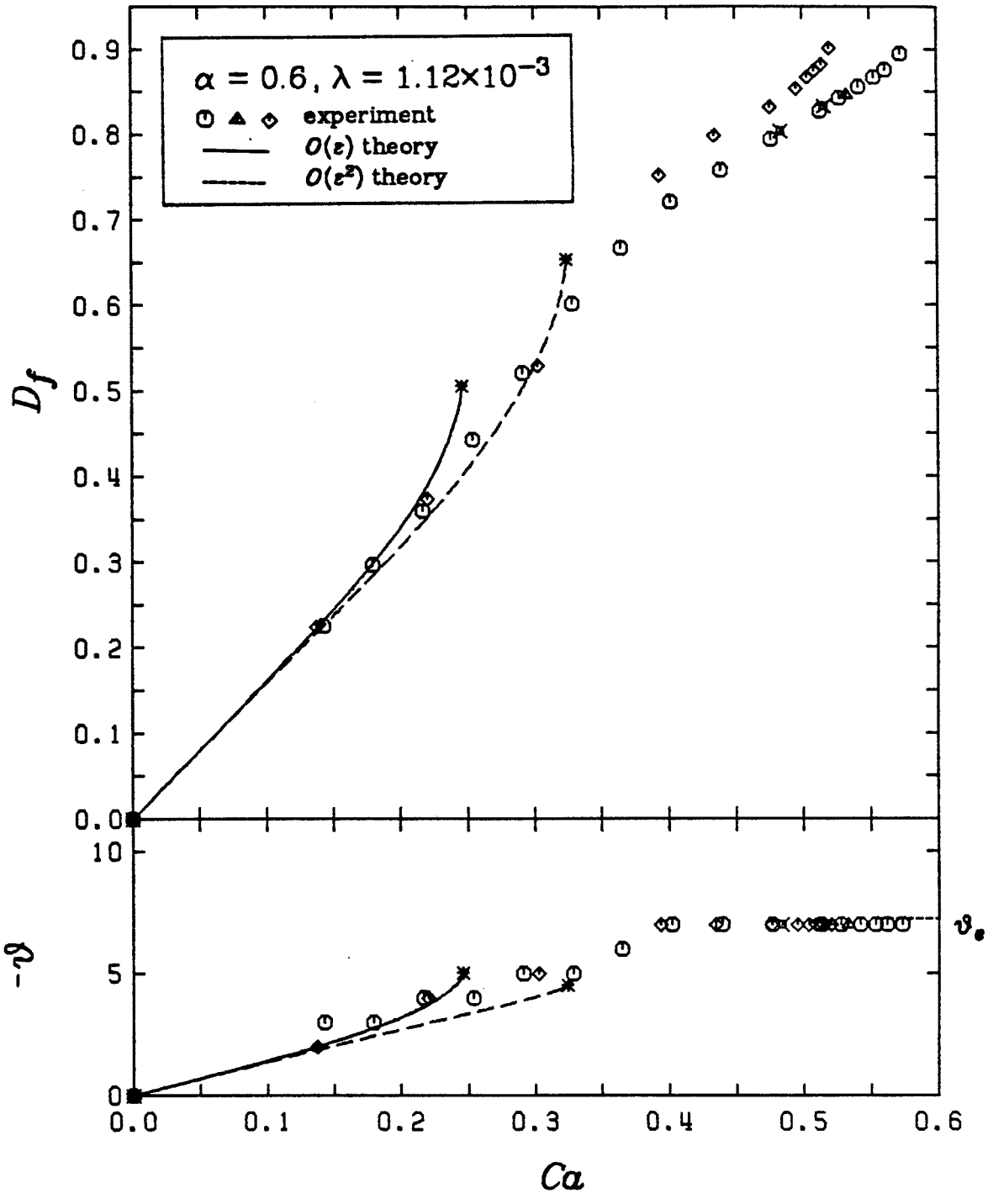

Figure A3.2
Deformation Curve for $\alpha = 0.6$, $\lambda = 1.12\times10^{-3}$

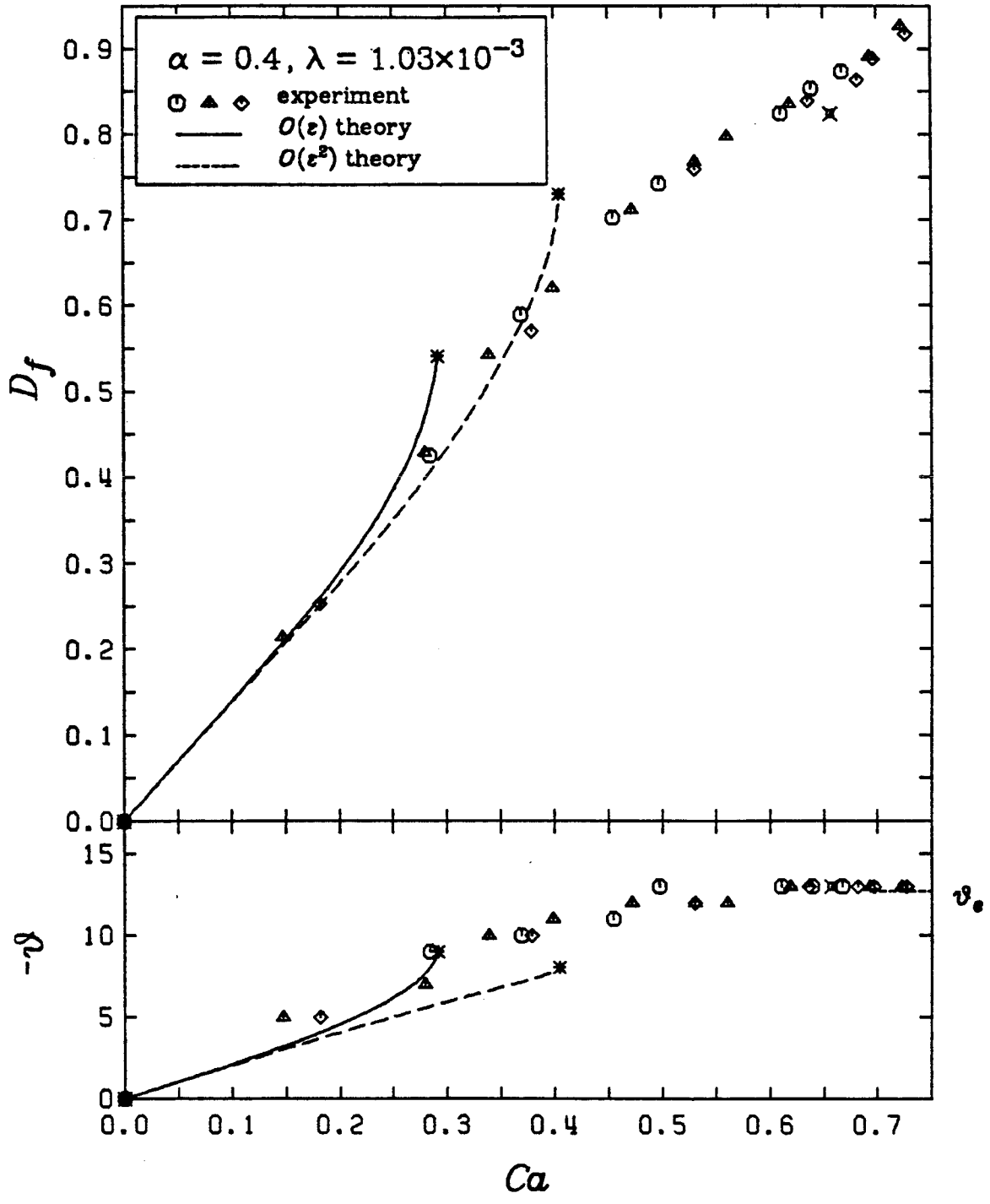

Figure A3.3
Deformation Curve for $\alpha = 0.4$, $\lambda = 1.03\times10^{-3}$

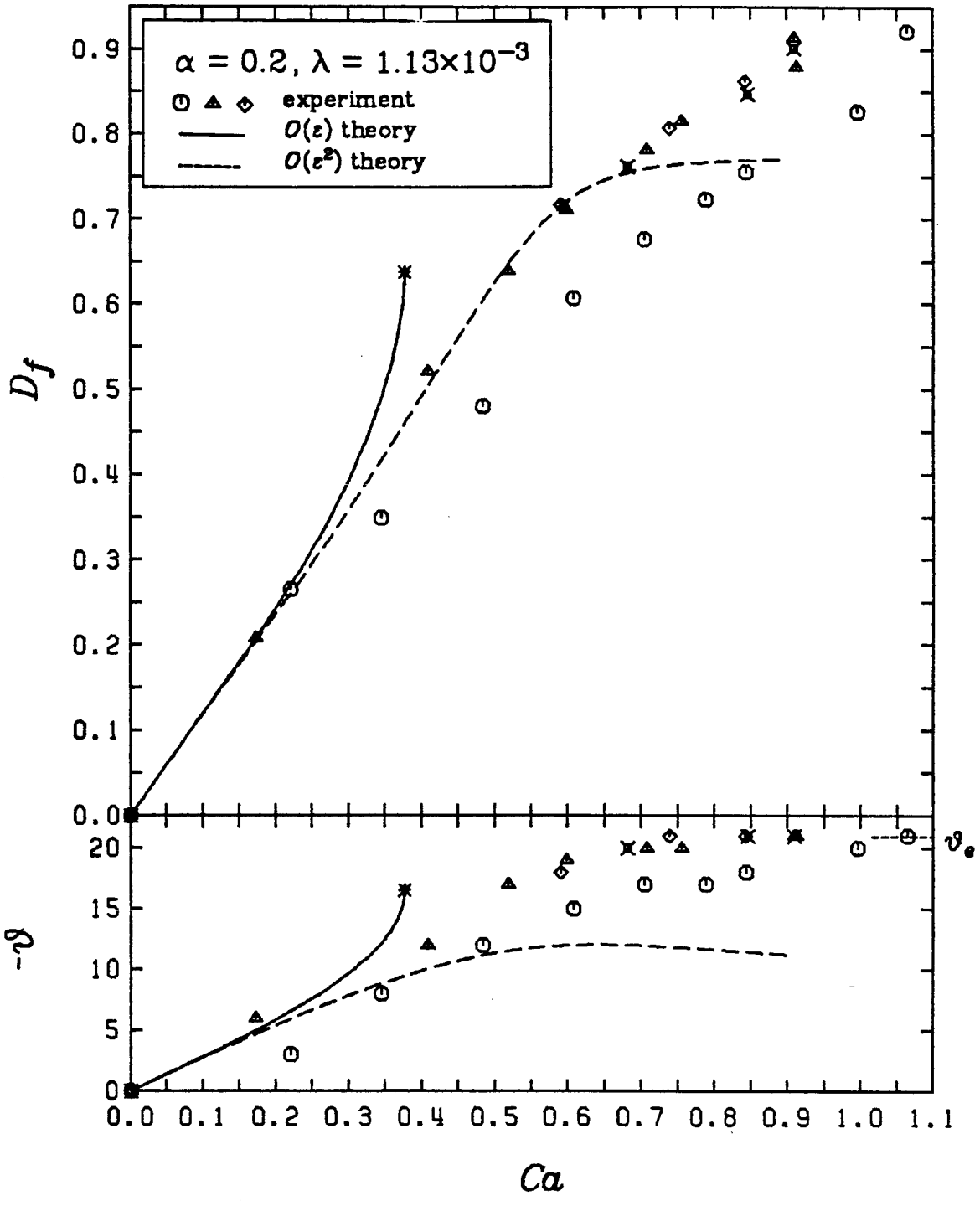

Figure A3.4
Deformation Curve for $\alpha = 0.2$, $\lambda = 1.13\times10^{-3}$

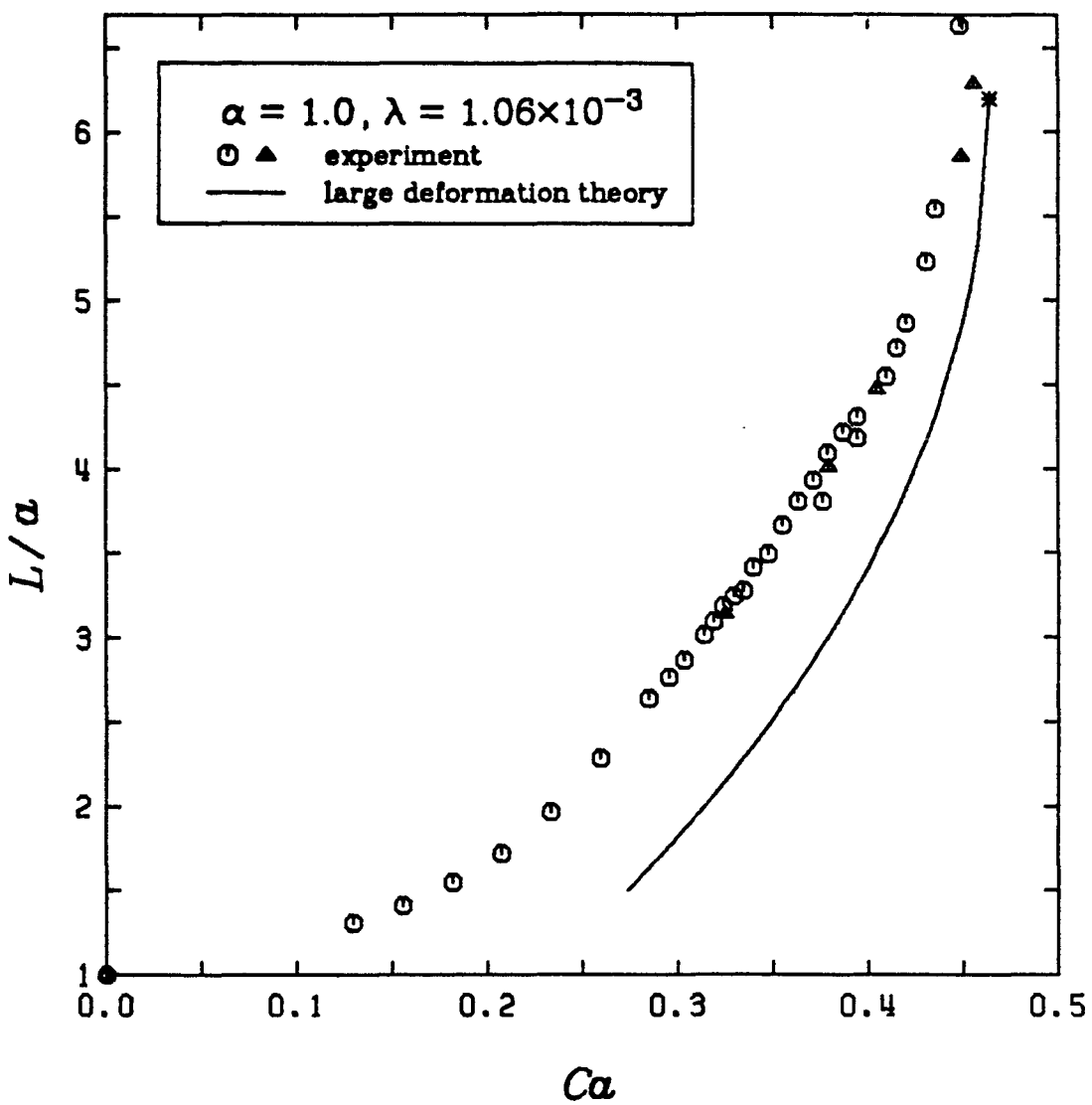

Figure A3.5
L/a vs. Ca for $\alpha = 1.0, \lambda = 1.06\times10^{-3}$

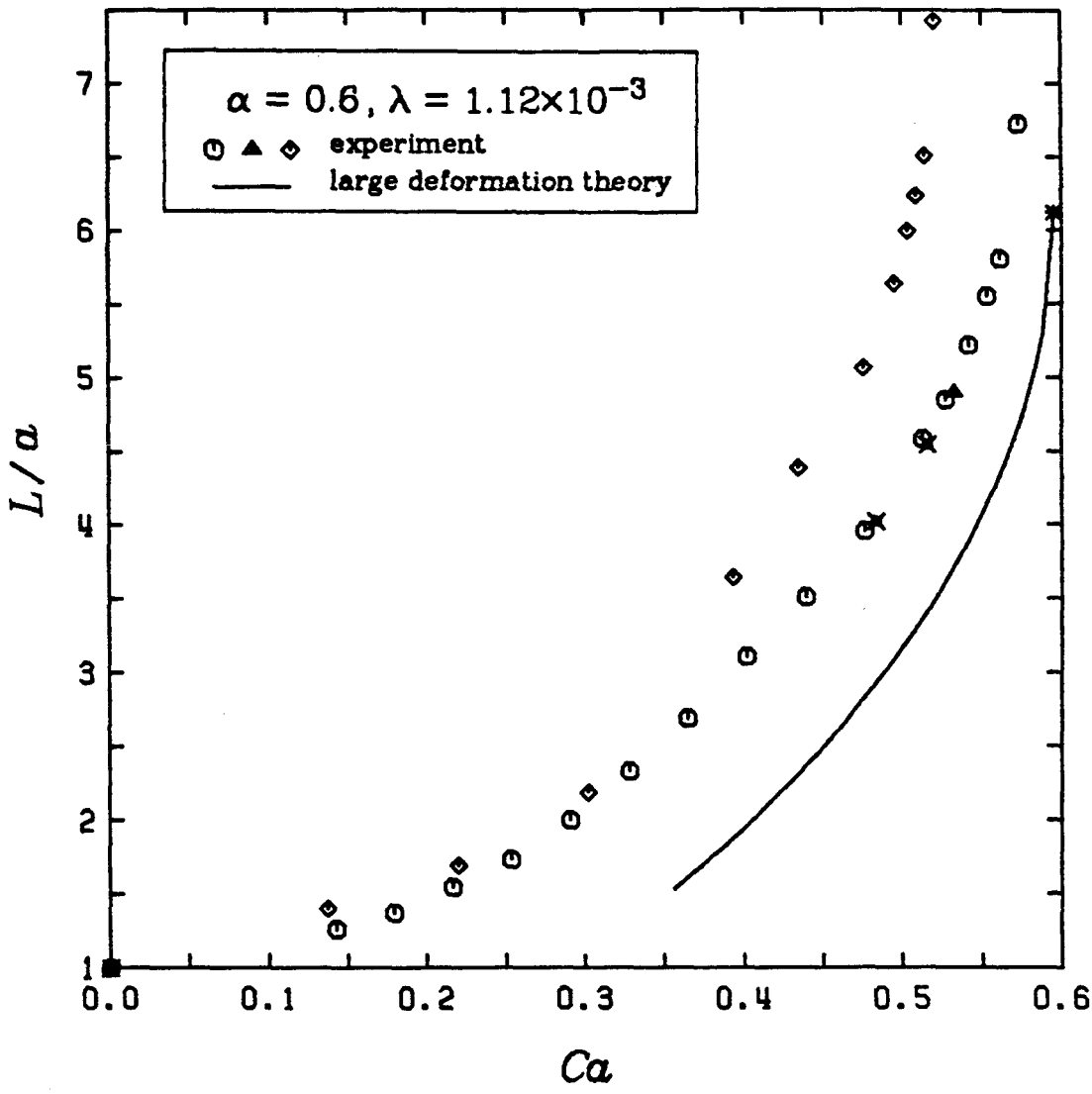

Figure A3.6
L/a vs. Ca for $\alpha = 0.6$, $\lambda = 1.12\times10^{-3}$

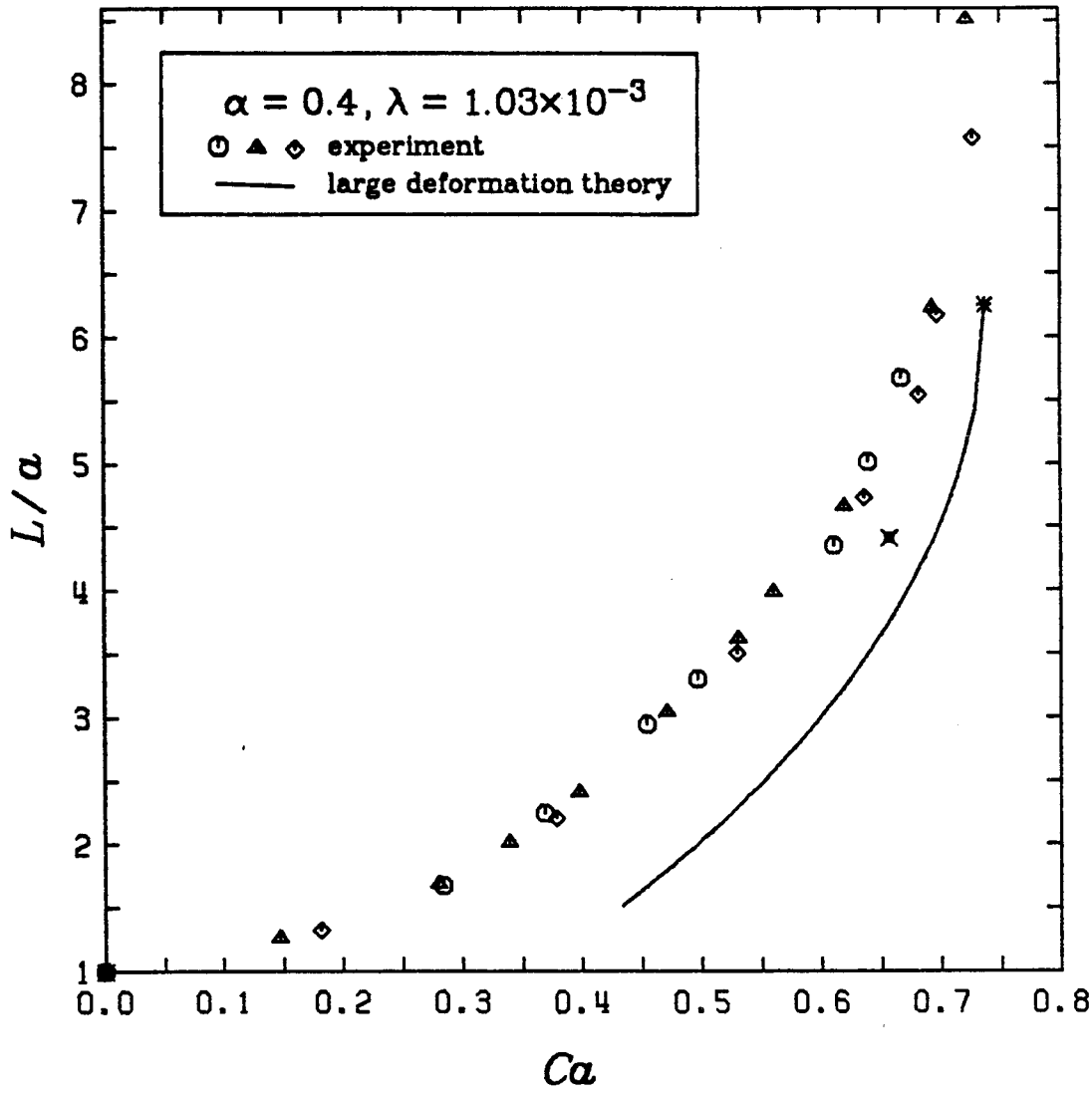

Figure A3.7
L/a vs. Ca for $\alpha = 0.4$, $\lambda = 1.03\times10^{-3}$

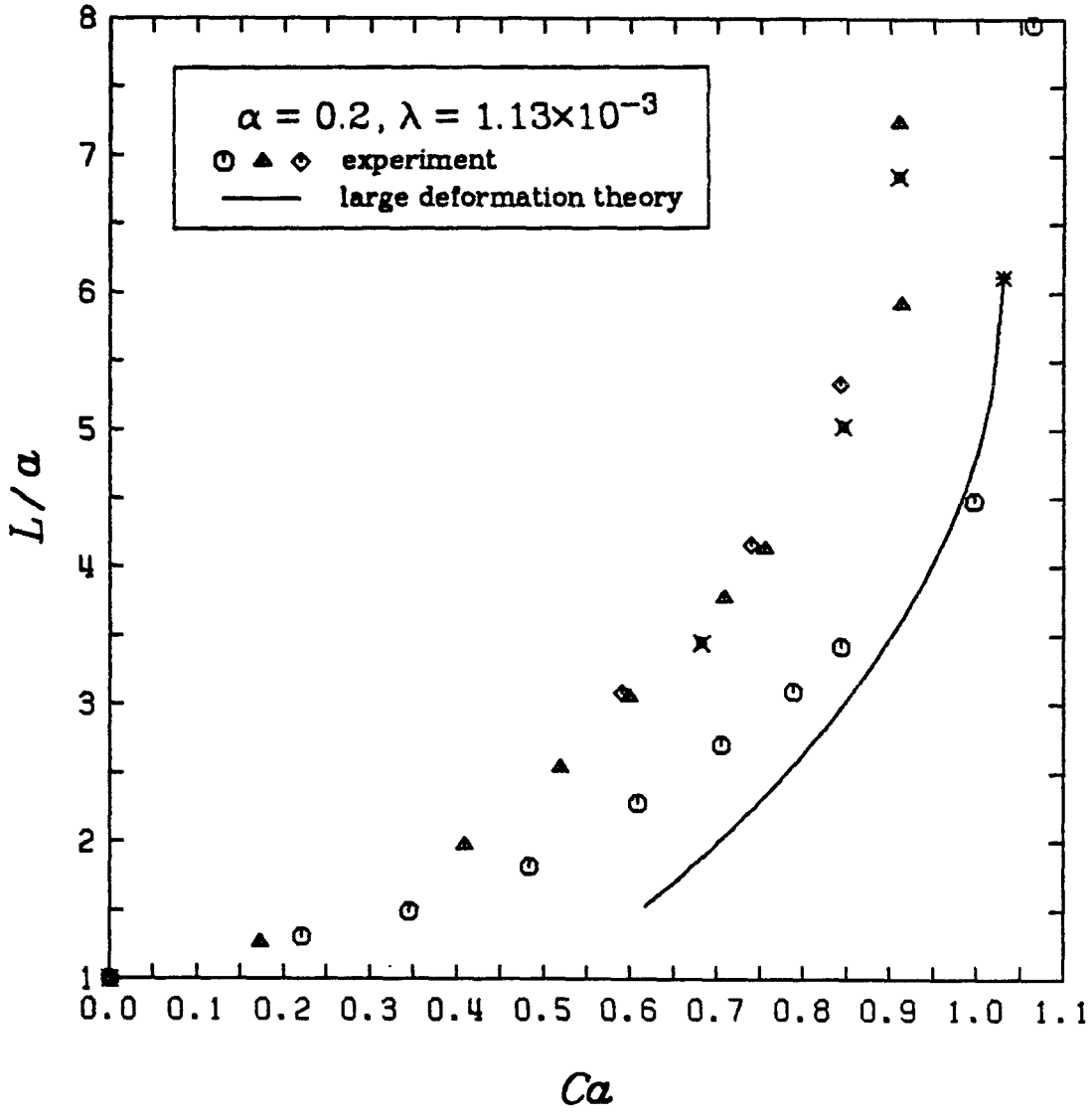

Figure A3.8
L/a vs. Ca for $\alpha = 0.2$, $\lambda = 1.13\times10^{-3}$

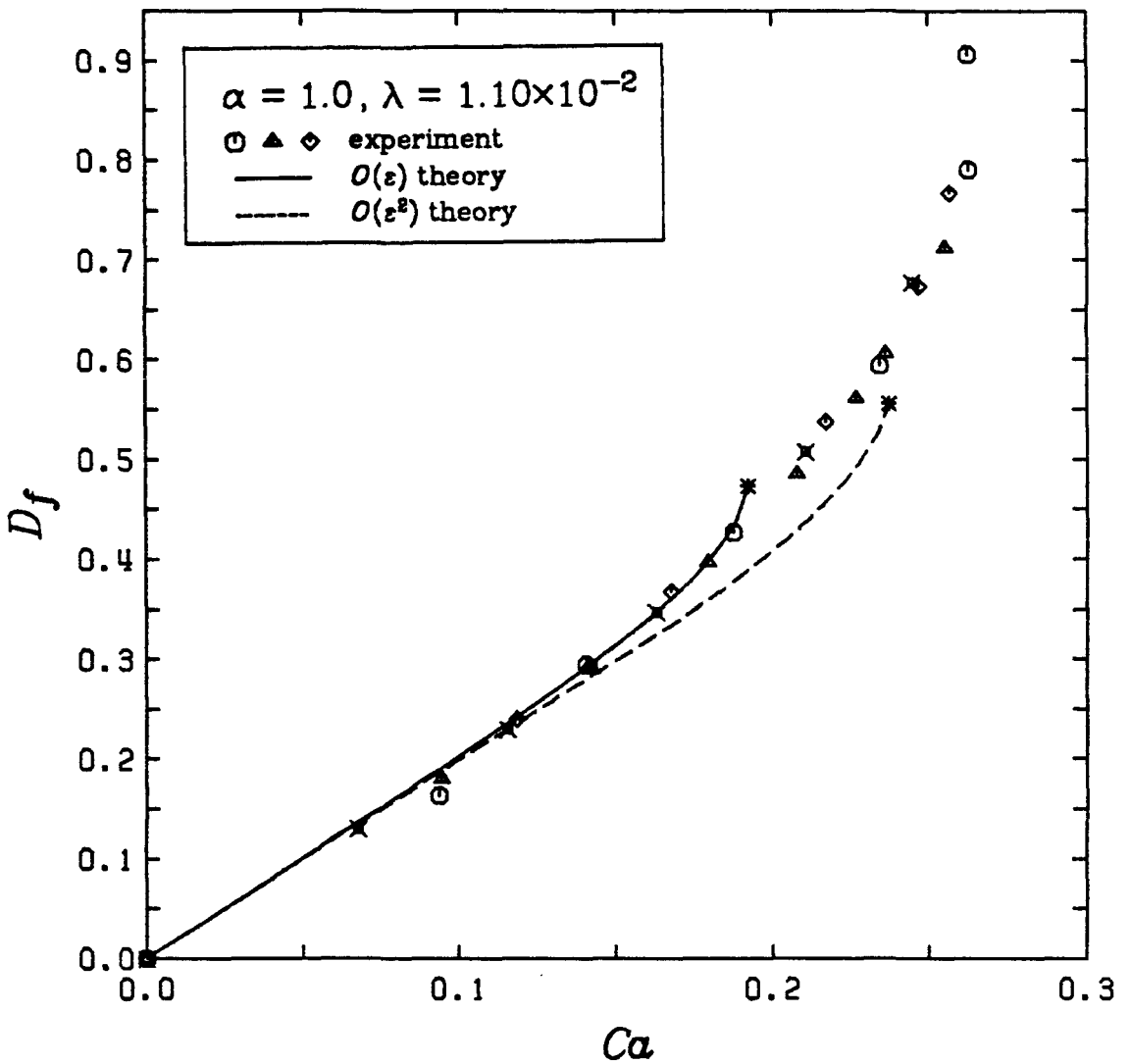

Figure A3.9
Deformation Curve for $\alpha = 1.0$, $\lambda = 1.10\times10^{-2}$

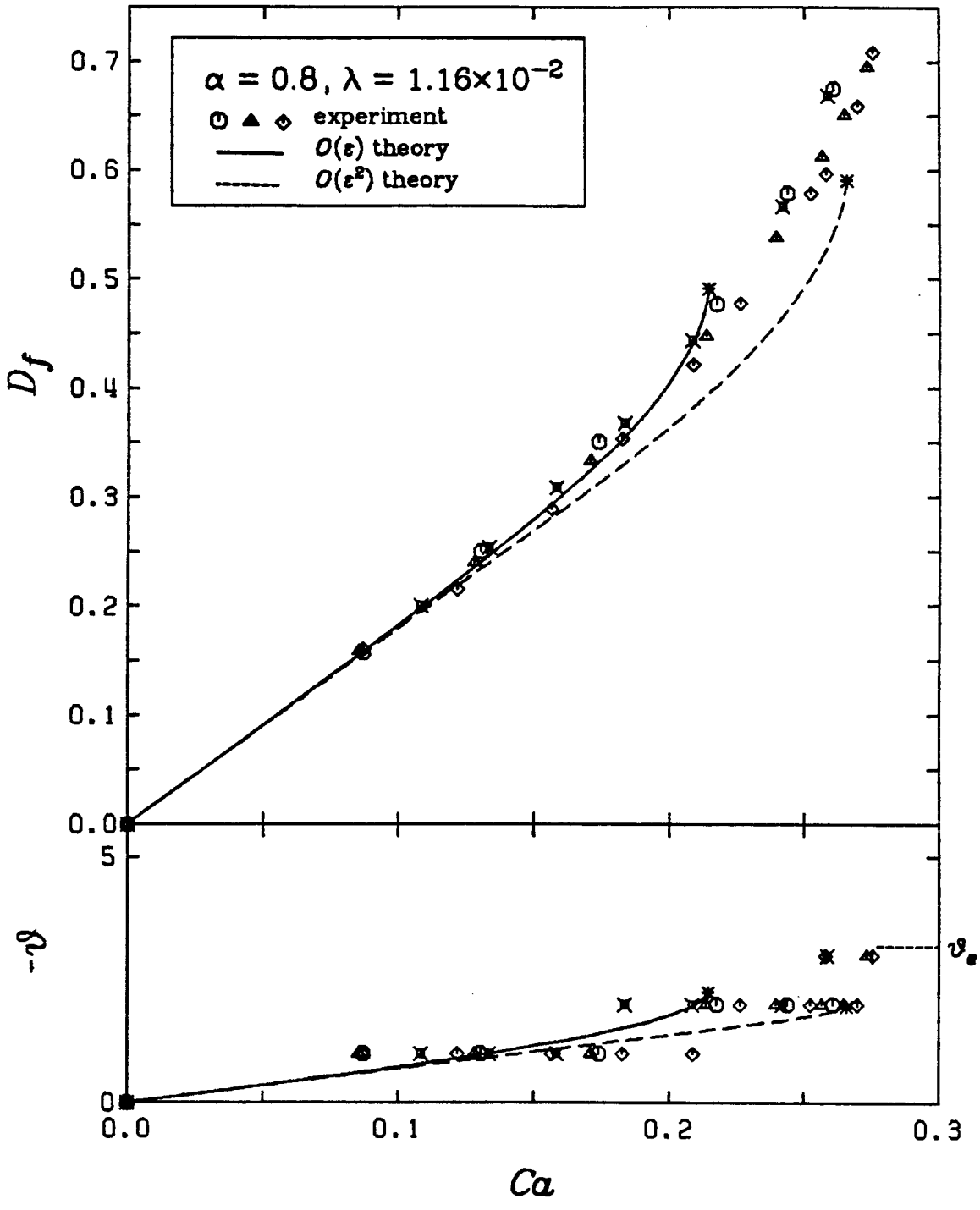

Figure A3.10
Deformation Curve for $\alpha = 0.8$, $\lambda = 1.16\times10^{-2}$

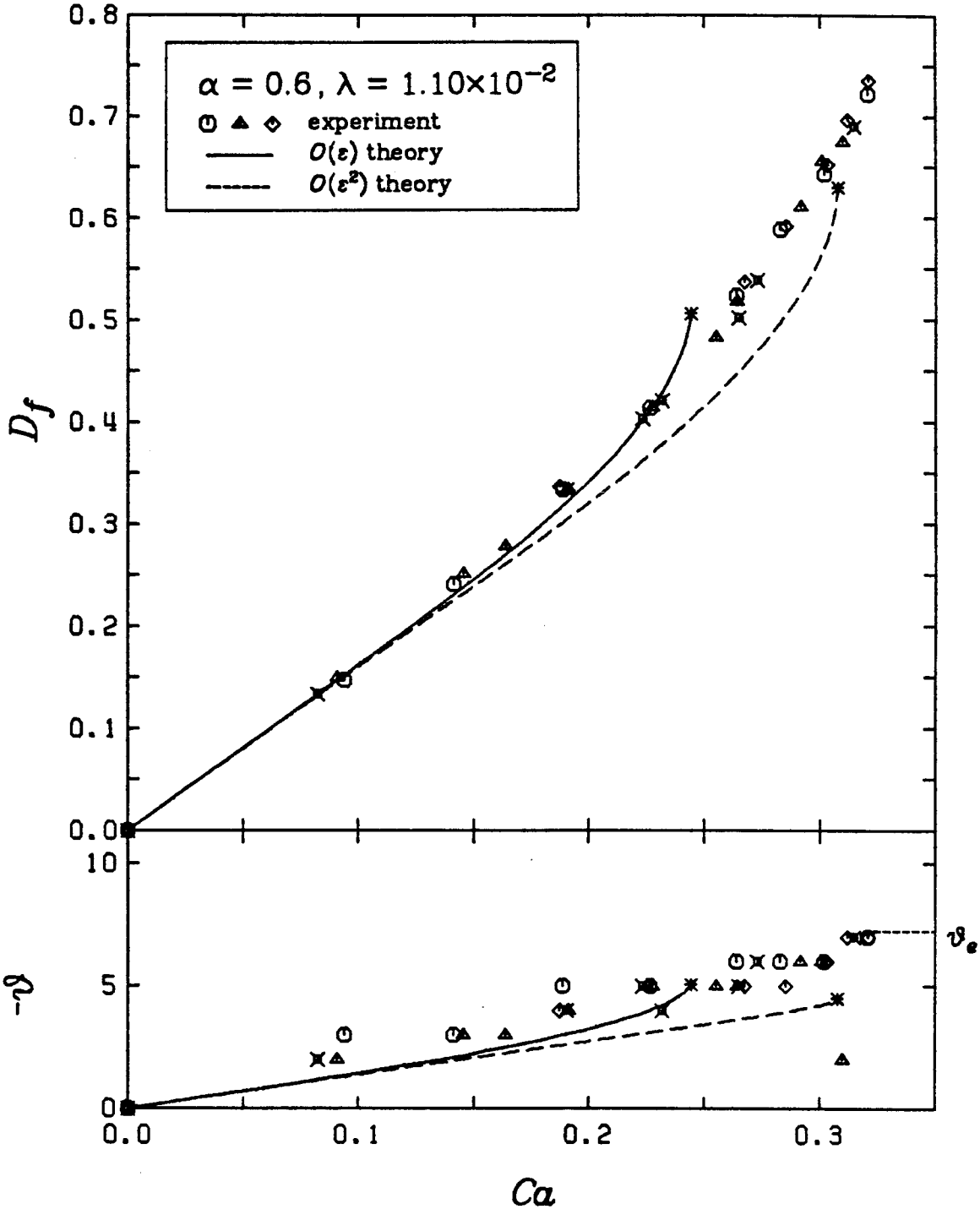

Figure A3.11
Deformation Curve for $\alpha = 0.6$, $\lambda = 1.10\times10^{-2}$

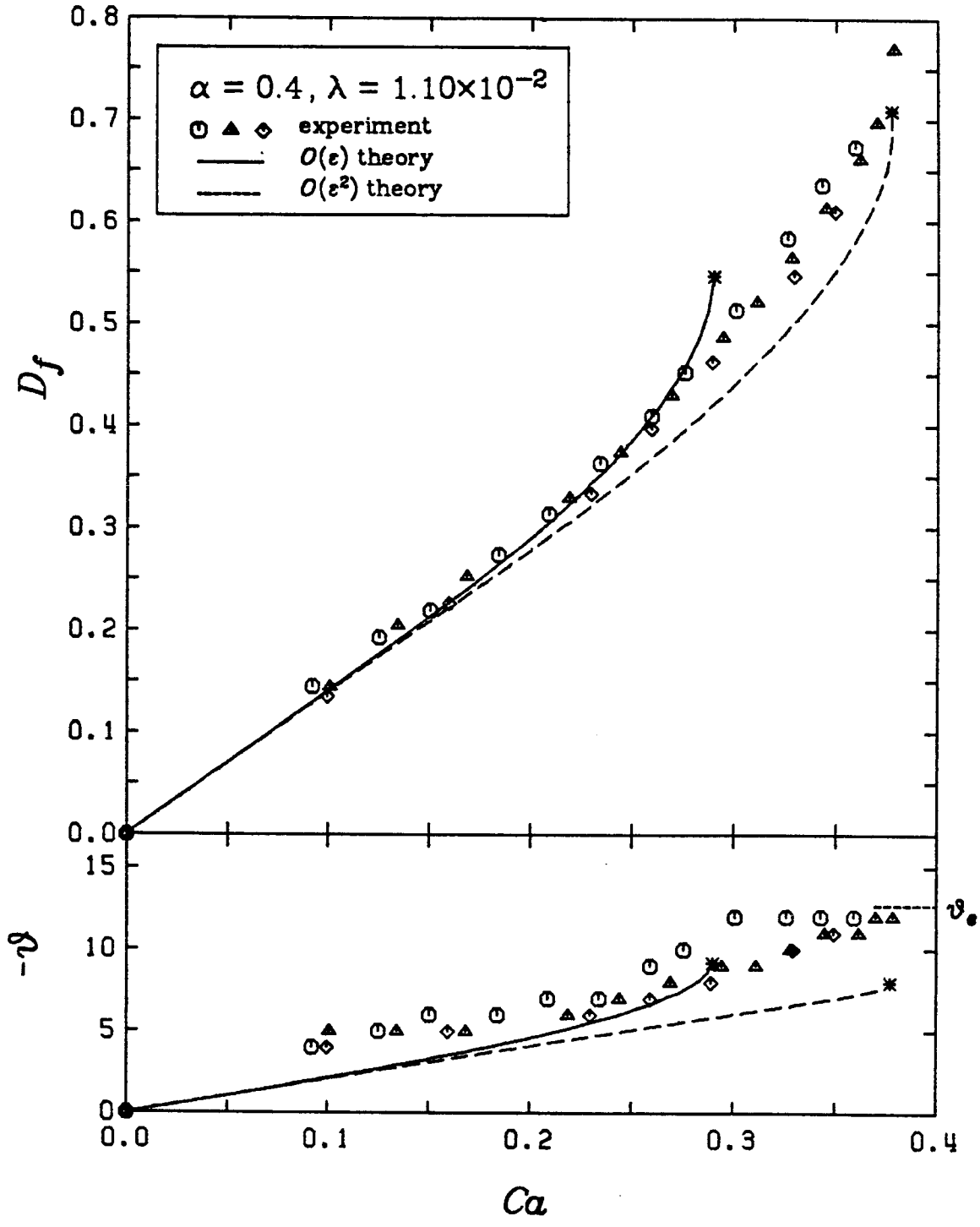

Figure A3.12
Deformation Curve for $\alpha = 0.4$, $\lambda = 1.10\times10^{-2}$

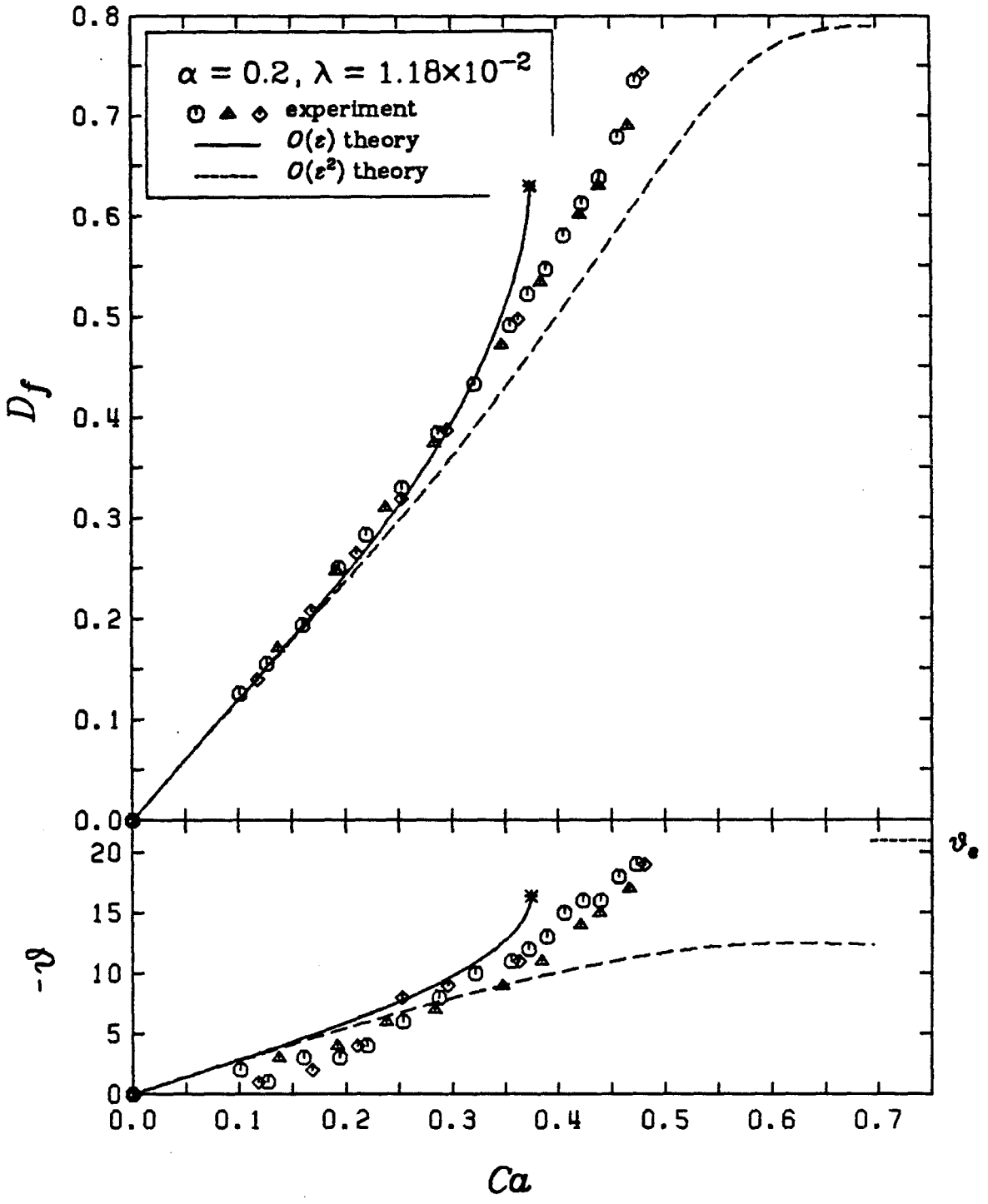

Figure A3.13
Deformation Curve for $\alpha = 0.2$, $\lambda = 1.18\times10^{-2}$

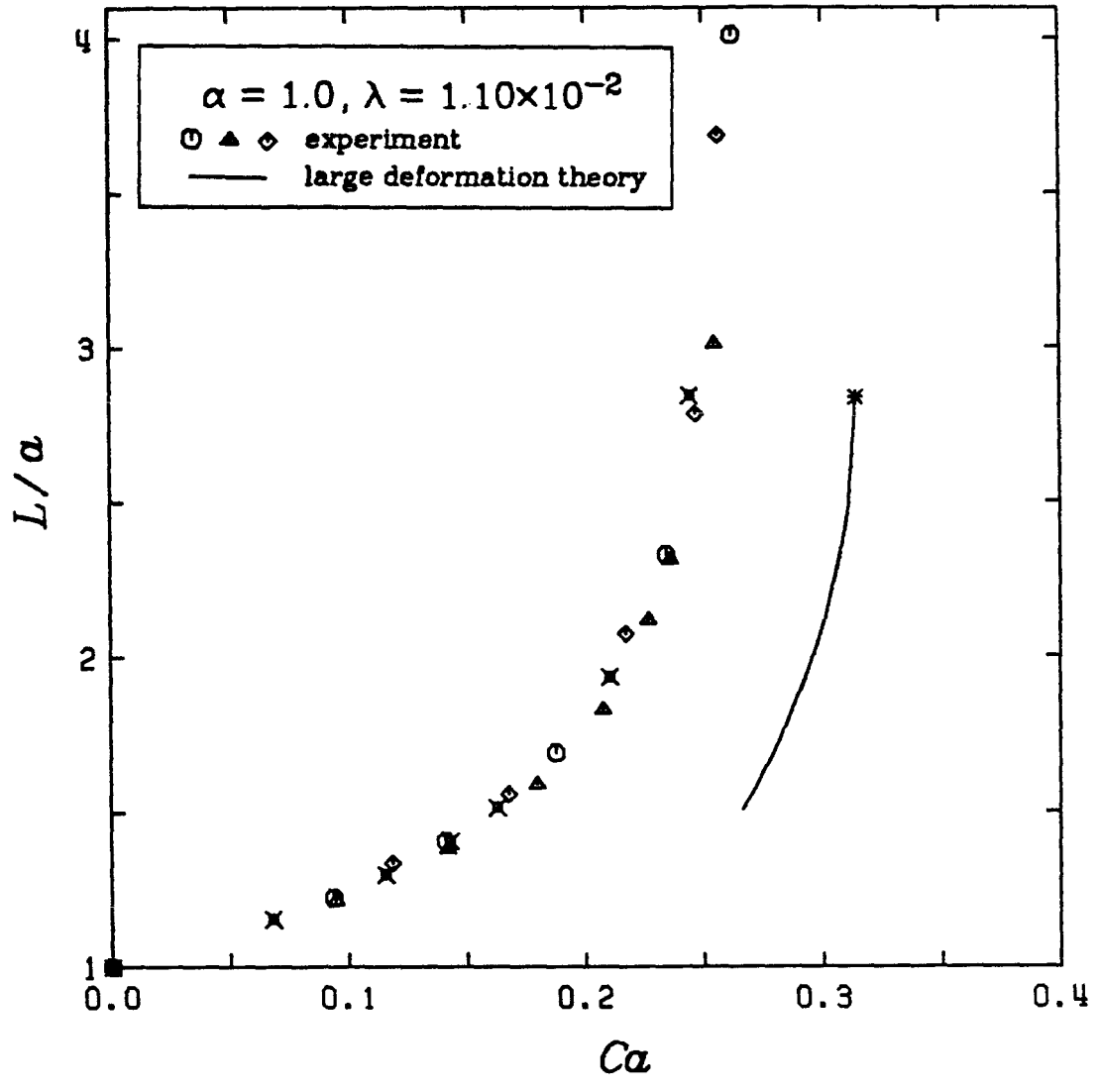

Figure A3.14
L/a vs. Ca for $\alpha = 1.0$, $\lambda = 1.10\times10^{-2}$

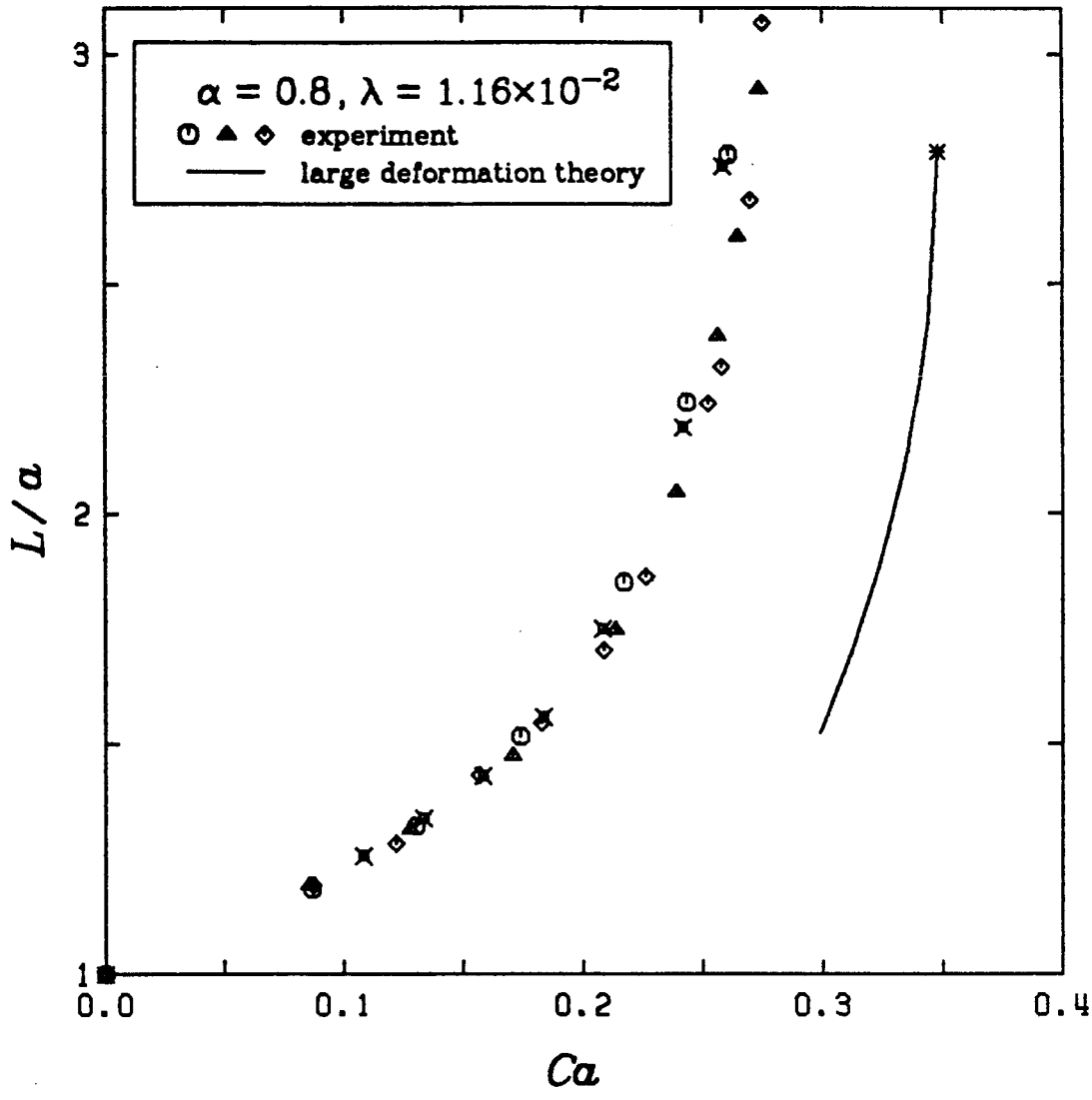

Figure A3.15
L/a vs. Ca for $\alpha = 0.8$, $\lambda = 1.16\times10^{-2}$

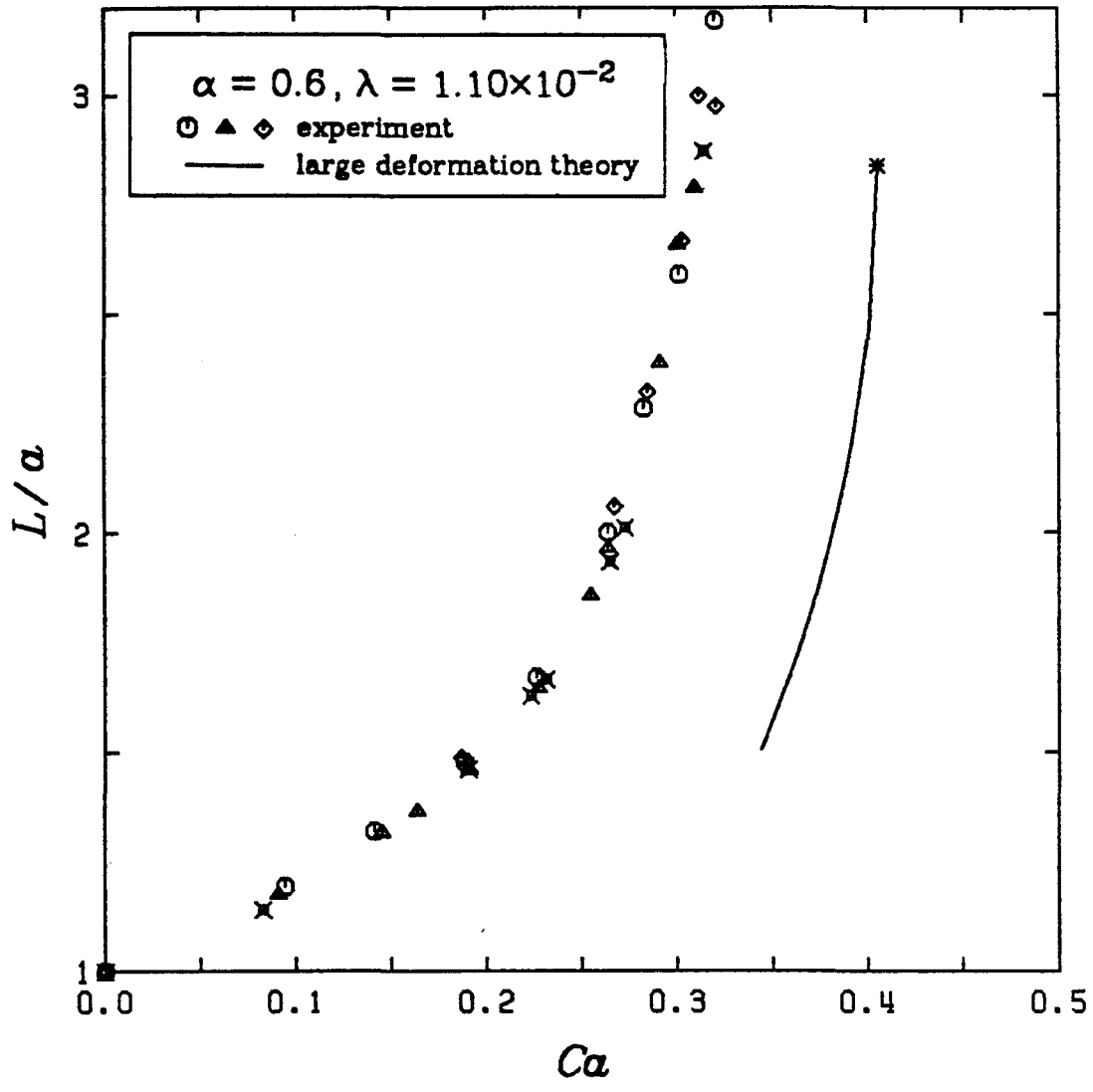

Figure A3.16
L/a vs. Ca for $\alpha = 0.6$, $\lambda = 1.10\times10^{-2}$

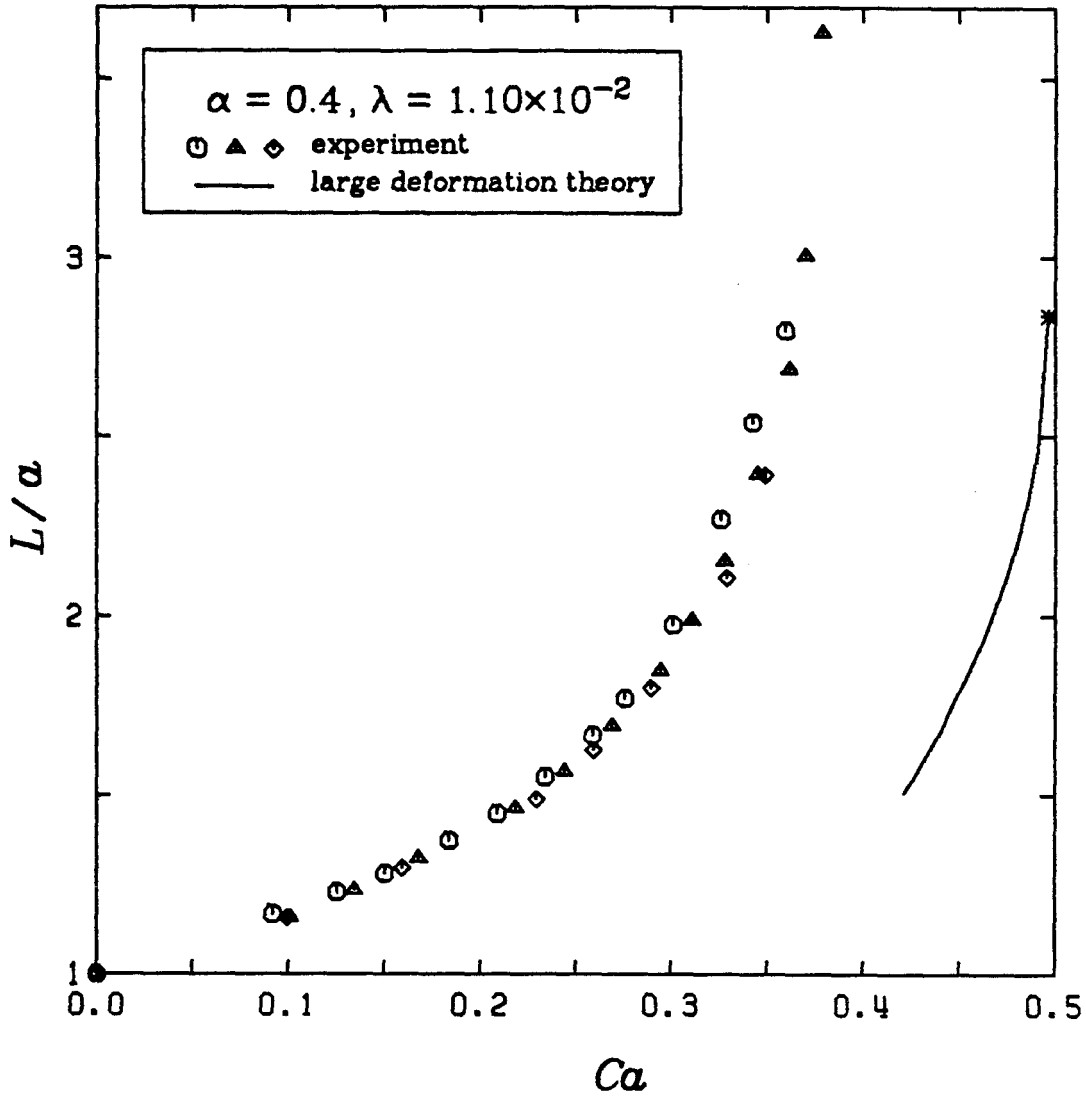

Figure A3.17
L/a vs. Ca for $\alpha = 0.4$, $\lambda = 1.10\times10^{-2}$

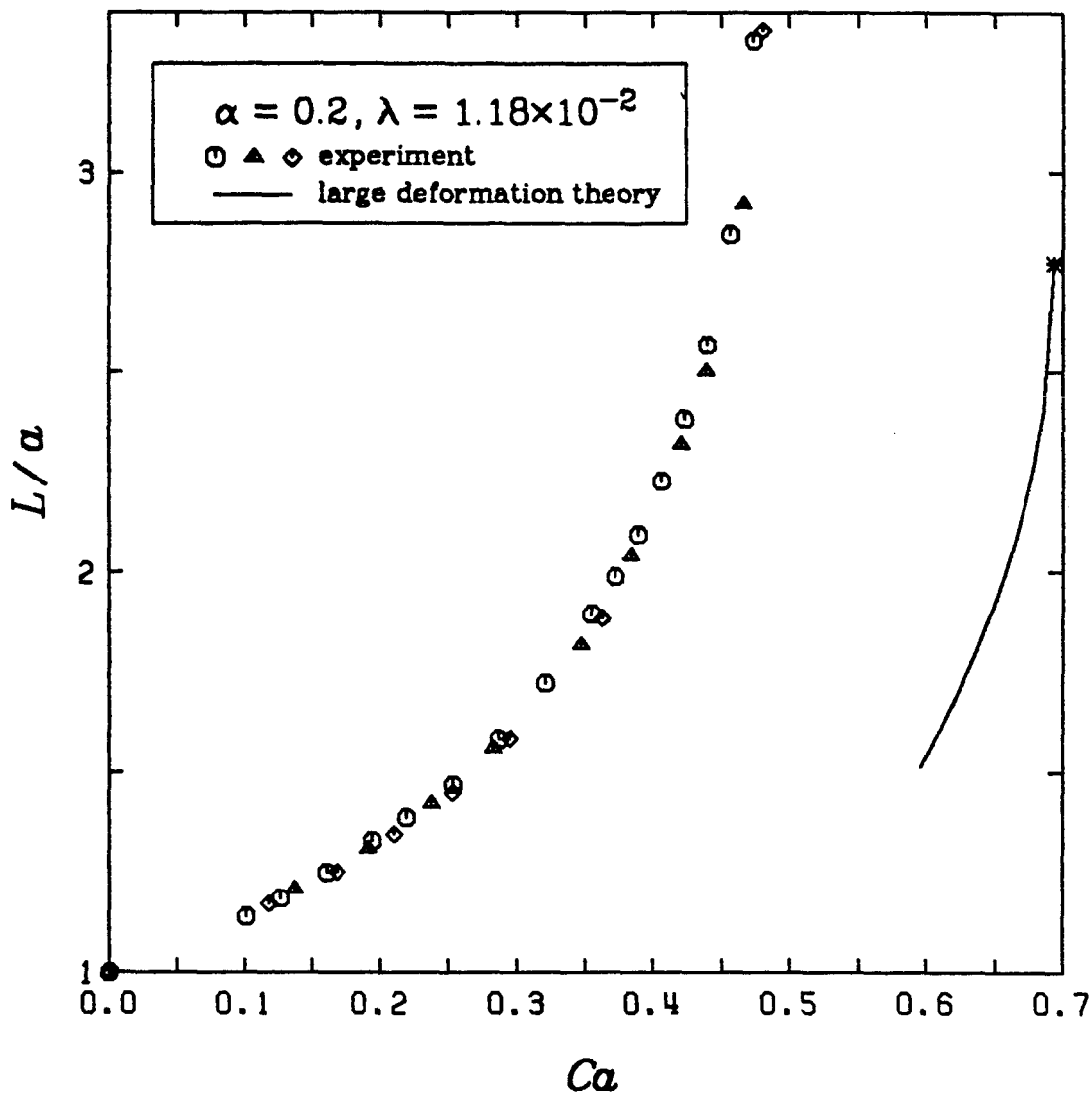

Figure A3.18
L/a vs. Ca for $\alpha = 0.2$, $\lambda = 1.18\times10^{-2}$

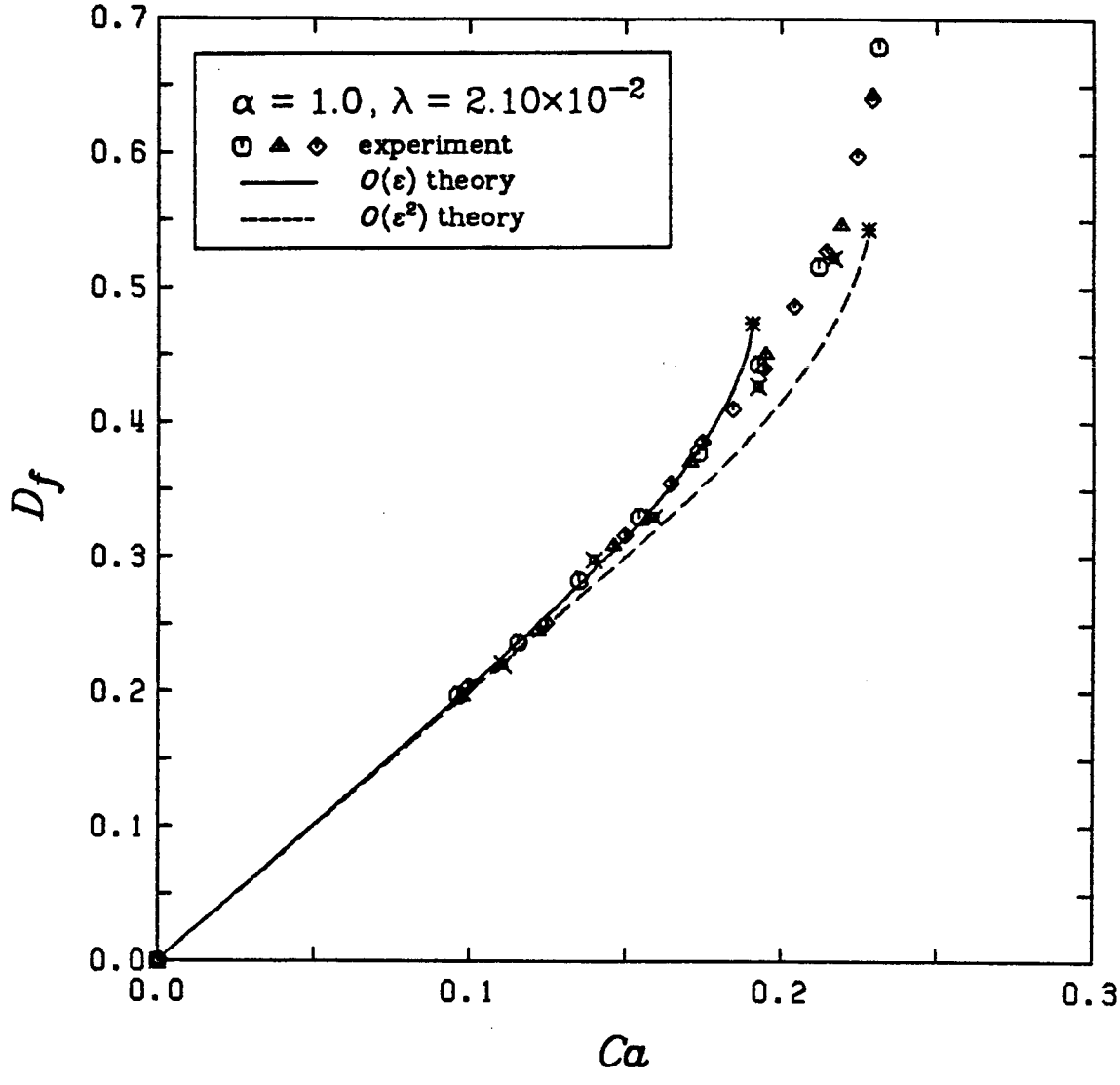

Figure A3.19
Deformation Curve for $\alpha = 1.0$, $\lambda = 2.10\times10^{-2}$

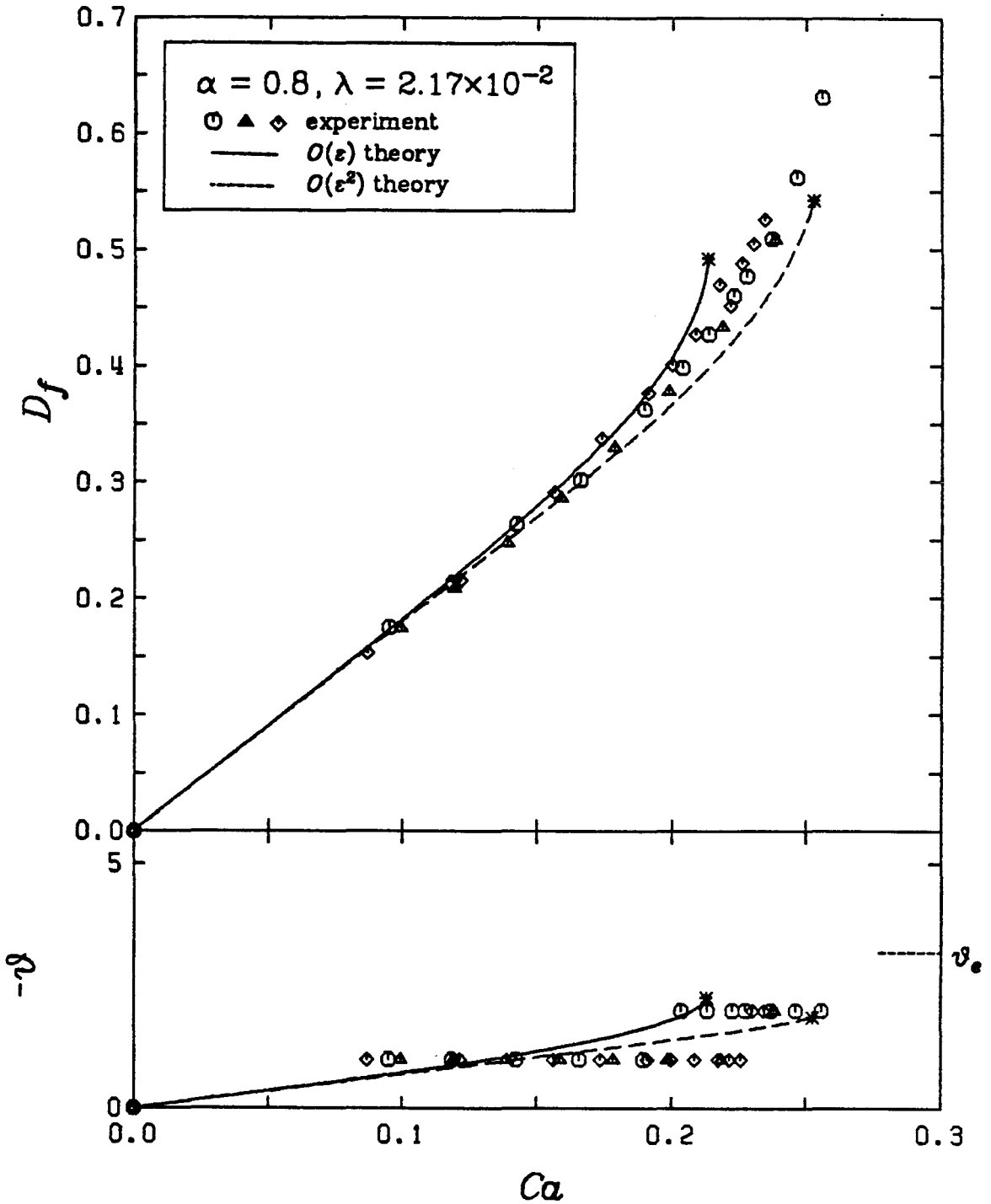

Figure A3.20
Deformation Curve for $\alpha = 0.8$, $\lambda = 2.17\times10^{-2}$

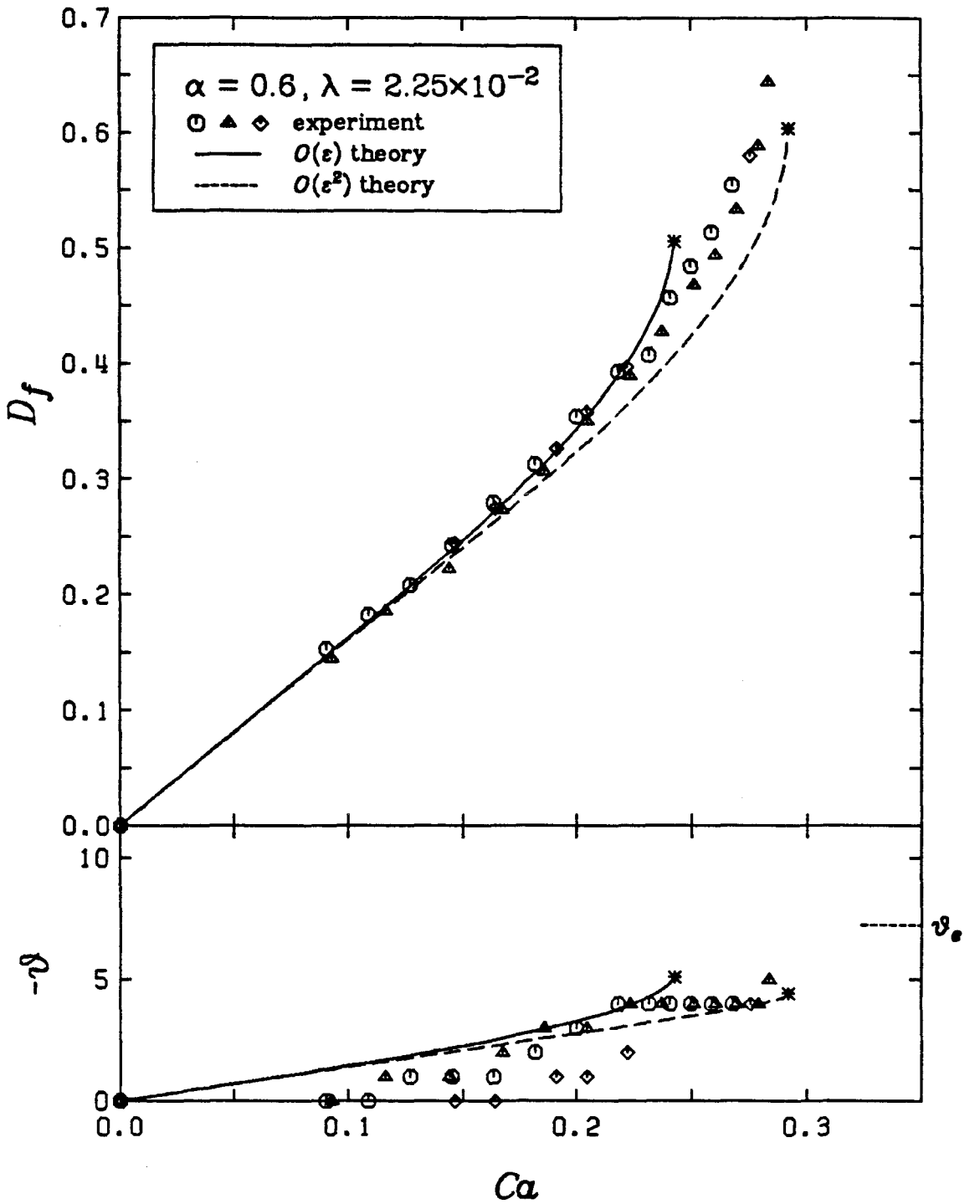

Figure A3.21
Deformation Curve for $\alpha = 0.6$, $\lambda = 2.25\times10^{-2}$

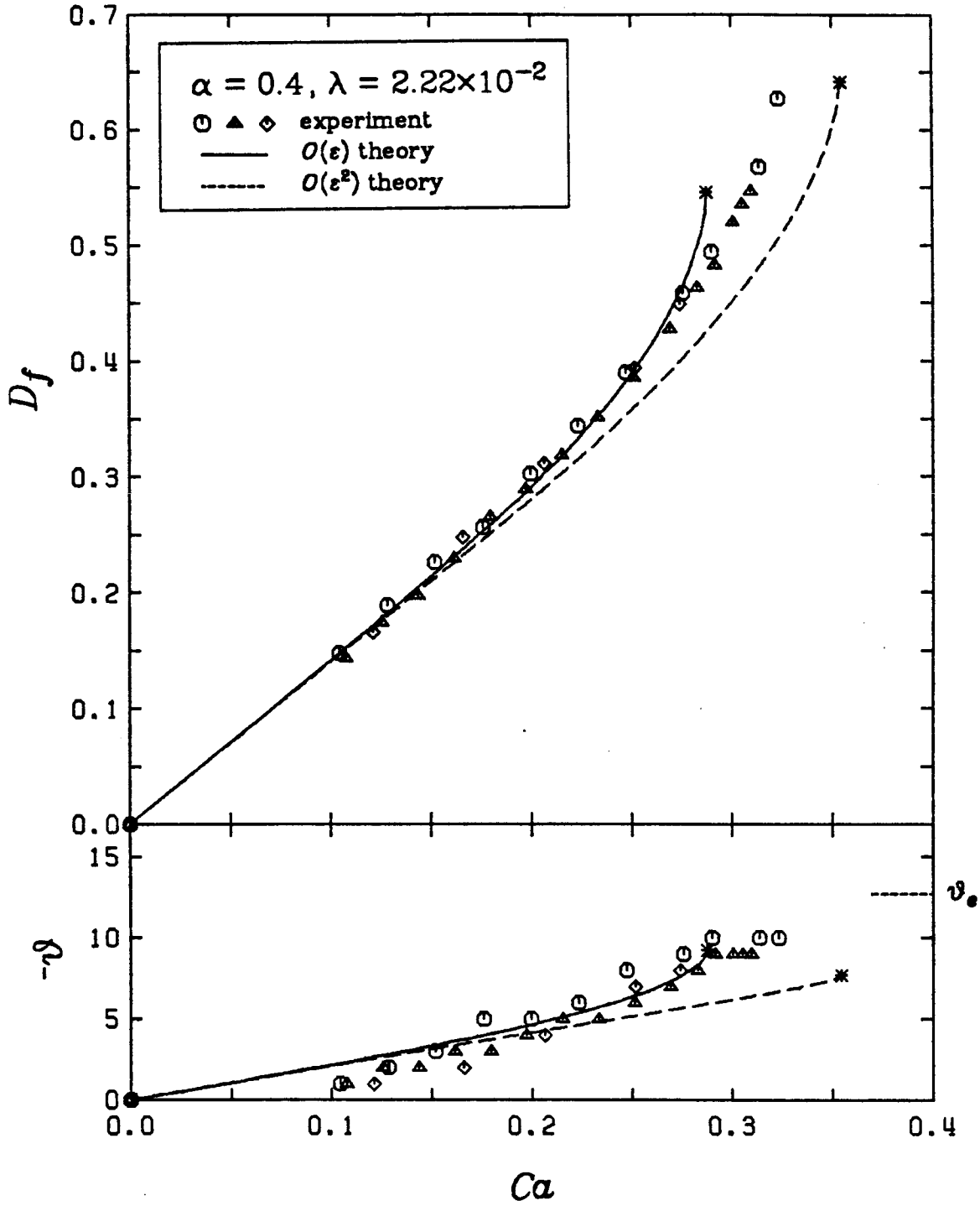

Figure A3.22
Deformation Curve for $\alpha = 0.4$, $\lambda = 2.22\times10^{-2}$

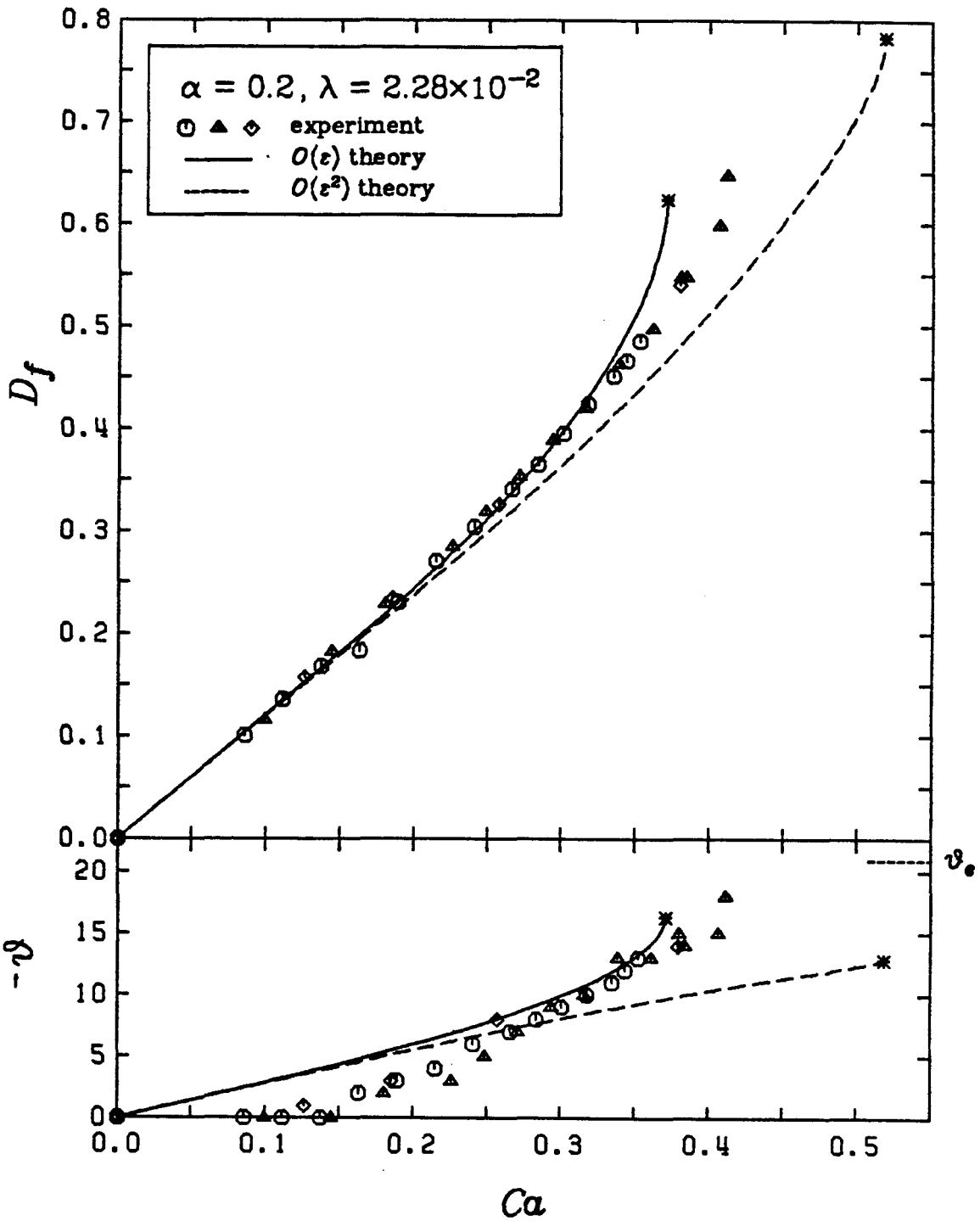

Figure A3.23
Deformation Curve for $\alpha = 0.2$, $\lambda = 2.28\times10^{-2}$

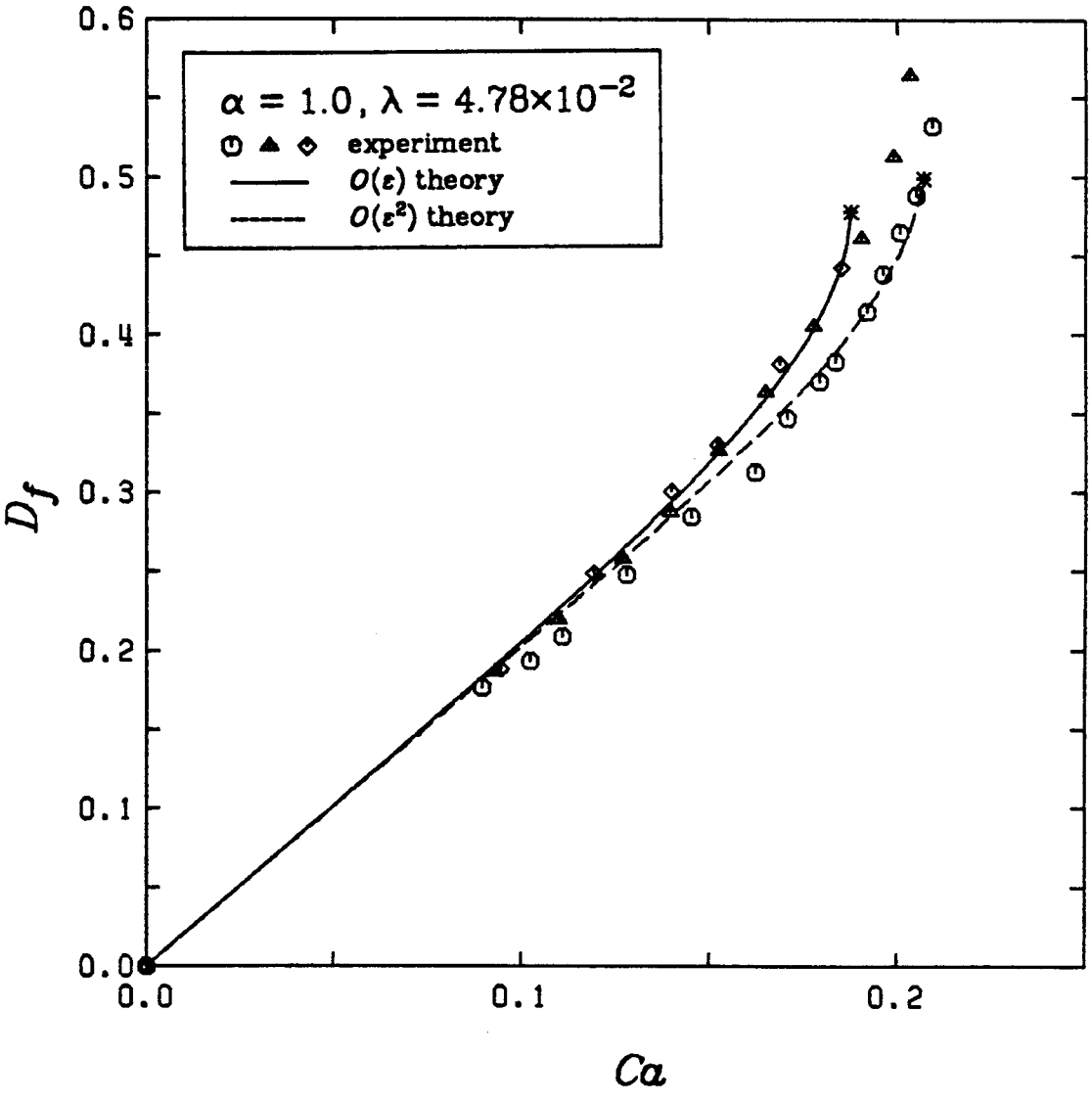

Figure A3.24
Deformation Curve for $\alpha = 1.0$, $\lambda = 4.78\times10^{-2}$

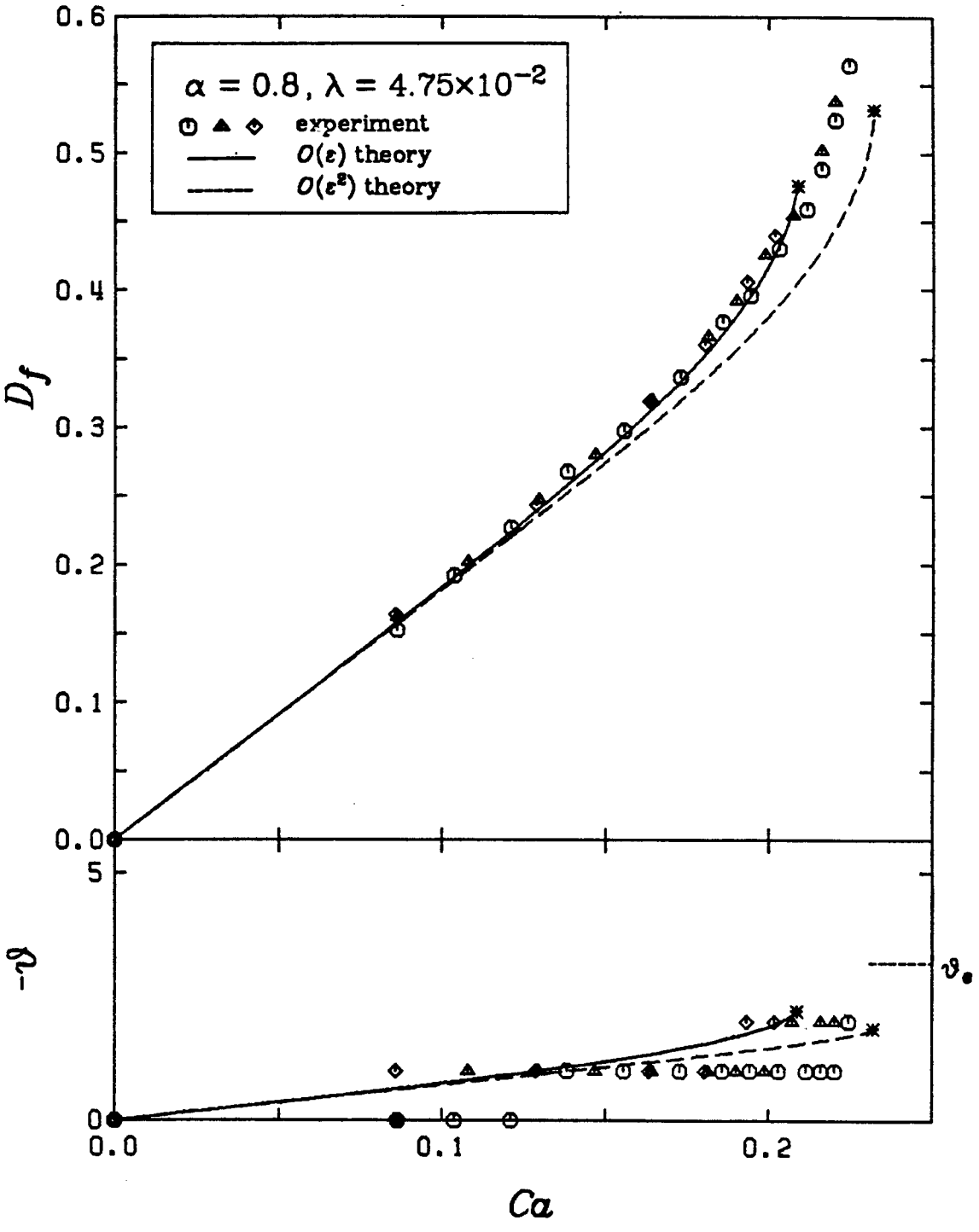

Figure A3.25
Deformation Curve for $\alpha = 0.8$, $\lambda = 4.75\times10^{-2}$

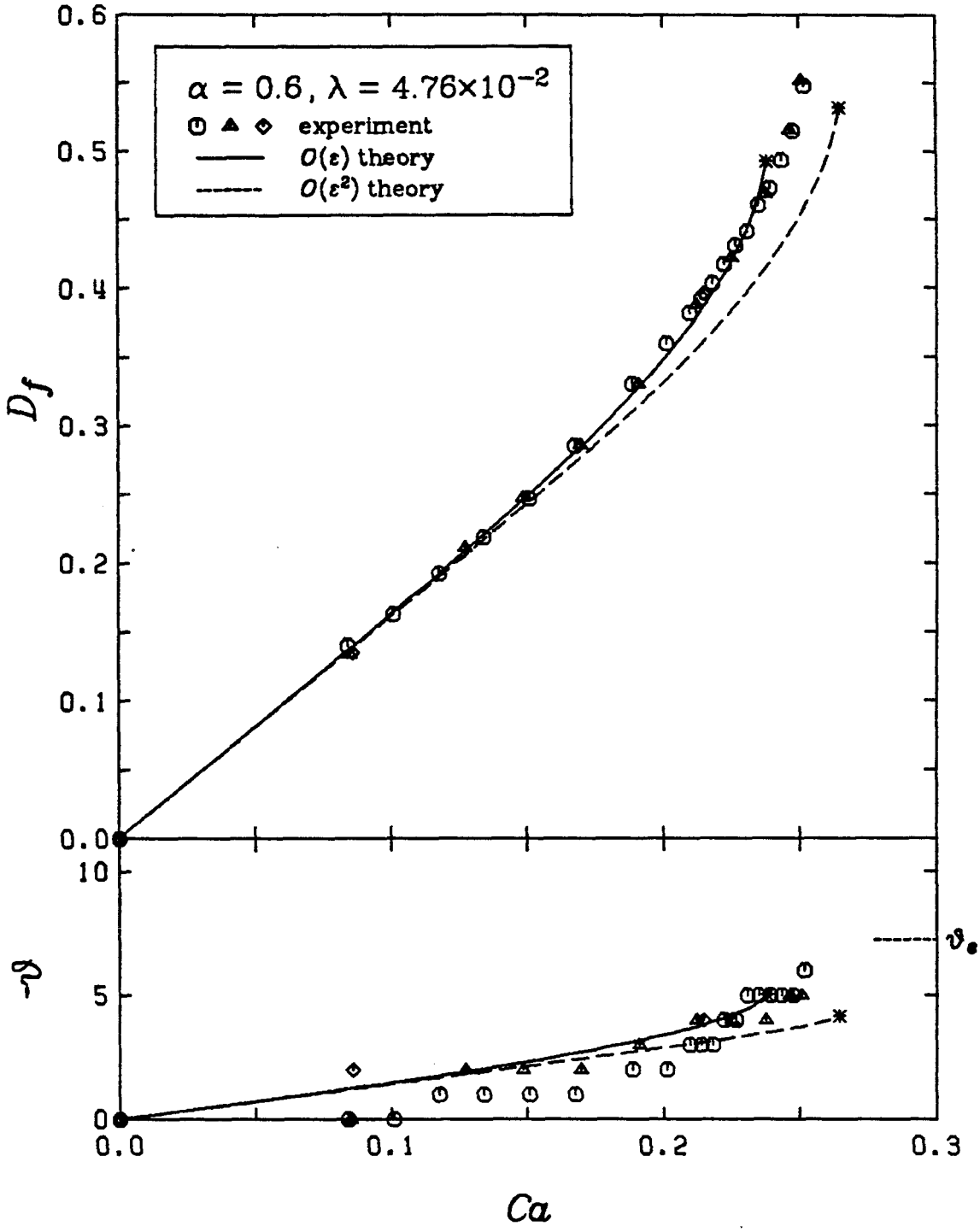

Figure A3.28
Deformation Curve for $\alpha = 0.6$, $\lambda = 4.76\times10^{-2}$

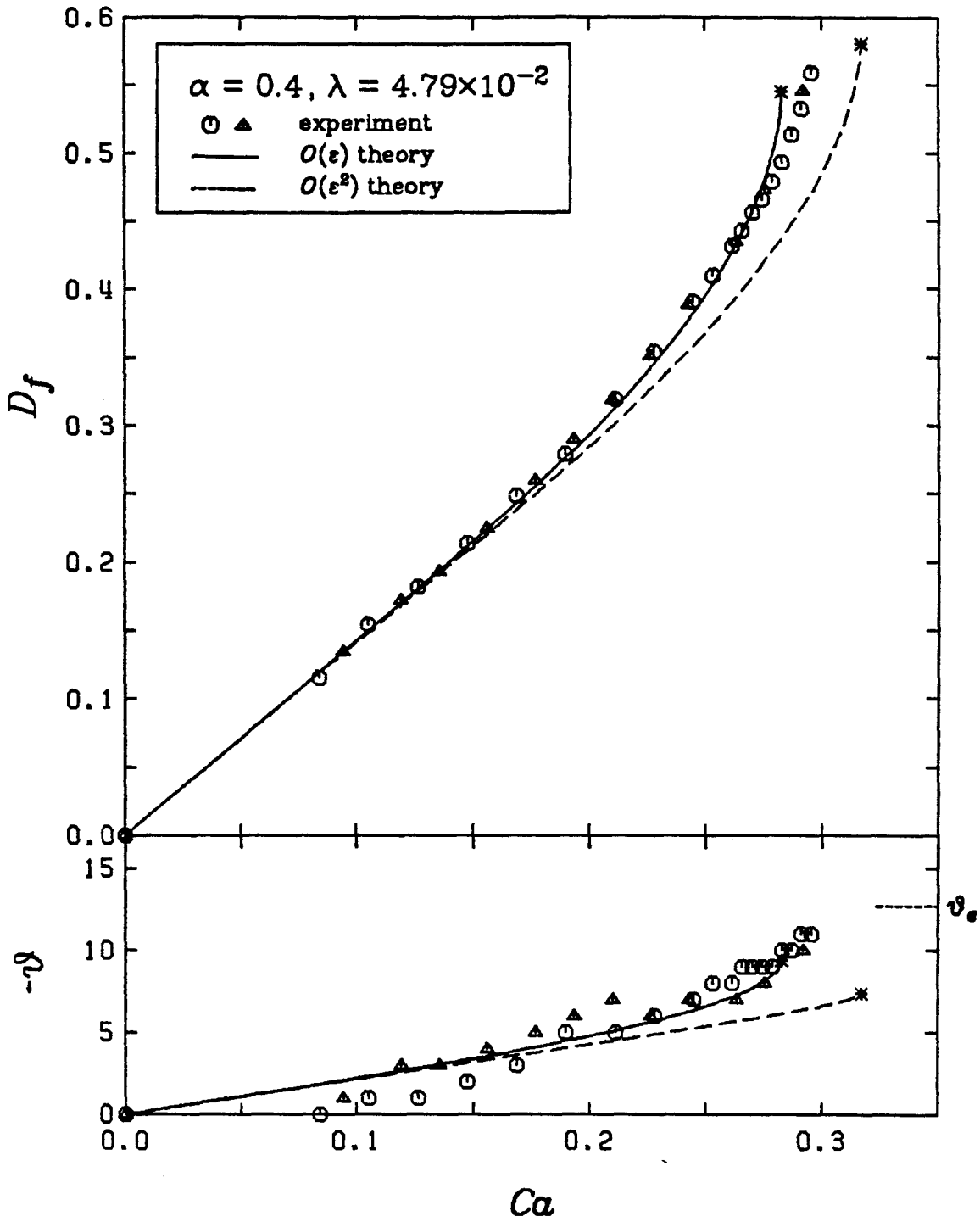

Figure A3.27
Deformation Curve for $\alpha = 0.4$, $\lambda = 4.79\times10^{-2}$

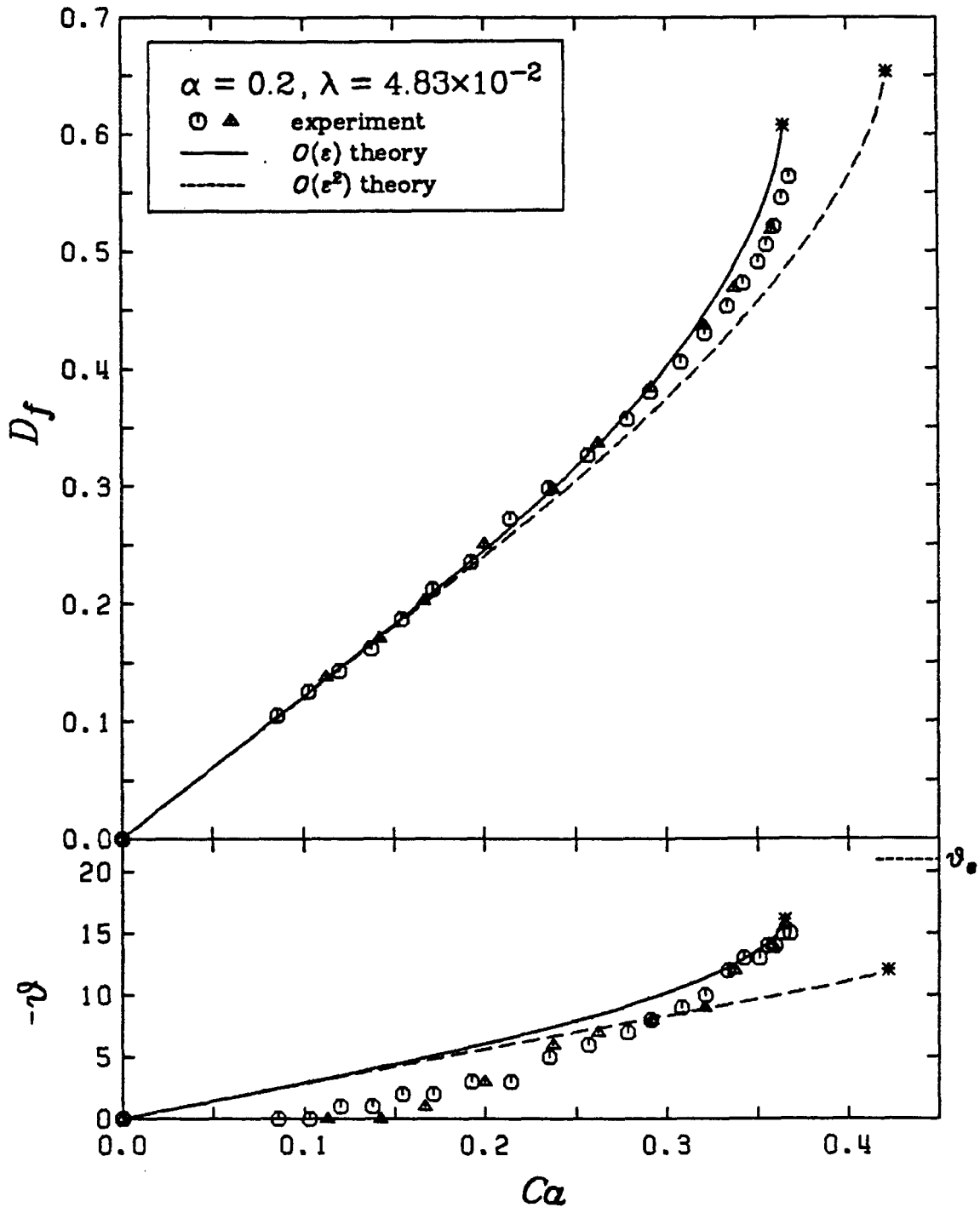

Figure A3.28
Deformation Curve for $\alpha = 0.2$, $\lambda = 4.83\times10^{-2}$

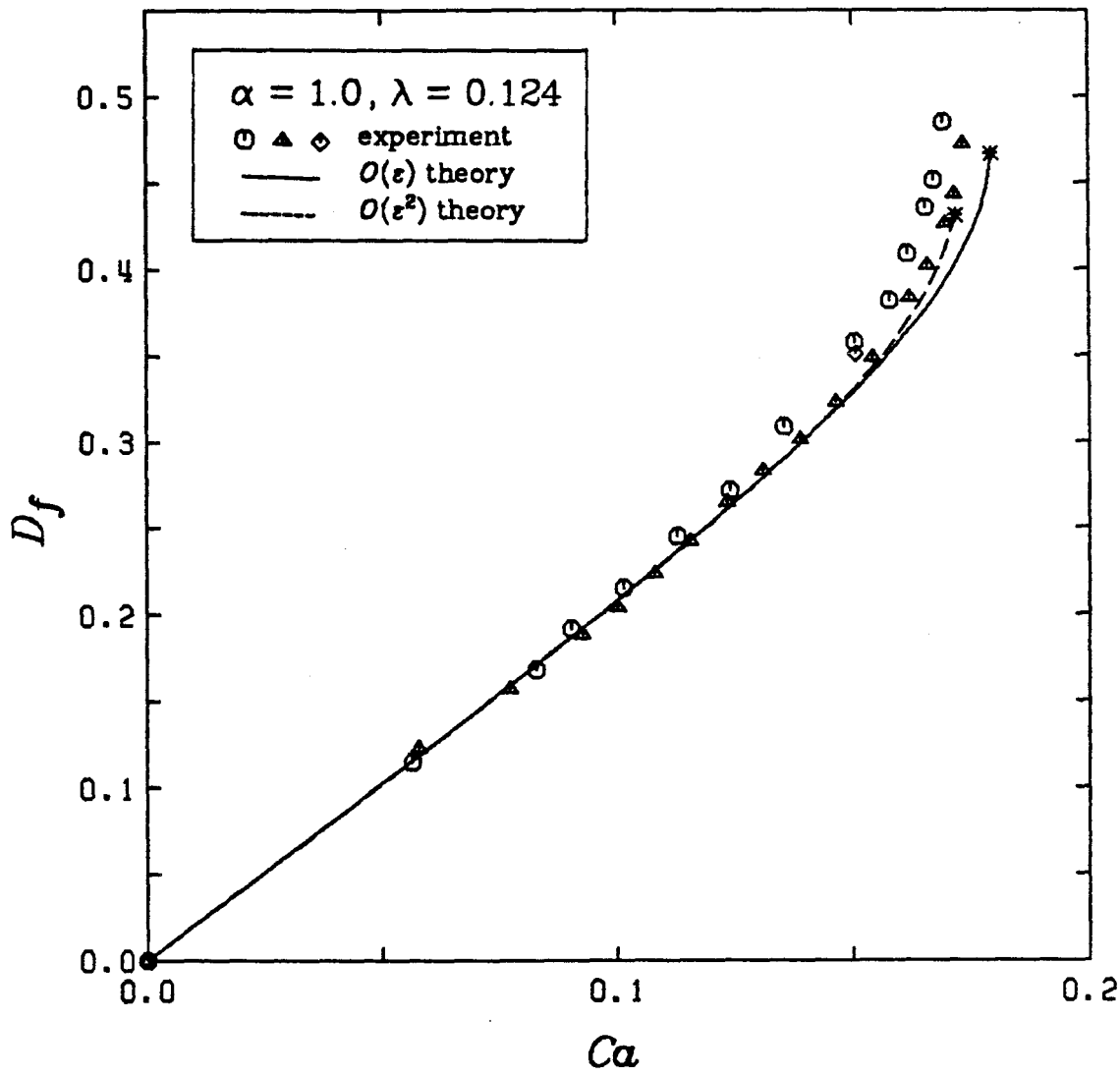

Figure A3.29
Deformation Curve for $\alpha = 1.0$, $\lambda = 0.124$

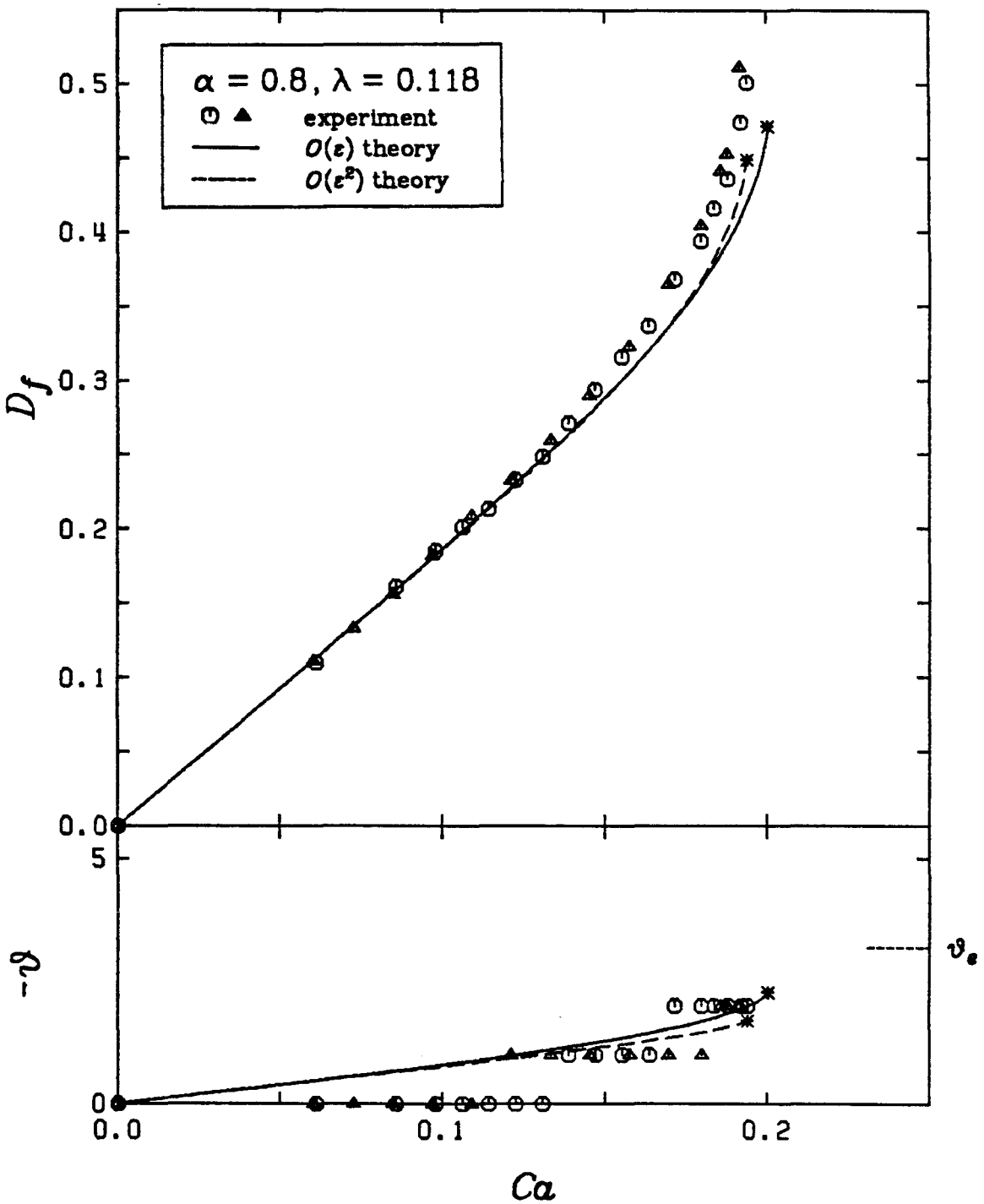

Figure A3.30
Deformation Curve for $\alpha = 0.8$, $\lambda = 0.118$

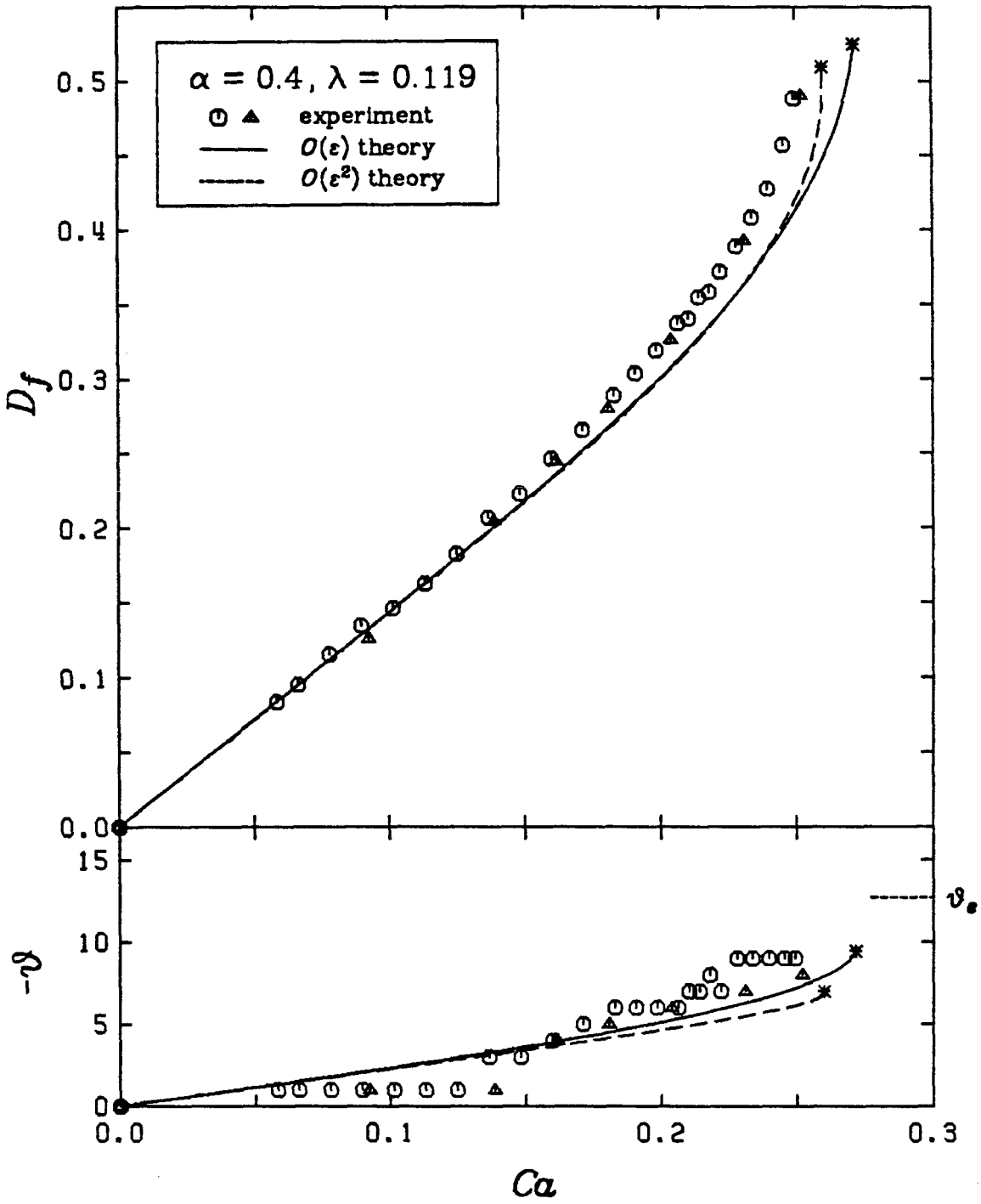

Figure A3.31
Deformation Curve for $\alpha = 0.4$, $\lambda = 0.119$

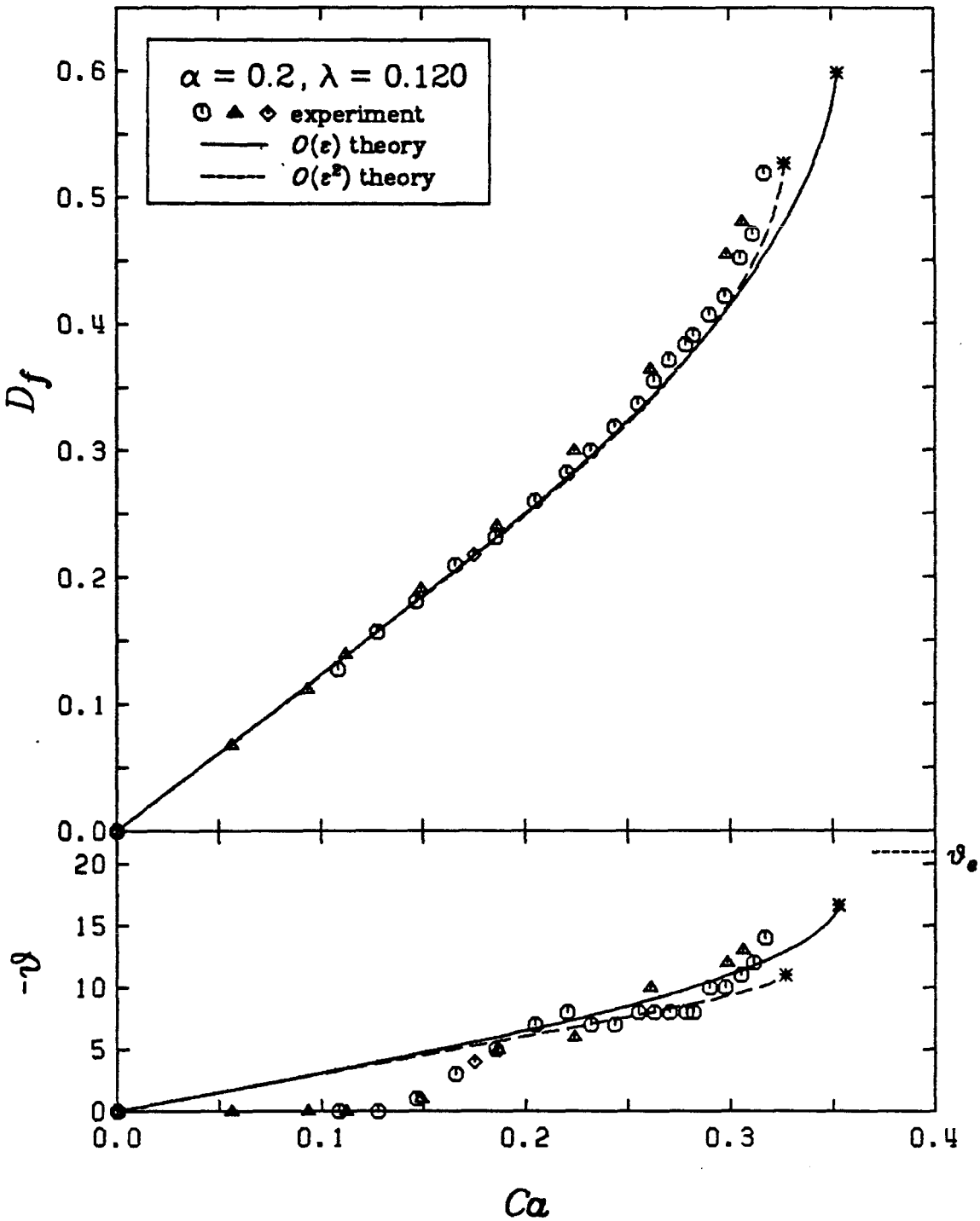

Figure A3.32
Deformation Curve for $\alpha = 0.2$, $\lambda = 0.120$

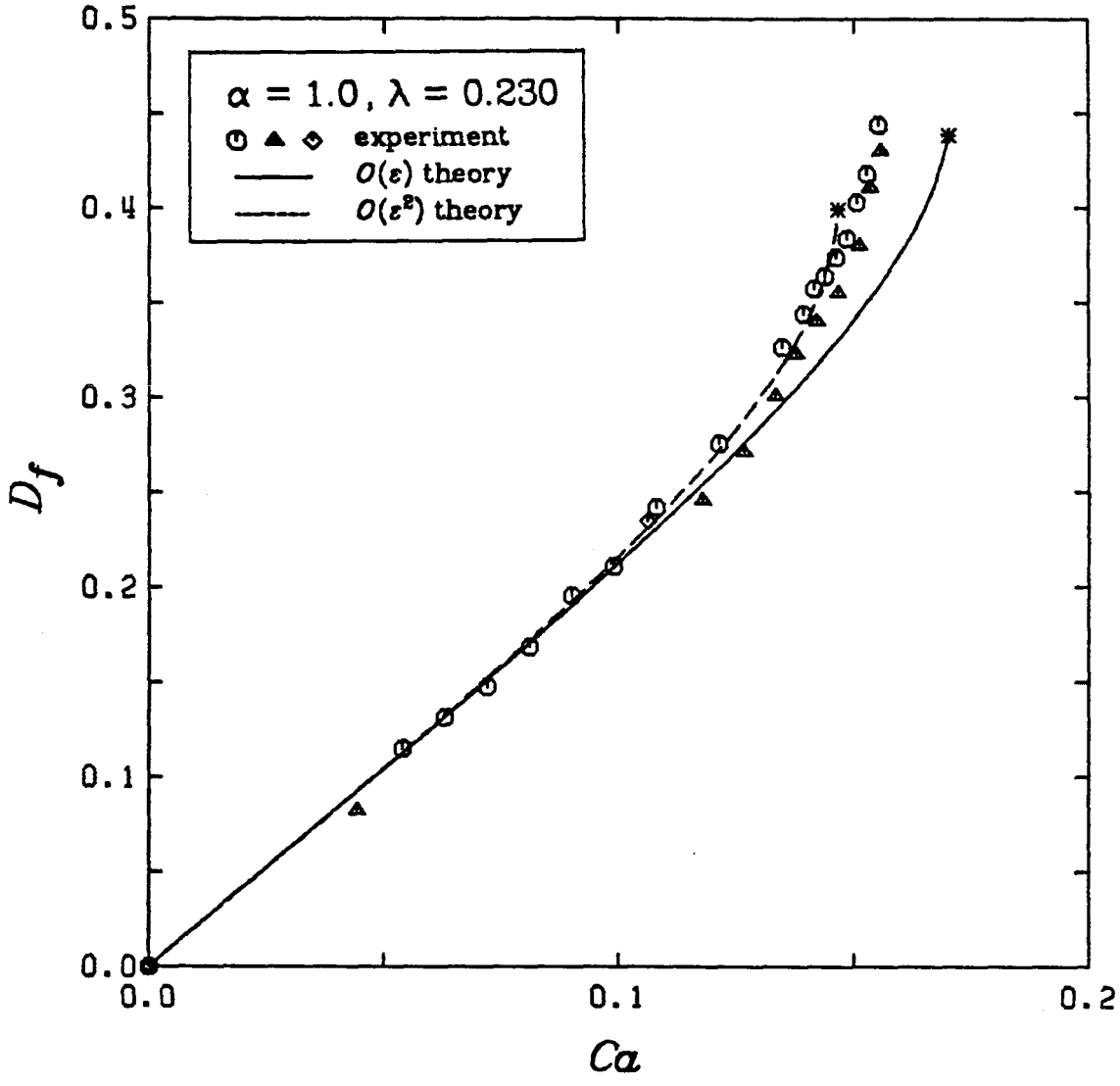

Figure A3.33
Deformation Curve for $\alpha = 1.0$, $\lambda = 0.230$

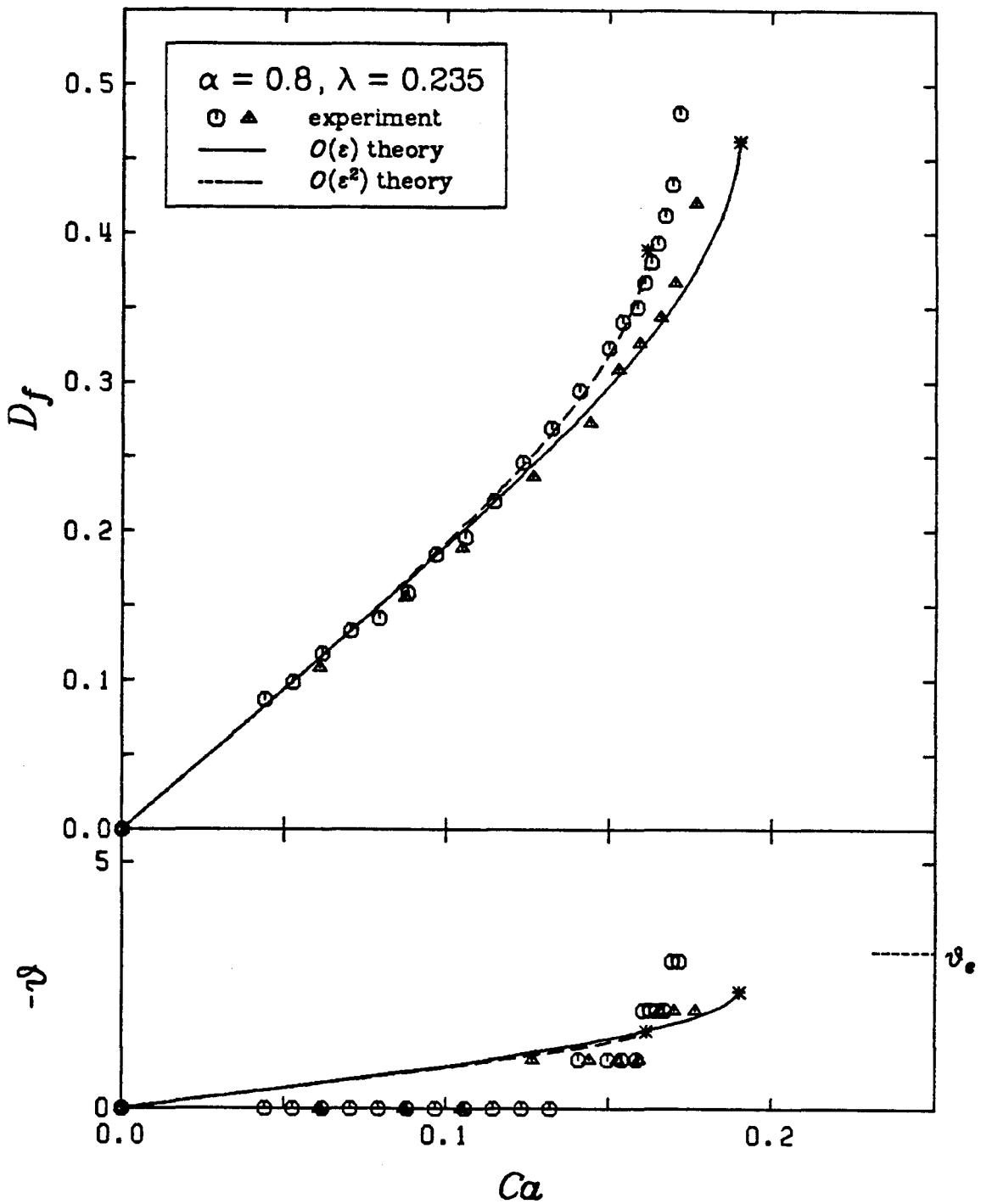

Figure A3.34
Deformation Curve for $\alpha = 0.8$, $\lambda = 0.235$

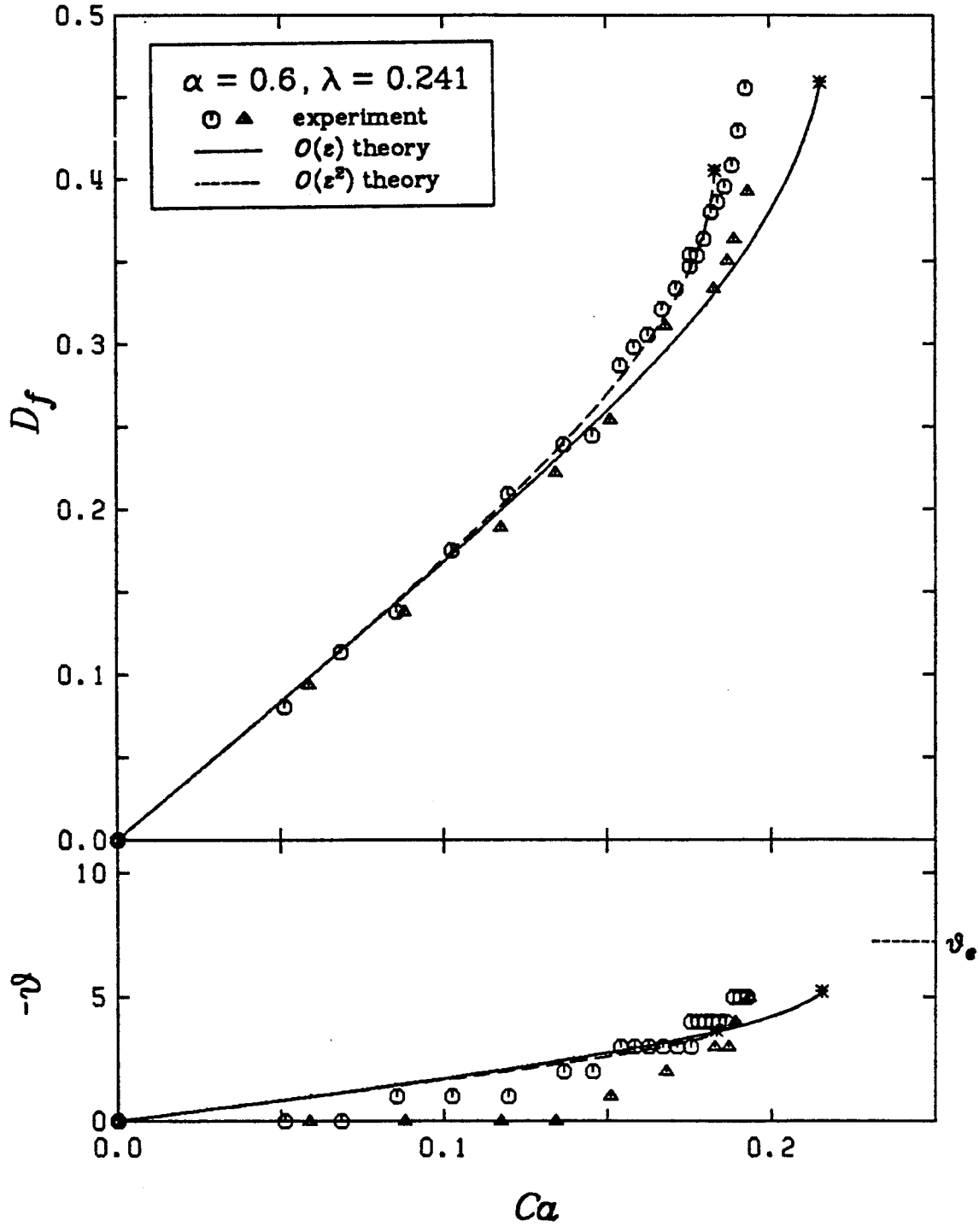

Figure A3.35
Deformation Curve for $\alpha = 0.6$, $\lambda = 0.241$

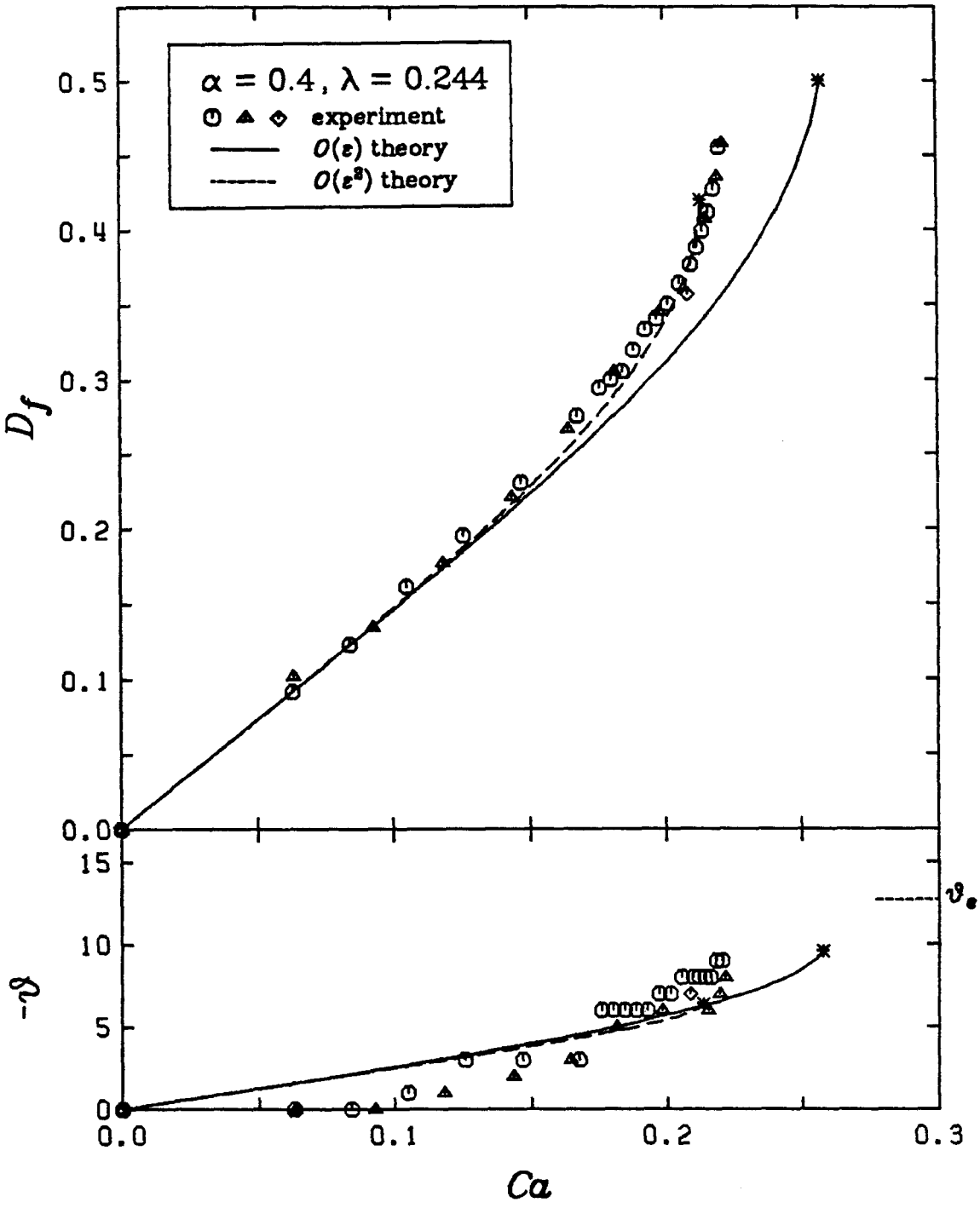

Figure A3.36
Deformation Curve for $\alpha = 0.4$, $\lambda = 0.244$

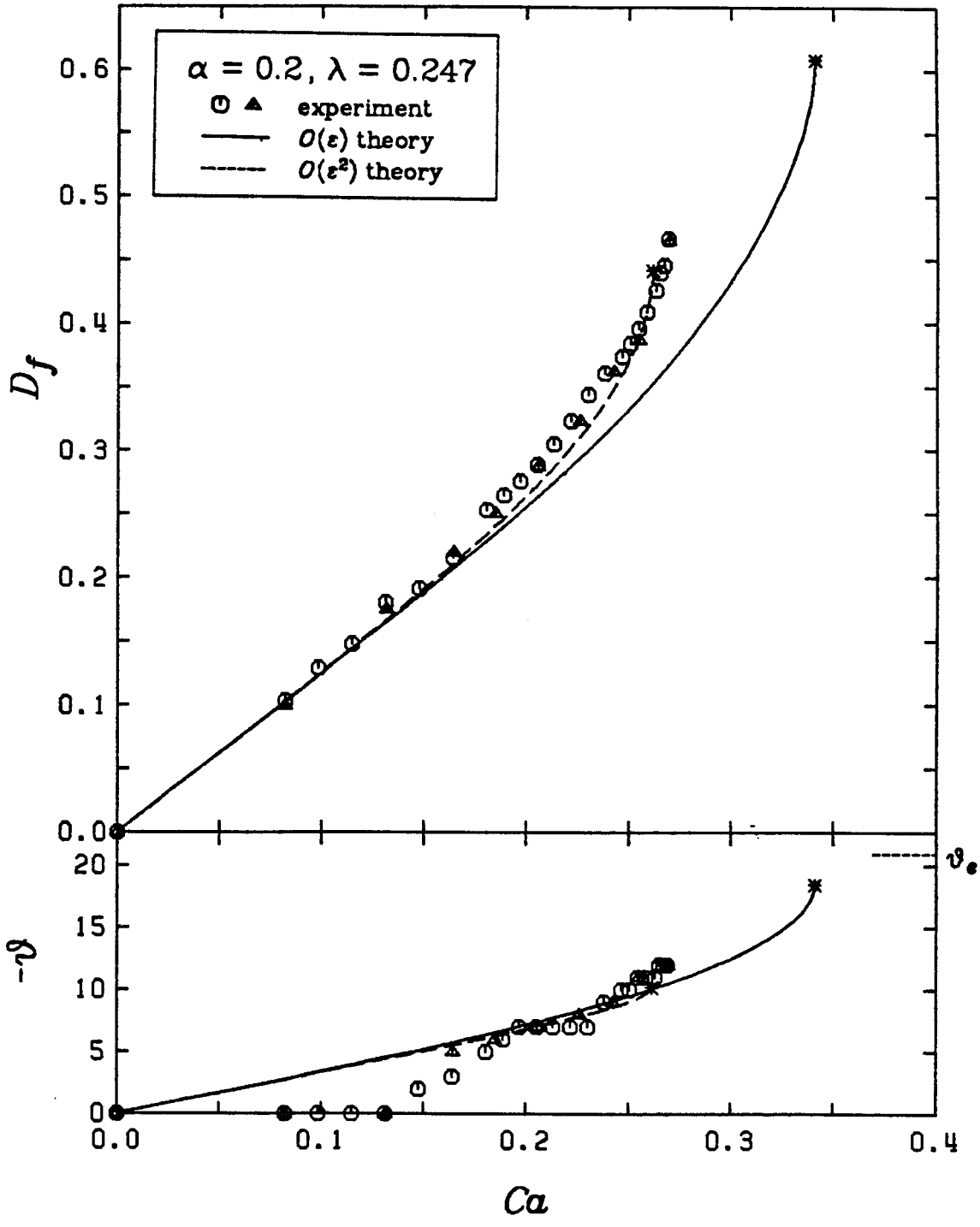

Figure A3.37
Deformation Curve for $\alpha = 0.2$, $\lambda = 0.247$

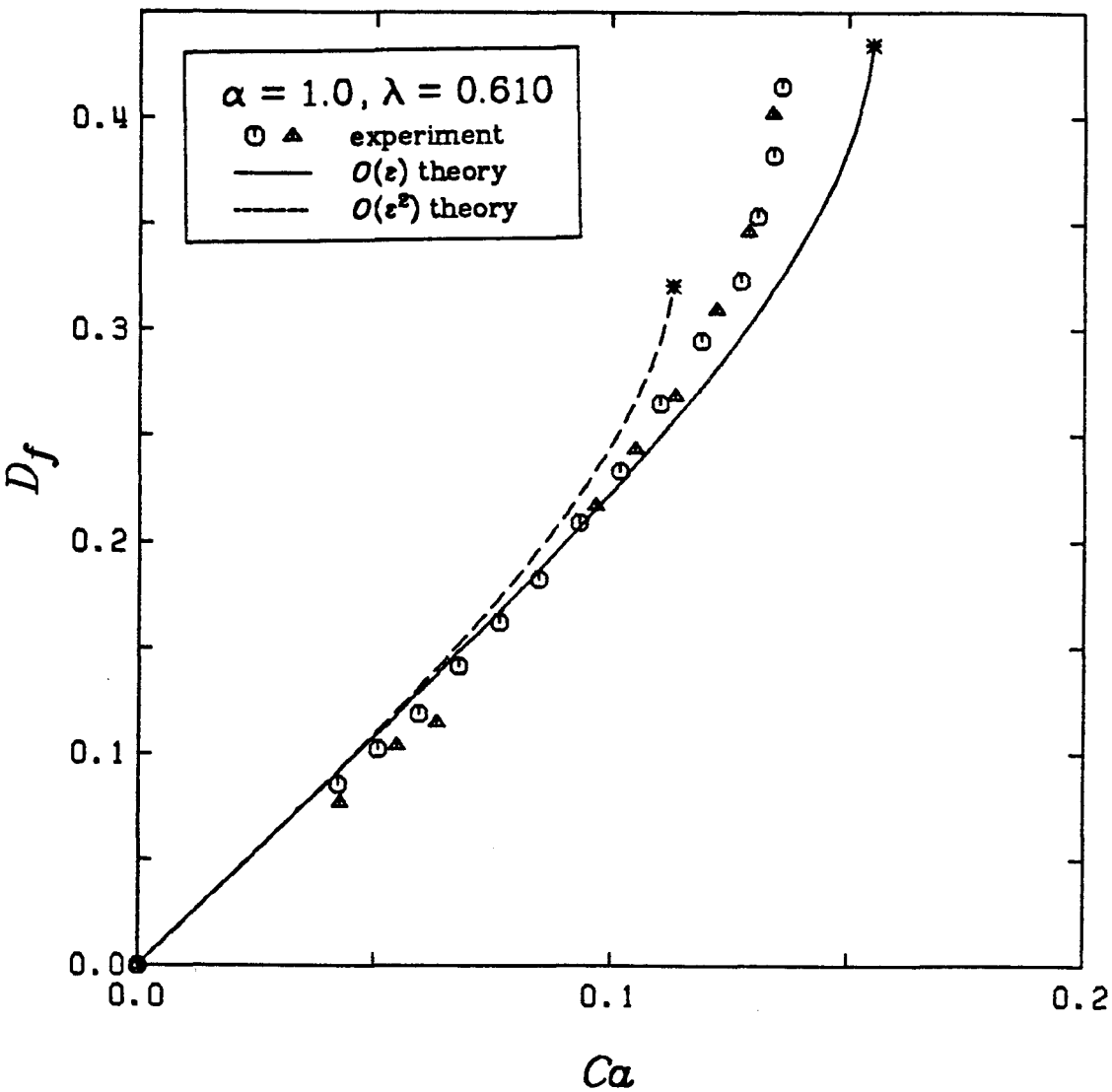

Figure A3.38
Deformation Curve for $\alpha = 1.0$, $\lambda = 0.610$

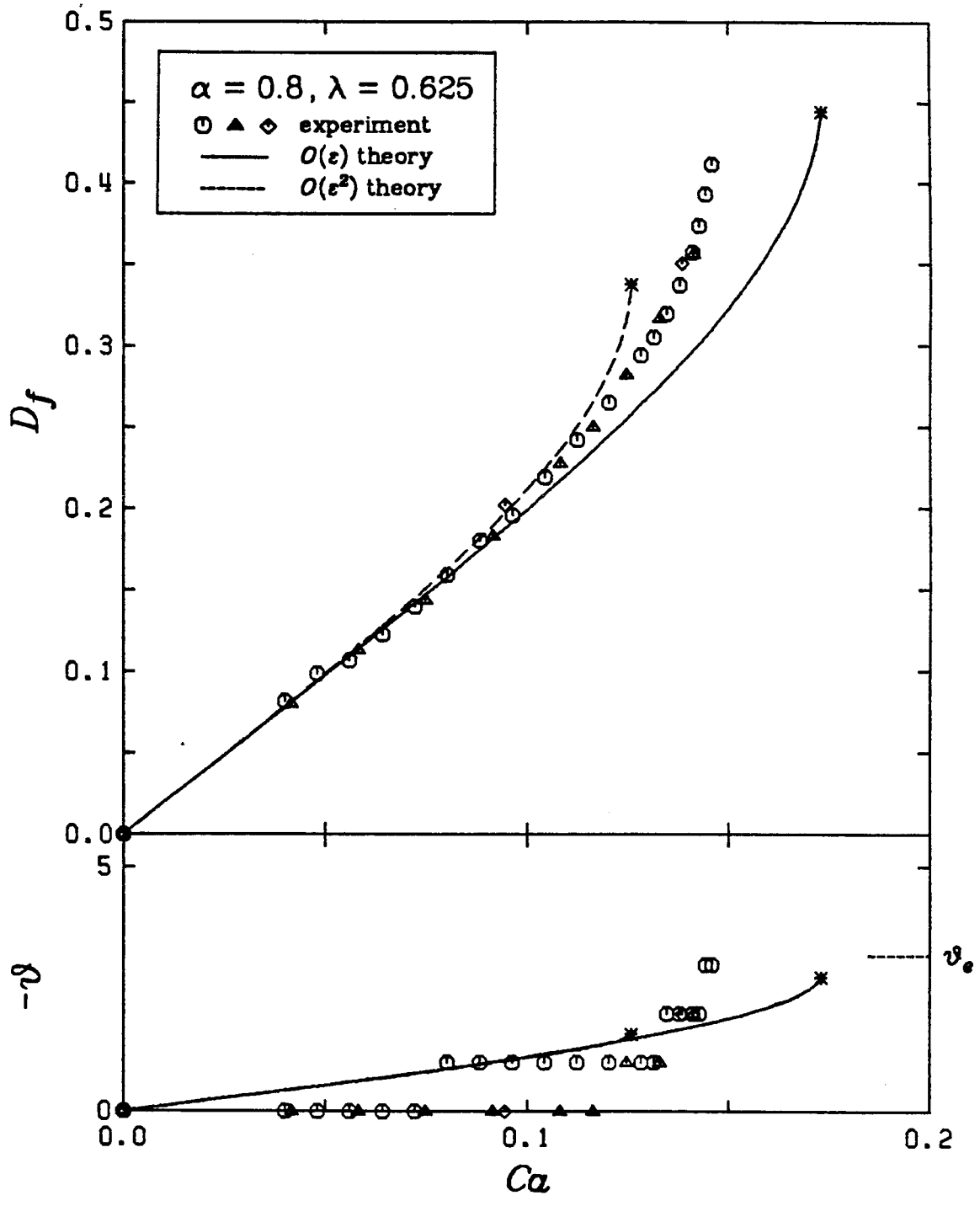

Figure A3.39
Deformation Curve for $\alpha = 0.8$, $\lambda = 0.625$

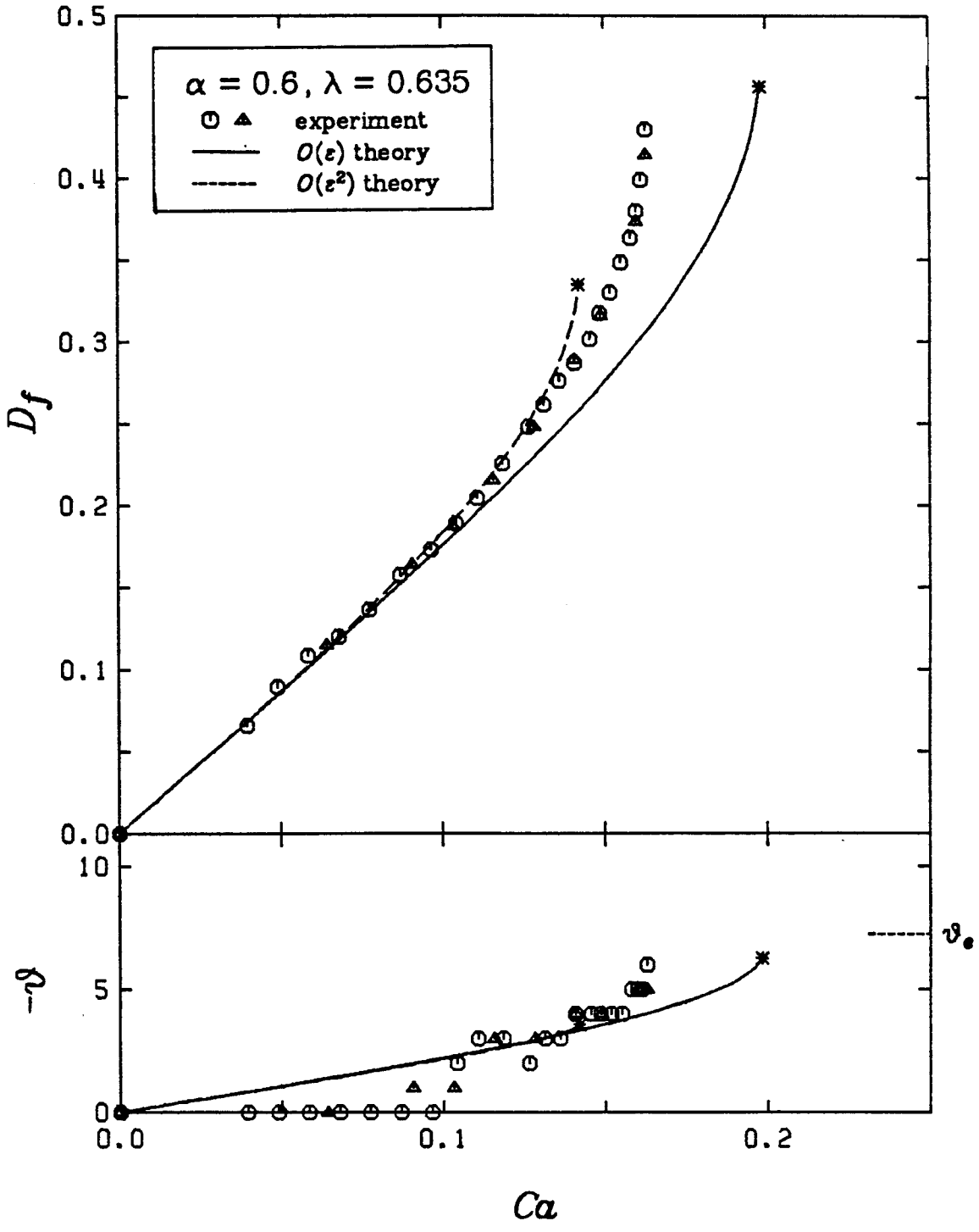

Figure A3.40
Deformation Curve for $\alpha = 0.6$, $\lambda = 0.635$

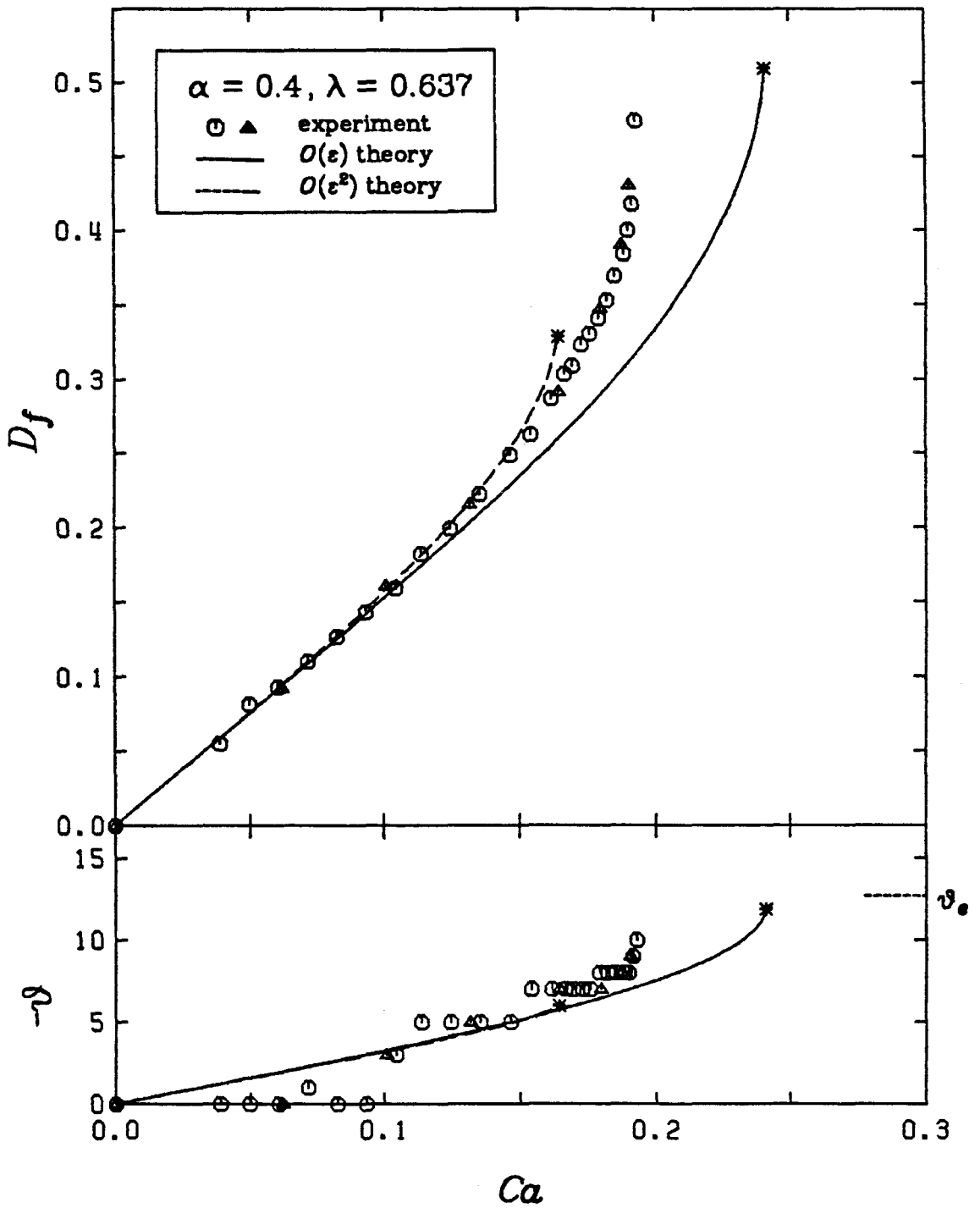

Figure A3.41
Deformation Curve for $\alpha = 0.4$, $\lambda = 0.637$

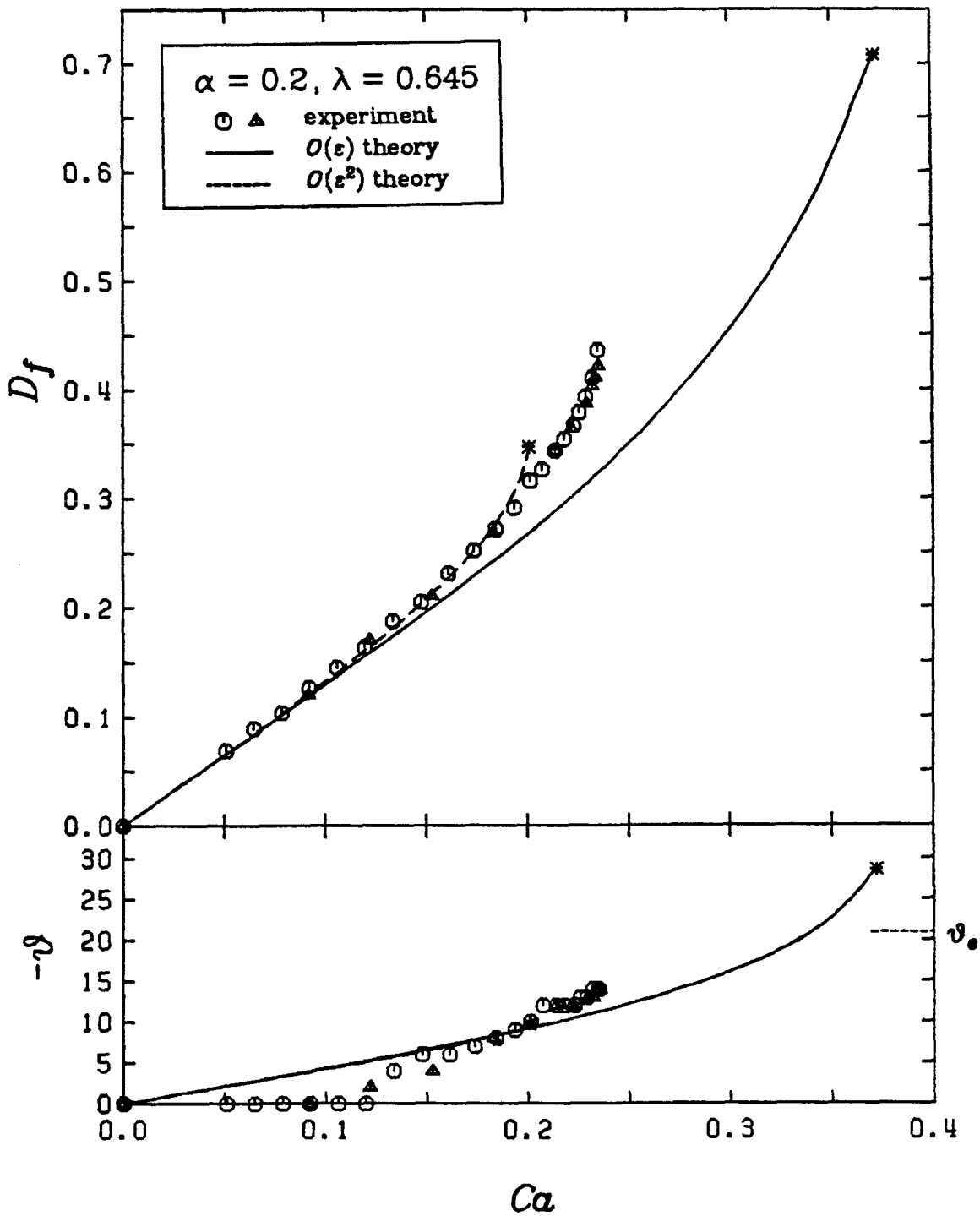

Figure A3.42
Deformation Curve for $\alpha = 0.2$, $\lambda = 0.645$

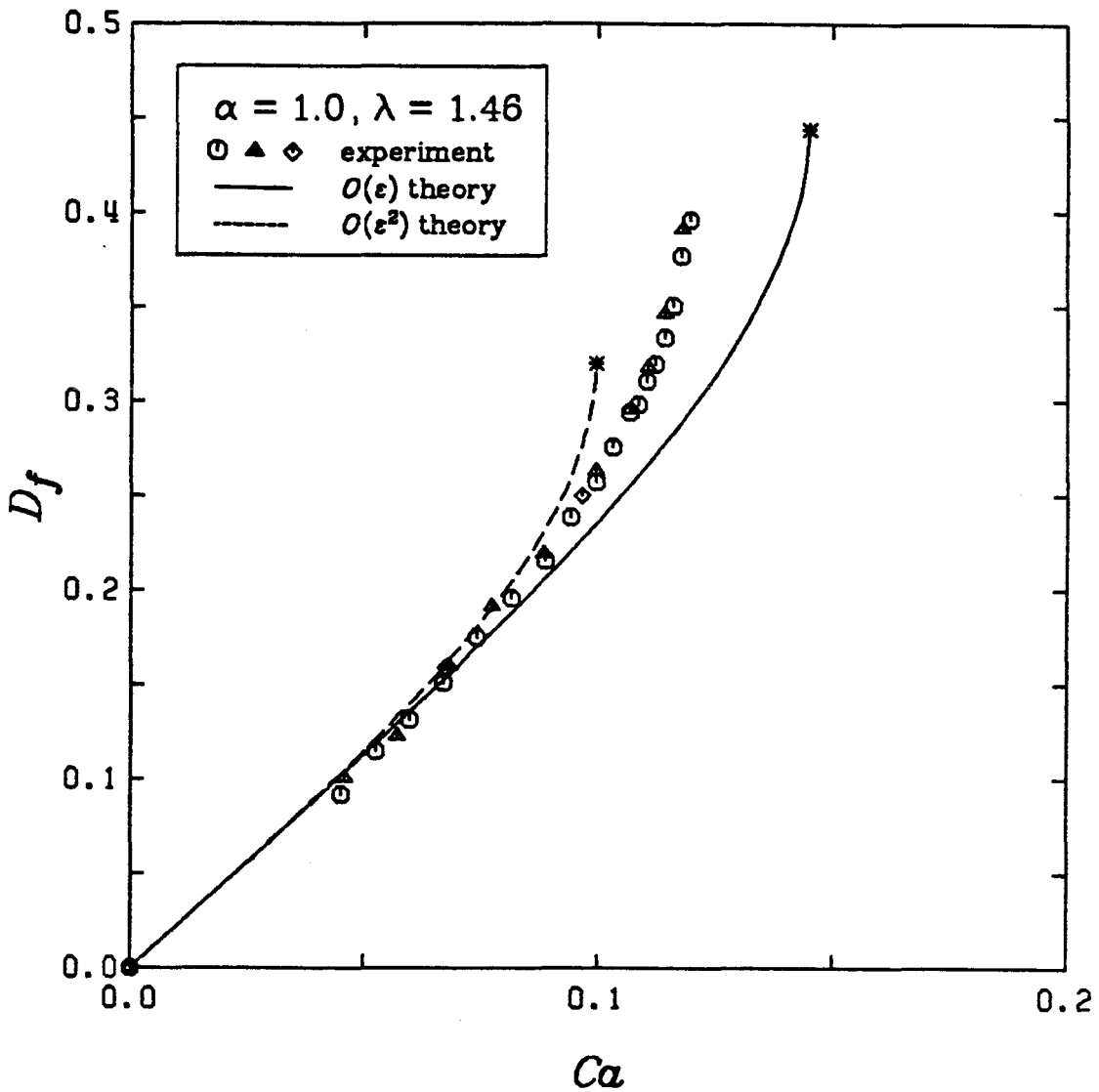

Figure A3.43
Deformation Curve for $\alpha = 1.0$, $\lambda = 1.46$

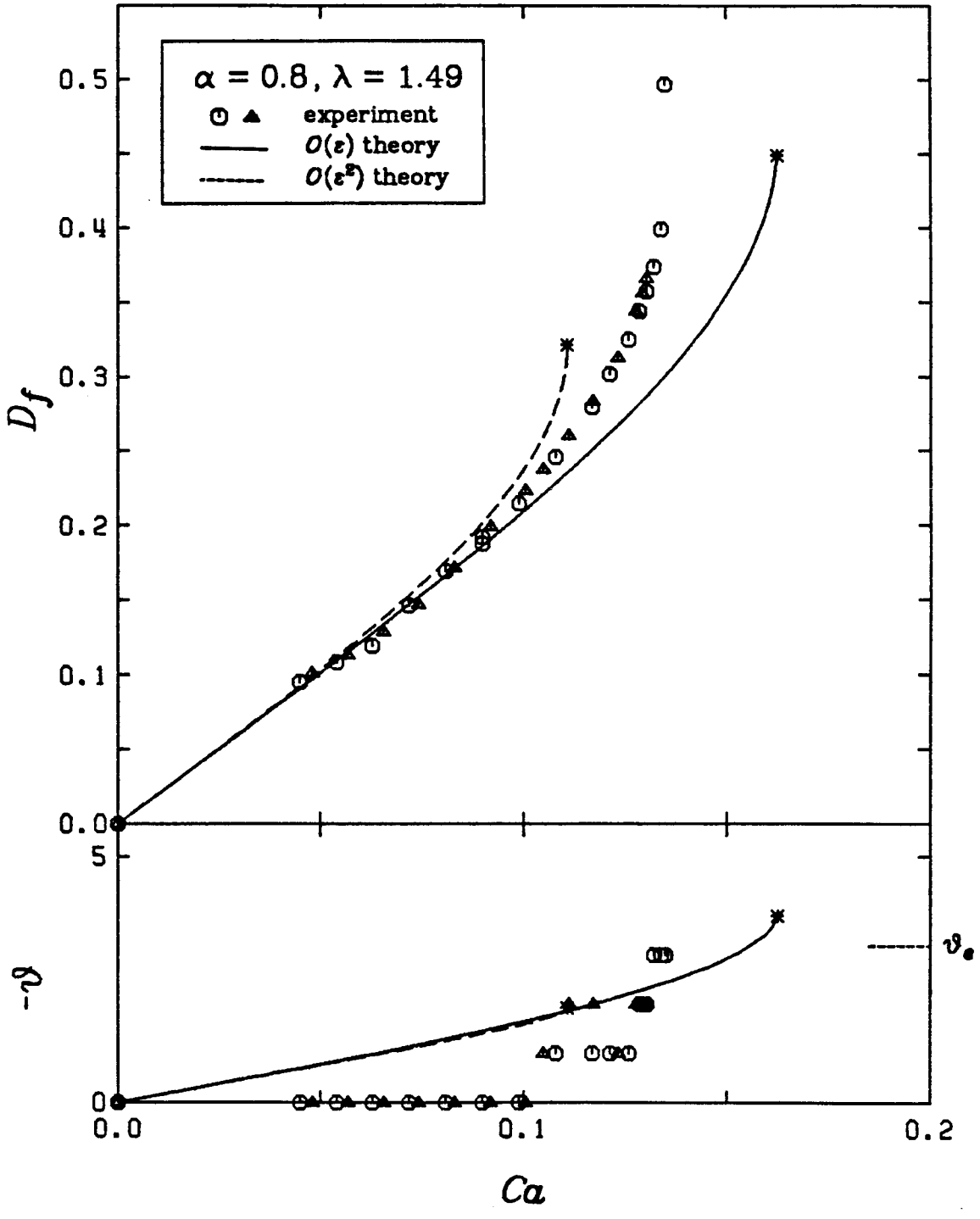

Figure A3.44
Deformation Curve for α = 0.8, λ = 1.49

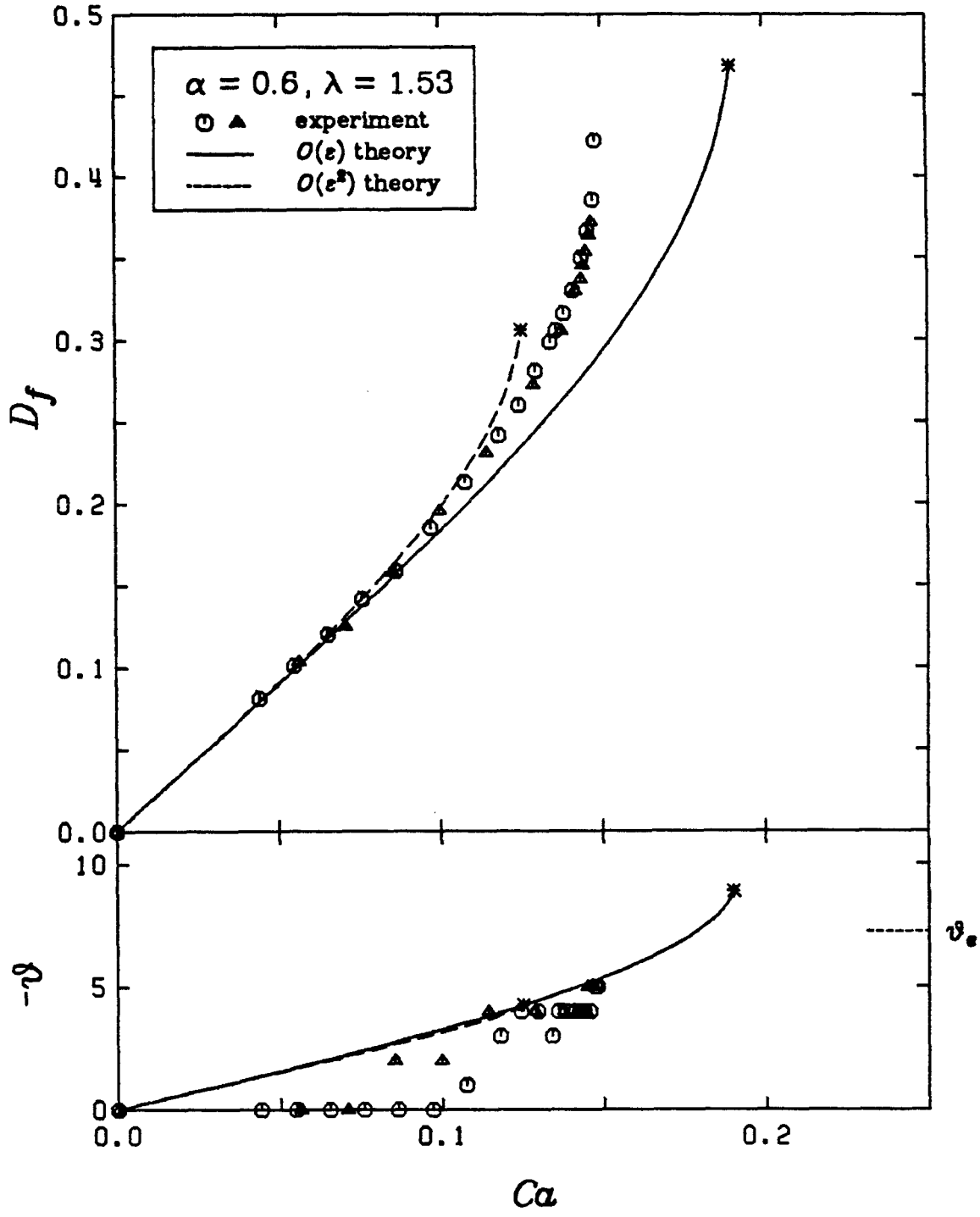

Figure A3.45
Deformation Curve for $\alpha = 0.6$, $\lambda = 1.53$

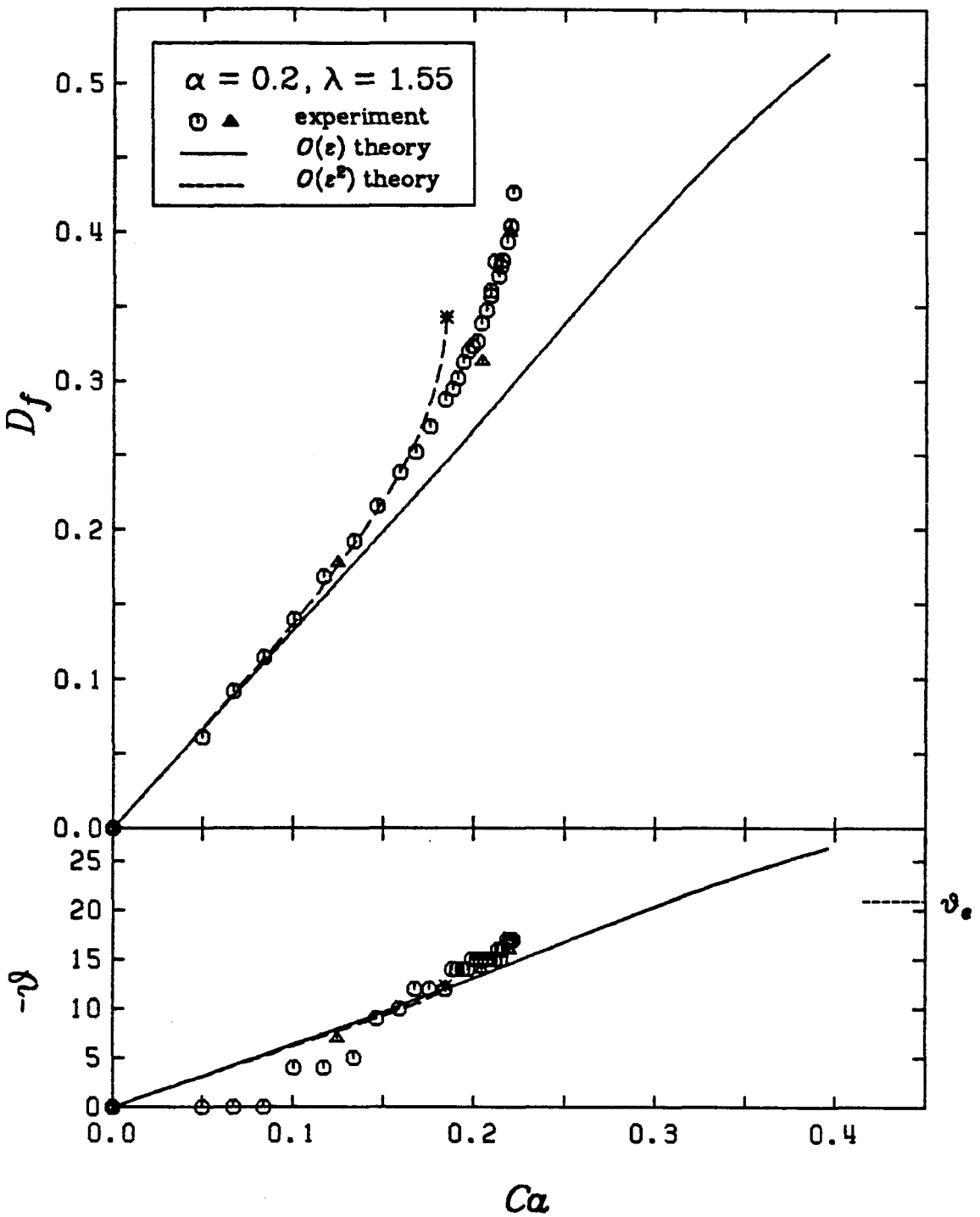

Figure A3.46
Deformation Curve for $\alpha = 0.2$, $\lambda = 1.55$

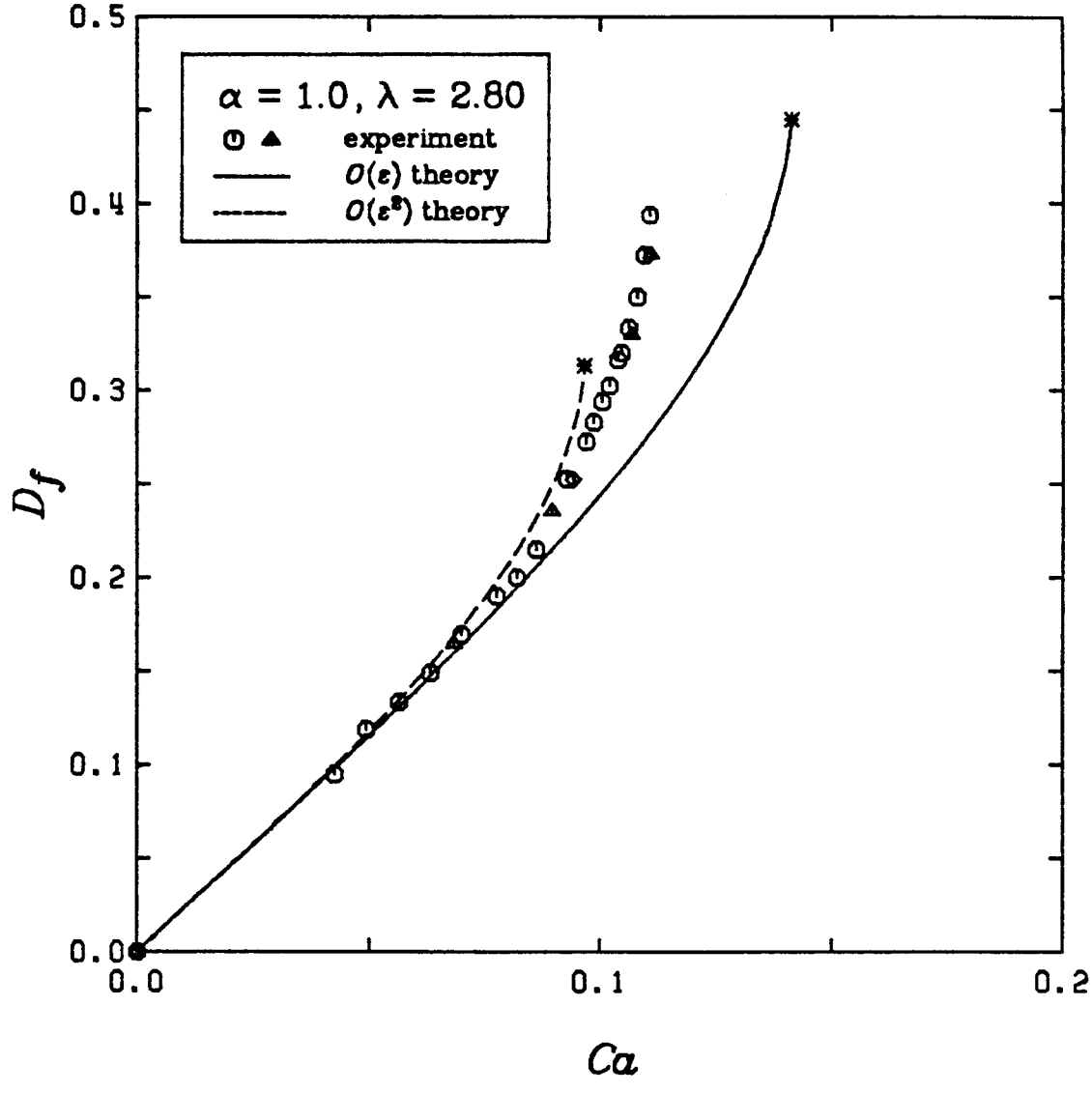

Figure A3.47
Deformation Curve for $\alpha = 1.0$, $\lambda = 2.80$

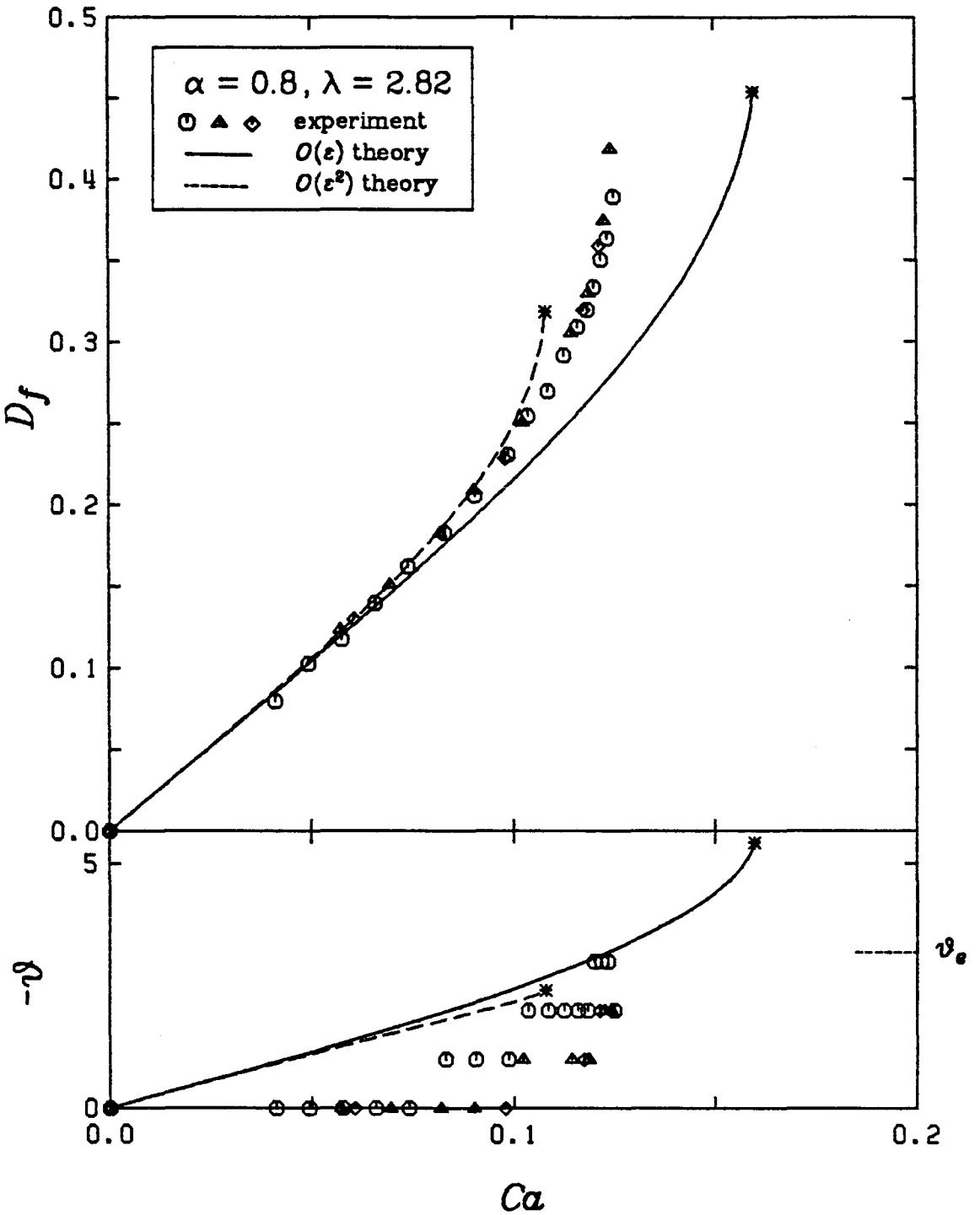

Figure A3.48
Deformation Curve for $\alpha = 0.8$, $\lambda = 2.82$

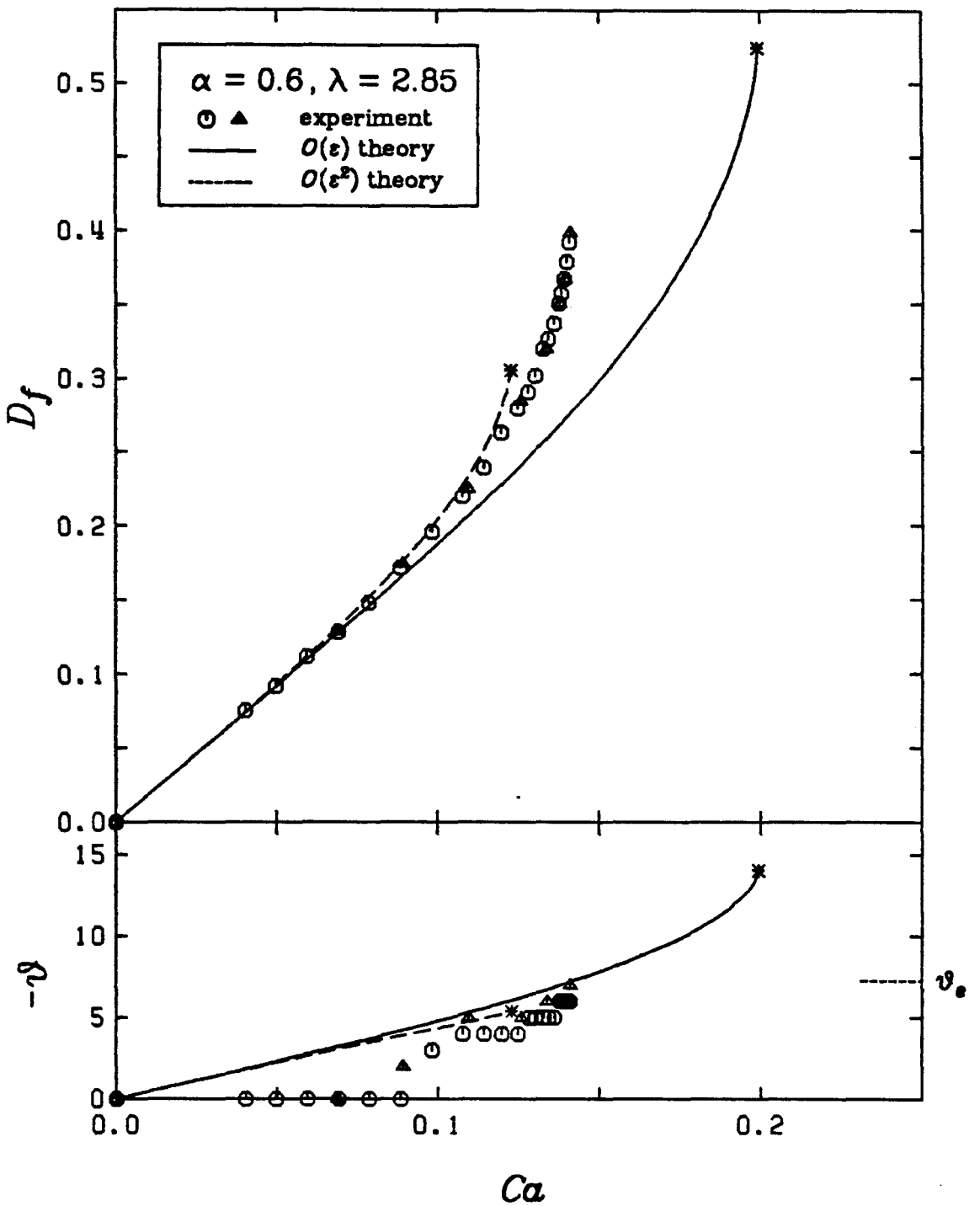

Figure A3.49
Deformation Curve for α = 0.6, λ = 2.85

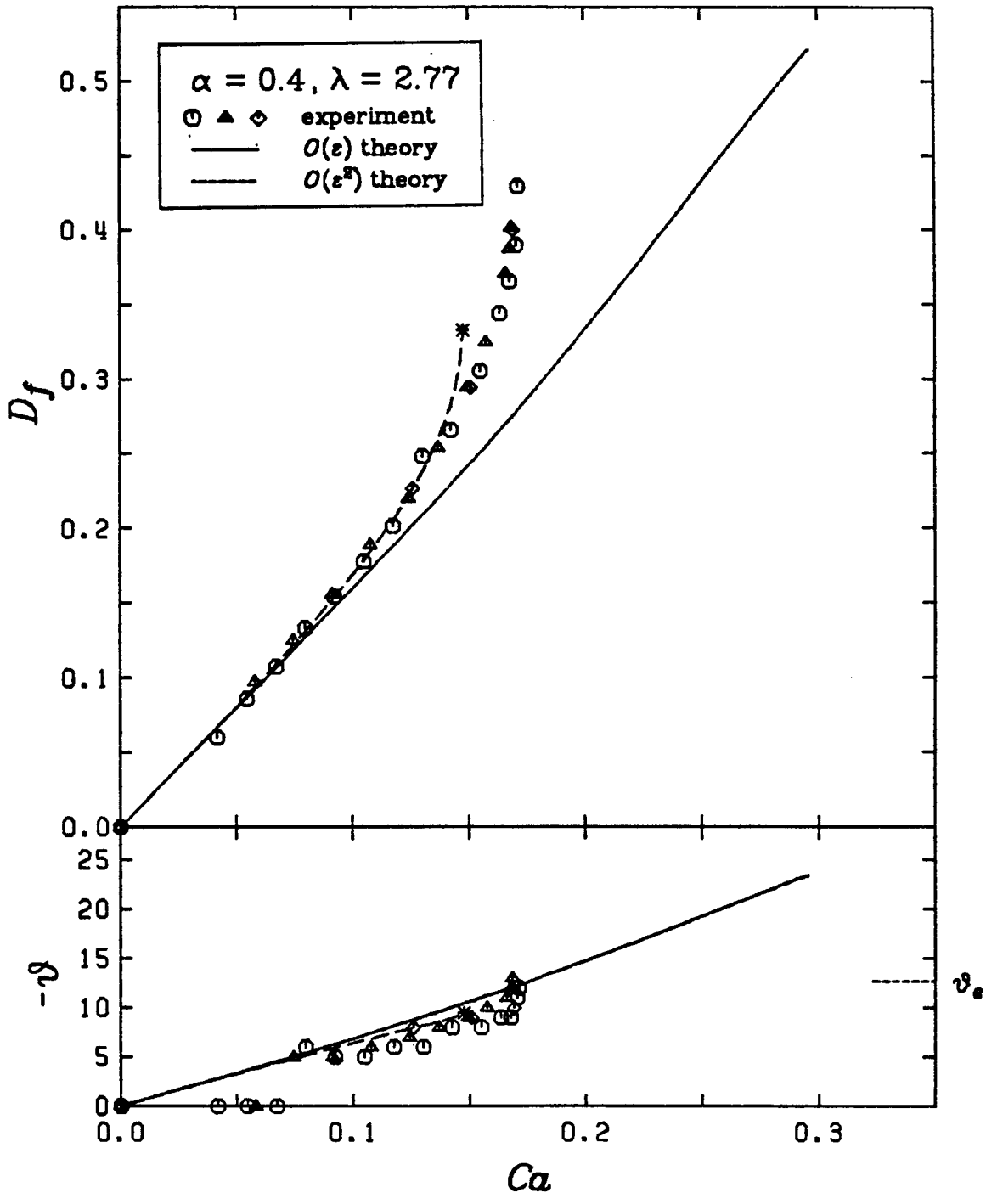

Figure A3.50
Deformation Curve for $\alpha = 0.4$, $\lambda = 2.77$

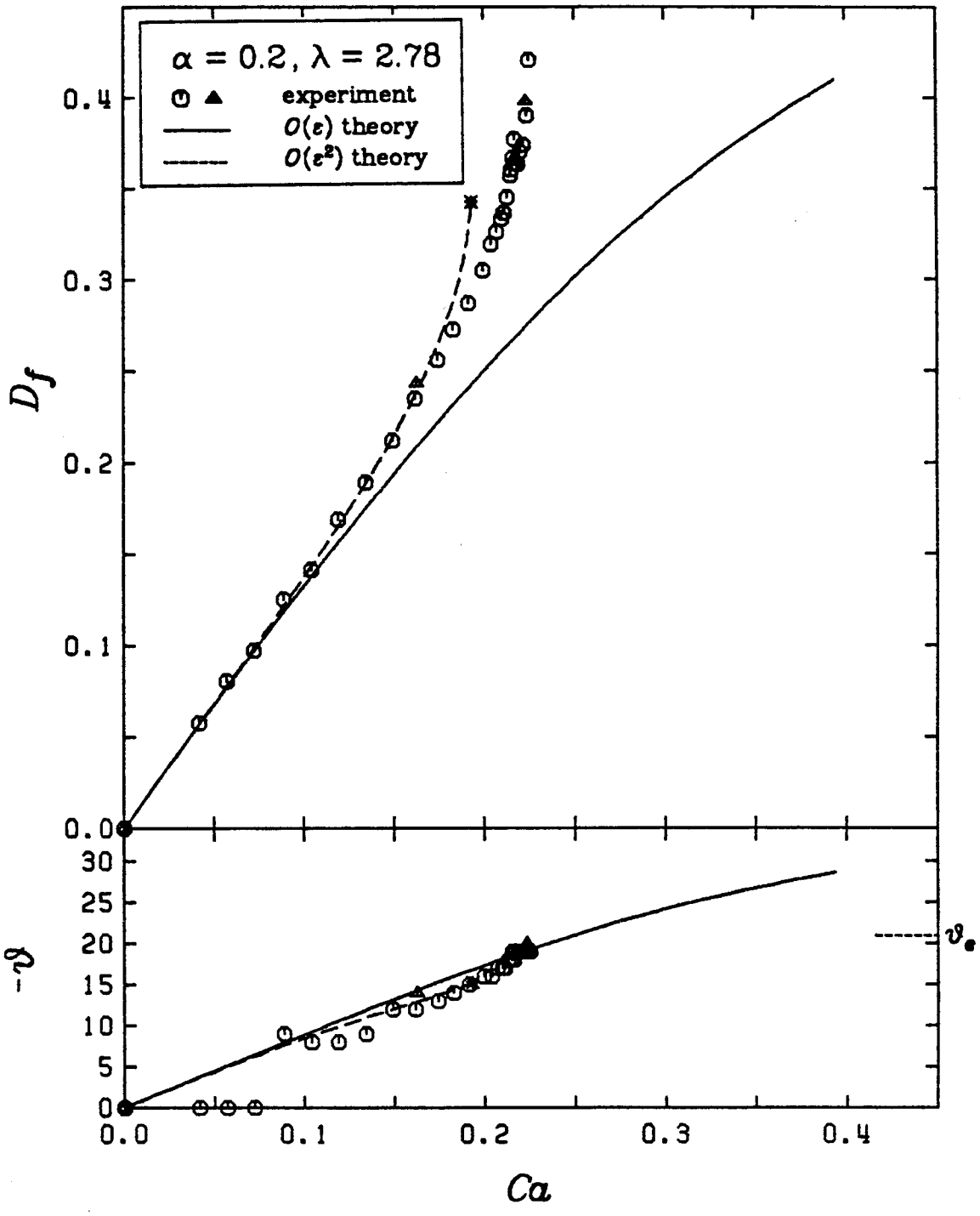

Figure A3.51
Deformation Curve for $\alpha = 0.2$, $\lambda = 2.78$

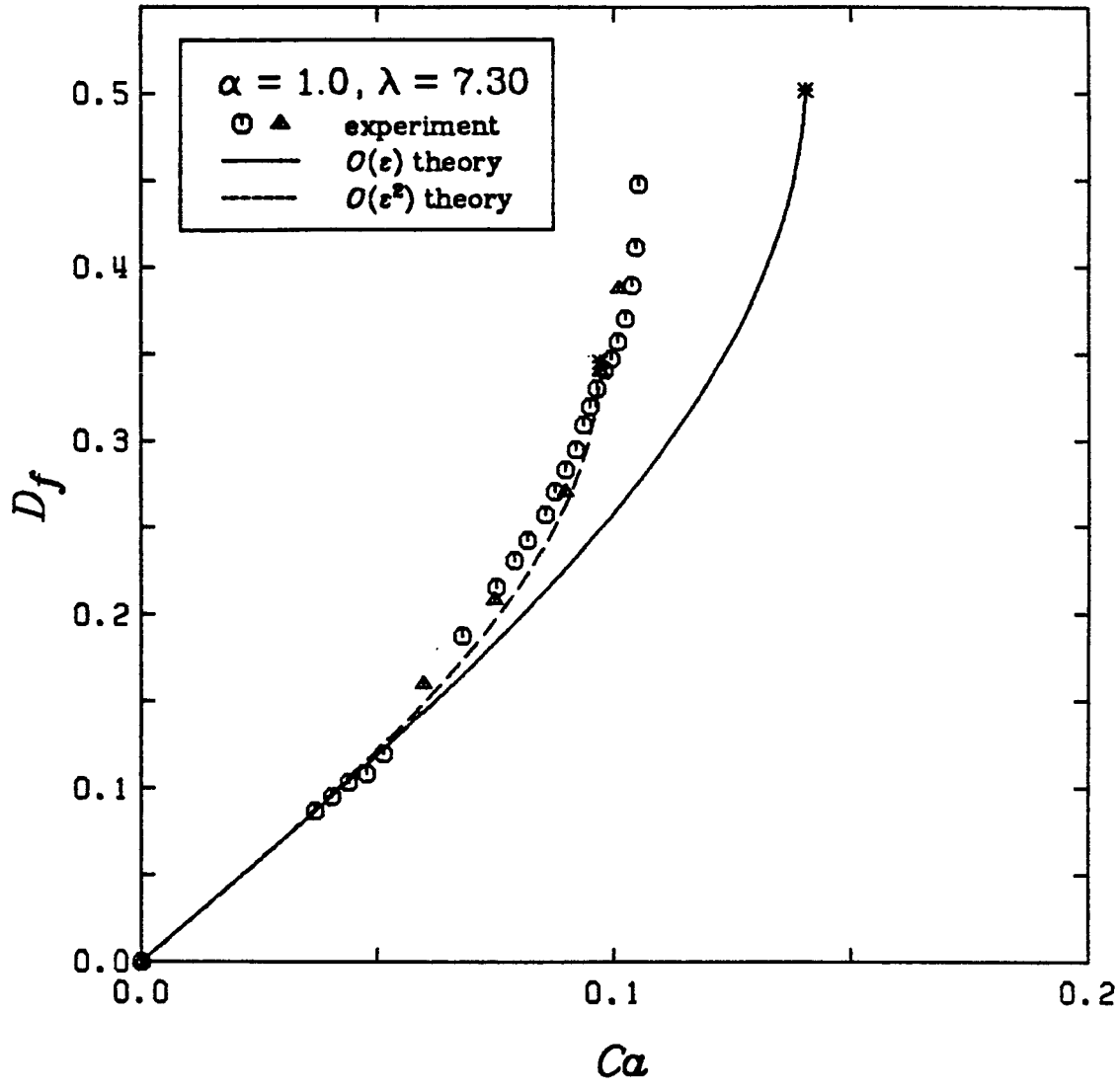

Figure A3.52
Deformation Curve for $\alpha = 1.0$, $\lambda = 7.30$

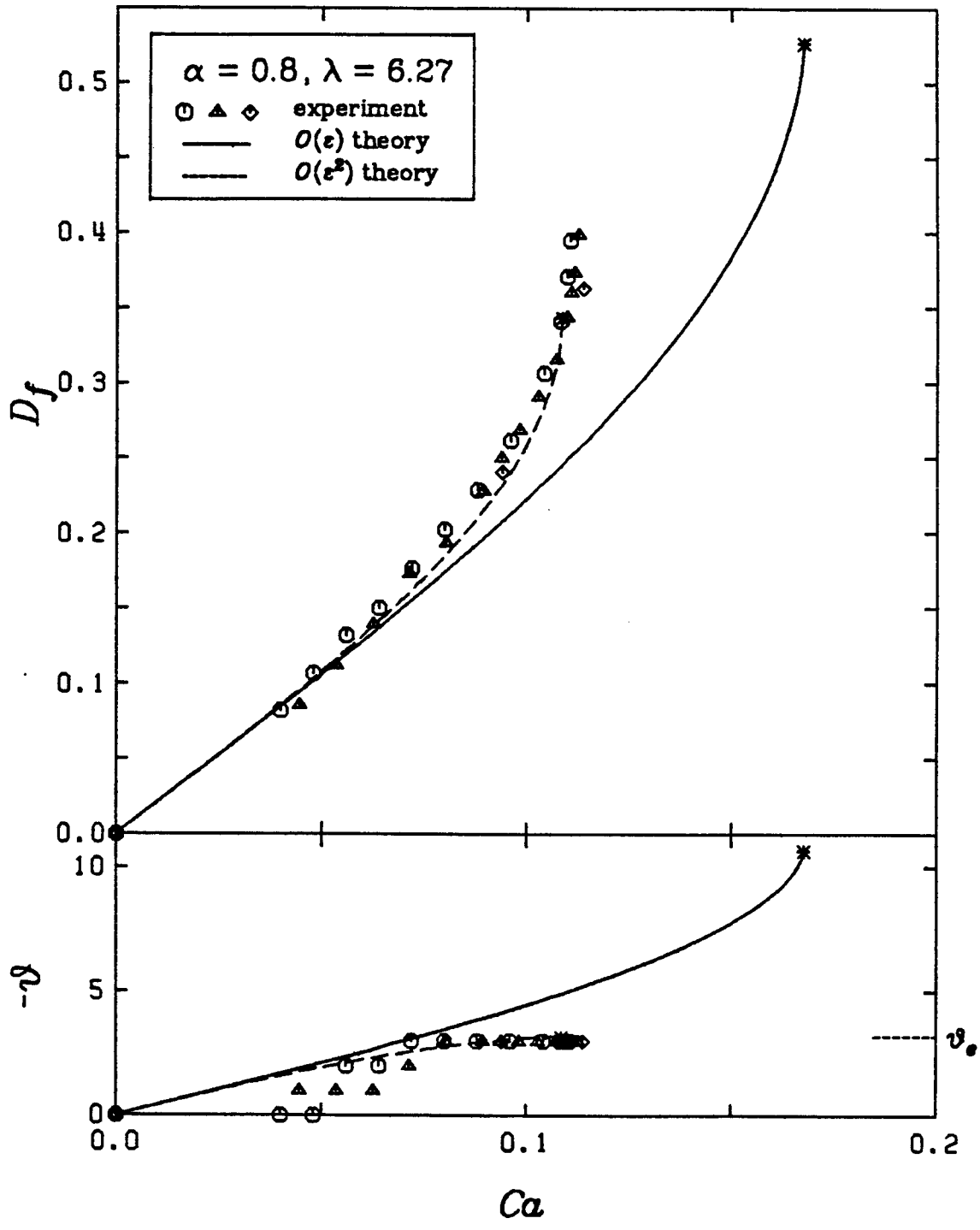

Figure A3.53
Deformation Curve for α = 0.8, λ = 6.27

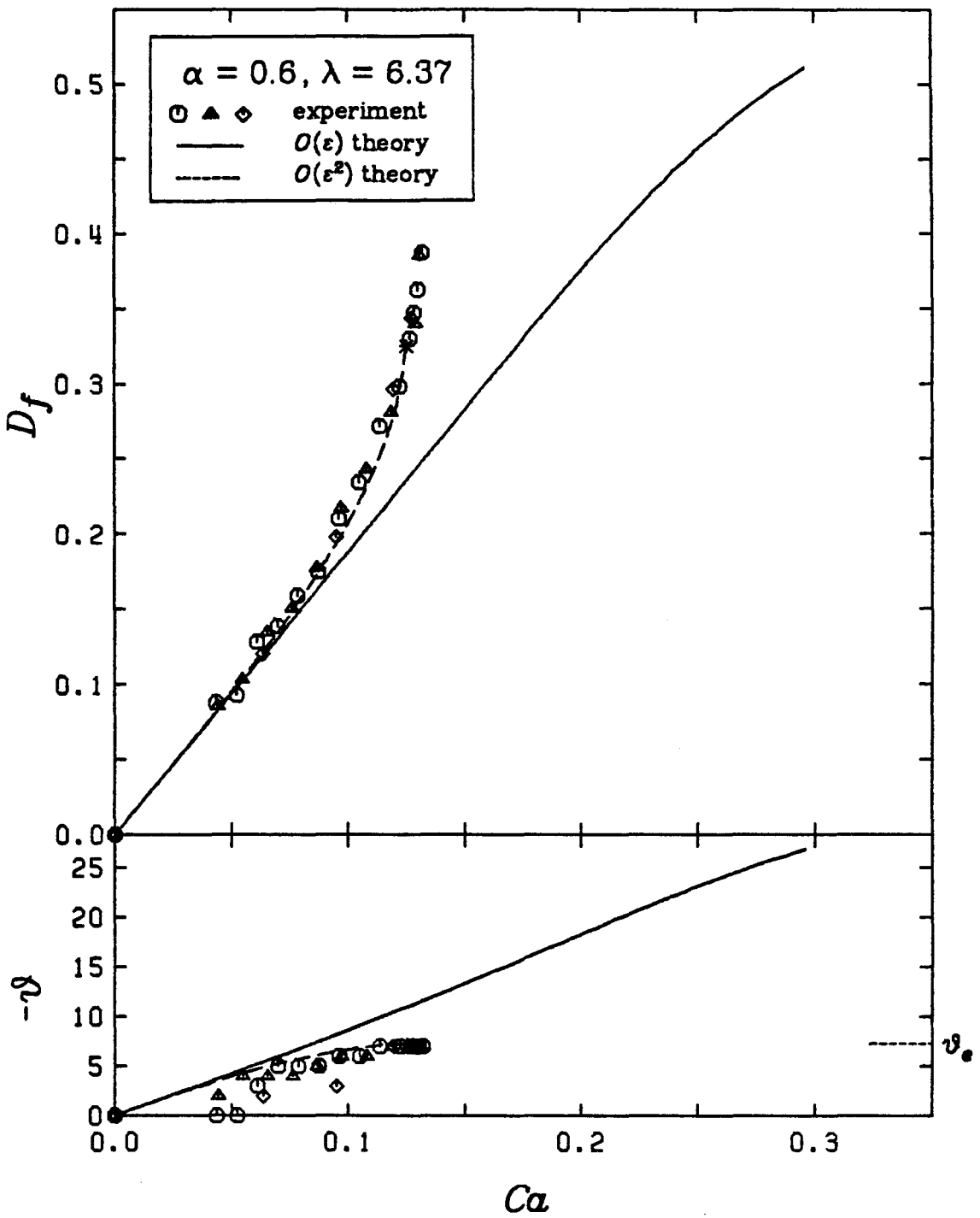

Figure A3.54
Deformation Curve for $\alpha = 0.6$, $\lambda = 6.37$

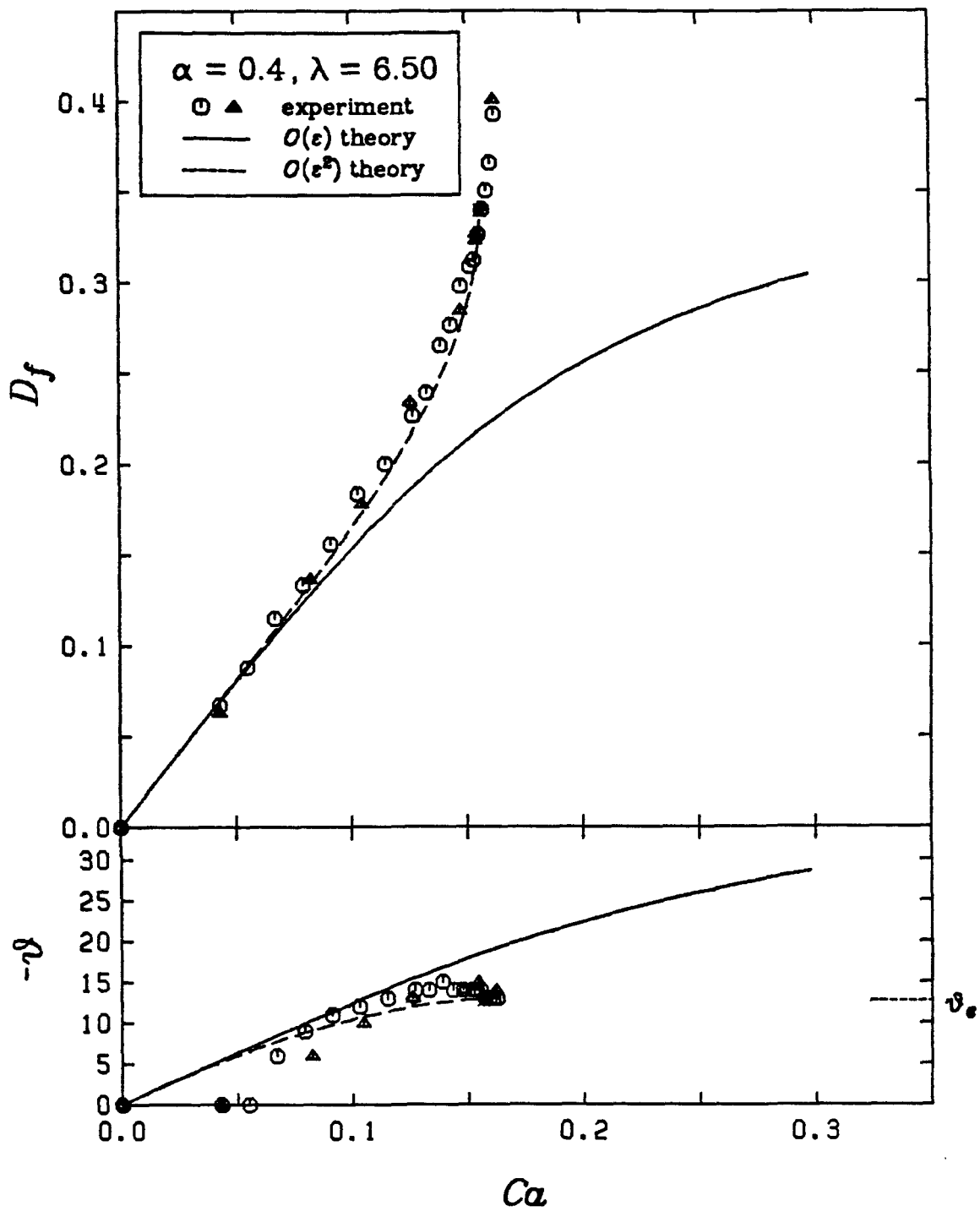

Figure A3.55
Deformation Curve for $\alpha = 0.4$, $\lambda = 6.50$

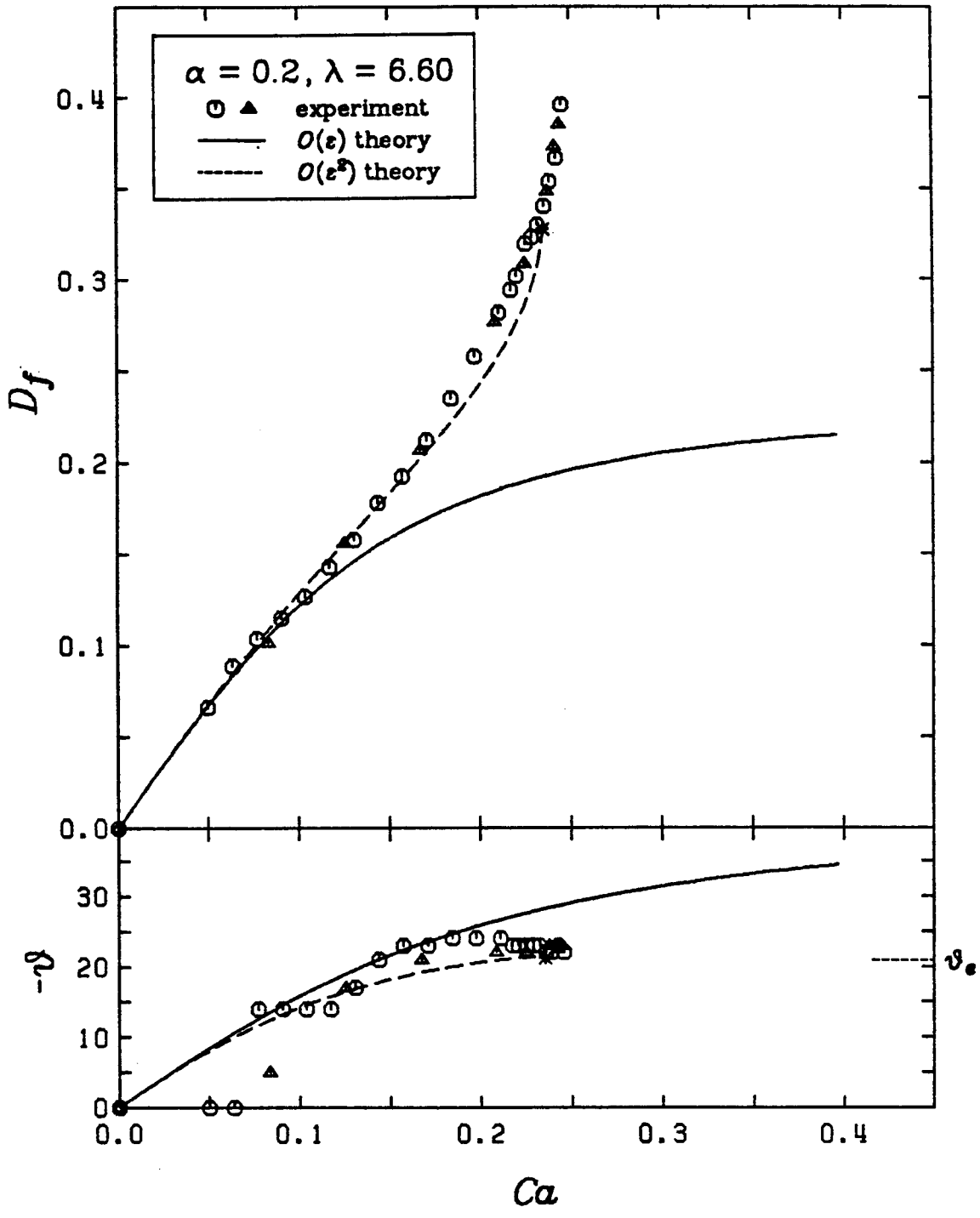

Figure A3.56
Deformation Curve for $\alpha = 0.2$, $\lambda = 6.60$

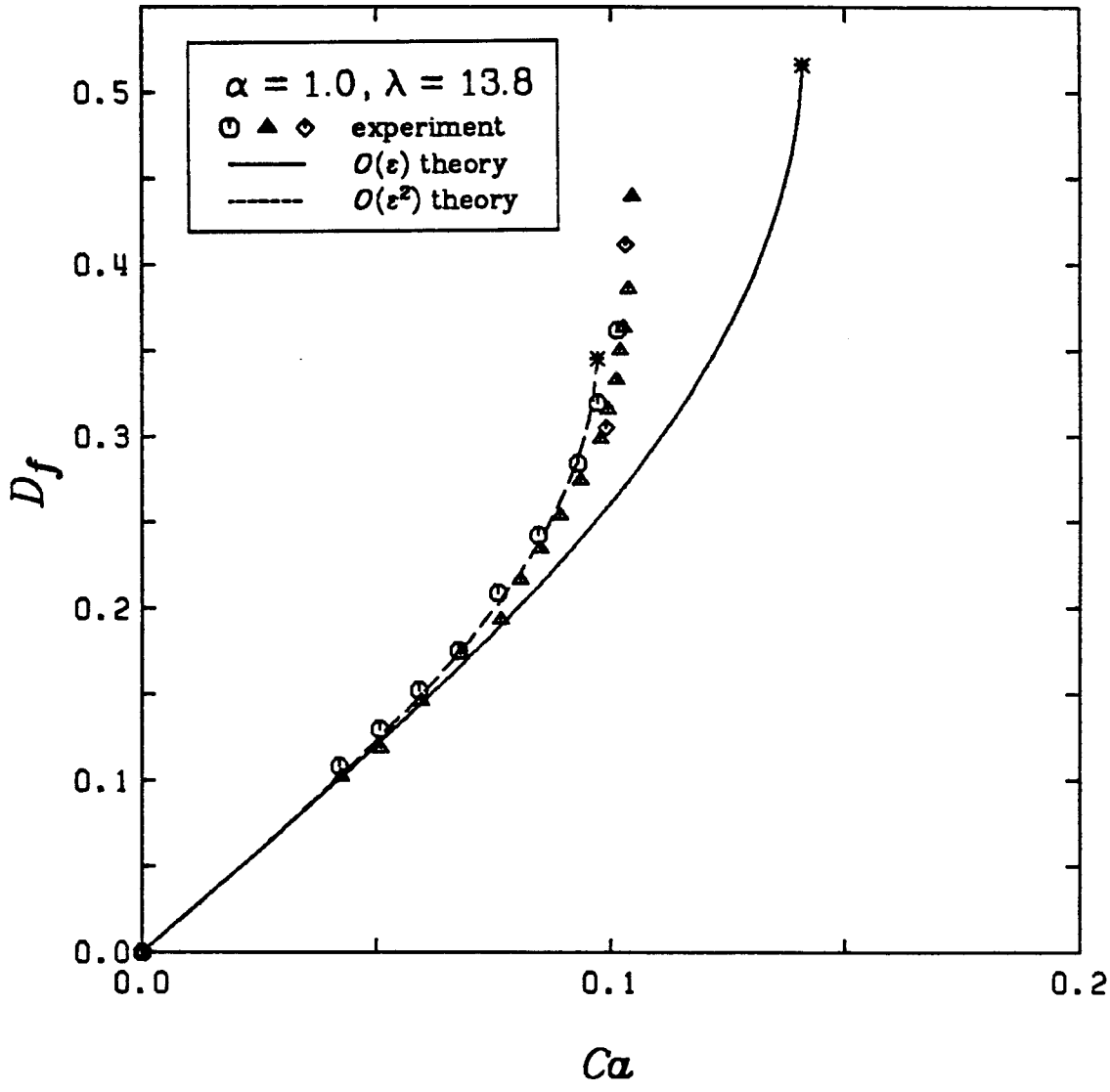

Figure A3.57
Deformation Curve for $\alpha = 1.0$, $\lambda = 13.8$

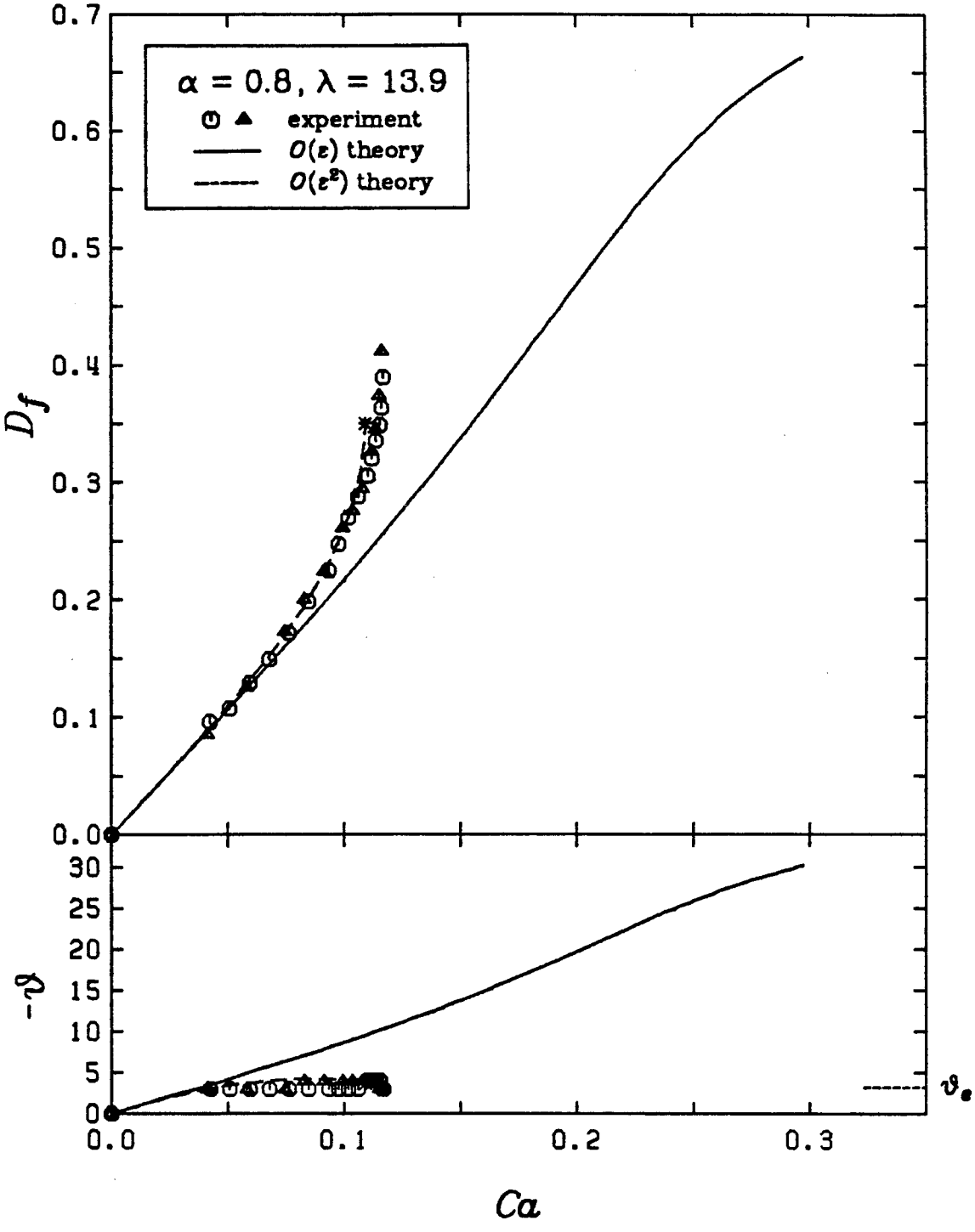

Figure A3.58
Deformation Curve for α = 0.8, λ = 13.9

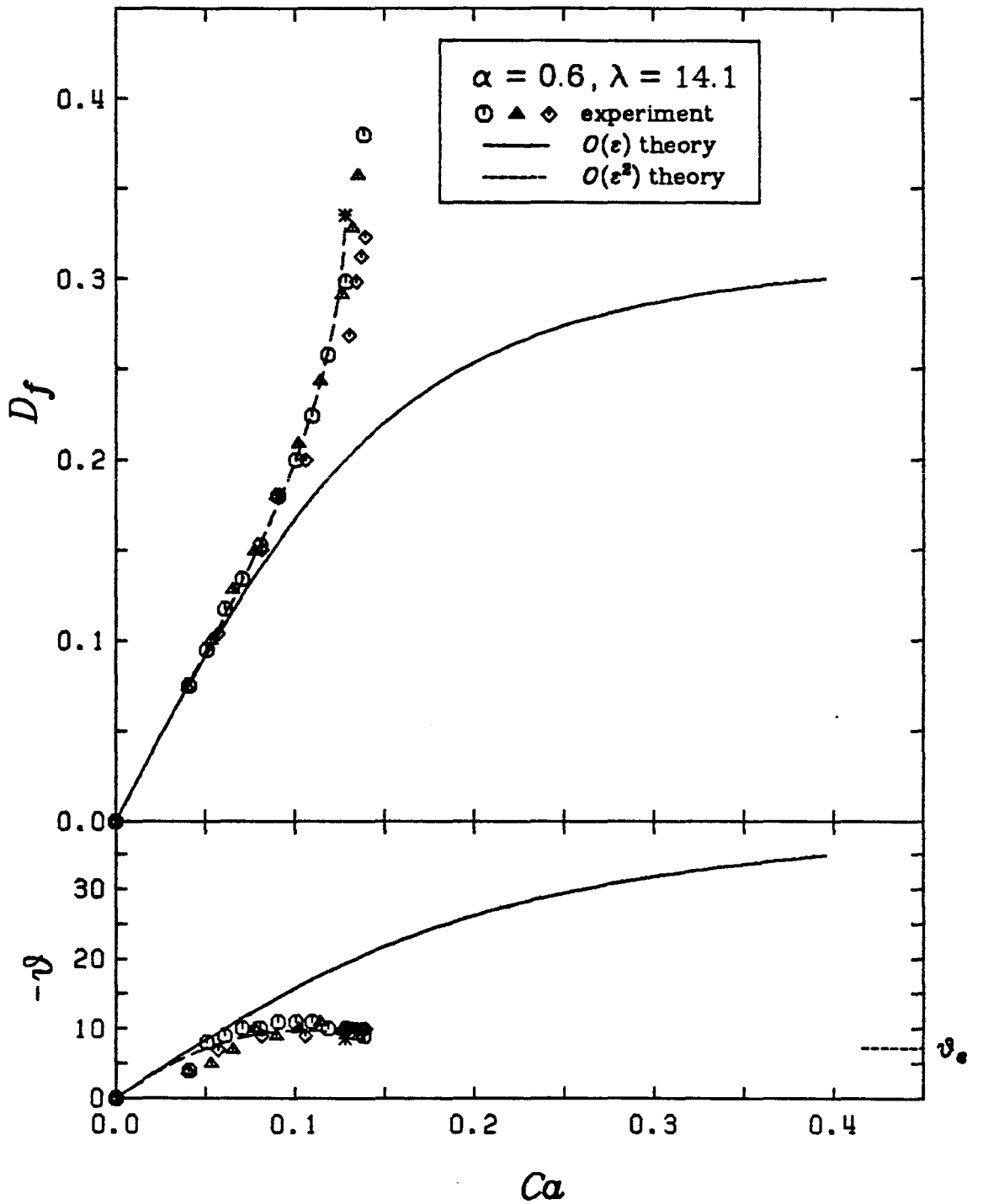

Figure A3.59
Deformation Curve for $\alpha = 0.6$, $\lambda = 14.1$

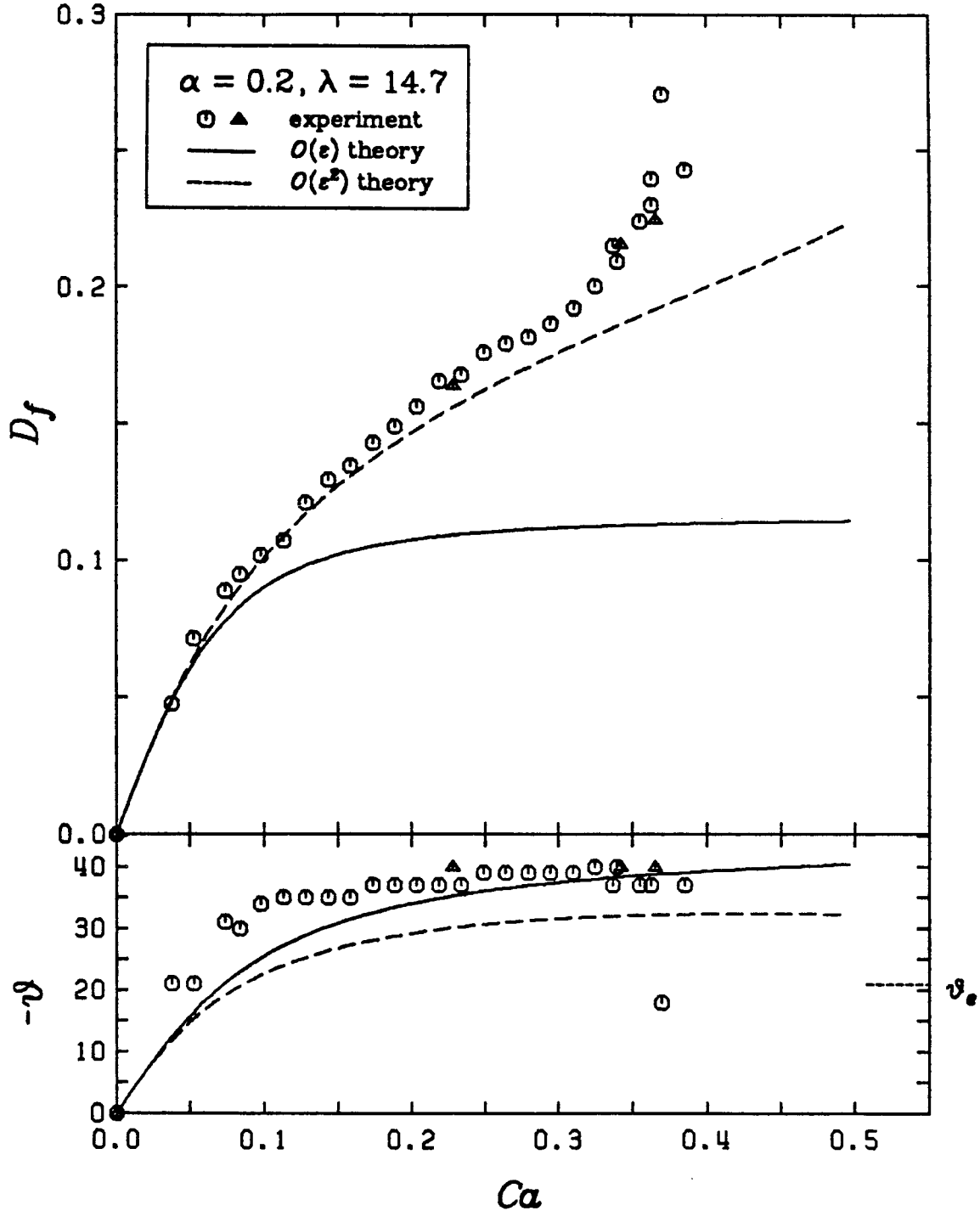

Figure A3.60
Deformation Curve for $\alpha = 0.2$, $\lambda = 14.7$

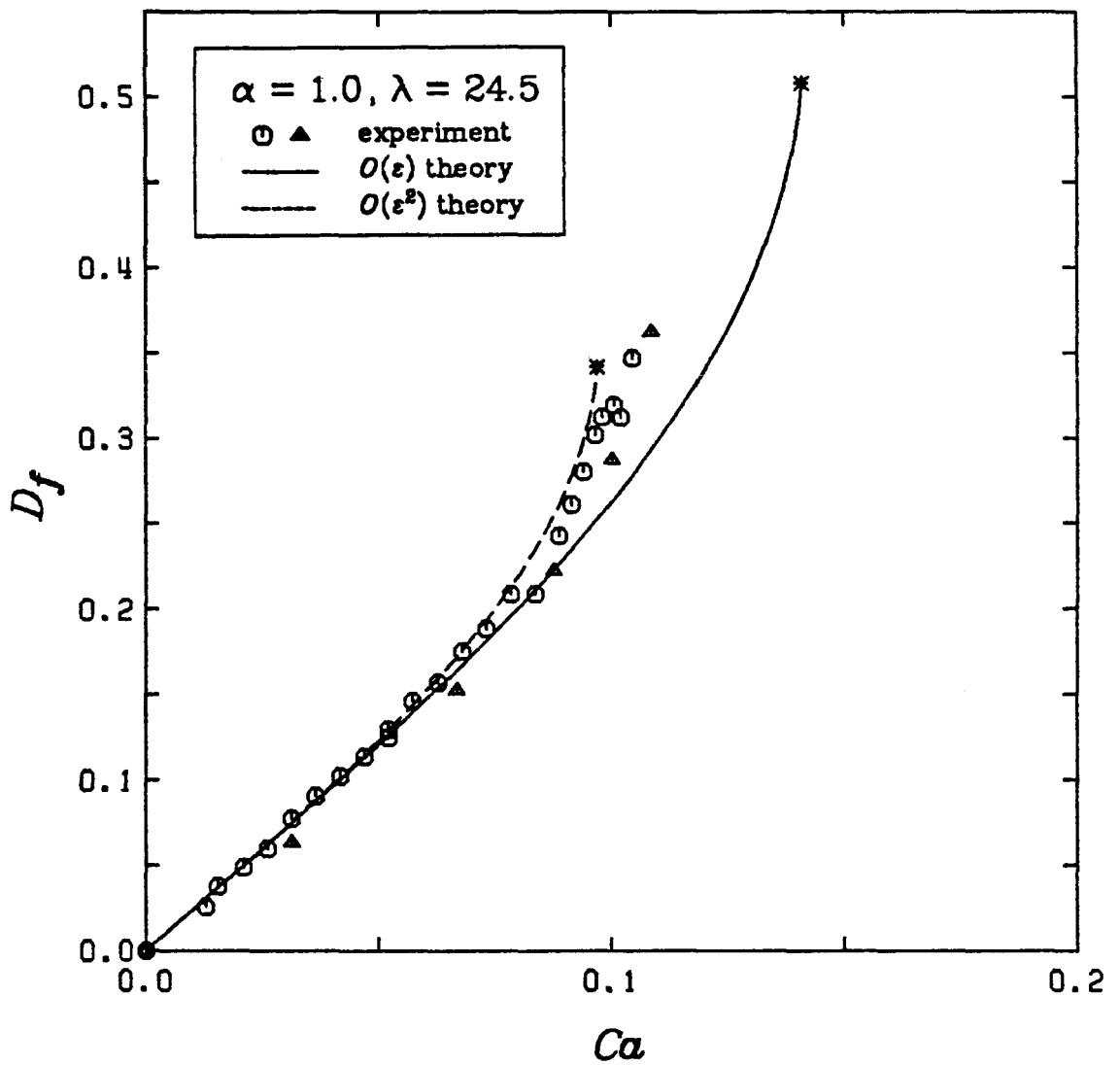

Figure A3.61
Deformation Curve for $\alpha = 1.0, \lambda = 24.5$

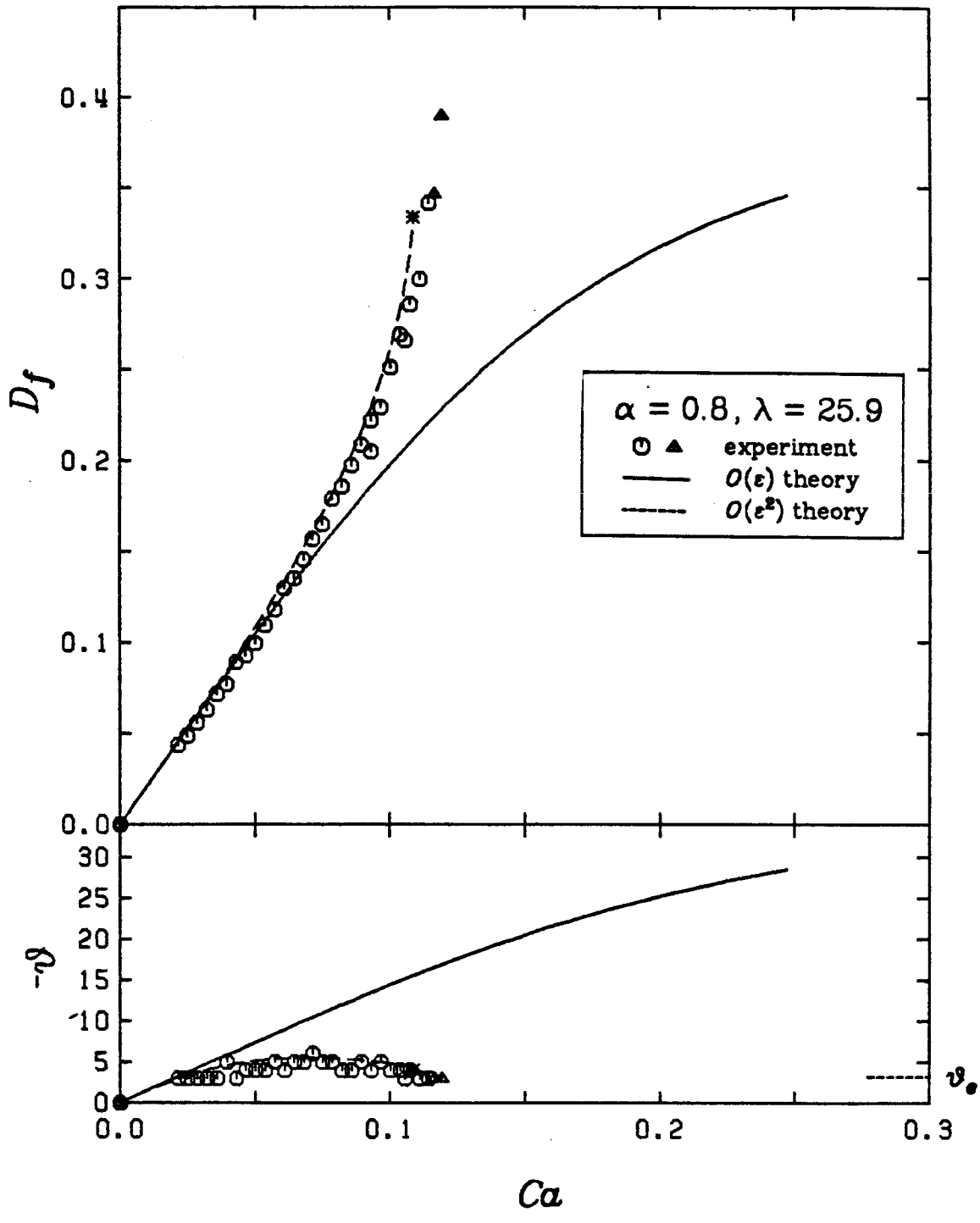

Figure A3.62
Deformation Curve for $\alpha = 0.8$, $\lambda = 25.9$

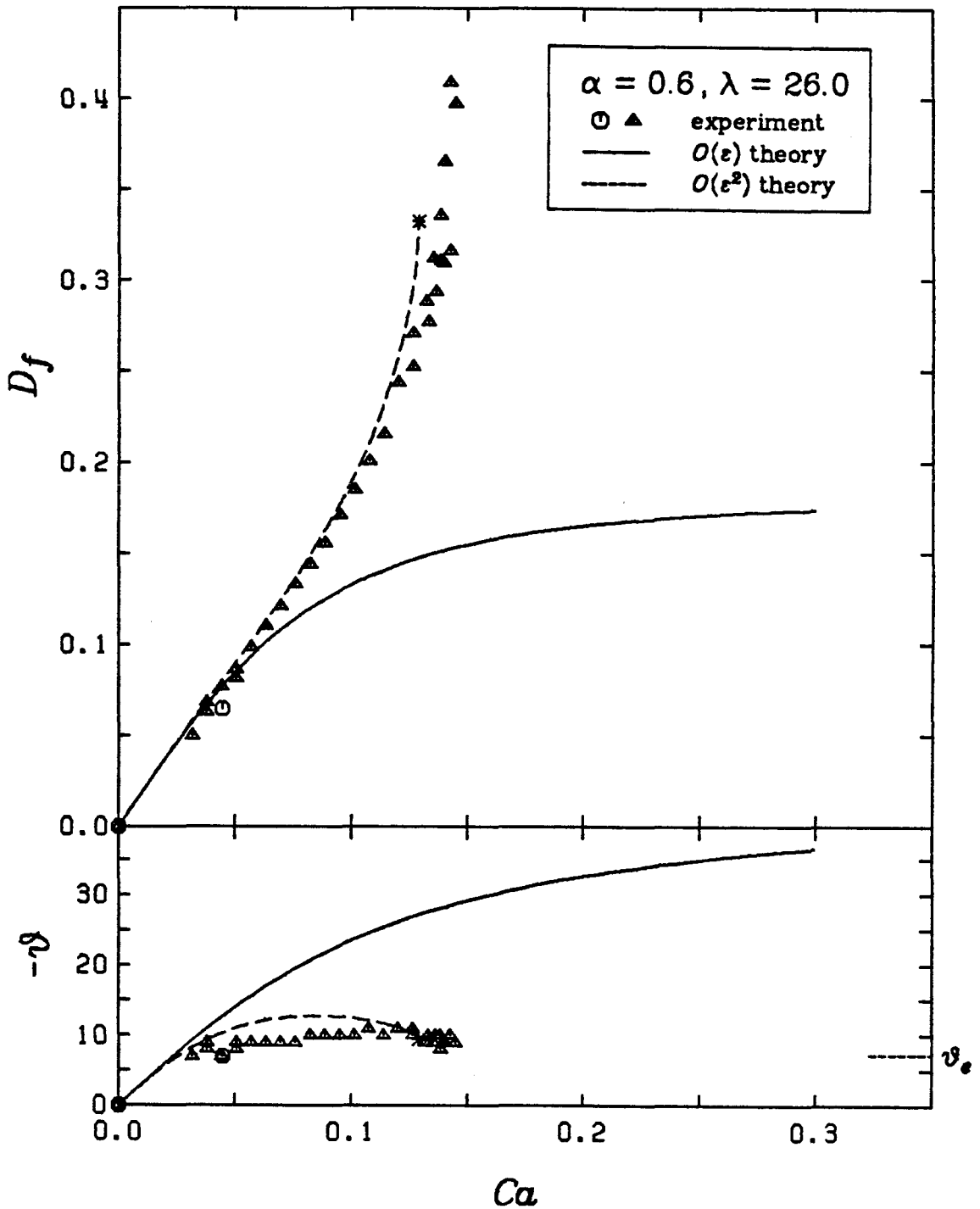

Figure A3.63
Deformation Curve for α = 0.6, λ = 26.0

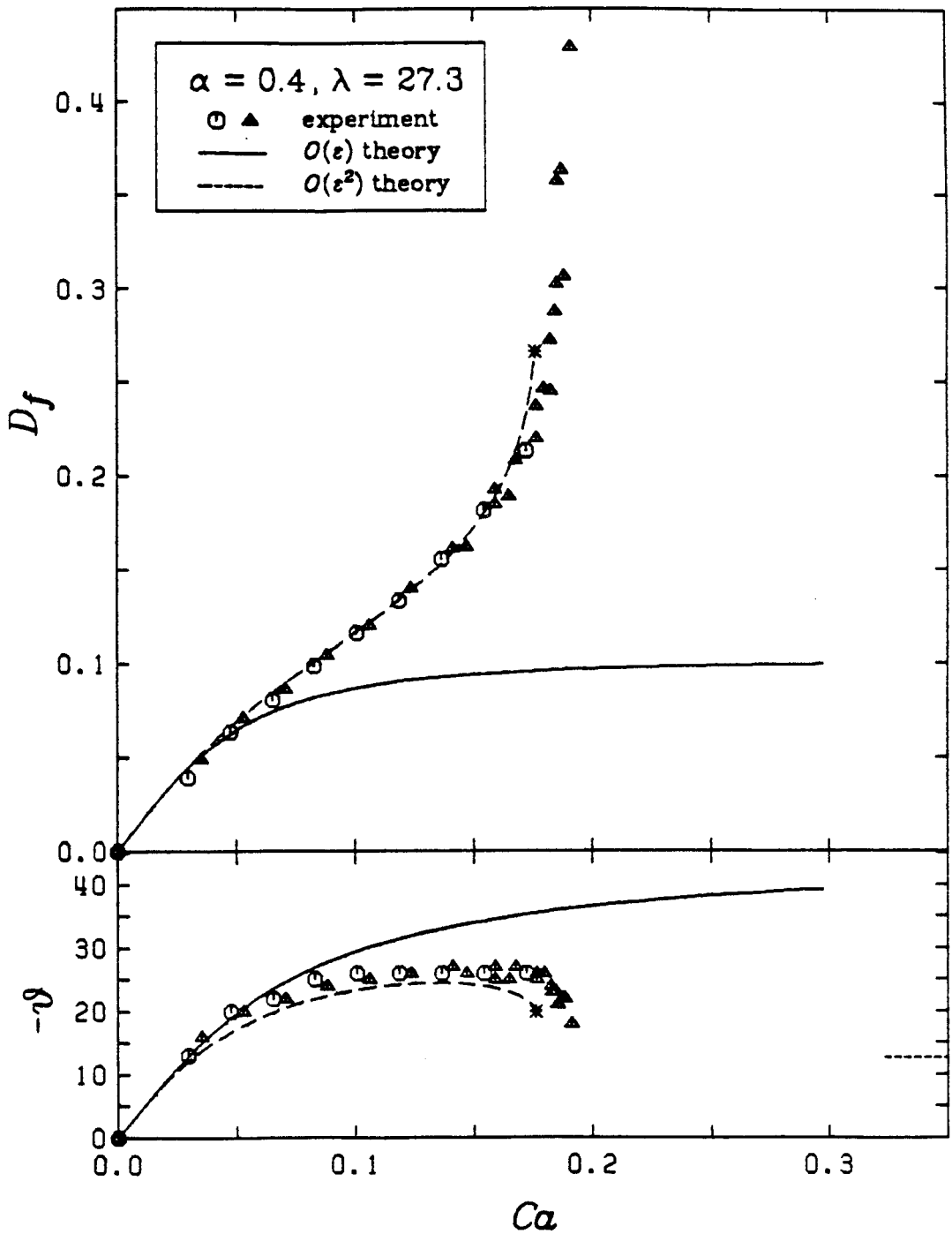

Figure A3.64
Deformation Curve for $\alpha = 0.4$, $\lambda = 27.3$